Imaging Changes in the Rodent Brain using Diffusion Weighted Multiple Boli Arterial Spin Labelling

Samantha Paterson BSc

Supervisors:

Dr. William Holmes

Dr. Jean Rodgers

Submitted in fulfilment of the requirements for the degree of Doctor of Philosophy to the Institute of Neuroscience and Psychology, College of Medical, Veterinary and Life Sciences, University of Glasgow

December 2019

Summary

This thesis combines the quantification of a new arterial spin labelling (ASL) sequence, and the development of a diffusion weighted ASL (DWASL) sequence, to examine blood brain barrier (BBB) impairment. The blood brain barrier (BBB) maintains the delicate neuroenvironment in the brain by controlling influx and efflux of cells and molecules. Many neurological disorders are effected by an impairment of the BBB. Current magnetic resonance imaging (MRI) methods to image BBB dysfunction involve the use of a contrast agent, which is invasive and not sensitive to subtle changes in BBB permeability. Non-invasive MR methods such as ASL, are able to measure perfusion and produce cerebral blood flow (CBF) maps of the brain. ASL however has an inherently low signal and therefore development of high signal-to-noise ratio (SNR) sequences are needed. Multiple boli ASL (mbASL) is a high SNR sequence that would be suitable for producing CBF maps but lacks quantification. Human African trypanosomiasis (HAT), a parasitic disease native to Africa, results in a progressive diffuse impairment of the BBB throughout the disease course. A murine model of HAT was used to examine water exchange and cerebral blood flow changes with DWASL.

Chapter 1 outlines the current literature on the blood brain barrier, HAT and splenomegaly. Chapter 2 introduces the theory of MRI, which is the imaging method used throughout the thesis. Chapter 3 provides a literature review of the ASL sequence and subsequent development of diffusion weighted ASL. The review outlines the main ASL sequences and introduces multiple boli ASL, followed by diffusion weighted ASL. These two sequences are used throughout this thesis.

Chapter 4, the first results chapter, experimentally validates the quantification of the mbASL sequence. Chapter 5 outlines the development of diffusion weighted mbASL which could potentially image changes in water exchange across the BBB. Chapter 6 and Chapter 7 use the HAT mouse model first to examine changes in the water exchange in the brain and then to serially image changes in spleen volume.

Multiple Boli ASL

Arterial spin labelling (ASL) is an MR technique that can be used to measure perfusion in the brain, where the sequence is inherently low in SNR due to the subtraction of labelled and non labelled images to examine blood flow. A new ASL sequence, multiple boli ASL, was developed as a high SNR alternative to the cur-

rent ASL sequences. However, the sequence lacked quantification with no current kinetic model able to describe mbASL as it uses a train of adiabatic pulses to label the arterial blood. The first thesis hypothesis is thus:

- Modification of the Buxton kinetic model will accurately describe the multiple boli ASL signal and produce cerebral blood flow values that agree with current literature.

To test this hypothesis, the mbASL sequence was successfully quantified and experimentally validated in rodents. The number of labelling pulses needed to obtain pseudo-continuous labelling was optimised and the distribution of signal at different delay times was fitted to the new mbASL kinetic model. High SNR mbASL images were produced with cerebral blood flow values agreeing with the literature.

Diffusion Weighted ASL

A current non-invasive method to image water exchange in the brain is diffusion weighted ASL. This sequence uses a diffusion gradient pair to separate the intravascular (IV) or extravascular (EV) signal from labelled water. It was hypothesised that:

- By adding diffusion gradients to the mbASL sequence, a diffusion weighted mbASL will be sensitive to changes in water exchange.

To test this theory, the diffusion weighted mbASL sequence was developed to use a new interleaving data collection and perform multiple b-values in the same scan. By increasing the delay time between labelling and imaging, a significant difference in signal was seen, showing the sequence was sensitive to changes in water exchange in the brain. The sequence produced similar results to studies in the literature using DWASL in humans.

Application of DWASL to HAT

Human African trypanosomiasis is a parasitic disease that affects sub Sahara Africa. A murine model of HAT, developed at the University of Glasgow, exhibits a diffuse BBB impairment that progressively worsens over the course of infection. Research

into the BBB impairment in HAT has been performed using contrast enhanced MRI, with no research using a non-invasive method. It was therefore proposed that:

- DWASL would be able to image changes in the permeability of the blood brain barrier in HAT infected mice that have not been detected using conventional contrast enhanced MR.

Exploration of this hypothesis showed no significant difference in the pseudo-permeability of the BBB between the uninfected and infected time points. Data from the late stage of the infection suggested a drop in the rate of water exchange. A further study monitoring the weight of the wet and dry brain to examine the water content in infected and non-infected mice saw a significant decrease in the water content of infected brains. Overall the study demonstrated the expected increase in water exchange did not occur, and instead suggested that the sequence is either not yet sensitive enough to detect the small changes in water exchange in the HAT infected brain or there are not large changes in water transfer as expected.

Serial Imaging of Splenomegaly

Splenomegaly is an enlargement of the spleen and a known symptom of HAT, which is observed in rodents, cattle and humans. Although the extent of the splenomegaly has been measured invasively by examining the organ post-mortem, the change in splenomegaly has not been measured serially. Therefore the following two questions were investigated:

- Is MRI able to image splenomegaly serially in a murine model of HAT and correlate with clinical and histological parameters?
- Do the procedures associated with serial MR scanning and blood sampling induce changes in the spleen of healthy mice?

Two experiments were conducted: to measure splenomegaly serially throughout five infection time points and to assess the effects of serial MR imaging and sampling on the spleen. Significant changes were seen in the spleen of infected mice compared to pre-infection in MR images. No changes were seen in the healthy mice. Haematological analysis demonstrated that the infected mice developed anaemia as the study progressed, where the healthy mice showed no haematological changes compared to the published normal range values.

"*If you walk the footsteps of a stranger*
You'll learn things you never knew, you never knew"

Alan Merkin

Contents

List of Figures

List of Tables

Acknowledgements

I would firstly like to offer my appreciation of my two supervisors Dr William Holmes and Dr Jean Rodgers. This thesis would not have been possible without either of you. Thank you to William for all your help and knowledge in teaching me MRI theory, how to use the scanner and all your feedback on abstracts and my thesis. Thank you to Jean for your patience in helping me learn a lot of new biology, teaching me about sleeping sickness, the spleen and histology and all your feedback. I can not forget all the support from Kyle when going through my histology slides! A huge thank you also goes to Dr Antoine Vallatos for not just his help and collaboration with the mbASL project, but for teaching me so much about programming, MR and DWASL over the years. I've enjoyed working on the mbASL model over a Starbucks!

None of my experiments would have been possible without Jim Mullins, Linda Carberry, Lindsay Gallagher and Conor Martin of GEMRIC. Thank you to Jim for setting up the scanner and helping me with scan preparation, along with solving the many problems I found throughout the way. My scanning sessions would have been a lot longer if it wasn't for our conversations about Marvel and Arrowverse! To Linda, Lindsay and Conor, I can not put into words how much I appreciate all your help with the animal and scanning portion of the last four years. I especially appreciate all the amazing teaching and training you have given me Lindsay. Thanks also go to Dr Jozien Goense, who without I would not have been able to finish this thesis in time. I have enjoyed my time at Glasgow with my fellow PhD students: Haitham, Abdulrahman, Mohammad, Rob and Majdi. Thank you for all the laughs, and being a great support during the ups and downs of a PhD.

I would not have been able to complete the research and writing without the support of my friends and family. To Anthony, thank you for always believing in me and being my rock throughout my time at university. Even when times were tough, thank you for being by my side supporting me through the stress of my analysis code never working, my worrying over nothing most of the time and my general panic I would never finish writing. To my sister Hazel, I appreciate all the cups of tea you have brought me, for always being a listening ear when I talk about my research constantly and reminding me to practise self-care when writing was taking over my life. To Lucy, Oscar and Charlie, thank you for being my small and cute stress relievers! Finally, to my Mum and Dad, thank you for always pushing me at school to be the best I could be and for helping me get to where I am today. You have shown me I could achieve something I could have only dreamed of and I will always be grateful for this.

Abstracts

Paterson, S., Vallatos, A., Rodgers, J., Gallagher, L., Carberry, L., Holmes, W. (2019). Imaging Changes in Blood Brain Barrier Permeability in a Human African Trypanosomiasis Mouse Model using Diffusion Weighted Multiple Boli Arterial Spin Labelling. *ESMRMB 2019 36th Annual Scientific Meeting. 3rd - 5th October 2019. Rotterdam.*

Paterson S., Vallatos, A., Holmes, W. (2019). Quantification of Multiple Boli Arterial Spin Labelling in Mice and Rats. *ESMRMB 2019 36th Annual Scientific Meeting. 3rd - 5th October 2019. Rotterdam.*

Paterson, S., Carberry, L., Holmes, W., Rodgers, J. (2019). Longitudinal Imaging of Splenomegaly in the Sleeping Sickness Infected Mouse. *ESMRMB 2019 36th Annual Scientific Meeting. 3rd - 5th October 2019. Rotterdam.*

Paterson, S., Vallatos, A., Rodgers, J., Holmes, W. (2019). Imaging Changes in the Blood Brain Barrier in the HAT infected mouse using Diffusion Weighted Multiple Boli Arterial Spin Labelling. *BC-ISMRM 2019. 16th - 18th September 2019. University of Sheffield.*

Paterson, S., Graff, C., Vallatos, A., Holmes, W. (2019). Quantification of Multiple Boli Arterial Spin Labelling in Rodents. *BC-ISMRM 2019. 16th - 18th September 2019. University of Sheffield.*

Paterson, S., Holmes, W., Carberry L., Rodgers, J. (2019). Serial imaging of splenomegaly in the sleeping sickness mouse. BC-ISMRM 2019. *BC-ISMRM 2019. 16th - 18th September 2019. University of Sheffield.*

Paterson, S., Graff, C., Vallatos, A., Holmes, W. (2019). Quantification of Multiple Boli Arterial Spin Labelling in Mice and Rats. *ISMRM 27th Annual Meeting & Exhibition. 11th - 16th May 2019. Montréal, QC, Canada.*

Paterson, S., Vallatos, A., Rodgers, J., Holmes, W. (2019). Imaging Blood Brain Barrier Permeability in a Human African Trypanosomiasis Mouse Model using Diffusion Weighted Multiple Boli Arterial Spin Labelling. *ISMRM 27th Annual Meeting & Exhibition. 11th - 16th May 2019. Montréal, QC, Canada.*

Paterson, S., Vallatos, A., Holmes, W. (2019). Adapting Diffusion Weighted Arterial Spin Labelling (DWASL) to use a Single Sided Bipolar Diffusion Gradient to Probe Microvascular Signal. *ISMRM 27th Annual Meeting & Exhibition. 11th - 16th May 2019. Montréal, QC, Canada.*

Paterson, S., Graff, C., Vallatos, A., Holmes, W. (2018). Quantification of Multiple Boli Arterial Spin Labelling in Mice and Rats. *BC-ISMRM 2018. 24^{th} - 26^{th} September 2018. University of Oxford.*

Paterson, S., Vallatos, A., Gallagher, L., Rodgers, J., Holmes, W. (2017). Using Diffusion Weighted Arterial Spin Labelling for Imaging Subtle Changes in Blood Brain Barrier Permeability using a Sleeping Sickness Mouse Model. *ESMRMB 2017 34th Annual Scientific Meeting. 19^{th} - 21^{st} October 2017. Barcelona.*

Paterson, S., Vallatos, A., Gallagher, L., Rodgers, J., Holmes, W. (2017). Using Diffusion Weighted Arterial Spin Labelling to probe Blood Brain Barrier Permeability using a Sleeping Sickness Mouse Model. *BC-ISMRM 2017. 11^{th} - 13^{th} September 2017. University of Liverpool.*

Paterson, S., Vallatos, A., Gallagher, L., Rodgers, J., Holmes, W. (2016). Developing a Novel Method for Imaging Subtle Changes in Blood Brain Barrier Permeability. (2016). *BC-ISMRM 2016. 7^{th} - 9^{th} September 2016. University of Leeds.*

Declaration

I, Samantha Paterson, declare that this thesis titled, “Imaging Changes in the Rodent Brain using Diffusion Weighted Multiple Boli Arterial Spin Labelling” and the work presented in it are my own. I confirm that:

- This work was done wholly or mainly while in candidature for a research degree at this University.
- Where any part of this thesis has previously been submitted for a degree or any other qualification at this University or any other institution, this has been clearly stated.
- Where I have consulted the published work of others, this is always clearly attributed.
- Where I have quoted from the work of others, the source is always given. With the exception of such quotations, this thesis is entirely my own work.
- I have acknowledged all main sources of help.
- Where the thesis is based on work done by myself jointly with others, I have made clear exactly what was done by others and what I have contributed myself.

Signed:

Date: 22/06/2020

Abbreviations

1BDP	one-barrier distributed parameter
ADC	Apparent diffusion coefficient
ADC	Analogue-to-digital converter
AQP4	Aquaporin-4
ATT	Arterial transit time
BBB	Blood brain barrier
CA	Contrast agent
CASL	Continuous arterial spin labelling
CBF	Cerebral blood flow
CBV	Cerebral blood volume
CE-MRI	Contrast enhanced magnetic resonance imaging
CI	Continuous inversion time
CNS	Central nervous system
DTPA	Diethylenetriamine pentaacetic acid
DWASL	Diffusion weighted arterial spin labelling
DWI	Diffusion weighted imaging
EPI	Echo planar imaging
EPISTAR	Echo planar imaging-based signal targeting by alternating radiofrequency pulses
EV	Extravascular
FAIR	Flow-sensitive alternating inversion recovery
FLAIR	Fluid attenuated inversion recovery
FLASH	Fast low angle shot
FOV	Field-of-view
FT	Fourier transform
FID	Free induction decay
Gd	Gadolinium
GE	Gradient echo
HAT	Human African trypanosomiasis
Hb	Haemaglobin
HCT	Haematocrit
HS	Hyberbolic secant
IgM	Immunoglobulin M
IP	Intraperitoneally

IR	Inversion recovery
ISMRM	International society of magentic resonance in medicine
IV	Intravascular
IV	Intravenously
IVIM	Intravoxel incoherent motion
mbASL	Multiple boli arterial spin labelling
MRI	Magnetic resonance imaging
NA	Number of averages
NBF	Neutral buffered formalin
NK	Natural Killer
NSF	Nephrogenic systemic fibrosis
NMR	Nuclear magnetic resonance
NP	Number of pulses
NSF	Nephrogenic systemic fibrosis
PASL	Pulsed arterial spin labelling
PBGS	Phosphate buffered saline plus glucose
pCASL	Pseudo continuous arterial spin labelling
PCR	Polymerase chain reaction
PET	Positron emission tomography
PGSE	Pulsed gradient spin echo
PLD	Post labelling delay
PS	Permeability surface area product
pTILT	Pseudo-continuous transfer insensitive labelling technique
RARE	Rapid acquisition with refocused echoes
RBC	Red blood cell
RF	Radio frequency
ROI	Region of interest
SAR	Specific absorption rate
SE	Spin echo
SLC	Solute carrier
SNR	Signal-to-noise ratio
SPA	Single pass approximation
SSDWASL	Single sided diffusion weighted arterial spin labelling
TE	Echo time
TI	Inversion time
TJ	Tight junction
TR	Repetition time
Tb	Trypanosoma brucei
WBC	White blood cell

List of Symbols

α	Flip Angle	$^\circ$
α	Labelling Efficiency	
α_E	Ernst Angle	$^\circ$
ΔP	Applied pressure difference	Pa
δ	Arterial Transit Time	s
η	Adiabatic Factor	
η	Viscosity	$Pa.s$
γ	Gyromagnetic Ratio	$rad \cdot s^{-1} \cdot T^{-1}$
$\hbar$	Plank Constant $/2\pi$	$1.0546 \times 10^{-34}\, Js$
λ	Blood-Brain Coefficient of Water	ml/g
μ	Magnetic Dipole Moment	$A\ m^2$
ω	Angular Frequency	Hz
τ	Delivery Arrival of Labelled Blood (PASL)	s
τ	Labelling Duration (CASL)	s
τ	Torque	Nm
τ_c	Correlation Time	s
$\mathbf{B}_0$	Equilibrium Magnetic Field	T
$\mathbf{B}_1$	Oscillating Magnetic Field	T
E	Energy	J
h	Plank Constant	$6.62607 \times 10^{-34}\, Js$
I	Nuclear Spin Quantum Number	$\frac{1}{2}$
K	Permeability	m^2
K_B	Boltzmann Constant	$1.38064852 \times 10e^{-23}\, m^2 kgs^{-2} K^{-1}$
K_w	Water exchange rate constant	min^{-1}
L_{im}	Imaging Slice	mm
L_{inv}	Labelling Slab	mm
L_i	Slab Edge to Slice Edge	mm

PS	Permeability surface area product	ml/100g/min
T	Temperature	K
T_1	Relaxation	s
T_2	Relaxation	s
T_2^*	Relaxation	s
t_p	Pulse Length	ms
v	Velocity	m/s
V_{blood}	Mean Blood Velocity	mm/s
V_c	Capillary distribution volume	ml/100g
$\mathbf{B}$	Magnetic Field	T
$\mathbf{M}$	Net Magnetisation	
b	b-value	s/mm^2
D	Diffusivity	mm^2/s
f	Cerebral Blood Flow	ml/100g/min
L	Spin Angular Momentum	
t	Time	s
TE	Echo Time	s
TR	Repetition Time	s

Symbols without units are constants and do not have a unit.

Chapter 1

The Blood Brain Barrier, Human African Trypanosomiasis and the Spleen

This chapter discusses the blood brain barrier (BBB) along with the current imaging methods and their limitations. A biological model for disruption of the BBB is human African trypanosomiasis (HAT). This disease is described along with the current research findings from investigation using MRI. The chapter closes by exploring the current literature surrounding the development of splenomegaly, a common clinical manifestation associated with trypanosome infection.

1.1 The Blood Brain Barrier and CNS

1.1.1 The Central Nervous System

The central nervous system (CNS) is comprised of the brain and spinal cord. The brain can be split into the brain stem, which is the continuation of the spinal cord and the cerebellum, and the cerebrum (Brodal 2010). The spinal cord contains grey and white matter. The grey matter contains motor neurons and sensory neurons, with the white matter containing ascending tracks which carry signals and descending tracks that let the brain control the spinal cord neurons. The cerebrum consists of two central hemispheres that are divided by the longitudinal cerebral fissure (Brodal 2010). The cerebrum includes the cerebral cortex (composed of a folded sheet of grey matter), hippocampus and basal ganglia. The brain contains interstitial fluid, which surrounds the neurons and glia. The ventricles and external surfaces of the brain contain cerebral spinal fluid (CSF), which is produced in

the ventricles by the choroid plexus (Segal 2000).

1.1.2 History of the Blood Brain Barrier

In the late 1800s, Paul Ehrlich experimentally showed that intravenously injected dye stains the tissue and organs of animals with the exception of the brain and spinal cord (Ehrlich 1900). Ehrlich attributed this lack of uptake to a low affinity of the nervous tissue to the dye. The concept of a barrier was first hypothesised by Max Lewandowsky in 1900 (Lewandowsky 1900). Lewandowsky intravenously injected sodium ferrocyanide and found no pharmacological effects on the nervous system, but symptoms appeared however, after direct injection of the sodium ferrocyanide into the brain. Following these experiments, the term 'blut hirn schranke' or 'blood brain barrier' was first coined by Lewandowsky. One of Ehrlich's students, Edwin Goldmann, further demonstrated the concept of this 'brain barrier' by using the dye trypan blue. When directly injecting the trypan blue in to the cerebral spinal fluid (CSF) of a dog, he found the brain was stained but the body of the animal was not. When he preformed the opposite experiment, by intravenously injecting the dye into the body of the animal, he found the body stained but not the brain (Goldmann 1909; Goldmann 1913). These experiments showed a clear division between the peripheral and cerebral compartments confirming the 'barrier' hypothesis.

Lina Stern, a Russian scientist, performed many experiments on the CNS by injecting different agents and dyes into the blood, cerebral ventricles and subarachnoid space in the 1920s. Stern's experiments showed amongst other observations, that all substances from the brain will eventually reach the blood, but not all substances in the blood will reach the brain, and that the subarachnoid space is connected to the cerebral ventricles (Vein 2008). Stern concluded that a barrier must exist to protect the CNS and called it the hematoencephalic barrier (Stern 1922; Stern 1921). Stern further found that certain treatments administered via the bloodstream did not cross into the CNS, most notably the injection of an anti-tetanus medication did not treat the tetanus once it was established in the CNS, unless injected directly into the brain (Vein 2008).

The fundamental features of the BBB were established by Reese and Karnovsky in 1967, by intravenous injection of horseradish peroxidase to mice and examination of the cerebral cortex using electron microscopy. The main findings showed that the peroxidase was not present beyond the vascular endothelium, but was seen in the lumina of the blood vessels, with low numbers of vesicles which did not appear to transport the peroxidase (Reese et al. 1967). Reese and colleagues believed that the tight junctions between the endothelial cells were responsible for preventing

the peroxidase from leaving the vessels and concluded that a barrier was present at the ultra-structural level. This study demonstrated that the brain endothelium was less permeable to peroxidase than of the heart or skeletal muscle, where peroxidase has been shown to penetrate through the endothelial cell layer, suggesting a difference in 'tightness' of the junctions present between the endothelial cells (Reese et al. 1967).

1.1.3 Blood Brain Barrier

The blood brain barrier is one of three barriers that exist in the central nervous system, along with the blood-CSF barrier and the arachnoid barrier (Figure 1.2). The primary function of the BBB is to regulate the exchanges between the blood and brain. It is a semi-permeable diffusion barrier, consisting of endothelial cells with tight junctions (TJs) formed between them. These junctions, formed from the membrane proteins claudin, occludin and junction adhesion molecules, plus cytoplasmic accessory proteins, regulate and restrict the movement of molecules in and out of the brain (Ballabh et al. 2004). The endothelial cells joined by tight junctions, line the capillary walls and are crucial in the prevention of toxic substances entering the brain. The endothelial cells can act as mediators between the blood and brain, whilst regulating the transport and metabolism of substances going between the blood and brain (Cardoso et al. 2010). The basement membrane, which separates the perivascular space from the brain parenchyma, surrounds the endothelial cells with pericytes embedded within the membrane. Pericytes, also known as vascular smooth muscle cells, help regulate microcirculatory blood flow and provide structural support to help maintain the integrity of the tight junctions (Gursoy-Ozdemir et al. 2017). Astrocytes are a type of glial cell, which provide support for the endothelial cells (Persidsky et al. 2006) and are important in the function of neurons. Astrocyte end-feet surround most of the brain capillary and interact with the basement membrane. The endothelial cells, tight junctions, basement membrane, pericytes, astrocytes, neurons and microglia cells together form the neurovascular unit (NVU) (Figure 1.1) that are essential for maintaining the health and function of the CNS (Cardoso et al. 2010).

1.1.3.1 Transport Across the BBB

There are multiple pathways that can be used to access the brain. Passive diffusion across the BBB occurs either through (transcellular transport) or between the vascular endothelial cells (paracellular transport) (Cardoso et al. 2010). Small lipophilic molecules such as carbon dioxide and oxygen can cross into the brain

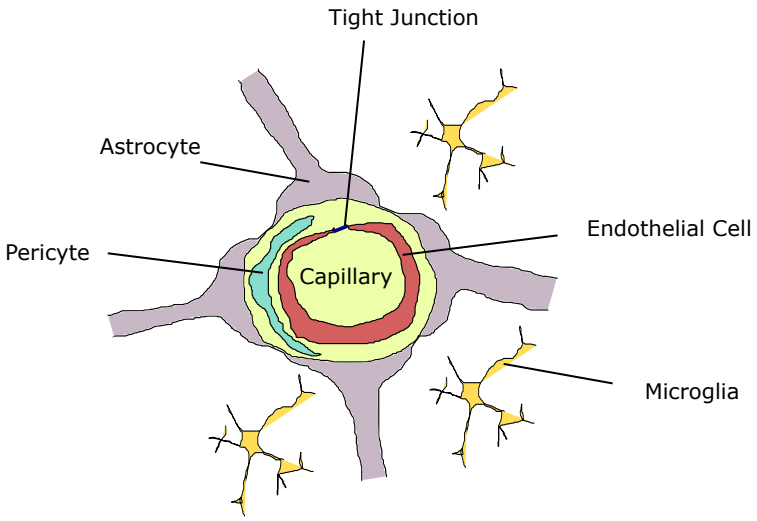

Figure 1.1: Components of the blood brain barrier

The blood brain barrier consists of endothelial cells joined by tight junctions. Along with astrocytes, pericytes, neurons and microglia, they make up the neurovascular units, crucial for maintaining homeostasis in the brain. The figure design is based on (Abbott, Ronnback, et al. 2006).

by transcellular diffusion. For paracellular transport, ions and solutes can diffuse between the cells, depending on their concentration gradient. Polar molecules, such as glucose and amino acids, cannot cross into the brain by diffusion pathways. These molecules are transported by solute carriers (SLCs) which are based in the lipid bilayer of the endothelial cell membrane at both the luminal and abluminal surfaces. This control helps to preserve the polarity of the barrier by limiting the free movement of the molecules from one side of the endothelium to the other (Abbott, Patabendige, et al. 2010). ATP-binding cassette (ABC) transporters are efflux pumps that consume ATP and transport lipophilic compounds out of the brain (Lalatsa et al. 2018) and function to protect the brain from toxic molecules. However, this also acts as a barrier to potential drug treatments, preventing many chemotherapeutic agents from entering the CNS.

1.1.3.2 Water Transport Across the BBB

Although water molecules can cross the BBB by crossing the cell plasma membrane directly (Papadopoulos et al. 2013), the primary water channel in the brain, formed by the protein aquaporin-4 (AQP4), plays a major part in water transportation in the brain. AQP4 is found in the astrocytes and the choroid plexus epithelial cells, suggesting that AQP4 facilitates the flow of water in and out of the brain. As water is a small molecule, it can diffuse through the endothelial cells of the BBB, with Papadopoulos' review on AQP4 showing that multiple studies support the idea that AQP4 plays a major part in determining the permeability of the BBB to water (Papadopoulos et al. 2013). Badaut et al. demonstrated that animals with a silenced AQP4 expression had a decreased water mobility measure of the apparent

diffusion coefficient (ADC) of the brain. Furthermore, Eugen et al. showed a seven fold-reduced osmotic water permeability in astrocytes that were taken from AQP4-deficient mice. Haj-Yasein demonstrated a reduction in brain water uptake in AQP4 knockout mice. Overall, there is a plethora of evidence supporting a role of AQP4 in the passage of water in and out of the brain.

1.1.4 The Blood-CSF barrier

The choroid plexus, found in the lateral, third and fourth ventricles, is responsible for the production of CSF (Abbott 2004). The capillaries in the stroma of the choroid plexus are fenestrated, allowing the movement of small molecules across the endothelial cells to enter the stroma of the choroid plexus. The blood-CSF barrier is formed by the choroid plexus epithelial cells which are joined by tight junctions and prevent molecules from entering the ventricular CSF (Figure 1.2). The choroid plexus is the main producer of CSF, with the CSF passing through the ventricles to circulate in the cerebral and spinal subarachnoid spaces. The blood CSF barrier lacks several of the cellular components comprising the BBB and is considered to be “leakier” than the more abundant BBB.

1.1.5 The Arachnoid Barrier

The CNS is surrounded by connective tissue known as the meninges. The meninges is comprised of three membrane layers: the pia mater, the arachnoid mater, and the dura mater. The dura mater forms the outermost layer and is attached to the arachnoid mater (Brodal 2010). It is comprised of dense fibrous tissue (Papadopoulos et al. 2013). The subarachnoid space is formed between the arachnoid barrier and the underlying pia and contains CSF. The arachnoid mater is composed of multiple layers, with the innermost layer cells joined together by tight junctions, which limits entry of molecules into the subarachnoid CSF (Haines 2018).

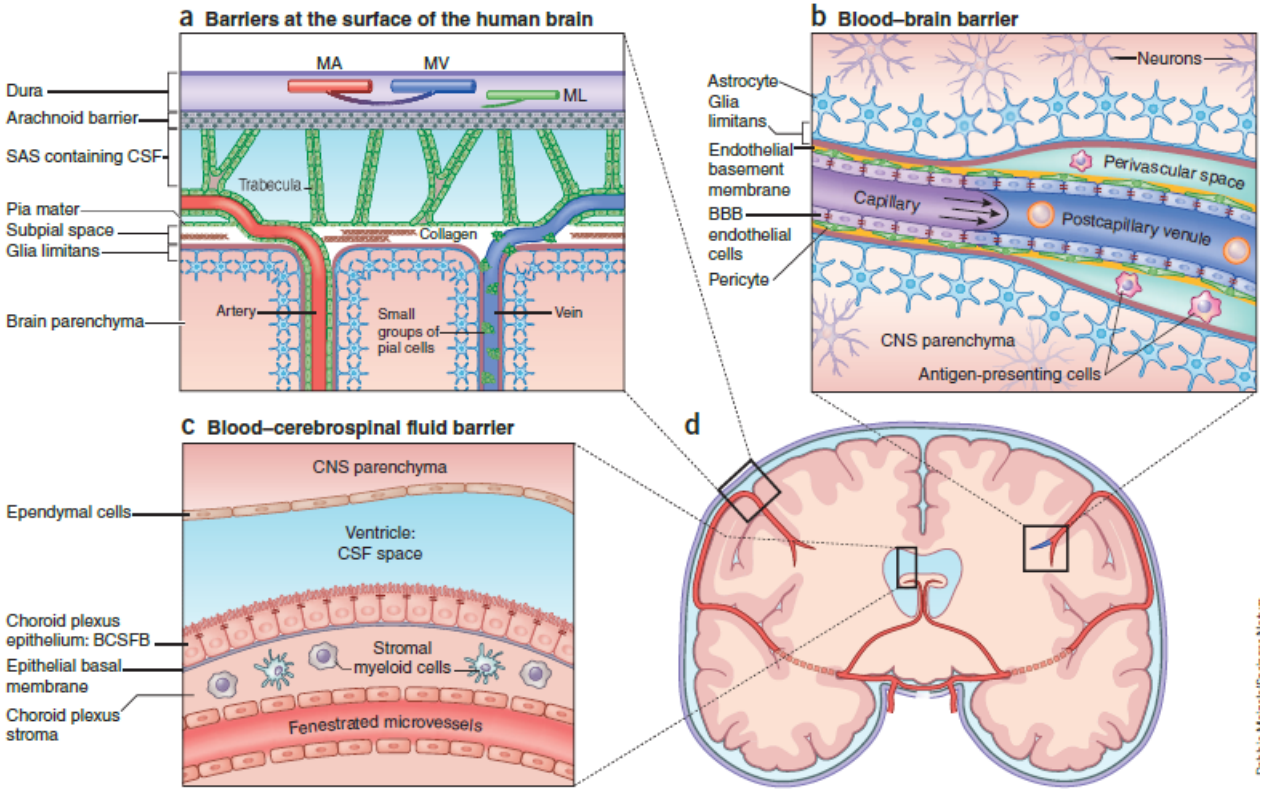

Figure 1.2: Artist impression of the different barriers in the brain

Figure adapted from (Engelhardt et al. 2017). a) The main barriers at the surface of the brain. The dura mater is supplied by the meningeal veins (MV) and meningeal arteries (MA). The arachnoid barrier surrounds the CSF and provides a barrier to the subarachnoid space (SAS). The pia mater coats the arteries and veins of the SAS with the subpial space and glia limitans separates the SAS from the the brain parenchyma. b) The blood brain barrier contains endothelial cells connected by tight junctions, and controls the transport of molecules in and out of the brain. The endothelial cells are coated in a basement membrane with pericytes embedded and the astrocyte and glia limitans connected to the membrane. c) The choroid plexus has a blood-CSF barrier. The choroid plexus produces CSF, with the barrier separating the CSF from the brain parenchyma. d) A coronal brain slice of the human brain.

1.2 Permeability

If a porous material allows a fluid to pass through it, it can be described as permeable. The permeability of a porous material is therefore a measure of how permeable the substance is, and is measured in m^2 or the darcy (1 darcy $\approx 10^{-12} m^2$). The permeability of a porous material can be described by Darcy's law, which relates the flow rate and properties of the fluid to the pressure gradient applied across the material:

$$v = \frac{K}{\eta}\frac{\Delta P}{\Delta x} \tag{1.1}$$

where v is the flow velocity of the fluid, K is the permeability of the material, η is the dynamic viscosity, ΔP is the applied pressure difference and Δx is thickness of the material (Ichikawa et al. 2012).

The blood brain barrier (BBB) can be considered a porous material due to the tight junctions between the endothelial cells. The exchange of molecules between the capillary and the tissue is limited by the size of the tight junctions and the different mechanisms in place to maintain homeostasis in the brain. An estimation of the permeability of the BBB can be described by:

$$K_w = \frac{PS}{V_c} \tag{1.2}$$

where K_w is the water exchange rate constant (min^{-1}), PS is the permeability surface area product of water (ml/100g/min) and V_c is the capillary distribution volume of water (ml/100g). K_w describes the exchange of water across the BBB and is used as an estimate of the permeability of the barrier.

1.2.1 Permeability and Disruption of the Blood Brain Barrier

The permeability of the blood brain barrier is controlled by multiple factors, including endothelial cells, astrocytes, pericytes and microglia cells. Astrocytes and microglia are involved in maintaining and protecting the BBB but can amplify inflammation and cellular damage when there is disruption of the BBB. Structural changes that affect the barrier can be endothelial cell damage during inflammation, breakdown of glia limitans and changes to the astrocytic end-feet (Varatharaj et al. 2017). The tight junctions are essential for the overall integrity of the BBB (Almutairi et al. 2016). Changes in the structure of the tight junctions or altered

protein expression can result in dysfunction.

The disruption of the BBB can cause serious issues in many disorders and diseases. In brain tumours, there is increased vascular permeability due to a poorly developed BBB, with a loss of tight junction integrity (Deeken et al. 2007). Cerebral oedema is also associated with tumours. Neuroinflammation is seen in diseases such as Alzheimer's disease and multiple sclerosis, with migration of leukocytes into the brain (Zenaro et al. 2017). This migration can cause signal changes which lead to the loss of tight junction molecules such as occludin. In ischaemic stroke, there is a disruption of the tight junctions, which leads to an increased permeability of the BBB and contributes towards cerebral oedema (Sandoval et al. 2008).

1.3 Current Methods for Probing Blood Brain Barrier Disruption

1.3.1 Contrast Agents

Current methods of imaging blood brain barrier disruption using MRI include the intravenous injection of an exogenous paramagnetic contrast agent (CA). The most commonly used contrast agents are gadolinium (Gd) based, where the gadolinium ion is chelated to a molecule, to reduce toxicity. An example of a contrast agent is gadolinium- diethylenetriamine pentaacetic acid (Gd-DPTA) (Carr et al. 1984). Gadolinium is paramagnetic due to having seven unpaired electrons in its 4f outer shell and is one of only four elements that can become magnetic at room temperature; iron, nickel and cobalt being the other three. This makes Gadolinium useful as an MRI contrast agent as it shortens the T_1 relaxation of the surrounding tissue, which is observed in a T_1 weighted image as bright signal. T_2 shortening is also seen where there is high concentration of the CA but the dominant effect will be seen for T_1. Contrast agents are unable to cross the blood brain barrier when it is intact due to their molecular weight and charge (Tofts 2003).

1.3.2 Dynamic Contrast Enhanced MRI

Quantitative measurements of blood brain barrier permeability can be performed using dynamic contrast enhanced MRI (DCE-MRI). The basic principle of DCE-MRI is to take an image without contrast enhancement followed by a series of images taken after the contrast agent has been administered as a bolus. By fitting the signal from each of the images taken to a tracer pharmacokinetic model, a value of

K_{trans} or permeability can be found. K_{trans} describes the transfer rate of molecules into the interstitial space from the plasma space (Barnes et al. 2016). To quantitatively measure K_{trans}, there are multiple kinetic models that have been developed to fit DCE-MRI data. Early versions of kinetic models for DCE-MRI were based on Toft's works in the early 1990s (Tofts 1997). They were able to measure K_{trans}, interstitial volume v_e, and cerebral blood volume (CBV). These models were not able to measure CBF due to low temporal resolution. More developed models using higher quality data from improved hardware and imaging sequences, are able to measure CBF along with the permeability-surface area product (PS) (Sourbron et al. 2013). Simpler methods that are semi-quantitative can be used to measure the area under a signal enhancement curve. A qualitative method for looking at changes in BBB integrity is by taking one image before the CA has been injected and one after, known as contrast enhanced MRI (CE-MRI). If the barrier is compromised, the CA will be able to cross into the brain tissue and the resulting subtracted image will have brighter regions where the CA resides.

1.4 Limitations to Using DCE-MRI for Probing BBB Changes

DCE-MRI has become the clinical standard in MRI for imaging permeability in the brain, however there are limitations to the method. DCE-MRI is able to show signal enhancement where there are large changes in BBB integrity. However, where there are small subtle changes in the BBB, the technique lacks sensitivity, failing to show changes in conditions such as dementia, acute stroke and glioma invasion (Armitage et al. 2011; Brix et al. 1991; Raja et al. 2018). This is due to the low concentration and weak relaxivity of contrast agents, which limits their ability to increase the relaxation rate of the tissue around them (Werner et al. 2008). This means there is a sensitivity threshold below which no changes will be detected, even if the BBB has been compromised. A study by Dickie et al. showed changes in BBB integrity in an Alzheimer's rat model using a water exchange technique. These changes were not detected using a contrast agent (Dickie et al. 2019), demonstrating the lack of sensitivity for current contrast agents.

Although the use of contrast agents has been approved in humans since the late 1980s (Lohrke et al. 2016), there have been reports of Gadolinium deposition detected in multiple tissues in the body (Grobner 2006; Kanda et al. 2014; McDonald et al. 2017). This questions the continued use of exogenous contrast agents. Furthermore, contrast agents are unsuitable for patients suffering from kidney disease, with reports of continued use of CAs causing nephrogenic systemic fibrosis

(NSF) in patients (Grobner 2006). The combination of low sensitivity to subtle changes in the BBB and questions over the continued use of contrast agents welcomes the introduction of non-invasive methods to image the BBB without the use of an exogenous contrast agent.

1.4.1 Using DWASL to Measure K_w

Multiple studies using DWASL have produced measurements of K_w in the brain. For example, a decrease in the value of K_w was seen in an ischaemic stroke model (Tiwari et al. 2017). In addition, a decrease in the exchange rate for patients with sleep apnea has been seen, where it was suggested the decrease comes from an increased permeability of the BBB to water (Palomares et al. 2015).

The exchange rate can be measured using various methods and models. A commonly used model is the single pass approximation (SPA) model (Section 3.3.2) which was used to determine the water exchange rate (St Lawrence, Owen, et al. 2012). DWASL was used to measure K_w, although St Lawrence suggested that the arterial transit time (ATT) and the signal from arterial blood could affect the results. Measuring K_w was also difficult due to the inherently low SNR from ASL sequences, and the lower SNR seen from the diffusion weighting of DWASL (St Lawrence, Owen, et al. 2012). To avoid the complexity of fitting to the SPA model, a simplified method was to measure the ratio of signal between a diffusion weighted ASL image and a non diffusion weighted image. This approximated the exchange of labelled signal between the capillaries and tissue (Wang, Fernandez-Seara, et al. 2007). Although this was not a quantitative measure of permeability, it gave a pseudo-permeability value that could estimate changes in the water exchange.

1.5 Human African Trypanosomiasis

Human African trypanosomiasis (HAT), more commonly known as sleeping sickness, is a parasitic disease that is endemic in Sub-Saharan Africa. Trypanosomes are single-celled protozoan organisms which belong to the genus *Trypanosoma*. These parasites are transmitted to humans via the bite of its vector, the tsetse fly (WHO 2013). *Trypanosoma brucei* is a species of Trypanosoma (Figure 1.3) comprising three subspecies. Two of these subspecies can infect humans; *T. b. rhodesiense*, found in East and Southern Africa and *T. b. gambiense*, which is mainly found in West Africa (WHO 2013). The third subspecies *T. b. brucei* is able to infect cattle and other animals. For *T. b. rhodesiense*, the parasite can mainly be found in

antelope and cattle reservoirs, with some human involvement. In contrast, for *T. b. gambiense*, the parasite reservoir is almost exclusively from humans.

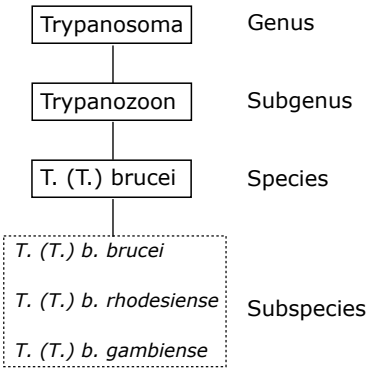

Figure 1.3: A simplified classification scale of the genus Trypanosoma

Trypanosomes were found to be the cause of the cattle disease known as nagana in 1895 by the Scottish pathologist and microbiologist David Bruce (Bruce 1895) and the parasite was known as *Trypanosoma brucei*. There had been reports of a sleeping disease which affected humans, with no known cause at the time. The first observation of trypanosomes in human blood was made by Robert Forde in 1901 in Gambia, and identified by Joseph Dutton in 1902 (Dutton et al. 1902). Dutton suggested that the species be named *Trypanosoma gambiense*. In the same year, Aldo Castellani found trypanosomes in the CSF of patients infected with sleeping sickness and suggested that the trypanosomes were the cause of the disease (Castellani 1903). Bruce confirmed this in 1903 and demonstrated that sleeping sickness is transmitted by tsetse flies. The parasite was subsequently name *Trypanosoma brucei gambiense*, after it was determined that *Trypanosoma brucei* and *Trypanosoma gambiense* were the same species. The third subspecies *T. b. rhodesiense* was discovered in 1910 by John Stephens and Harold Fantham (Stephens et al. 1910).

1.5.1 Life Cycle of *Trypanosoma brucei*

The start of the life cycle of the trypanosome occurs when an infected tsetse fly bites a susceptible animal or human (Vickerman 1985). Mature metacyclic trypanosomes enter the mammalian blood stream and multiply by binary fission, transforming into long slender trypomastigotes. The trypanosome surface is covered by a variable surface glycoprotein (VSG) coat, allowing constant antigenic variation, meaning the trypanosomes can avoid the host's immune response (Vickerman et al. 1988). The long slender forms are replaced by the short stumpy forms which are then ingested by the tsetse fly when it feeds on its host. In the midgut, the stumpy forms undergo multiple biochemical and anatomical changes, transforming into the procyclic stage, with a loss of the VSG coat. This development is

associated with a switch of the primary energy source from glucose to proline (Vickerman 1985). In the salivary glands, they transform in trypomastogites and acquire a surface coat. Following this, they transform into the infective form metacyclic (Vickerman et al. 1988). The mature metacylics are transferred to the mammalian host by the feeding of the tsetse fly and the cycle begins again (Figure 1.4).

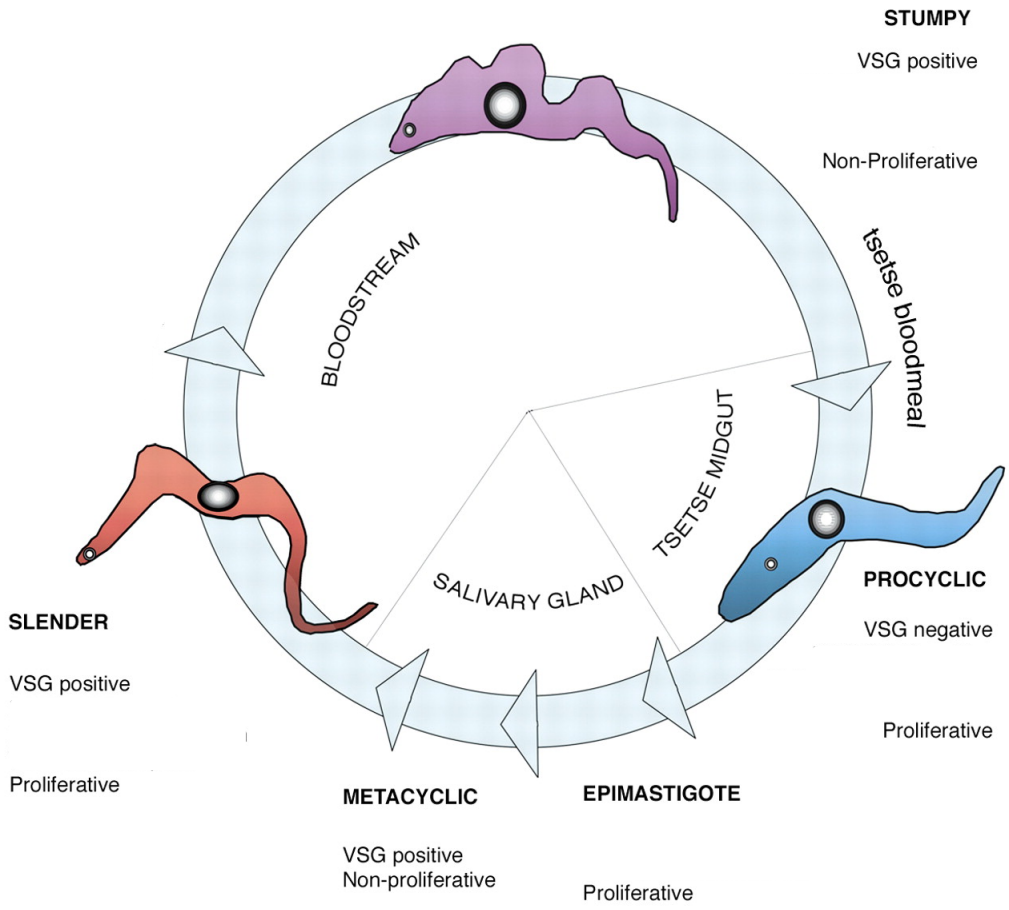

Figure 1.4: Trypanosome brucei development cycle

Figure adapted from (Matthews 2005). The life cycle of the trypanosome will start when trypanosomes are injected into a mammalian host. After transforming into stumpy forms they are taken in a blood meal from the tsetse fly and ingested into the midgut. After losing their glycoprotein coat and undergoing multiple transformations in the midgut and salivary glands, the metacylics regain their coat and can infect the mammalian host when the tsetse fly feeds again.

In the mammalian host, the parasites initially reside in the blood and lymph nodes from where they disseminate to many organs including the skin, spleen, liver, heart and eyes. This is known as the haemolymphatic, or early-stage of the disease. The late or encephalitic-stage occurs when the parasite crosses the BBB and enters into the CNS (Kennedy 2008). During the late-stage, neuroinflammation develops with infiltration of lymphocytes, macrophages and plasma cells into the brain, most prominently in the white matter. Perivascular cuffing with inflammatory cells and the activation of astrocytes is also a commonly reported characteristic of late-stage sleeping sickness (Kennedy 2008), along with microglia activation later in the neuroinflammatory response.

1.5.2 HAT and the Blood Brain Barrier

Although the presence of trypanosomes within the brain has been recognised for over a century, it remains unclear how the parasites gain access to the CNS. Studies investigating BBB function have been performed using the injection of fluorescent dye (Philip et al. 1994) to assess damage in a rat model of the disease. A loss of barrier integrity was seen as the infection advanced to the later stage, with fluorescence detected at day 21 post-infection in localised areas before becoming more widespread. Crucially, there was no correlation between the areas of the BBB damage and presence of parasites. In a study by Mulenga *et al.*, the effect of trypanosomes on the tight junctions of the BBB was investigated (Mulenga et al. 2001). Staining for the tight junction markers occludin and ZO-1, showed no difference between the control and infected groups, suggesting that there is no damage to the tight junctions during the infection. Small numbers of trypanosomes were detected in the brain parenchyma from day 12 post-infection with the majority confined to the blood vessels. From day 40 post-infection on-wards, numerous parasites were detected in the brain. No loss of occludin or leakage of IgG into the parenchyma was seen, suggesting that a loss of tight junction integrity is not needed for trypanosomes to invade the brain (Mulenga et al. 2001). There is also suggestion that trypanosomes transmigrate through the vessels in the choroid plexus and then cross the blood-CSF-barrier before entering the brain parenchyma via the perivascular space (Schmidt 1983). However further work is required to establish the invasion pathways unequivocally.

1.5.3 Symptoms, Diagnosis and Treatment of HAT

1.5.3.1 Symptoms of HAT

In the early stage of the disease, symptoms are usually non-specific and present a few weeks after a tsetse fly bite. These include headaches, weight loss, fatigue and fever. Misdiagnosis can happen at this stage as symptoms can overlap with other illnesses. As the disease progresses, the symptoms become more serious with the development of lymphadenopathy and enlargement of the spleen and liver. Issues with cardiac and opthalmological functions are also seen (Kennedy 2013). Symptoms associated with the late stage of the disease include mental and motor system disturbances and the presence of abnormal reflexes. The late stage sleep disturbances are what gives HAT its alternate name ‘sleeping sickness’, due to the high number of patients reporting problems such as a reversal of the sleep/wake cycle, insomnia or uncontrolled sleep and changes to their sleep pattern (Kristensson et al. 2010).

The disease is currently determined as having progressed to the later stage when there is a white blood cell count above $5/\mu$L, or the detection of trypanosomes in the cerebral spinal fluid (CSF) (WHO 2013). This is checked via lumbar puncture. Accurate determination of the stage of the disease is crucial to direct the most effective chemotherapeutic strategy due to the toxicity of the regimens require for treatment of late stage infections (Section 1.5.3.3). Typically, the clinical differences in symptoms of HAT are used to determine if the disease is in its early or late stage. However many of these symptoms are present in both stages which can make determining the disease stage difficult (WHO 2013). Eventually the symptoms will manifest into a coma and eventual death if the infection remains untreated. This can occur in a matter of weeks to months in cases of *T. b. rhodiense* or months to years for *T. b. gambiense*.

1.5.3.2 Diagnosis of HAT

The typical method of diagnosing *T. b. rhodesiense* is to examine a wet blood smear of peripheral blood to detect trypanosomes. This is problematic in *T. b. gambiense*, where the very low parasitemia level is often below the threshold for microscopic detection. Clinical signs can be misleading when determining the stage of the disease and therefore are not used in diagnosis.

According to the World Health Organisation (WHO), the difference in the early and late stage of HAT is determined by the level of parasite and white blood cell count in the CSF (WHO 2013) described above. Since the concentration of immunoglobulin (IgM) level in the CSF increases when there is parasite involvement in the CNS, this can be examined for diagnostic purposes. However, this is impractical for stage determination due to the lack of reagents and facilities in rural health centres (Lejon et al. 2005).

1.5.3.3 Treatment of HAT

Current treatment of HAT depends on the form and stage of the disease. Drugs used as early stage treatments cannot penetrate the BBB and late stage treatments are toxic and require hospitalisation. For chemotherapy of early stage *T. b. gambiense*, the drug pentamidine is used and for *T. b. rhodesiense*, the drug suramin. One of the main issues with the use of these drugs is that they are unavailable as an oral treatment and must be given parenterally as a course of intramuscular (IM) or intravenous (IVen) injections respectively.

The only drug for treating late stage *T. b. rhodesiense* infections is melarsoprol.

This requires hospitalisation for treatment as it must be administered as 10-daily infusions given by a strictly intravenous route. Until recently, melarsoprol was used to treat all cases of late-stage HAT, and although effective, the development of post-treatment reactive encephalopathy (PTRE) occurs in 5-10 % of patients, where half will die (Kennedy and Rodgers 2019). A new treatment for late stage *T. b. gambiense* means that melarsoprol is no longer the first line treatment for this variant of the disease. Since 2009 a combined regimen of oral nifurtimox and IVen eflornithine has been the recommended treatment for late-stage *T. b. gambiense* (Lejon et al. 2005). However this is not suitable for treatment of late-stage *T. b. rhodesiense* infection which still replies on the use of melarsoprol.

1.5.4 Current Statistics

T. b. gambiense is the most prevalent of the two forms of HAT, accounting for approximately 97% of all HAT cases (WHO 2013). There has been a steady decline in cases in the last 10-20 years, with input from multiple areas including the WHO, African governments, non-government organisations, research charities and the pharmaceutical industry to curb the disease. Effective disease surveillance and treatment to reduce disease transmission has caused case numbers to decrease rapidly since the 1990s when the last epidemic was seen (WHO 2013). The disease almost exclusively affects Africa, with the exception of a few traveller cases. The number of reported cases of HAT was 2,164 in 2016, a decrease of 92 % compared to 2000 when 26,550 were recorded (Franco et al. 2018). Preliminary figures from the WHO suggest that less than 1500 cases of *T. b. gambiense* occurred in the year 2017 but it is believed there is under reporting in the amount of cases for both strains of the disease (Barrett, 2018). Almost 57 million people are at risk of infection from *T. b. gambiense* with a lower 12.3 million people at risk from *T. b. rhodesiense* (WHO 2013).

1.5.5 The Use of MRI in HAT

1.5.5.1 Clinical MRI

The literature regarding HAT and MRI is scarce. Studies are limited to case reports from single patients who contracted HAT whilst in Africa with subsequent diagnosis once they have left Africa. An African patient living in Germany presented symptoms that were initially diagnosed as Lyme disease. Following no response to the treatment for Lyme disease, further tests were performed and the patient was diagnosed with *T. b. gambiense*, with parasites detected in a brain biopsy

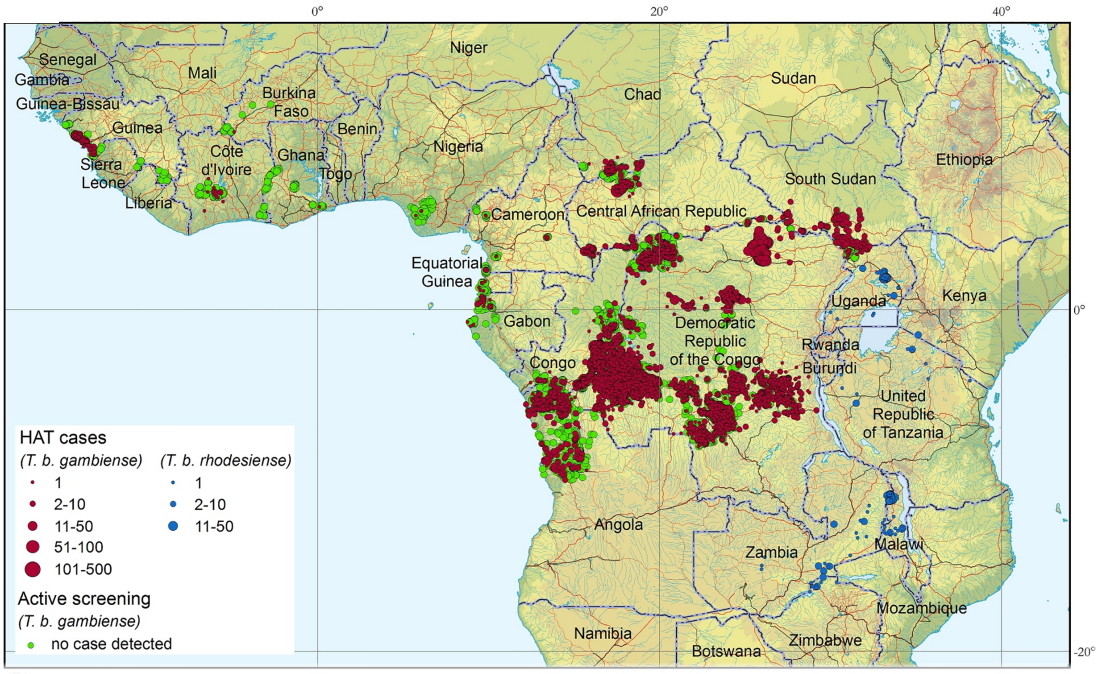

Figure 1.5: The distribution of HAT between 2012-2016

Figure adapted from (Franco et al. 2018). Cases of *T. b. gambiense* are typically seen in West Africa, with cases of *T. b. rhodesiense* seen in Southern and Eastern Africa. For 2012-2016, 22,281 cases of HAT were reported.

using PCR. This biopsy was initially performed to rule out lymphoma or gliomatosis cerebri. MRI findings showed deep grey matter and hemispheric white matter enhancement on T_2-FLAIR images. A follow-up scan 2 years later, after successful treatment with eflornithine and rehabilitation, showed reduction of the white matter signal changes along with no-detectable trypanosome-specific antibodies (Wengert et al. 2014).

Over a four-year period, serial MRI was performed on a female refugee from Angola diagnosed with late-stage *T. b. gambiense*, two years after her arrival in the Netherlands (Kager et al. 2009). Initial T_2-weighted and FLAIR MR images showed a hyperintense signal in the white matter, before a diagnosis was made. After 14 days of treatment with eflornithine, MRI findings showed similar hyperintense white matter regions along with perivascular enhancement near the right basal nuclei, with more overt changes in the right hemisphere. Nine months after treatment, MRI images showed only minor improvement, although there had been considerable physical and mental improvement. Follow-up scans at two and four years post-treatment detected small areas of the hyperintense signal, with the right lateral ventricle enlarged, as seen in previous scans, consistent with brain tissue loss (Kager et al. 2009).

Patel *et al.* described a series of three cases of HAT, two cases of *T. b. gambiense* and one *T. b. rhodesiense* case, where MRI was performed (Patel et al. 2018). Case 1 describes a 58-year-old Nigerian woman diagnosed with *T. b. gambiense* where T_2W FLAIR images showed the characteristic high signal intensity in the deep white

matter seen in other cases reports. The T_2W FLAIR images were complemented by diffusion weighted imaging (DWI) and an apparent diffusion coefficient (ADC) map, along with susceptibility weighted imaging (SWI). DWI showed restricted diffusion in the posterior limbs of the internal capsules with microhaemorrhages seen in the globus pallidus, thalamus and left internal capsule using SWI. Following treatment with nifurtimox and eflornithine, a 4-month review showed resolution of the restricted diffusion and an improvement of the high signal in the white and grey matter (Patel et al. 2018). In Case 2, a 62-year-old Sierra Leone male was diagnosed with *T. b. gambiense* after microscopy of bone marrow following admission to an intensive care unit revealed trypanosomes, which were subsequently detected in the peripheral blood. He was treated with nifurtimox and eflornithine. T_2W FLAIR images showed bilateral high signal intensity in the deep white matter, which extended to the cerebellum and brain stem. A follow-up MRI three months after the initial scans showed improvement in the deep white matter signal with blooming artefact seen on a SWI image. Case 3 discusses a 38-year-old British man who travelled throughout Africa for two years, and was diagnosed with HAT during a visit to hospital in South Africa due to fatigue, febrile episodes, headaches and distorted sleep. Following unsuccessful chemotherapy and multiple relapses, T_2W MRI showed hyperintense signal in the white matter along with restricted diffusion in the internal capsules and corpus callosum. A follow-up scan six months after his final treatment showed reduced T_2W hyperintensity in the deep white matter and resolution of the restricted diffusion.

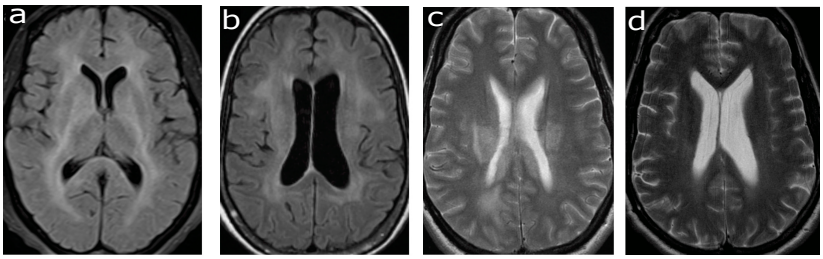

Figure 1.6: Clinical MRI images for three patients with HAT

Adapted figure from (Patel et al. 2018) with MRI results for three cases of HAT. Figure a) shows a T_2W FLAIR from Case 1 with high signal seen in the deep white matter. Figure b) shows the same symptoms for the patient from Case 2. Figure c) is from Case 3 with high signal intensity seen and a 6 month follow up scan for Case 3 is shown in Figure d) where there is reduced hyperintensity.

Although there is limited MR data in HAT cases, the findings highlight the presence of hyperintense signal in the deep white matter and grey matter from T_2W FLAIR images (Figure 1.6). Furthermore, restricted diffusion and microhaemorrhages were seen in all cases, although in different brain regions. Follow up scans showed a reduction in the hyperintensities although some residual signal enhancement can remained present in MRI images years after final drug treatments. Additional preclinical studies are therefore needed to explore the integrity of the BBB in relation to HAT in greater detail.

1.5.5.2 Pre-Clinical MRI

MRI has been employed in a murine model using CE-MRI to show that there is a reduction in BBB integrity during the late-stage infection in a HAT mouse model (Rodgers, McCabe, et al. 2011). A comparison of signal change between images taken from uninfected animals and mice scanned at day 28 post-infection showed a mean increase of 20.4% in signal after contrast injection, indicating the presence of BBB impairment in the infected mice. This loss of integrity does not correlate with the mild neuroinflammatory reaction, with no trypanosomes detected on histological examination of the brain parenchyma of the infected mice. These results could indicate that at this point in the infection the brain still maintains the tight regulatory process that is responsible for the control of inflammatory cell transmigration and proliferation in the brain.

Further research to determine when BBB impairment becomes apparent in the HAT murine model was undertaken using the same mouse model (Rodgers, Bradley, et al. 2017). In this model, late-stage is defined as day 21 post-infection, when early-stage drugs can no longer treat the parasite infection, indicating parasites are established within the brain. By comparing MRI results from various time points (uninfected controls, days 7, 14, 21, 28 post-infection), a significant change in CE-MRI was seen from day-14 post-infection onward (Figure 1.7) along with a significant neuroinflammatory response. Parasites were detected in the brain by quantitative PCR, from day-7 post-infection. Both the immune response and early parasite detection, along with BBB impairment, indicate that significant changes occur before the onset of late-stage disease. It was shown that the amount of parasite detected in the brain does not correlate with the level of impairment of the BBB.

MRI has also been used for imaging changes in BBB impairment following treatment for HAT. In this study, mice were treated with a curative regimen comprising oral melarsoprol cyclodextrin complex, beginning at day 21 post-infection. CE-MRI was performed at 24-hours, 8-days and 15-days following drug treatment. These scans showed complete resolution of the BBB impairment present at day 21 post-infection with signal changes comparable to those found in uninfected mice (Rodgers, Jones, et al. 2011).

These results are crucial to the on-going research into diagnosing and treating HAT in humans. In addition they challenge the criteria currently used for stage determination in HAT as they show that inflammation and parasite detection as well as BBB-impairment are present before CNS stage infection has established.

At present, there is no *in-vivo* research of MRI in HAT without the use of a contrast agent. Current research shows HAT is a well characterised model showing pro-

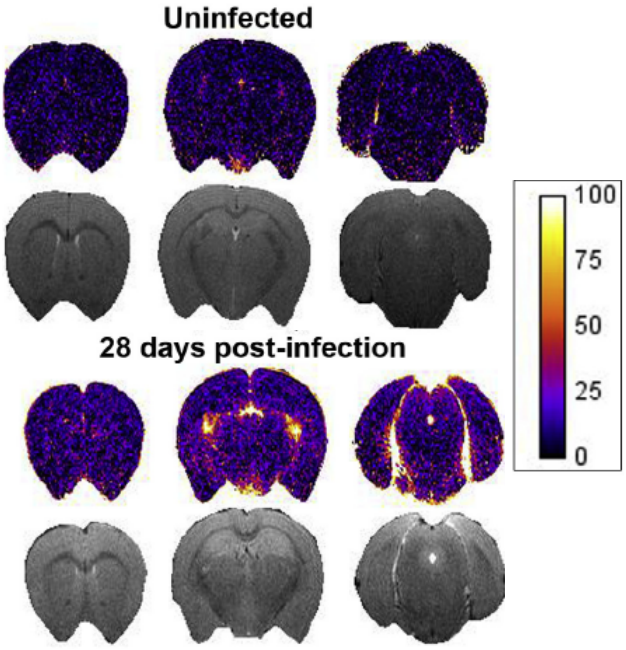

Figure 1.7: Evidence of BBB impairment in HAT

Adapted figure from (Rodgers, Bradley, et al. 2017). Percentage signal change maps and corresponding T_2 weighted MR image from an uninfected mouse and a mouse infected with HAT at day 28 post-infection. Signal change can be seen clearly in the infected mouse, with enhancement in the cerebral cortex, thalamus and pons. The signal enhancement demonstrates BBB impairment in this murine model.

gressive breakdown in the BBB, with BBB changes apparent over the whole brain. This makes HAT a desirable model to explore changes in permeability that could be tracked over time through the early and late stages of infection.

1.6 The Spleen

The spleen, located in the abdomen, is the largest secondary immune organ, consisting of two distinct compartments, the red pulp and white pulp (Cesta 2006). It is dark red, with a triangular cross-section and elongated shape. The spleen accounts for approximately 0.2 % of the body weight of a rat and is responsible for initiating the immune response to blood-borne antigens by the production of IgM antibodies. The spleen is the major second line of defence against these antigens in the blood stream that are not recognised by the body's immune system (Tilanus 2005). The spleen filters the blood to remove old or abnormal red blood cells and immunoglobulin-coated blood cells. For some haematological diseases, this organ helps to produce red blood cells when bone marrow fails and hematopoiesis cannot take place.

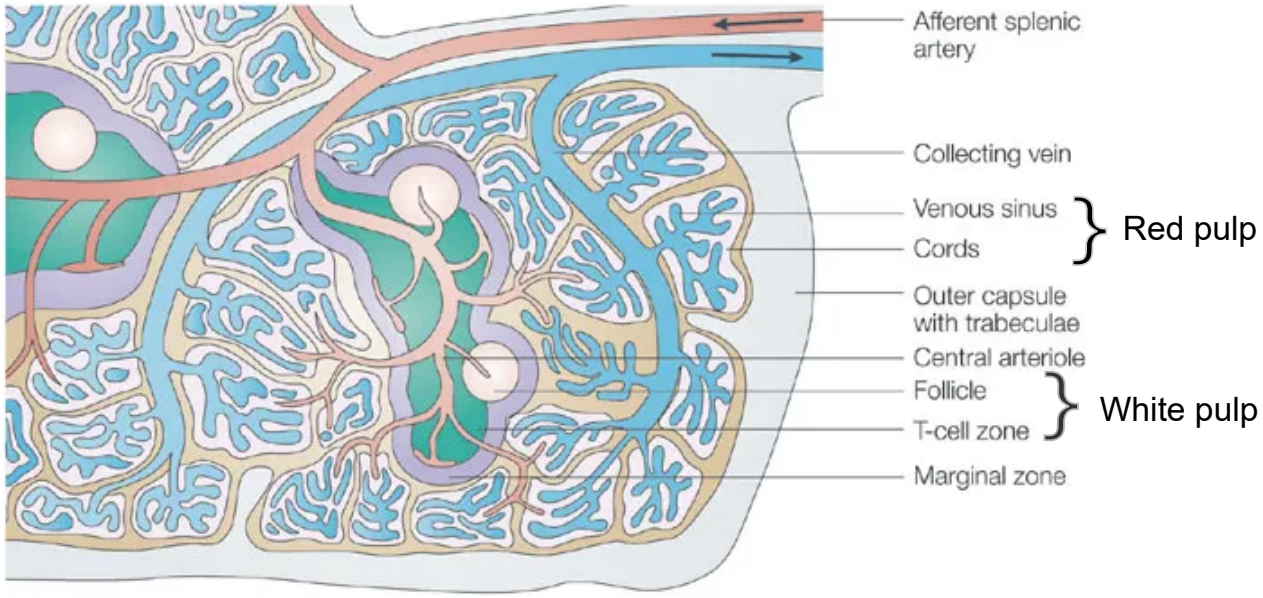

Figure 1.8: Schematic of the Spleen

The blood supply to the spleen comes from the afferent splenic artery, which branches into central arterioles and are sheathed by the white pulp. The white pulp contains T-cells, B-cells and periarteriolar lymphatic sheath. The ends of the central arterioles are surrounded by cords in the red pulp. Image taken from (Mebius et al. 2005).

The spleen is supplied with blood via the splenic artery which branches off from the celiac artery, with the splenic vein draining the spleen (Kindt et al. 2007). The smaller branches of the spleen are sheathed by lymphoid tissue, forming the white pulp (Figure 1.8). The red and white pulp are separated by the marginal zone. Around a quarter of the body's lymphocytes are stored in the spleen. The most important cells for splenic function are macrophages, monocytes, natural killer (NK) cells and T and B cells (Kindt et al. 2007). T cells and B cells are both a type of lymphocyte cell. They originate from stem cells in the bone marrow, with the immature T cells maturing in the thymus before moving to the spleen, lymph nodes or lymphoid tissue. B cells will mature in the bone marrow before moving to multiple sites in the body. When B cells interact with foreign antigens, they become antibody secreting cells called plasma cells. This is usually achieved with help from T helper cells (Cano RLE 2013). Plasma cells are produced in large numbers when an antibody response is needed and reside mostly in the lymph nodes and white pulp of the spleen (Elmore 2006).

1.6.1 Red Pulp

The red pulp is a blood filter that removes any foreign bodies and damaged erythrocytes, along with storing iron, platelets and erythrocytes. The main function of the red pulp is blood filtration. The red pulp has sinuses that are filled with platelet rich blood. Between these sinuses there are cellular cords made of reticular cells and fibres. The cords do not have an endothelial cell lining (Mebius et al.

2005). These cords are mixed with macrophages, B- and T- cells, plasma cells and monocytes. Reticulocytes are able to pass through the epithelial cell layer of the splenic cords and continue into the blood stream whereas the older or abnormal blood cells are trapped by the splenic cords. The macrophages in the red pulp will phagocytose ageing red blood cells and regulate the the recycling of iron (Bronte et al. 2013). The red pulp constitutes approximately 70 % of the total spleen volume in a normal adult (Kindt et al. 2007).

1.6.2 White Pulp

The white pulp initiates the cellular immune response to blood-borne antigens and stores around a quarter of the body's lymphocytes (Cesta 2006). The white pulp has periarterial lymphatic sheaths (PALS) surrounding the arterial vessels, in particular the central artery and central arterioles and follicles. These PALS contain tightly packed T-cells and dendritic cells. The follicles contain B- and T- cells. B-cells are generally found in the innermost area of the follicle, with the surrounding marginal zone containing the T-cells (Kindt et al. 2007). The normal histopathology of the spleen will be discussed in great detail in Chapter 7 of this thesis.

1.6.3 Splenomegaly in HAT

Splenomegaly describes the enlargement of the spleen, due to an increase in cellularity and vascularity (Tilanus 2005). This can occur in response to infection, disease, altered splenic blood flow or immune disorders. The increase in the size of the spleen can range from mild to massive (McKenzie et al. 2018). In humans, a normal spleen measures approximately 10cm in length but can reach 40cm in splenomegaly. The three main mechanisms that cause splenomegaly are congestion, infiltration and increased splenic function. If there is a blockage in the vasculature of the spleen, this can lead to the pooling of blood in the red pulp which in turn leads to dilated veins and sinuses. The spleen can also enlarge due to physiological stress. This could be from infection, blood loss or hemodilution, where the spleen will usually return to its normal size. An increase in spleen size can also be observed over the course of pregnancy.

One of the many symptoms of HAT is splenomegaly (Kennedy 2013) and this has also been reported in animals infected with trypanosomes. Murray et al. reported an enlargement of the spleen in mice infected with *T. brucei* (stabilate TREU 667) with a mean weight of 1.44g at day 21 post-infection compared to a normal spleen weight of 0.13g (Murray et al. 1974a). In addition this study showed an increase

in the number of erythrocytes and macrophages in the spleen and also in other organs and tissues of the body following trypanosome infection. In another study investigating the causes of anaemia in trypanosomiasis, splenomegaly was reported in mice infected with *T. brucei* stabilate TREU 667. An increase from a mean spleen weight of 0.23g to 0.85g was seen in mice infected for 30 days. In the early stage of the disease there was a loss of erythrocyte volume, indicating anaemia. At eight weeks after infection, there was an increase in plasma and blood volume reported with the number of erythrocytes increasing (Amole et al. 1982). Anosa et al. reported a 26 fold increase in the spleen weight in a group of infected mice (*T. brucei* stabilate EATRO 110) compared to uninfected mice. The mice that were determined anaemic had a larger spleen weight compared to the non-anaemic mice at the end of the experimental infection. The spleens of these mice contained a larger number of activated macrophages, along with an increase in the population of plasma cells, lymphocytes and mott cells (Anosa et al. 1984). The infected mice had tightly packed cells in the spleen, with transformed lymphocytes present in the infected mice but not the uninfected mice. Overall there was a large increase in the cell population per unit area and a general enlargement of the spleen overall.

Splenomegaly has also been reported in clinical cases of HAT. Clinical observations of patients with HAT saw splenomegaly in both early and late stage patients infected with *T. b. rhodesiense* (MacLean et al. 2010). Mild anaemia was also recorded in many of the patients. Ultrasound investigations in two patients diagnosed with HAT in Italy in 2004 detected splenomegaly with the spleen measuring 20cm and 19.5cm. These patients also displayed haematological changes including a marked decrease in leukocyte numbers and haemoglobin with an increase in the concentration of IgM (Bisoffi et al. 2005). The development of splenomegaly is more frequently observed in children rather than adults (WHO 2013).

1.6.4 Imaging of the Spleen

There has been no exploration of splenomegaly in trypanosome infected mice using MR imaging. MRI imaging of the spleen has been documented however, with and without the use of contrast agent. The spleen shows a high signal intensity (in comparison to the liver) in T_2 weighted images and a lower signal intensity in T_1 weighted images (Palas et al. 2013). Giraudeau et al. used $^{19}\mathrm{F}$ MRI to image the mouse liver and spleen. They measured the T_1 value of the spleen as 2200ms and partial oxygen pressure as 75mmHg. Although this study was aimed at examining values of oxygen tension, they also produced an anatomical $^{1}\mathrm{H}$ image showing the spleen (Giraudeau et al. 2012). Smirnov et al. used magnetically labelled particles for imaging the mouse spleen. By injecting hybridoma cells that were labelled with

anionic $\gamma - Fe_2O_3$ superparamagnetic iron oxide nanoparticles, they were able to show changes in the spleen MRI signal intensity (Figure 1.9). The signal in the spleen dropped due to the collection of these iron oxide nanoparticles (Smirnov et al. 2004).

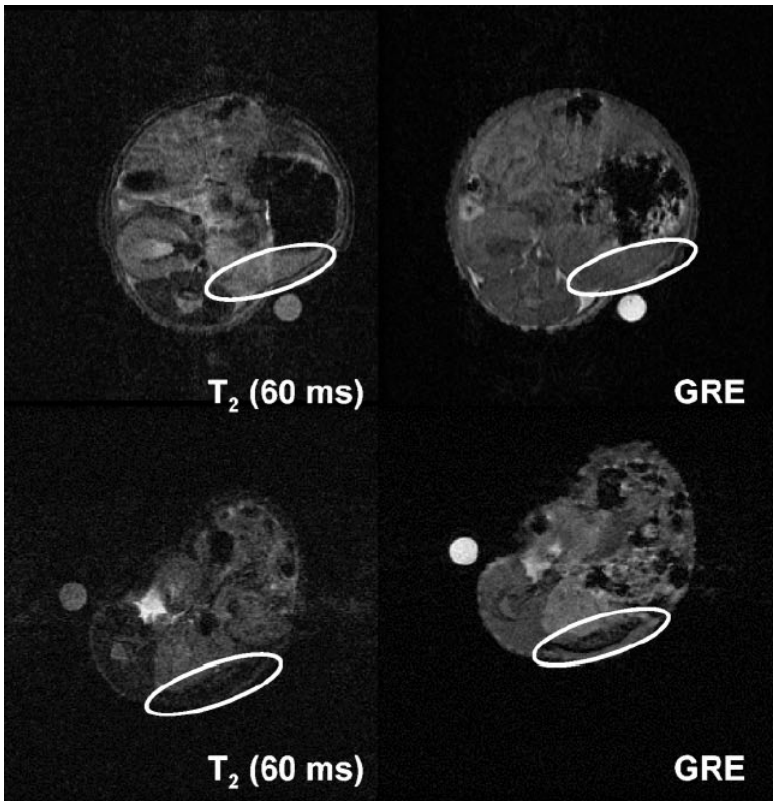

Figure 1.9: MRI of a mouse spleen after injection of magnetic particles

Image modified from (Smirnov et al. 2004). The spleen is indicated by the white ellipse. MR imaging of the mouse using a gradient echo sequence (GRE) was taken 24 hours after IP injection of magnetically labelled hybridomas. The signal in the spleen dropped in the injected mice compared to the control. The aim of the research was to show signal intensity changes could be shown in the spleen using a 1.5T clinical magnet.

1.7 Relevance to the Thesis

The aim of the research was to investigate the permeability of the BBB non-invasively. To do this, HAT was chosen as a murine disease model that had known BBB impairment. The disease would be able to provide a progressive diffuse impairment of the BBB that could be imaged over the course of the infection. Further research into the disease revealed limited knowledge of the splenomegaly in HAT, therefore an experiment was designed to serially investigate splenomegaly for the first time in HAT non-invasively.

Chapter 2

Magnetic Resonance Imaging

In this chapter, the basics of nuclear magnetic resonance and magnetic resonance imaging is outlined. Information has come from multiple sources (Bushong 1996; Feynman et al. 2006; Young et al. 2011; Levitt 2008; Tofts 2003; Callaghan 1991), unless specifically stated. There are many other books and papers on the topic.

2.1 Nuclear Magnetic Resonance

2.1.1 Principles of Magnetic Resonance

Magnetic resonance exploits the properties of the nucleus, focusing on how it reacts with the world around it. Some nuclei have the intrinsic property known as nuclear spin angular momentum, sometimes called spin. When considering a rotating body in a classical physics description, it can be described as having angular momentum and interacting with the gravitational field around it. Nuclei possess an intrinsic spin angular momentum, L. The particles that make up the nucleus (electrons, protons and neutrons) also possess angular momentum and interact with the electromagnetic field around them. The values of nuclear spin angular momentum are quantised (for $I \neq 0$), and have discrete integer or $\frac{1}{2}$ integer values:

$$L = [I(I+1)]^{1/2}\hbar \tag{2.1}$$

where I is the nuclear spin quantum number and $\hbar$ is Planck's constant.

Some nuclei possess a magnetic moment, which describes the tendency of an object to interact with an external magnetic field. The magnetic moment arises from

the gyromagnetic ratio, γ, a constant which is specific to each nuclei and its spin angular momentum. The magnetic moment, μ, is thus:

$$\mu = \gamma \mathbf{L} \tag{2.2}$$

This thesis will be concerned with only hydrogen nuclei $^1\mathrm{H}$, which have a nuclear spin quantum number $I = \frac{1}{2}$ and, thus, two energy levels $(2I + 1)$, known more commonly as the spin-up and spin-down states. In the absence of a magnetic field, these two states are degenerate with the spin direction for an ensemble of nuclei being randomly distributed. If a nucleus is then placed in a magnetic field, the magnetic moment μ will equal:

$$\mu = \gamma L = \gamma \hbar I \tag{2.3}$$

Classically, in the presence of an external magnetic field, the nuclear magnetic moment will experience a torque and, hence, will proceed to precess about the magnetic field direction. The energy, E, associated with μ is:

$$\mathbf{E} = -\mu \cdot \mathbf{B} = -\gamma \cdot \hbar \cdot I \cdot \mathbf{B} \tag{2.4}$$

where **B** is the static magnetic field.

This static magnetic field will cause a separation in energy levels of the spin-up and spin-down states, known as Zeeman Splitting (Figure 2.1). This quantisation of the spin angular momentum, L, occurs along the direction of the magnetic field. When the magnetic moment is parallel with the static field direction (spin-up), it has a lower energy (E_-) with m = -1/2, and when opposed to the field (spin-down), a higher energy (E_+) with m = +1/2, where m is the z-component of the spin angular momentum.

The energy difference between the two states is as follows:

$$\Delta E = E_- - E_+ = [-(-\frac{1}{2})\gamma \cdot \hbar \cdot \mathbf{B}] - [-(\frac{1}{2})\gamma \cdot \hbar \cdot \mathbf{B}] = \gamma \hbar \cdot \mathbf{B} \tag{2.5}$$

Planck's equation states:

$$\Delta E = \hbar \omega \tag{2.6}$$

By combining Equations 2.5 and 2.6 , this gives the following relationship:

$$\gamma \hbar \mathbf{B} = \hbar \omega_0 \tag{2.7}$$

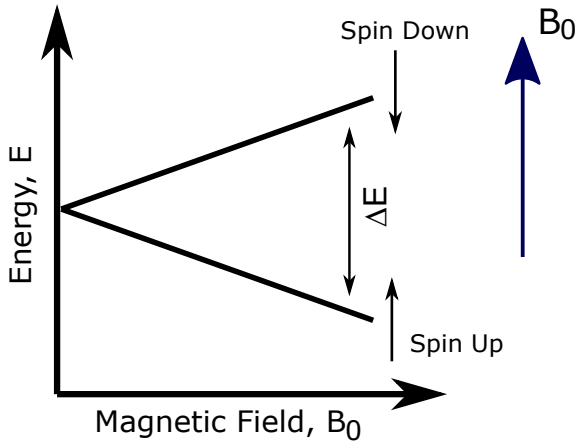

Figure 2.1: Zeeman Splitting

The separation of the energy level into two states is known as Zeeman Splitting. The spin-up and spin-down states are shown, with the static magnetic field denoted by $\mathbf{B}_0$.

Which gives the Larmor equation:

$$\omega_0 = (-)\gamma \mathbf{B}_0 \tag{2.8}$$

where the sign of γ depends on the nucleus in question. Equation 2.8 describes the angular frequency, ω_0, associated with nuclei (I = $\frac{1}{2}$) precessing in an external magnetic field, $\mathbf{B}_0$. A classical derivation of Equation 2.8 can be seen in Appendix A. For the hydrogen nucleus at 7 Tesla, the value of γ is 42.58 MHz/T which gives a precession frequency, ω_0, of $\sim$ 300 MHz.

In an external magnetic field, the population of the two spin states is given by a Boltzmann distribution, with more spins in the spin-up state at the lower energy level (Figure 2.2). A vector summation of this ensemble of spins is called the net magnetisation:

$$\mathbf{M} = \sum_i \mu_i \tag{2.9}$$

The total number of spins is $N = N_- + N_+$ with the ratio of the spins states being:

$$\frac{N_+}{N_-} = e^{\frac{\Delta E}{K_B T}} = e^{\frac{\hbar \gamma B}{K_B T}} \tag{2.10}$$

where $\Delta E = E_- - E_+$, K_B is the Boltzmann constant and T is temperature in Kelvin.

When thermal energy is greater than the energy difference between spin states ($K_B T >> \hbar \gamma B$), then this becomes:

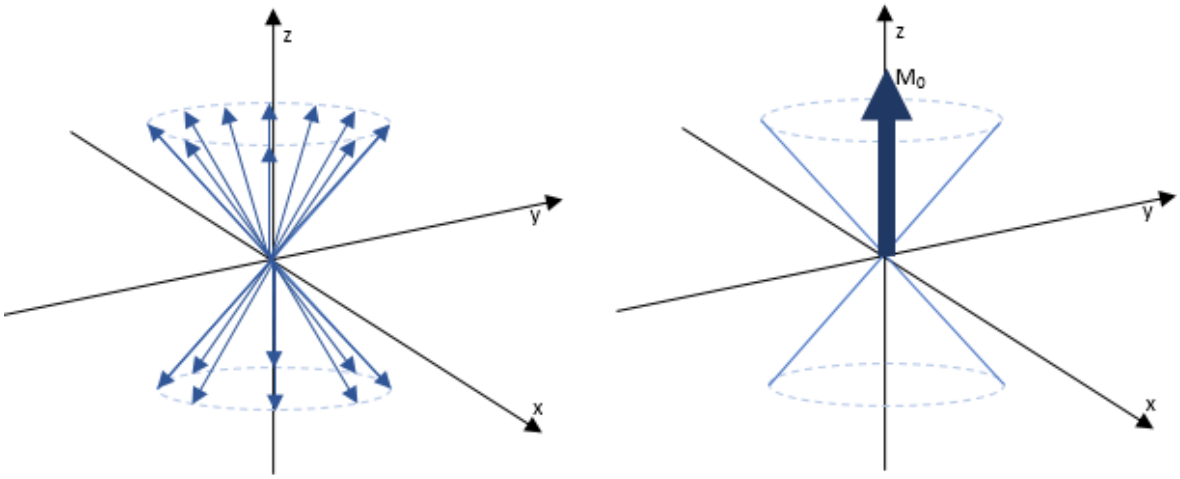

Figure 2.2: Distribution of nuclear spins

The net magnetisation arising from a larger number of spins in the spin up state.

$$\frac{\Delta N}{N} = \frac{N_- - N_+}{N_+ + N_-} \approx \frac{\hbar\gamma \mathbf{B}_0}{2K_B T} \tag{2.11}$$

This relationship shows that the number of excess spins in the lower state can be increased by either increasing the magnetic field strength or decreasing the temperature of the sample (not viable for biological samples). By increasing the number of the lower state spins, this creates a larger net magnetisation which increases the overall MR signal. For the hydrogen nucleus at room temperature in a 7T magnet, $\frac{\Delta N}{N} \approx 10^{-6}$. From Avogadro's constant, one mole of water contains 10^{23} water molecules. This means in each 1ml of water, the signal for $\sim 10^{17}$ spins are available for imaging.

2.1.2 The Bloch Equations

The net magnetisation will precess around the magnetic field $\mathbf{B}_0$ with a frequency, ω_0, and will have a spin angular momentum $\mathbf{L}$. The rate of change of angular momentum is equivalent to torque, τ and so:

$$\frac{d\mathbf{L}}{dt} = \tau = \mathbf{M} \times \mathbf{B} \tag{2.12}$$

This means that:

$$\frac{d}{dt} L = \frac{d}{dt} \frac{M}{\gamma} = \mathbf{M} \times \mathbf{B} \tag{2.13}$$

and therefore:

$$\frac{d\mathbf{M}}{dt} = \gamma \mathbf{M} \times \mathbf{B} \tag{2.14}$$

Equation 2.14 is the basis of the Bloch equations. Expanding the cross product will give the following for the individual components of magnetisation:

$$\begin{aligned} \frac{dM_x}{dt} &= \gamma(M_y B_z - B_y M_z) \\ \frac{dM_y}{dt} &= \gamma(B_x M_z - M_x B_z) \\ \frac{dM_z}{dt} &= \gamma(M_x B_y - B_x M_y) \end{aligned} \tag{2.15}$$

If an external, static magnetic field is applied in the z-direction, the B_x and B_y components will be equal to zero and, hence, spins will precess around the B_z direction. This simplifies the Bloch equations to:

$$\begin{aligned} \frac{dM_x(t)}{dt} &= \gamma M_y(t) B_z \\ \frac{dM_y(t)}{dt} &= -\gamma M_x(t) B_z \\ \frac{dM_z(t)}{dt} &= 0 \end{aligned} \tag{2.16}$$

The equations in 2.16 hold in the absence of relaxation mechanisms, described in Section 2.2. By incorporating relaxation effects into Equation 2.16:

$$\begin{aligned} \frac{dM_x(t)}{dt} &= \gamma M_y(t) B_z - \frac{M_x(t)}{T_2} \\ \frac{dM_y(t)}{dt} &= -\gamma M_x(t) B_z - \frac{M_y(t)}{T_2} \\ \frac{dM_z(t)}{dt} &= -\frac{M_0 - M_z}{T_1} \end{aligned} \tag{2.17}$$

Following a 90° pulse, the solutions to Equation 2.17 are:

$$\begin{aligned} M_x(t) &= e^{\frac{-t}{T_2}}[M_x(0)cos(\omega_0 t) + M_y(0)sin(\omega_0 t)] \\ M_y(t) &= e^{\frac{-t}{T_2}}[M_y(0)cos(\omega_0 t) - M_x(0)sin(\omega_0 t)] \\ M_z(t) &= M_z(0)e^{\frac{-t}{T_1}} + M_0(1 - e^{\frac{-t}{T_1}}) \end{aligned} \tag{2.18}$$

2.1.3 RF Pulses & Frame of Reference

In MRI, the frame of reference is the coordinate system used to view the precession of the net magnetisation. The net magnetisation can precess with a frequency from 10s to 100s of MHz, with a frequency of 300 MHz for a 7T static field, when viewed in the laboratory frame. By introducing the concept of a rotating frame of reference and transforming the coordinates of the laboratory frame so that the new frame is rotating at the $\mathbf{B}_1$ frequency, the net magnetisation will appear stationary due to the effects of the $\mathbf{B}_0$ field disappearing.

When an ensemble of $^1\mathrm{H}$ nuclei is placed in a static magnetic field, $\mathbf{B}_0$, precession around the $\mathbf{B}_0$ direction will occur. If an oscillating magnetic field (referred to as $\mathbf{B}_1$) is applied perpendicular to $\mathbf{B}_0$, this will cause $\mathbf{M}$ to precess around the $\mathbf{B}_1$ direction. This short oscillating field is known as a radio frequency pulse (RF pulse). Once this pulse has been turned off, the net magnetisation will return to equilibrium. The amount of rotation that the net magnetisation experiences because of the RF pulse is known as the flip angle. For the most basic of pulses, namely, the rectangular RF pulse of constant amplitude $\mathbf{B}_1$, the flip angle, α, can be described using the pulse length, t_p, and gyromagnetic ratio:

$$\alpha = \omega_1 \, t_p = \gamma \mathbf{B}_1 t_p \tag{2.19}$$

The use of a rotating frame of reference means that the effects of the $\mathbf{B}_0$ field disappear and the $\mathbf{B}_1$ field appears static rather than rotating. The net magnetisation is now acted upon only by the $\mathbf{B}_1$ magnetic field, meaning that the net magnetisation will precess with a frequency $\omega_1 = \gamma \mathbf{B}_1$. As $\mathbf{B}_1$ is much smaller than $\mathbf{B}_0$, the precession can be measured in kHz rather than MHz.

2.1.4 Adiabatic Excitation

Adiabatic excitation is a special case of RF excitation, where the $\mathbf{B}_1$ field is applied very gradually. In the rotating frame, the rotation is at the frequency of the $\mathbf{B}_1$ field, ω_1. If the $\mathbf{B}_1$ field is applied off-resonance, the effect of the $\mathbf{B}_0$ field does not disappear from the rotating frame completely, and B'_z is given by:

$$B'_z = \frac{\omega_0 - \omega_1}{\gamma} = B_0 - \frac{\omega_1}{\gamma} \tag{2.20}$$

When ω_1 is at the Larmor frequency, B'_z is zero. From this, a B_{eff} field is produced, which is the resultant vector between $\mathbf{B}_1$ and B'_z. The magnetisation $\mathbf{M}$ will precess around this B_{eff} field. For adiabatic excitation, the $\mathbf{B}_1$ field is applied below

resonance ($\omega_1 < \omega_0$), very gradually increased to resonance ($\omega_1 = \omega_0$) and then above resonance ($\omega_1 > \omega_0$). Adiabatic conditions are required for the magnetisation to precess around and follow the B_{eff} field as it sweeps through the frequency range. The $\mathbf{B}_1$ field needs to be strong enough and applied slowly enough, with the adiabatic condition expressed as:

$$|\frac{d\theta}{dt}| \ll \gamma |B_{eff}| \tag{2.21}$$

Where:

$$\theta = \arctan(\frac{B_1(t)}{B_{z'}(t)}) \tag{2.22}$$

is the angle that B_{eff} makes with the z-axis. This can be arranged to give the adiabatic factor η:

$$\eta = \gamma \frac{|B_{eff}|}{|\frac{d\theta}{dt}|} \tag{2.23}$$

After $\mathbf{B}_1$ has been swept through the frequency range, $\mathbf{M}$ will be inverted by 180°, which is known as adiabatic inversion. Compared to normal amplitude modulated rectangular RF pulses, these adiabatic pulses are amplitude- and frequency-modulated. They are mostly insensitive to $\mathbf{B}_1$ inhomogeneity and frequency offset effects. This is due to the pulses being less sensitive to RF miscalibration. The flip angle is not proportional to $\mathbf{B}_1$ magnitude and pulse length compared to the typical rectangular pulses, but depends on how the $\mathbf{B}_1$ field varies in amplitude and phase throughout the inversion. The adiabatic pulses used in this thesis are hyperbolic secant pulses.

2.2 Relaxation

Following excitation by an RF pulse, a spin ensemble will return to precess at its equilibrium, $\mathbf{B}_0$. This return to equilibrium is known as relaxation. T_1 relaxation describes the relaxation of the longitudinal component of magnetisation, with T_2 relaxation describing the relaxation of the transverse component.

2.2.1 T_1 Relaxation

The return of the net magnetisation along the z-axis is known as longitudinal, spin-lattice or T_1 relaxation. This relaxation is due to the interactions between the spins and the surrounding lattice. The resulting recovery is illustrated in Figure 2.3.

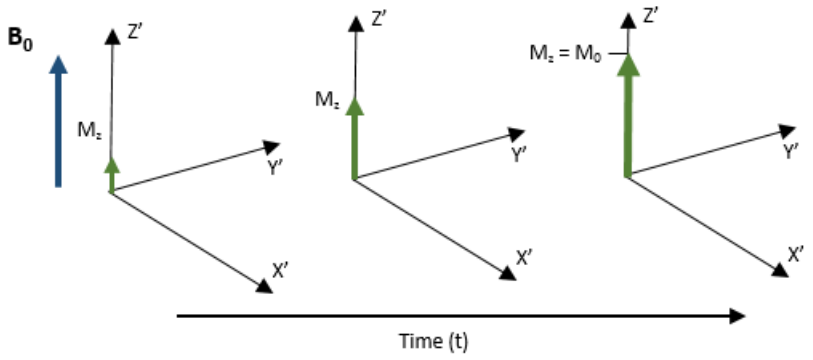

Figure 2.3: T_1 Relaxation

Following RF excitation, as time increases, the value of the magnetisation in the z direction will increase until it reaches M_0. The rotating frame is shown.

After the RF pulse is switched off, the spins system starts to lose energy as it returns to the equilibrium state, M_0. In quantum mechanical terms, this can be described as the spins losing energy as they transition from a higher to a lower energy state. This heat energy is absorbed by the surrounding environment and re-establishes thermal equilibrium. Following a 90° pulse, the recovery of the signal follows an exponential curve, and is characterised by the following (for $t \geq 0$):

$$M_z(t) = M_0(1 - e^{\frac{-t}{T1}}) \tag{2.24}$$

Known as 'saturation recovery', this recovery is characterised by the time constant T_1. A correlation time τ_c , describes the characteristic time for a molecule to rotate one radian. These rotations will cause fluctuations in the local magnetic field of nearby nuclei. Smaller molecules that tumble faster will have smaller correlation times than lager molecules. Water molecules have a correlation time of $\sim 10^{-12}s$. If the value of $\frac{1}{\tau_c}$ is close to the Larmor frequency, the value of T_1 will be short. For pure liquids, such as water, the T_1 value is largely dependent on the strength of the magnet, with increasing field strength giving a longer T_1 value. The T_1 of water at 7T is approximately 3 seconds. For *in-vivo* experiments, the value of T_1 is dependent on the surrounding tissue. Water molecules have restricted movement in tissue, with an exchange between the hydrogen molecules of the water and tissue. This results in a longer average correlation time and shorter T_1 values. Larger molecules, such as fat, will also have shorter T_1 values.

2.2.2 T_2 Relaxation

Transverse relaxation is the loss of signal in the transverse plane due to a loss of phase coherence. Due to the random tumbling motions of magnetic moments in a liquid, the individual magnetic moments have their own local fluctuating magnetic fields. Although these fields are small compared to the main $\mathbf{B}_0$ field, as the magnetic moments interact with each other (dipole-dipole interactions) this will cause a fluctuating local field which changes the precessional frequencies of individual magnetic moments. Following excitation, the difference in precession frequency results in a loss of phase coherence and the loss of transverse signal (Figure 2.4).

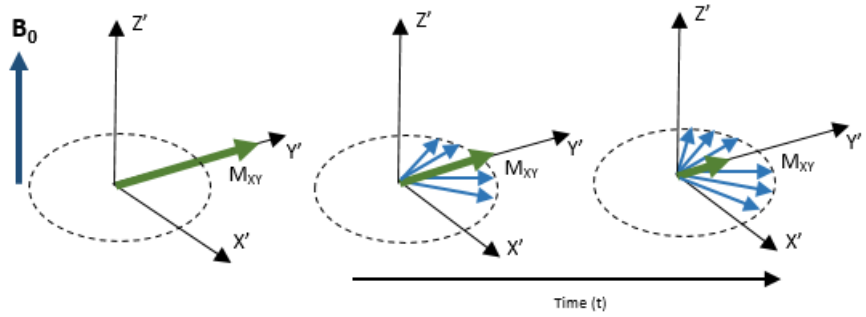

Figure 2.4: T_2 Relaxation

Following RF excitation, as time increases, the spins will dephase and there is a loss of **M** in the transverse plane.

The T_2 relaxation decay can be described as follows (for $t \geq 0$):

$$M_{xy}(t) = M_0 e^{\frac{-t}{T_2}} \tag{2.25}$$

The decay of the net magnetisation **M** is not caused only by dipole-dipole interactions, but also by inhomogeneities in the $\mathbf{B}_0$ magnetic field. The combination of dipole-dipole interactions and magnetic field inhomogeneities results in a faster loss of transverse magnetisation. This faster relaxation time is known as T_2*. The rate at which T_2* decays is described as:

$$\frac{1}{T_{2*}} = \frac{1}{T_2} + \frac{1}{T_2'} \tag{2.26}$$

where T_2' is the effect from the field inhomogeneities.

In pure water $T_1 = T_2$, however T_2 values will generally decrease as the magnetic field strength increases. The value of T_2 in biological tissue is always shorter than T_1. For a biological sample which has large molecules, there will be a higher probability of interactions (from the longer correlation times) between the spin local magnetic fields of the molecules. This results in more frequent energy exchanges and a shorter T_2.

2.3 Origin of the MR Signal

After an RF pulse has tipped the net magnetisation, **M**, to have a component that precesses in the transverse plane at ω_0, an oscillating magnetic field is generated. This will induce a small current in a receiver coil placed in the transverse plane. This signal is known as a free induction decay (FID). Faraday's law of induction says that a changing magnetic field will induce a current in a conductor. The current generated in the coil is proportional to the rate of change of the magnetic field, where the induced current will oppose the applied field.

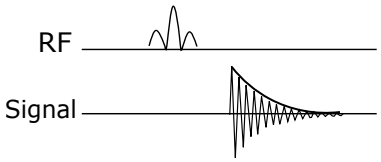

Figure 2.5: The FID signal generated from an RF pulse

Following a 90° RF pulse, the net magnetisation will precess in the transverse plane. As the net magnetisation returns to its equilibrium position, the oscillating magnetic field that is generated will be detected as a small current, producing the FID.

In the xy-plane before relaxation occurs, the signal from **M** can be split into real and imaginary components:

$$\begin{aligned} S_x &\propto M_x cos(\theta) \\ S_y &\propto M_y sin(\theta) \end{aligned} \tag{2.27}$$

The real component of the signal is proportional to M_x and the imaginary component of the signal is proportional to M_y (Figure 2.6).

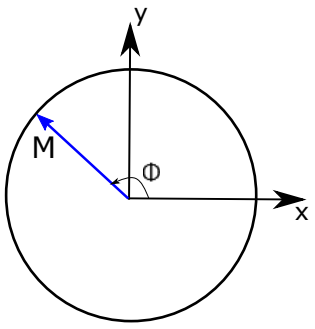

Figure 2.6: Phase of a net magnetisation of spins in a magnetic field

The precession of **M** in a magnetic field, $\mathbf{B}_0$, at the Larmor frequency ω_0 will have a phase value θ.

The phase is given by $\theta = \omega_0 t$ and, using Euler's formula, the signal is:

$$S \propto (cos(\theta) + isin(\theta))$$
$$S \propto e^{i\theta} \propto e^{i\omega_0 t} \propto e^{i\gamma \mathbf{B}_0 t} \tag{2.28}$$

where γ is the gyromagnetic ratio, $\mathbf{B}_0$ is the static magnetic field and t is the time after the RF pulse is applied.

2.3.1 Gradients and Slice Selection

In an ensemble of spins, the individual magnetic moments will precess at the same frequency, ω_0. If a small additional magnetic field is applied, that linearly varies with position, this will cause the precession frequency to be dependent on position (Figure 2.7). This is called a magnetic field gradient and is defined (for the x-direction) as:

$$G_x = \frac{\delta B_z}{\delta x} \tag{2.29}$$

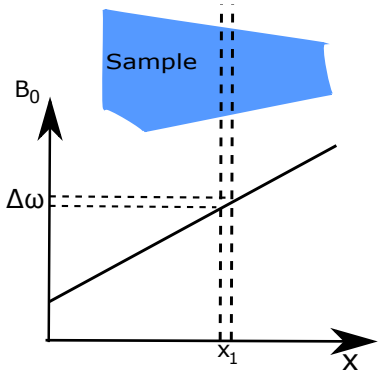

Figure 2.7: Gradient application

A sample with a gradient applied to linearly vary the precession frequencies of the magnetic moments contained in the selected slice.

In the laboratory frame, the magnetic field is:

$$B = \mathbf{B}_0 + G_x \cdot x_1 \tag{2.30}$$

where the precession frequency is defined as:

$$\omega = \gamma \mathbf{B}_0 + \gamma G_x \cdot x_1 \tag{2.31}$$

This precession frequency holds for the laboratory frame of reference. In the rotating frame of reference, $\omega_1 = \omega_0$ when on-resonance:

$$\omega = \gamma G_x \cdot x_1 \tag{2.32}$$

The signal for a sample x_1 is given by:

$$ds \propto \rho(x_1) e^{i\gamma G_x \cdot x_1 t} dx \tag{2.33}$$

with $\rho(x_1)$ the spin density of the sample at position x_1.

By combining Equations 2.31 and 2.33, the signal of the sample at the x_1 position is:

$$ds_{(G_x,t)} = \rho(x_1) e^{i\gamma G_x \cdot x_1 t} dx \tag{2.34}$$

The signal (in the rotating frame) for the sample over x is thus:

$$S_{(G_x,t)} \propto \int_{-\infty}^{\infty} \rho(x) e^{i\gamma G_x \cdot x t} dx \tag{2.35}$$

The MR signal will result in a summation of the signals from all the magnetic moments contained in the sample.

By using the substitution $k_x = \frac{1}{2\pi}\gamma G_x t$, the signal in one-dimension is:

$$S_{(k)} \propto \int_{-\infty}^{\infty} \rho(x) e^{i2\pi k_x \cdot x} dx \tag{2.36}$$

and for two dimensions:

$$S_{(k_x,k_y)} \propto \int_{-\infty}^{\infty}\int_{-\infty}^{\infty} \rho(x,y) e^{i2\pi(k_x \cdot x + k_y \cdot y)} dx\, dy \tag{2.37}$$

Thus, there is a Fourier relationship between $S_{(k_x,k_y)}$ and $\rho(x,y)$.

2.3.2 Encoding, k-Space and Fourier Transform

Magnetic field gradients can be used to select a slice for imaging. Here, a gradient is applied perpendicular to the direction of the slice select direction. While this gradient is turned on, the frequencies of the magnetic moments will vary along the gradient direction (Figure 2.7). When a narrow bandwidth RF pulse is applied at the same time as the gradient and the precession frequency matches that of the magnetic moments in the slice, the magnetic moments of the same frequency as the RF pulse will be excited. To frequency encode the signal, this gradient is applied perpendicularly to the the slice and phase direction.

To encode the sample in the direction perpendicular to the read and slice directions, a gradient, known as the phase encoding gradient, is applied. This gradient causes the magnetic moments precession frequency to depend on position and causes a permanent phase shift once the gradient is turned off. This phase shift (ϕ) can be described by:

$$\phi = \gamma G_y \cdot t \tag{2.38}$$

where G_y is the strength of the gradient and t is the time of the gradient.

Data points are collected in a cartesian coordinate grid known as 'k-space'. The MR signal is sampled at multiple points with each data point being a complex signal that contains real and imaginary components. The low frequency data in the middle of k-space contains information about the bulk of the image. The high frequency data at the periphery of k-space contains the finer details of the image.

Application of a Fourier transform in both the frequency and phase encoding directions (2DFT) will produce a spin density value for each data point with a real and imaginary output. It should be made clear that each point in k-space does not translate directly to each pixel in the final image. Each k-space point contains spatial frequency and phase information about the whole image. The final MR image is constructed by taking the magnitude of the complex spin density data.

2.4 Pulse Sequences

An MRI pulse sequence describes the temporal combination of gradients (x, y, z) and RF pulses. These are used to acquire an MR image. The most relevant sequences to this thesis are described below.

2.4.1 Gradient Echo & Spoiled Gradient Echo MRI

For gradient echo MRI, an excitation pulse (where the flip angle $\alpha < 90°$) is simultaneously applied with a slice selective gradient, followed by a small refocusing gradient (half the size of the slice selective gradient) (Elster 1993). A read dephase gradient is used to rapidly dephase the spins in the transverse plane by altering their resonant frequencies (Figure 2.8). The read gradient is applied again in the opposite direction, creating the gradient echo (both of these gradients have the same area). Gradient echo can be using for imaging, with a line of k-space collected for each TR.

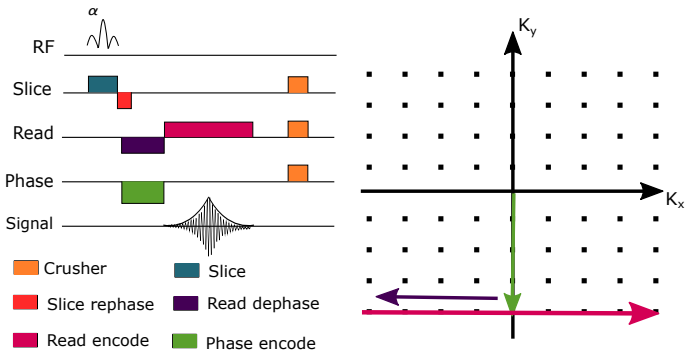

Figure 2.8: Acquiring one data point in k-space using a gradient echo sequence

The gradient echo sequence uses a combination of dephase and rephase gradients to produce the MR signal. The different gradients are indicated on the image by different colours. When used for imaging, each line of k-space is filled in one TR.

The phase gradient is applied at the same time as the read dephase gradient to phase encode the spins. This is repeated for each line of k-space. The time taken for this to occur, and more accurately, the time between each excitation pulse, is known as the repetition time (TR). The time between the middle of the excitation pulse and the middle of the echo is called the echo time (TE). The value of the phase gradient determines which line of k-space is collected during the read gradient. Small values of the flip angle are typically used, with the optimal angle for the maximum signal given by the Ernst angle:

$$\alpha_E = \arccos\left(e^{-\frac{TR}{T_1}}\right) \tag{2.39}$$

Compared to the conventional gradient echo sequence, in a spoiled gradient echo sequence, spoiler gradients are used to purposely disrupt the T_2 signal before the next TR starts. This permits weighting of the signal for for T_1 (see Section 2.4.6).

2.4.2 Spin Echo MRI

The spin echo sequence is a combination of a 90° and 180° pulse. The sequence starts with a 90° RF excitation pulse with a slice selective gradient simultaneously applied (Figure 2.9). This excitation pulse tips the net magnetisation into the transverse plane where a FID will occur but is not imaged. By applying a 180° refocusing pulse along simultaneously with a slice selective gradient, the net magnetisation within the slice is refocused. The time between the middle of the RF pulse and the middle of the spin echo is the echo time. The refocusing pulse occurs at half of TE. The spin echo sequence acquires k-space in the same way as a gradient echo, with one line of k-space acquired during each TR.

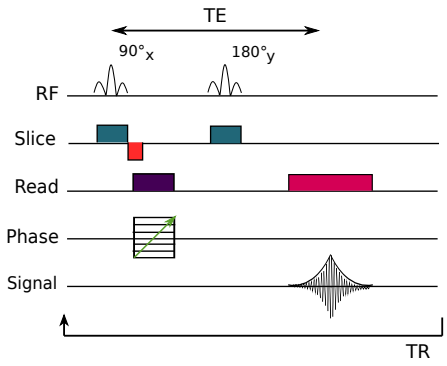

Figure 2.9: A spin echo MRI sequence

A spin echo sequence uses a refocusing 180° pulse to generate an echo after the first FID. It is this echo that is used for the MR signal. As seen for GE-MRI, a single line of k-space is acquired for each TR.

2.4.3 RARE

A faster acquisition method than spin-echo imaging is rapid imaging with refocused echoes (RARE) (Hennig et al. 1986). This sequence uses different phase encoding gradients for each additional echo, compared to a conventional spin-echo sequence which uses one phase encoding gradient per TR. The RARE sequence allows for fast acquisition of data to fill k-space (Figure 2.10) meaning multiple k-space lines can be filled in each TR. It is often referred to as a 'fast spin-echo' or 'turbo spin-echo' sequence.

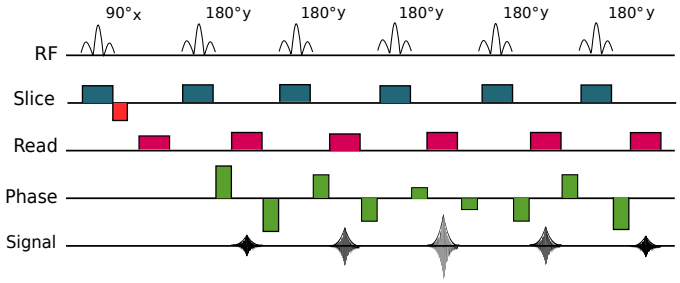

Figure 2.10: A RARE sequence schematic

A RARE sequence uses a combination of different phase encoding gradients to generate multiple echos in the same TR. RARE can acquire multiple lines of k-space in the same TR, making it faster than conventional spin echo.

2.4.4 Echo Planar Imaging

Echo planar imaging (EPI) is one of the fastest MRI acquisition methods. EPI can acquire the full k-space in one excitation, or in multiple 'shots', making the overall scan duration shorter than other MR sequences. EPI can use either a spin echo sequence (T_2 weighted) or a gradient echo sequence (T_{2*} weighted). To fill k-space, multiple gradient echoes which have different phase steps are acquired by using rephasing (blipped) gradients (Figure 2.11). The read gradient is pseudo-continuously applied, with the polarity changing between positive and negative. To change each k-space line, short phase gradients are applied before each new echo (blipped EPI) (Stehling et al. 1991).

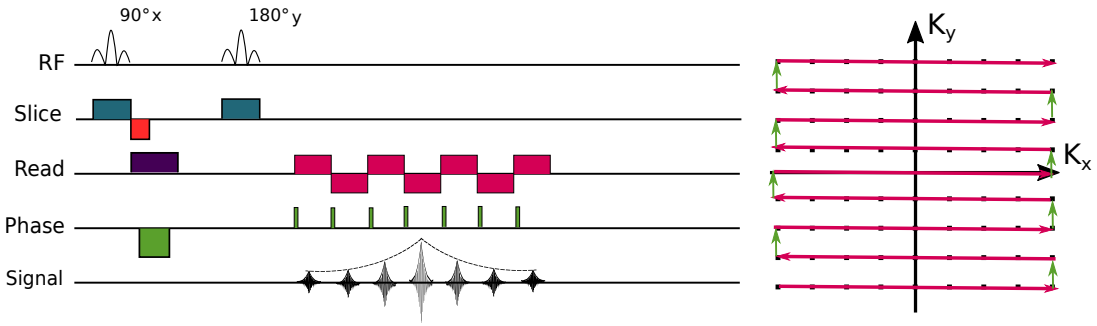

Figure 2.11: A schematic of the spin echo EPI sequence

EPI can be used to collect the entire k-space in one TR by using using multiple rephasing gradients with a pseudo-continuously applied read gradient.

Although EPI has a reduced imaging time and uses less RF power than other sequences, it has limited spatial resolution and can be more sensitive to motion artefacts and magnetic field inhomogeneities.

2.4.5 Inversion Recovery

An inversion recovery sequence (see Figure 2.12) uses a spin-echo, EPI or RARE sequence preceded by an 180° inversion pulse. This inversion pulse tips the net

magnetisation from being aligned with the positive z-axis to the negative z-axis. IR sequences can be used to examine the T_1 contrast of different tissues. By first applying the 180° inversion pulse, a small time delay (the inversion time, TI) is used before a spin echo sequence. Immediately after the 90° excitation pulse of the spin echo, different tissues in the imaging sample will have varying values of longitudinal magnetisation. This will result in different levels of contrast in the MRI image dependent on the value of TI used, with the resulting image being T_1 weighted.

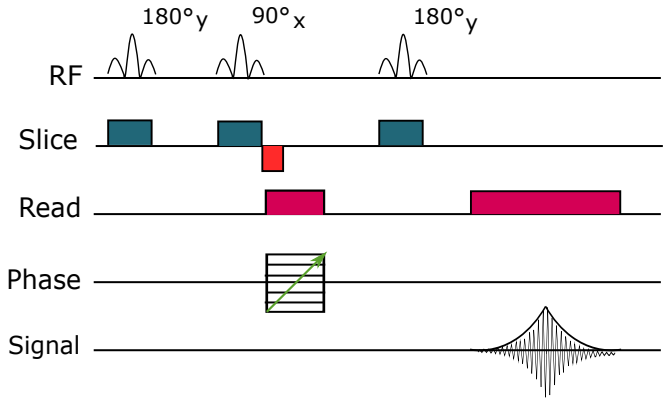

Figure 2.12: An inversion recovery sequence schematic

An IR sequence has an 180° inversion pulse placed before a spin-echo, EPI or RARE. The sequence can be used to examine the contrast of different tissues.

Inversion recovery sequences can be used to suppress the signal from a certain type of tissue by using an appropriate TI value that is similar to the T_1 value of the tissue to be suppressed. When using a conventional spin echo sequence for IR, the TI value can be chosen by:

$$TI = T_1[ln(2) - ln(1 + e^{-\frac{TR}{T_1}})] \tag{2.40}$$

If TR $>>$ T_1, then Equation 2.40 can be reduced to:

$$TI = T_1 \cdot ln(2) \approx 0.69 \times T_1 \tag{2.41}$$

2.4.6 Image Contrast

Depending on the values of TR and TE used for certain pulse sequences, an image can become 'weighted' towards either T_1, $T2$, spin density or a combination of them. This is extremely useful because different tissues and organs in the body have different T_1 and T_2 values. These values depend on both the type of tissue and on the strength of the magnet. As the strength of the magnet increases (for

example from 3T to 7T), the T_1 of a biological sample will increase, whilst the T_2 will decrease. To change the contrast in an image, a combination of TR and TE is used (Table 2.1). It is usually the value of TR that influences the T_1 weighting and TE that influences the T_2 weighting.

TR	TE	Weighting
Short	Short	T1
Long	Short	Proton Density
Long	Long	T_2

Table 2.1: Different image weightings for spin echo MRI

To create a T_1-weighted image, the value of TR must be small compared to the T_1value of the tissue or organ that is being imaged. This weights the image to T_1 as there is less time for the longitudinal component of the magnetisation to relax back to equilibrium. This highlights the difference between the relaxation time of the different tissues in the body. To minimise the effect of T_2 and T_2* relaxation, a small TE value is also needed.

By comparison, to create T_2 or T_2* weighted images, the value of TR needs be much larger than the T_1 of the tissue or organ being imaged. By increasing TE, there is a greater weighting of T_2 or T_2*. Although different sequences can be weighted for T_1 and T_2, for T_1 weighting an inversion recovery or RARE sequence (spin echo) with a short TR can be used. For T_2 weighting, a spin echo sequence can be used and, for T_2*, a gradient echo sequence.

2.4.7 Diffusion Weighted Imaging

Brownian motion, first discovered by Robert Brown in 1827, is the random movement of particles when suspended in a liquid. The movement is from molecular motion and can be used to describe the movement of molecules in a biological sample. Different molecules have varying levels of free, hindered and restricted molecular motion dependent on their properties and position. Einstein described the movement of molecules as a random walk and demonstrated that they diffuse by:

$$D = \frac{K_B T}{6\pi\eta R} \tag{2.42}$$

where D is diffusivity, R is the radius of the Brownian particle, η is viscosity and K_B is the Boltzmann constant.

The molecular movement in a sample can be measured by the use of a pulsed field gradient spin echo (PGSE) sequence (Figure 2.13), introduced by Stejskal and Tanner (Stejskal et al. 1965).

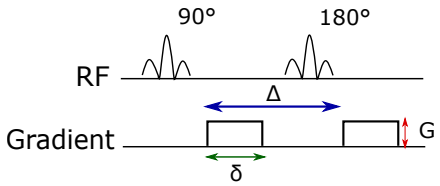

Figure 2.13: A schematic of the PFG sequence

The PFG sequence uses two gradients placed around a 180° pulse. After the 90° pulse, the first gradient will dephase the spins in the transverse plane. The second pulse will rephase them. If there has been a displacement of spins during Δ, the spins will not rephase completely and is identified as a drop in measured signal.

Consider a sample of fluid in a magnetic field where the focus is on a single water molecule. After a 90° pulse, the molecule will precess in the transverse plane. When the first gradient pulse is applied, the molecule will acquire a phase (in the rotating frame):

$$\Theta_1 = \gamma\delta \boldsymbol{G_x} \cdot \boldsymbol{x}_1 \tag{2.43}$$

where $\boldsymbol{x}_1$ is the initial position of the particle and δ is the duration of the gradient.

During an observation time, Δ, the molecule will displace from the position $\boldsymbol{x}_1$, to a new position $\boldsymbol{x}_2$. This could be due to multiple reasons such as diffusion, dispersion or flow.

A 180° pulse is applied with a second gradient pulse following, resulting in a phase shift of:

$$\Theta_2 = \gamma\delta \boldsymbol{G_x} \cdot \boldsymbol{x}_2 \tag{2.44}$$

With a resultant phase shift:

$$\Theta = \Theta_1 - \Theta_2 = \gamma\delta \boldsymbol{G_x} \cdot \boldsymbol{x}_1 - \gamma\delta \boldsymbol{G_x} \cdot \boldsymbol{x}_2 = \gamma\delta \boldsymbol{G_x} \cdot (\boldsymbol{x}_1 - \boldsymbol{x}_2) \tag{2.45}$$

If $\boldsymbol{X} = \boldsymbol{x}_2 - \boldsymbol{x}_1$ and $q = \frac{1}{2\pi}\gamma\delta \boldsymbol{G_x}$ then:

$$\Theta = -2\pi \mathbf{q} \cdot \boldsymbol{X} \tag{2.46}$$

The signal is given by:

$$s(q) = s(0)e^{-i\Theta} = e^{-i2\pi q \cdot \boldsymbol{X}} \tag{2.47}$$

It is important to note that the signal depends upon the displacement and not the initial or final position. The total signal is an integral over all values of displacement $\mathbf{X}$, where $P(\boldsymbol{X}, \Delta)$ is the probability of a displacement $\boldsymbol{X}$.

$$S(q,\Delta) \propto \int_{-\infty}^{\infty} P(X,\Delta) e^{i2\pi qX} dX \tag{2.48}$$

This equation demonstrates a Fourier relationship between the probability of displacement and the amplitude of the echo. A free unrestricted diffusion of molecules, or Gaussian distribution of molecules, will give a probability distribution of:

$$P(X,\Delta) = \frac{1}{\sqrt{4\pi D\Delta}} e^{\frac{-X^2}{4D\Delta}} \tag{2.49}$$

The signal intensity can thus be written using Equations 2.48 and 2.49:

$$S = S_0 e^{-4\pi q^2 D(\Delta - \frac{\delta}{3})} = S_0 e^{-\gamma^2 G^2 \delta^2 D(\Delta - \frac{\delta}{3})} \tag{2.50}$$

By using the relation:

$$b = \gamma^2 G^2 \delta^2 (\Delta - \frac{\delta}{3}) \tag{2.51}$$

Equation 2.50 can be simplified to:

$$S = S_0 e^{-bD} \tag{2.52}$$

The signal attenuation due to relaxation is approximately independent of the applied diffusion gradient. By dividing by S_0, this eliminates any relaxation effects and the only dependence is on diffusion.

2.4.8 Using PGSE to Image Diffusion

A typical PGSE sequence is shown below in Figure 2.13. A pair of pulsed field gradients are applied around the 180° RF pulse in a spin echo sequence. The molecular displacement itself is unaffected by scan parameters. By changing the parameters of Equation 2.50, for example, the gradient strengths or observation times, will change the amount of rephasing caused by the second gradient. If there has been molecular displacement during the observation time, Δ, this will show as a drop in signal intensity.

2.5 Scanner Hardware

An general overview of the magnet and hardware used in MR imaging is presented. The main magnet consists of multiple coils that work together (Figure 2.14). In

this thesis, a 7T Bruker pre-clinical imaging system is used.

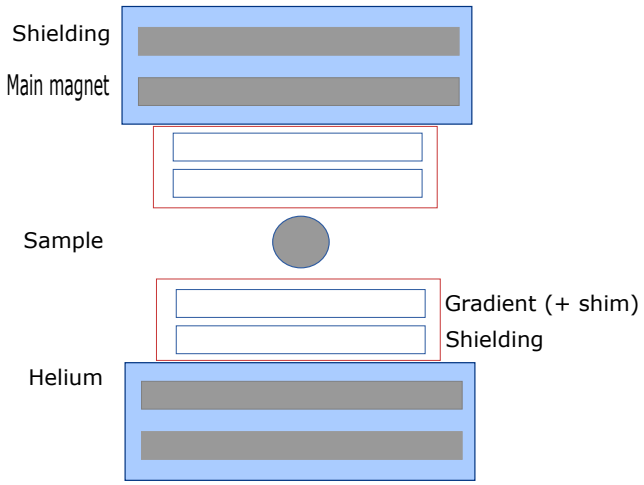

Figure 2.14: The coils used in an MRI scanner

2.5.1 The Main Magnet

The main magnet contains the coil that carries the current that produces the main $\mathbf{B}_0$ field. Typical superconducting magnets use niobium-titanium wire or niobium-tin wire. Once the coil is charged with current, to keep its superconducting properties, the coil must be cooled in a bath of liquid helium at 4K. Either an additional dewar of liquid nitrogen (77K) is used to slow the boil off of the the liquid helium or a cold head compressor is used to compress the evaporating helium back to liquid. The middle of the magnet (known as the bore of the magnet) is the most homogeneous region and is where the sample is placed for scanning.

2.5.2 Shim Coils

Superconducting shim coils placed in the cryostat have currents passed through them to create field gradients that maintain the homogeneity of the $\mathbf{B}_0$ field. Resistive shims are outside the cryostat. First order shimming is provided by the gradient coils whereas second order and above shimming is provided by additional coils. The use of resistive shims means shimming can be adjusted for each patient.

2.5.3 Gradient Coils

Gradient coils are used to produce the pulsed field gradients in the three directions needed for imaging. These coils work at room temperature by passing a direct

current through the coils, producing a constant gradient which results in a linear change of the magnetic field needed for frequency and phase encoding. The Z-direction coils are usually a Maxwell pair whereas the X- and Y- gradient coils are saddle coils. This is to allow the three sets of gradients to fit together.

2.5.4 RF Coils

Radio frequency (RF) coils are used to produce the $\mathbf{B}_1$ field. These coils are designed to transmit the RF radiation, to receive the corresponding signal, or both. A volume resonator can receive and transmit the RF radiation and is used for full body imaging. Surface coils are smaller receive coils that can be placed next to a body part to receive a higher signal. An example of this is using a head surface coil for brain imaging. The RF coil transmits the RF radiation, which has the oscillating $\mathbf{B}_1$ field component. This is applied perpendicular to the $\mathbf{B}_0$ field and is transmitted as short RF pulses close to the Larmor frequency.

For this research, a 4-channel phased array mouse head surface coil and rat head surface coil were used for receiving the signal. A phased array coil differs from a single surface coil in that it has multiple surface coils that emit separate signals. These signals will be based on the position of each coil and can provide extra information that is not received from a signal coil. This also reduces the scan time as it reduces the number of phase encoding steps needed to fill k-space.

2.5.5 Shielding

Shielding is used to reduce the fringe magnetic field produced from the MRI scanner. This is achieved by active shield coils that are placed outside the main magnetic field coils (but still in the helium dewar) and produce a magnetic field that opposes the main $\mathbf{B}_0$ field. Shielding of external RF in the magnet room is provided by a Faraday cage.

2.5.6 Electronics

In addition to the main magnet and coils, multiple electronics are needed to be able to run an MRI experiment. Figure 2.15 below shows the basic electronic components of the MRI scanner.

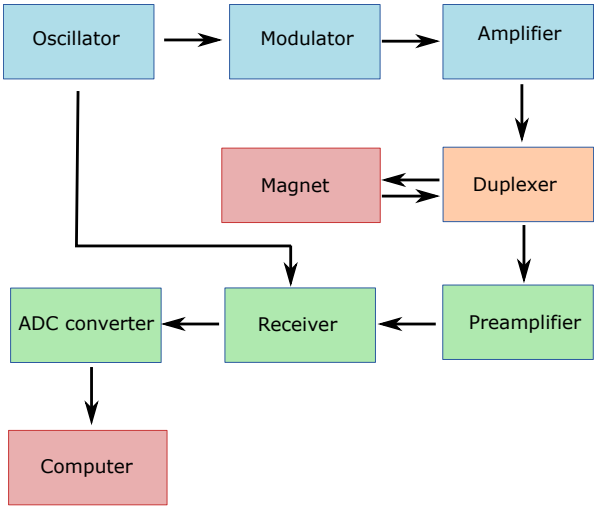

Figure 2.15: The electronics for a MRI scanner

2.5.6.1 Oscillator

The oscillator produces an oscillating electrical voltage that has a defined frequency at or near the Larmor frequency. This carrier wave is sent to the modulator and to the receiver electronics as a reference signal.

2.5.6.2 Modulator

The modulator is used to split the continuous oscillating carrier wave into small pulses known as 'RF pulses', and modify the amplitude to change the pulse shape.

2.5.6.3 Amplifier

The RF amplifier amplifies the pulses received from the modulator that will be used for the imaging sample. This generates the large current that will be needed for the RF coils. The flip angle of the RF pulse is controlled by the amplifier, by changing the gain of the amplifier using a transmit attenuator. The PharmaScan MR scanner used for this thesis uses a 300W or 1kW amplifier.

2.5.6.4 Duplexer & Preamplifier

The RF coil detects a weak signal ($\sim$mV) from the sample and the duplexer directs this to the pre-amplifier where the signal is scaled to a larger voltage (V). The duplexer is used to ensure there is a switch between the transmit and receive electronics. The receiver electronics are extremely sensitive for detecting the

small signal emitted from the sample and would be damaged by the high powered transmit signal.

2.5.6.5 Receiver & ADC Converter

At 7T, the MRI signal oscillates at 300MHz, which can not be processed by the ADC converter. Hence, the receiver uses the reference wave from the oscillator for comparison to the receiver signal. Using a rotating frame of reference, this converts the receiver signal to a lower frequency signal that can be processed. The analogue-to-digital converter (ADC) is used to convert the analogue signal into a digital output which is stored in the computer.

2.5.6.6 Computer

The computer console is used to control the scanner and run the MRI sequences. The pulse sequences, gradients and other parameters can be controlled from this input. The computer system also includes the image reconstruction methods to generate the final MRI images.

Chapter 3

Literature Review of ASL and DWASL

3.1 Abstract

This chapter first introduces the concept of arterial spin labelling (ASL) with a literature review on the different types of ASL, before summarising the recent work on multiple boli ASL (mbASL). Following this is a review of diffusion weighted ASL (DWASL). These two sequences form the basis of the next three results chapters.

3.2 Arterial Spin Labelling

3.2.1 The first ASL Experiment

Arterial spin labelling (ASL) is a non-invasive imaging technique, that uses the endogenous blood water flowing into the brain as a contrast agent. The method introduced by Detre et al., was developed initially to measure cerebral perfusion (Detre et al. 1992). In this experiment, saturation pulses were used to magnetically label the arterial blood spins in the neck region as it travelled toward the brain. Once a steady state of the labelled arterial blood spins was established in the brain, the RF pulse was turned off and an image of the brain taken (label image). Another image of the brain, known as the control image, was then taken, with the labelling slice applied above the head, to account for magnetisation transfer (MT) effects. By subtracting the two images, with and without labelling, the resulting image will be perfusion weighted. Detre proposed that ASL could be sensitive to cerebral blood flow (CBF) changes and could produce quantitative CBF maps.

Detre modified the Bloch equations (described in Section 2.1.2), to account for

flow effects. Here the longitudinal magnetisation in the brain (M_b) is given as:

$$\frac{dM_b}{dt} = \frac{M_b^0 - M_b}{T_1} + fM_a - \frac{f}{\lambda}M_b \tag{3.1}$$

where M_b^0 is the fully relaxed value of M_b, λ is the blood-brain coefficient of water, M_a is the concentration of longitudinal magnetisation of arterial blood water and f is blood flow. To be able to fully quantify the method, multiple assumptions were made. Detre assumed the labelled spins were exchanging immediately with the brain tissue. Labelled spins, described by $\frac{fM_b}{\lambda}$, replaced the spins leaving the brain through venous flow. The ASL model also assumed a complete saturation of blood water and negligible relaxation of the spins until after exchange with tissue water. At t = 0, where $M_a = 0$ after labelling, equation 3.1 was solved to give:

$$M_b(t) = \frac{M_b^0}{1 + f\frac{T_1}{\lambda}}\{1 + \frac{fT_1}{\lambda}exp(-t(\frac{1}{T_1} + \frac{f}{\lambda}))\} \tag{3.2}$$

This meant M_b would be dependent on both f and the T_1 of blood water, with an apparent time constant given by:

$$\frac{1}{T_{1app}} = \frac{1}{T_1} + \frac{f}{\lambda} \tag{3.3}$$

Detre assumed that M_b decreased to a steady state magnetisation, M_b^{ss}, which could be calculated by setting $t = \infty$ and solving Equation 3.2:

$$\frac{M_b^{ss}}{M_b^0} = \frac{1}{1 + f\frac{T_1}{\lambda}} \tag{3.4}$$

The flow can thus be calculated by solving Equations 3.3 and 3.4:

$$f = \frac{\lambda}{T_{1app}}(1 - \frac{M_b^{ss}}{M_b^0}) \tag{3.5}$$

The sequence was able to produce ASL images where an average change of signal between the two images was 3.1% for a rat. With no cerebral blood flow the signal change was expected to be zero in a dead rat, but a signal change of 1 % was found. Detre attributed the value to spectrometer instability. To account for the signal from the arterial intravascular volume, spoiler gradients were used around the 180° pulse in the imaging module. These spoiler gradients were used to suppress the signal, with the contribution from the intravascular water being 0.6% of the whole brain. Detre suggested the signal would make a small contribution, but that

it could contribute to an over estimation of CBF.

Detre calculated the average value of cerebral blood flow for the rat brain to be 106 ml/100g/min, which he compared to a literature value of 100 ml/100g/min. The good comparison with literature showed the assumptions used were reasonably valid. To further validate the ASL model, CBF maps were produced using rats with hypercapnea, where the average CBF value found was 227 $\pm$ 18 ml/100g/min.

3.2.2 Continuous ASL

Williams et al. introduced a different method for inverting arterial blood, namely using adiabatic fast passage (Williams et al. 1992). This method was the first to be known as 'Continuous ASL' due to the long low power RF pulse that was used (Figure 3.1). By using an adiabatic pulse for the inversion, rather than a saturation pulse, an increase in temporal resolution was achieved, with the additional benefit of being easier to implement. This new method produced mean CBF values of 139 ml/100g/min in the rat brain. The implementation of CASL in human studies was challenging, due to the need for additional hardware (an extra coil for the continuous RF pulse applied), along with the restrictions for specific absorption rates (SAR). To compensate for this, a new ASL technique was developed that used a short inversion pulse over a large labelling slab. This technique became known as pulsed arterial spin labelling (PASL).

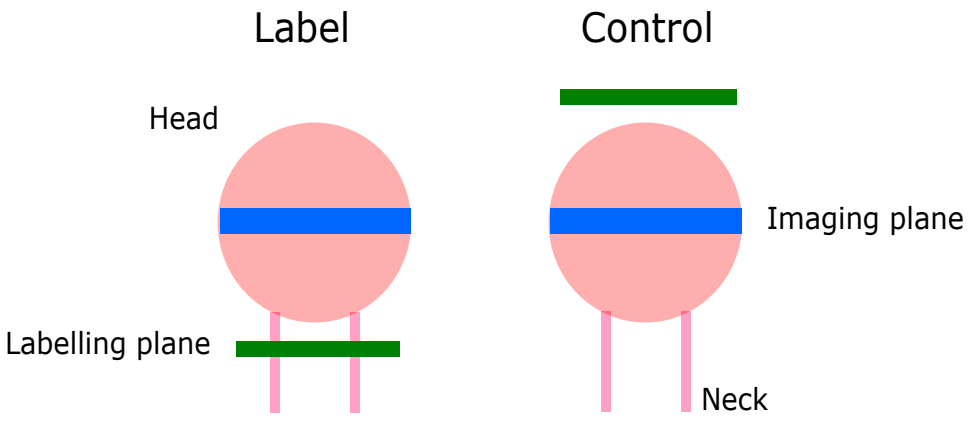

Figure 3.1: Continuous ASL schematic

Labelling takes place in the neck region using a long continuous RF pulse for CASL. The labelling pulse is placed above the head for the control image to account for MT effects.

3.2.3 Pulsed ASL

3.2.3.1 EPISTAR

Pulsed ASL was first introduced in 1994 by Edelman et al (Edelman et al. 1994). This technique was known as echo-planar imaging and signal targeting with alternating radio frequency (EPISTAR). Two echo-planar images had an interleaved acquisition where one of the images had an RF inversion pulse applied to label the blood (Figure 3.2). The RF pulse was 23ms in length, with a slab thickness of 90mm, and much shorter than the pulse used in CASL. After application of the RF pulse, a short delay was used before imaging, to allow time for the labelled arterial blood to reach the imaging slice. A changeable delay time before imaging allowed the signal from the labelled blood to be from the major arteries (400ms), the distal branch arteries (800ms) or the capillaries and tissue ($>$ 1000ms).

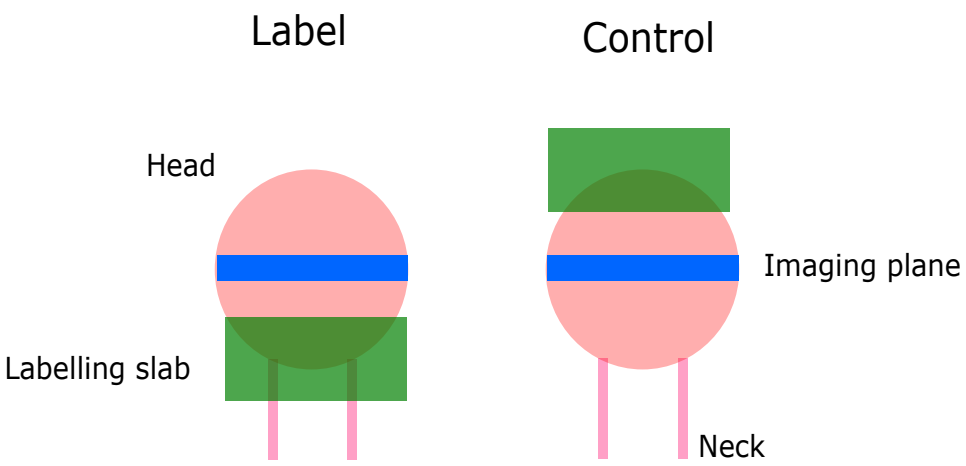

Figure 3.2: Pulsed ASL schematic

The first pulsed ASL experiments used a thick slab to label the blood using a single short RF pulse. The pulse was placed above the head to account for MT effects for the control image, similar to CASL.

A control inversion region was used to counteract magnetisation transfer effects, as used by Detre et al. previously. There were issues with the control region intersecting part of the brain, with the signal from veins appearing bright after subtraction due to spin tagging. Quantitative maps of CBF were not produced in this paper, however the technique was used to look at changes in brain activation using the blood oxygenation level-dependent (BOLD) technique. Edelman used PASL to show changes in the image signal intensity in the activated brain. The PASL sequence showed considerable improvement over the initial work of Detre and Williams. There was reduction in SAR, in addition to increased efficiency and a reduced scan length from using an EPI sequence for image acquisition.

3.2.3.2 FAIR

Another approach to using a single pulse for perfusion imaging was introduced as flow-sensitive alternating inversion recovery (FAIR) by Kim et al in 1995 (Kim 1995). Kim based FAIR on a protocol by Kwong et al (Kwong et al. 1995), and used slice-selective inversion recovery imaging for identifying brain changes between sensory activation and rest in humans. For FAIR, two inversion recovery images were acquired, one with a non-selective inversion pulse and the other with a slice-selective inversion pulse (Figure 3.3). An EPI module was used for image acquisition.

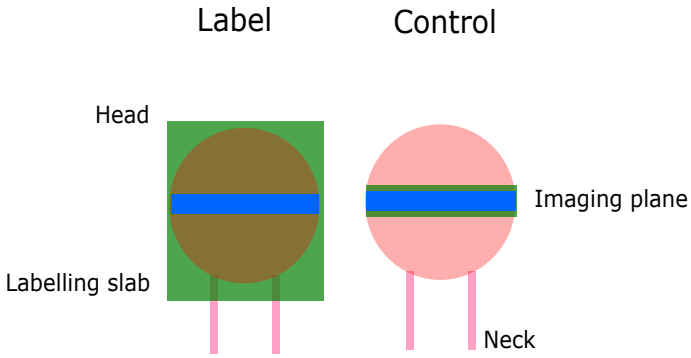

Figure 3.3: FAIR Schematic

FAIR uses a non-slice-selective inversion pulse that covers the head for a human and covers most of the body or the full body in rodents. For the control image, the inversion slice inverts only the imaging slice. This inversion slice is slightly larger than the imaging slice.

For the slice-selective inversion (control), the blood water spins flow from outside the inversion slice to the intravascular compartment and then exchange with the tissue water. These spins are fully relaxed. For the non-slice-selective inversion (label), the inflowing spins are inverted and relax back to equilibrium due to spin-lattice relaxation. Kwong's protocol was able to qualitatively measure CBF. Kim used FAIR to measure a quantitative value of CBF, and compared relative CBF changes between rest and activated states in the brain. The FAIR sequence was able to compensate for magnetisation transfer effects as the same RF inversion pulse was applied in both label and control, with the control image having a slice-selective gradient.

3.2.4 Pseudo-Continuous ASL

To compensate for the limitations of CASL, a variation of CASL called pseudo-continuous ASL was introduced (Dai et al. 2008). Pseudo-continuous ASL (pCASL) replaced the long RF pulse in CASL with a train of short duration, small flip angle, slice selective RF pulses. A large number of pulses were used over a typical 2-3s labelling duration with a small gap ($\sim$1ms) between them. pCASL reduced the magnetisation transfer effects due to the larger gradients used in CASL. These

gradients increased the resonant offset of the RF pulses, which reduced MT effects and increased the labelling efficiency (Alsop, Detre, et al. 2015). There was an advantage to pCASL as it used only one coil, thereby addressing the additional hardware issue of CASL. Furthermore, it did not need the continuous application of RF power, lowering SAR levels (Dai et al. 2008).

3.2.5 Comparison of ASL Techniques

Usually PASL will have a higher labelling efficiency than CASL/pCASL. However, CASL and pCASL have a higher signal and SNR. This is due to the temporal duration of the labelled bolus. In PASL, the labelled bolus is limited by the slab size which in turn is limited by the dimensions of the transmit RF coil. CASL and pCASL have a longer temporal duration which is proportional to the volume of labelled blood. Overall, this means that CASL/pCASL have a higher signal and SNR compared to PASL. Furthermore, there is a larger gap for labelled spins to travel in PASL compared to pCASL so there are larger T_1 decay effects (Alsop, Detre, et al. 2015).

Both PASL and pCASL have the advantage over CASL of not needing an extra coil for labelling, meaning it is easier to implement on MRI systems. It has also been shown that pCASL has a higher labelling efficiency than CASL (Wu et al. 2007). pCASL is the current recommendation for clinical practise by the 2015 white paper from the ISMRM perfusion study group (Alsop, Detre, et al. 2015).

3.2.6 Multiple Boli Arterial Spin Labelling

Multiple boli arterial spin labelling (mbASL) is a newly developed ASL sequence that uses a train of adiabatic inversion pulses to label multiple boli of arterial blood as it travels through the neck region (Figure 3.4) (Vallatos et al. 2018). mbASL combines the high signal seen from pseudo-continuous labelling and the inversion slab in PASL. The idea of a train of adiabatic pulses originates from Moffat et al. (Moffat et al. 2005). The sequence was designed as an alternative to the original CASL techniques that used flow driven adiabatic inversion. The train of pulses removed the need for an additional labelling coil, whilst the use of adiabatic pulses kept the labelling efficiency similar to pCASL 3.5. Moffat was able to produce CBF maps that agreed with literature values and used them to examine a rat tumour model. The sequence was not optimised however and was described as a pseudo-continuous ASL. However, subsequently, the name pCASL has been widely used to describe a different ASL sequence.

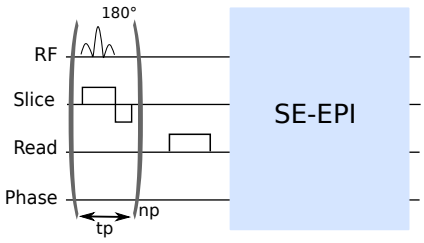

Figure 3.4: mbASL Sequence

The mbASL sequence uses a train of adiabatic pulses to label multiple boli of blood as it passes through the neck region. Following the labelling train, a short inversion time (TI) is used to allow the labelled blood to travel to the imaging plan. A spin echo EPI readout is used to create the images.

A similar idea to mbASL was introduced by Ouyang et al. called pseudo-continuous transfer insensitive labelling technique (pTILT). This sequence used a train of approximately 100 RF pulses to produce an ASL sequence similar to pCASL. The difference between pTILT and mbASL is the use of adiabatic pulses, with pTILT having a lower SNR compared to pCASL sequences (Ouyang et al. 2011).

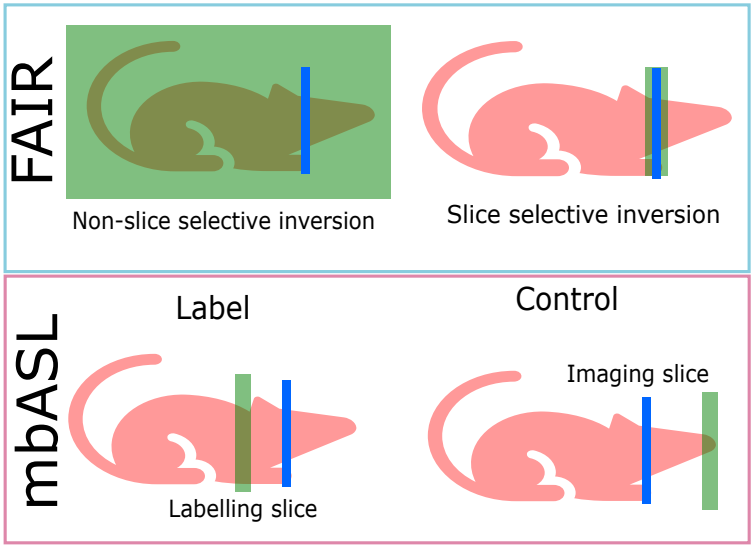

Figure 3.5: Positioning of the mbASL labelling pulse

mbASL uses a labelling slice in the neck region for the label image. The labelling slice is placed above the head for the control image to account for MT effects.

In Vallatos et al. paper, multiple parameters were examined with the aim of optimising the sequence to be used with mice and rats. The number of pulses needed for an optimal signal in mice and rats were shown to be different, with rats needing a much higher number of pulses compared to mice. By varying the delay time between labelling and imaging, it was shown that the labelled bolus signal peaked at different delay times dependent on the rodent strain. Experiments performed on phantoms examined the use of various hyperbolic secant pulses for labelling. The adiabatic parameters were varied to find the highest inversion efficiency. The mbASL sequence was compared to the standard manufacturer's FAIR sequence (Bruker), where it was found that mbASL had a higher overall signal and SNR. For mice, at least a 20% increase in signal was seen in the brain compared

to FAIR and a 60% increase in SNR. The increase in signal for rats was higher, with between 100% and 200% for the different pulse types examined and an increase in SNR of between 300% and 600% (Figure 3.6). Vallatos suggested that mbASL would have an advantage over FAIR, particularly for rats. This is due to the short length of the volume resonator typically used in pre-clinical MRI system, where the full body of the rat is not fully inverted.

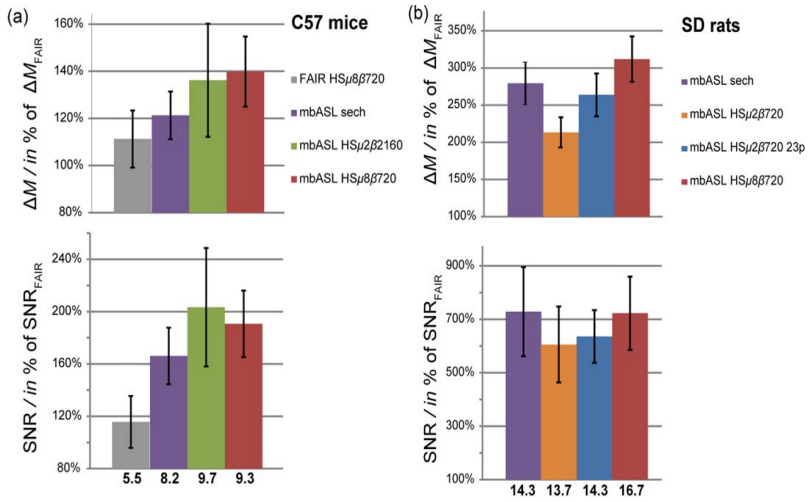

Figure 3.6: Signal increase for mbASL compared to FAIR

The signal increase for mbASL compared to the Bruker FAIR sequence for mice and rats, adapted from (Vallatos et al. 2018). Multiple brain regions were examined with a 20% signal increase for mice and 60% for rats over FAIR.

Vallatos discussed a number of limitations of the mbASL sequence. CBF quantification was not achieved, as the sequence was a hybrid of PASL and pCASL, and as such, could not be described by current ASL kinetic models. A suggestion was made that quantification for the thicker labelling slices could be made using a kinetic model for PASL and for thinner labelling slices, a pCASL model. Furthermore, optimisation of associated parameters, such as the placement and size of the labelling slice compared to the rodent, was needed.

3.3 Diffusion Weighted ASL

3.3.1 The Early Use of Crusher Gradients

The use of diffusion gradients in an ASL MRI sequence was first seen in the early 1990s by Williams et al (Williams et al. 1992), where vascular 'crusher' gradients were used to eliminate the contribution of the signal from labelled blood in the arteries and veins. The assumption was made that these labelled spins do not contribute to a change in signal intensity due to the small amount of arterial blood in the brain (Williams et al. 1992). This idea was proven to be incorrect by Henkel-

man et al. in their 1994 paper on measuring perfusion in the rat brain using IVIM (Henkelman et al. 1994). By using a perfluorinated hydrocarbon (PFC) blood substitute, which was believed to be unable to cross the blood brain barrier (BBB), the NMR signal measured would be only from flow of the PFC in the intravascular space. By applying different values of gradient around the 180° pulse of the spin echo sequence, they showed that signal attenuation occurred at a faster rate with a small b-value compared to a larger b-value. The initial assumption in the IVIM model, first introduced by Denis Le Bihan (Le Bihan et al. 1986), was that only blood flow in the capillaries was contributing to the signal. This was contradicted by the experimental data, which showed that IVIM was sensitive to flowing blood in both the capillaries and the parent vasculature. This study provided evidence that a single 'apparent diffusion coefficient' was not enough to explain the range of diffusion values seen in the experiment. These findings were important as the inclusion of the signal from arteries could cause an overestimation of CBF values when quantification was applied.

3.3.2 Introducing the Two Compartment Model

Alsop and Detre first introduced the idea of a 'two compartment model' in 1996 to address the issue of the signal from both the vasculature and the tissue contributing to the images (Alsop and Detre 1996). Introducing a short delay time after the labelling pulses reduced the sensitivity of the sequence to transit time effects. The length of the post labelling delay (PLD) affected the contribution of the vascular component and, ultimately, the transit time of the labelled spins became a function of the PLD. Alsop showed that by choosing a suitable length of PLD, the signal from the large vessels was reduced and that the use of bipolar gradients was needed only if the transit time of the labelled spins to the vasculature was longer than the PLD. Ye et al. were able to show in 1997 how substantial the signal drop was in the ΔM image (49 %), from the effect of applying bipolar gradients. The decrease of the signal in the control image with the same gradient strength was seen to be only 3%. This was explained for the two different conditions. When no crusher gradient was applied, the ΔM signal would be an equal combination of the signal from the labelled arterial blood water and the labelled water contained in the tissue. Consequently, when large crusher gradients were applied, the ΔM signal was predominately from the labelled tissue water. Overall, there was seen to be a dependence on the amplitude of the gradients for the ΔM signal.

Following Alsop and Detre's work, in 2000 St Lawrence et al. suggested a more accurate two compartment model, that would take into account restricted water exchange (St Lawrence, Frank, et al. 2000). This was in comparison to the one-

compartment Kety model (Kety 1951), which assumed a free diffusion of the water tracer between the tissue and capillaries. However, it was known that water is not a freely diffusible tracer and, therefore, earlier models have underestimated CBF values. The Kety model also assumed that the tagged water was located mainly in the brain tissue. St Lawrence used a modification of the one-barrier distributed parameter (1BDP) model, that assumed the labelled water that diffused into tissue relaxed before it exchanged back into the capillaries. This was a reasonable assumption due to the short T_1 relaxation time for water of $\sim$1s at 1.5T. This model was referred to as the single-pass approximation model (SPA). The SPA model suggested that the signal from the arteries can be reduced by using crusher gradients, but this signal contribution should still be considered in the kinetic model. This was from the suggestion that crusher gradients would not affect the contribution from the capillaries in human ASL experiments. Overall, the SPA model was a more realistic model for measuring CBF values than the Kety model as it took into account different relaxation rates in the tissue and capillaries (St Lawrence, Frank, et al. 2000).

3.3.3 Flow Encoding Arterial Spin Tagging (FEAST)

The work on introducing a delay time and accurate two-compartment model did not address measuring the time taken for the labelled spins to travel through the vasculature to the tissue. Wang et al. introduced a new ASL method to measure this arterial transit time (ATT): by taking the ratio of the ΔM signal from a gradient-echo EPI ASL image with and without bipolar gradients. From this, they could determine a transit time for tissue (Wang, Alsop, et al. 2003). An alternative method at this point was to take images at multiple PLDs. The ASL sequence with no gradient would have signal contributions from both the arterial compartment and capillary/tissue compartment. The sequence with bipolar gradients would suppress the vascular signal, leaving only the signal from the capillary/tissue compartment. By taking a ratio of the two signals, the tissue transit time could be determined. Using Alsop's two compartment model described above, they used a PLD that was longer than the arterial transit time but shorter than the tissue transit time. The assumption was that the labelled spins stayed in the vascular (arteries) and microvascular (capillary) compartments rather than fully exchanging into the tissue. Although this paper used bipolar gradients as a way to measure tissue transit time, it was again a method of suppressing the arterial signal. They were able to show that the strength of the gradient and length of the pulse were important factors when determining the tissue transit time, and that a longer gradient can in turn produce a longer tissue transit time. The strength of the diffusion gradient determined the optimal PLD, with a larger gradient meaning a longer PLD could

be used. Wang et al. suggested that the PLD needed to be long enough for all the labelled blood to enter into the imaging plane but short enough that the majority had not passed into the microvasculature.

3.3.4 When Perfusion Meets Diffusion

Until the early 2000s, most studies had been focused on using ASL as a method to non-invasively calculate CBF values in the brain, with or without diffusion gradients. Modelling of the ASL signal was becoming more sophisticated with Wang et al. using the DWASL method to accurately measure water permeability in the brain in 2007 (Wang, Fernandez-Seara, et al. 2007). This was also one of the first papers to define diffusion weighted ASL as a sequence. By taking images at multiple b values from b = 0 to 300 s/mm^2, and fitting the data to a bi-exponential model, a weighting factor for the signal from the flow dispersion in the capillaries and the signal from the diffusion in the tissue could be measured. By measuring the signal at different PLDs, they were able to statistically show that the capillary weighting became less when the PLD was longer. Dependent on the value of the diffusion gradient or PLD, the DWASL sequence could be made sensitive to the signal from the arteries, capillaries or tissue. Wang showed the DWASL method could separate the signal from the capillary and tissue compartments (known as the intravascular (IV) and extravascular (EV) compartments) and had the potential to probe water permeability values in the brain. The MRI data were used with the SPA model and a value for the permeability surface-area product (PS) and, hence, the water permeability, K_w in the brain was calculated. This measure of permeability is not a true permeability of the BBB, but an estimation.

The DWASL sequence was applied to a brain tumour patient, with an increase in water permeability seen in the tumour region. A potential limitation to the technique was that there could be variations in ATT between normal tissue and tumour tissue. This research provided evidence that DWASL could be used to non-invasively measure the water permeability in the brain.

3.3.5 Combining Techniques

In 2011, St. Lawrence et al. combined the DWASL method with the FEAST method to measure ATT and water permeability in the brain in a single scan time. By using a combination of PLD times and b-values, they first determined the optimal values for suppressing either the arterial or capillary signal (St Lawrence, Owen, et al. 2012). This was used in their two-stage protocol where they measured ATT by

using b = 0 and 10 s/mm^2 and a short PLD time and used b = 0 and 50 s/mm^2 with a longer PLD to separate the signal in the two compartments to be coming from the capillaries and tissue, respectively. They were able to produce results for ATT that were in agreement with values obtained using the FEAST method from Section 3.3.3 and results for K_w, the exchange rate of water across the BBB, that compared with positron emission tomography (PET). This DWASL technique was used to look at the water exchange across the BBB in obstructive sleep apnea by Palomares et al. in 2015. By using DW-pCASL to measure the ATT, K_w and CBF values they were able to show a difference in results between sleep apnea patients and control patients (Palomares et al. 2015). The value of K_w was lower in both the white and grey matter for the sleep apnea patients in addition to a reduced ratio of the signal from DW-pCASL (b = 50)/pCASL (b = 0) compared to the control group. The drop in K_w indicated an increase permeability of the BBB to water. The decrease in ratio of signal between the two sequences (DW-pCASL/pCASL) also indicated that there was a change in BBB integrity. Although a small sample size was used, which was one of the limitations of the study, they were able to show that the DW-pCASL sequence was sensitive to changes in the water exchange rate of the BBB and, hence, could be used to examine permeability changes in the brain.

3.3.6 DWASL in Pre-Clinical Studies

The majority of literature on DWASL has focused on data obtained clinically. In the early literature examining the effect of signal from the vascular compartment, Silva et al. examined the combination of IVIM and ASL in their 1997 paper using rats (Silva et al. 1997). This study was focused on using diffusion gradients to attenuate the vascular signal so it would not cause an effect when measuring perfusion. Multiple b-values were applied, with the signal being fitted to a bi-exponential model and thus demonstrating a split in the the signal from spins in the vascular or tissue compartments. Overall, this study was described as IVIM and can be thought of as an early introduction to the DWASL sequence, which is now used in more recent literature.

A study by Kim et al. used the same process of combining IVIM and ASL to quantitatively measure cerebral blood volume in 2006 (Kim and Kim 2006). This research was used to demonstrate that the pseudo-diffusion component was from the spins in the arterial blood, and that by separating the signal from the arterial blood and the tissue, the arterial blood volume can be measured. They achieve this using diffusion gradients. Although this technique was not being applied to measure BBB permeability, it demonstrates a different use of diffusion gradients and ASL that is useful for non-invasively imaging changes in the brain.

In 2017 Tiwari et al. applied DWASL to an ischaemic stroke model in rats (Tiwari et al. 2017). A continuous ASL sequence with diffusion gradients of b = 0 and 50 s/mm^2 was used for imaging. Abnormal values of K_w were seen two days after stroke which were similar to values obtained by DCE-MRI and histology. No significant results using DWASL for K_w values at 90 minutes post-stroke were seen, which showed a lack of sensitivity in the sequence at early stages in stroke. Overall, the study showed that DWASL could be applied successfully in a pre-clinical model, although limitations with signal and SNR needed to be addressed for the sequence to show viable results.

Another pre-clinical application of DWASL was shown by Wells et al. using a multi-directional DWASL sequence. Using a diffusion-weighted FAIR sequence for imaging, a b-value of approximately b = 20 s/mm^2 was applied in the X, Y and Z gradient directions. They showed that DWASL could be sensitive to flow in different directions, which provided a novel approach to imaging micro-vascular flow patterns using non-invasive MRI. It was suggested the protocol could be applied in a disease model which has changes in cerebral blood flow (Wells, Thomas, et al. 2017).

3.3.7 Combining IVIM and ASL

More recent research from 2018 has reintroduced the concept of IVIM-ASL first seen by (Silva et al. 1997). This study was focused on exploring the IVIM signal in the brain and more specifically, where the signal for IVIM comes from in the arterial tree, Zhang et al. used an ASL prepared IVIM sequence. By applying a time-encoded pCASL module before the typical IVIM sequence, they acquired IVIM data at multiple PLDs (Zhang et al. 2018). This allowed the group to show that the typical single compartment model used in IVIM did not explain the observed complex diffusion properties in the brain. By using different PLDs, they monitored labelled blood at different points in its transit to the brain. They fitted the acquired data to a bi-exponential model, which demonstrated the difference in diffusion values between faster and slower flowing blood in the arterial tree. Due to the time-encoded sequence which supplied data at a range of PLDs, they were able to explore the origin of the IVIM signal, which had not been typically examined in previous IVIM studies.

3.3.8 Applying DWASL using a 3D Readout

DWASL sequences typically use a 2D readout with a pCASL ASL module. Shao et al., in their 2019 paper, used the suggestion of the ISMRM white paper (Alsop, Detre,

et al. 2015) and implemented a 3D GRASE readout for imaging with DWASL (Shao et al. 2019). They were able to quantify K_w using a modification of the SPA model. Separation of the fraction of signal from the capillary and tissue compartments was performed by using a diffusion weighting of b = 50 s/mm^2. The DWASL sequence was applied to a group of elderly patients with a significant increase in values of K_w found for patients with diabetes and hypercholesterolemia. This suggested that DWASL could be used to image changes in water permeability with K_w as an imaging biomarker for neurovascular disease.

Chapter 4

Theoretical and Experimental Assessment of a mbASL Kinetic Model

4.1 Introduction

This chapter describes the development and validation of a theoretical model for the quantification of a new high SNR ASL technique (mbASL) that has been developed and optimised for use in rodent imaging. For mbASL to provide a compelling alternative to currently employed ASL sequences such as pCASL or PASL, high SNR needs to be combined with a robust quantification model and thus be able to produce CBF values that agree with the literature. To do this, a modified kinetic model was developed and experimentally assessed in three animal strains. High SNR mbASL images and CBF maps were produced for all rodents, with CBF values that match the literature. The structure of this chapter was as follows:

1. The development of an mbASL kinetic model
    - Introduction of the standard kinetic model and modifications required to model mbASL
    - Theoretical assessment on the effect of various mbASL parameters on the resulting ASL signal
2. Experimental assessment of the mbASL kinetic model
    - Optimal number of pulses for maximising signal
    - Arterial transit time measurement
    - Fitting the mbASL model to experimental data
    - Producing quantitative CBF maps using mbASL

4.2 Cerebral Blood Flow Quantification using ASL

Cerebral blood flow (CBF) is typically defined as the volume of arterial blood that is delivered to the capillary bed of a unit volume of brain tissue per unit time (Alsop, Detre, et al. 2015). Hence, CBF is normally measured in units of ml/100g/min.

Detre introduced the first model for quantification of CBF using arterial spin labelling (ASL), described in detail in Chapter 3. This early model makes a number of assumptions, including no relaxation of labelled spins until after they exchange with the tissue and that all the blood water has been saturated. Detre also assumed there was instantaneous exchange of all labelled blood water between the capillaries and tissue. Some sources of error have been identified in the measurement of CBF in early studies. By not considering arterial transit time (ATT), this can result in errors for estimation of CBF (Wegener et al. 2007). It was found that by introducing a post-labelling delay time, this allows time for the majority of the labelled blood to enter the imaging slice.

CBF measurements using ASL are usually validated against microsphere-based or autoradiography techniques. Although these are considered the gold-standard for measuring CBF, they are invasive and terminal. Generally, there has been good agreement of ASL measurements compared to these techniques, although reported values can vary, both clinically and pre-clinically. The ISMRM white paper gives a CBF value range of between 40 - 100 mL/100g/min (Alsop, Detre, et al. 2015) in grey matter in humans. Parkes et al. reported CBF values from 53 - 62 mL/100g/min in the whole brain and 58 - 68 mL/100g/min in the grey matter for men and woman (Parkes et al. 2004). A review paper of CBF values obtained from ASL compared to positron emission tomography (Fan et al. 2016) from 2001 - 2016, found a mean CBF of 42 $\pm$ 9 mL/100g/min for ASL in the whole brain, with 44 $\pm$ 9 mL/100g/min for PET. These results were within 15 % of each other.

Reported values of CBF in rodents are generally higher than those for clinical studies. Muir et al. reported a whole brain CBF value of 107 $\pm$ 8 mL/100g/min in mice using a labelling coil placed at the heart (cardiac-spin-labelling technique) with 76 - 110 mL/100g/min in rats using continuous ASL. Muir et al. reported higher values of 150 - 280 mL/100g/min using CASL (Muir et al. 2008). CBF values varied depending on the anaesthetic gases used. Wegener et al. reported mean CBF values of 103 $\pm$ 1 mL/100g/min in air and 180 $\pm$ 31 mL/100g/min for 5% CO_2 for Wistar rats. For a rat stroke model, Baskerville et al. reported CBF values of 157 - 177 mL/100g/min for the contralateral hemisphere and 9 - 104 mL/100g/min for the ipsilateral hemisphere (Baskerville et al. 2012). For comparison between three rat cohorts, Larkin compared multiphase pCASL measurements of CBF against autoradiography measurements. They reported values of 100 - 111 mL/100g/min from

multiphase pCASL and 108 - 122 mL/100g/min for autoradiography (Larkin et al. 2019).

There are multiple kinetic models which have been used to quantify CBF measurements, with the Buxton model the most widely used (Buxton et al. 1998), detailed in Section 4.3.1. Multiple assumptions have been made to provide a simplified kinetic model to estimate CBF. The ISMRM white paper (Alsop, Detre, et al. 2015) suggests a simplified CBF model based on using a single inversion delay when scanning. This model assumes that the entire labelled bolus has arrived in the tissue being imaged and experiences T_1 relaxation. Furthermore, it is also assumed there is no outflow of labelled blood due to the tissue water pool being much larger than the blood water pool.

Neither of the simplified models from the ISMRM white paper or Buxton's general kinetic model would be able to fully describe the signal produced from the mbASL sequence due to its hybrid nature. However, Buxton's model for PASL would be the closest model to describe mbASL, and can be modified to take account of the train of adiabatic inversion pulses used. Therefore, mbASL can be potentially described as a multiple PASL due to the larger thickness of the labelling slab.

4.3 Theory

4.3.1 The Buxton Kinetic Model

In his 1998 paper, *A General Kinetic Model for Quantitative Perfusion Imaging with Arterial Spin Labelling*, Buxton et al. (Buxton et al. 1998) produced a set of equations that quantitatively describe the CASL and PASL sequences.

The general kinetic model is described as:

$$\begin{aligned}\Delta M(t) &= 2M_{0b}f\int_0^t c(t')r(t-t')m(t-t')dt' \\ &= 2M_{0b}fc(t) * [r(t)\ m(t)]\end{aligned} \tag{4.1}$$

where M_{0b} is the initial magnetisation, f is cerebral blood flow (CBF) and t is time following labelling, measured in seconds. $*$ represents convolution. The model is divided into three different signal conditions: the delivery function c(t), the residue function r(t) and the magnetisation function m(t). These three functions describe the net magnetisation in the tissue at a time t. The delivery function (which is specific to PASL or CASL) describes the labelled blood arriving at time

t. The residue function is the amount of labelled blood still in the tissue after a time t. The magnetisation relaxation function describes the T_1 relaxation of the labelled blood water before arriving in the tissue (Buxton et al. 1998). The standard model is summarised as:

$$
\begin{aligned}
c(t) &= 0 && 0 < t < \delta \quad (a) \\
&\quad \alpha e^{\frac{-t}{T_{1b}}}(\textit{pulsed}) && \delta < t < \tau + \delta \quad (b) \\
&\quad \alpha e^{\frac{-\delta}{T_{1b}}}(\textit{continuous}) \\
&\quad 0 && \tau + \delta < t \quad (c) \\
r(t) &= e^{\frac{ft}{\lambda}} \\
m(t) &= e^{\frac{-t}{T_1}}
\end{aligned}
\tag{4.2}
$$

Buxton assumed the following three conditions for the ΔM signal: (a) the time before any labelled blood arrives in the imaging slice and hence no ASL signal. (b) Labelled blood is arriving in the imaging plane and blood is also still being labelled. (c) The signal when the labelling is finished but any remaining labelled blood is still arriving into the imaging plane.

By combining Equations 4.1 & 4.2, the ΔM signal for pulsed ASL can be described as:

$$
\begin{aligned}
\Delta M(t) &= 0 && 0 < t < \delta \quad (a) \\
&= 2M_{0b} f (t - \delta) \alpha e^{\frac{-t}{T_{1b}}} q_p(t) && \delta < t < \tau + \delta \quad (b) \\
&= 2M_{0b} f \tau e^{\frac{-t}{T_{1b}}} q_p(t) && \tau + \delta < t \quad (c)
\end{aligned}
\tag{4.3}
$$

with

$$
\begin{aligned}
q_p(t) &= \frac{e^{kt}(e^{-k\delta} - e^{kt})}{k(t - \delta)} && \delta < t < \tau + \delta \\
&= \frac{e^{kt}(e^{-k\delta} - e^{-k(\tau+\delta)})}{k\tau} && \tau + \delta < t
\end{aligned}
$$

$$
k = \frac{1}{T_{1b}} - \frac{1}{T_1'}
$$

$$
\frac{1}{T_1'} = \frac{1}{T_{1t}} + \frac{f}{\lambda}
$$

where δ is the arterial transit time (ATT), α is labelling efficiency, τ is the duration of the delivery of labelled blood, λ is the tissue/blood partition coefficient of

water and T_{1b} and T_{1t} are the spin lattice relaxation times of blood and tissue respectively.

The signal for continuous ASL can be described as:

$$\begin{aligned}
\Delta M(t) &= 0 && 0 < t < \delta \quad (a) \\
&= 2M_{0b} f T_1' \alpha e^{\frac{-\delta}{T_{1b}}} q_{ss}(t) && \delta < t < \tau + \delta \quad (b) \\
&= 2M_{0b} f T_1' \alpha e^{\frac{-\delta}{T_{1b}}} e^{\frac{-(t-\tau-\delta)}{T_1'}} q_{ss}(t) && \tau + \delta < t \quad (c)
\end{aligned} \tag{4.4}$$

where

$$q_{ss}(t) = \begin{cases} 1 - e^{\frac{-(t-\delta)}{T_1'}} & \delta < t < \tau + \delta \\ 1 - e^{\frac{-\tau}{T_1'}} & \tau + \delta < t \end{cases}$$

4.3.2 Producing Theoretical Graphs Using the Buxton Model

By varying different parameters in the kinetic model, Buxton showed their effect on the overall signal. Figures 4.1 and 4.2 replicates the parameters Buxton used in his paper using the PASL and CASL standard models (Buxton et al. 1998). These graphs were produced using MATLAB code produced by myself for this study. The decay of the signal in CASL depends on τ, which Buxton defined as the labelling duration. With a long labelling duration a plateau of signal is reached before a decay after labelling is stopped (Figure 4.2d). This is in contrast to PASL, which shows no plateau, as only a single inversion pulse is applied (Figure 4.1d). Variation of the value of T_1 tissue showed minimal effect on the signal from PASL and CASL. The magnitude of the signal increased as the value of CBF increased. Delta also makes a similar effect on both sequences, with an increase in delta showing a delayed arrival of signal compared to a short value of delta, and a loss of signal from T_1 relaxation.

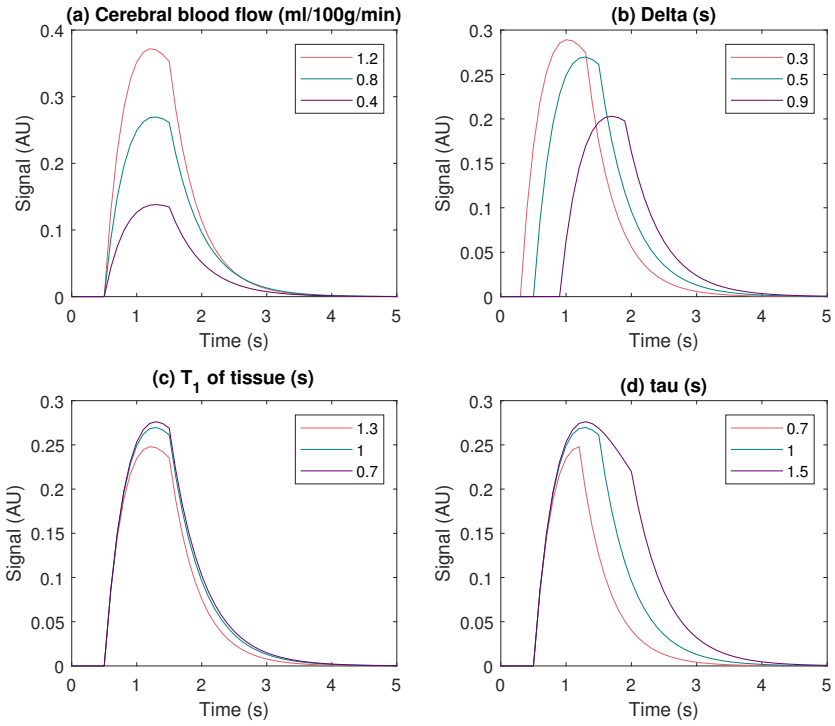

Figure 4.1: Theoretical Buxton signal graphs for PASL

Theoretical graphs produced using the Buxton standard kinetic model for PASL. Graphs show the signal against time (s). The (green) line parameters are: f = 0.8, δ = 0.5s, τ = 1s and T_1 tissue = 1s. The top left graph shows an increase in signal as CBF increases. The top right shows by varying δ, the arrival of labelled blood and signal changes. The bottom left shows the effect of changing the T_1 of tissue and the bottom right shows the distribution of signal change as τ increases.

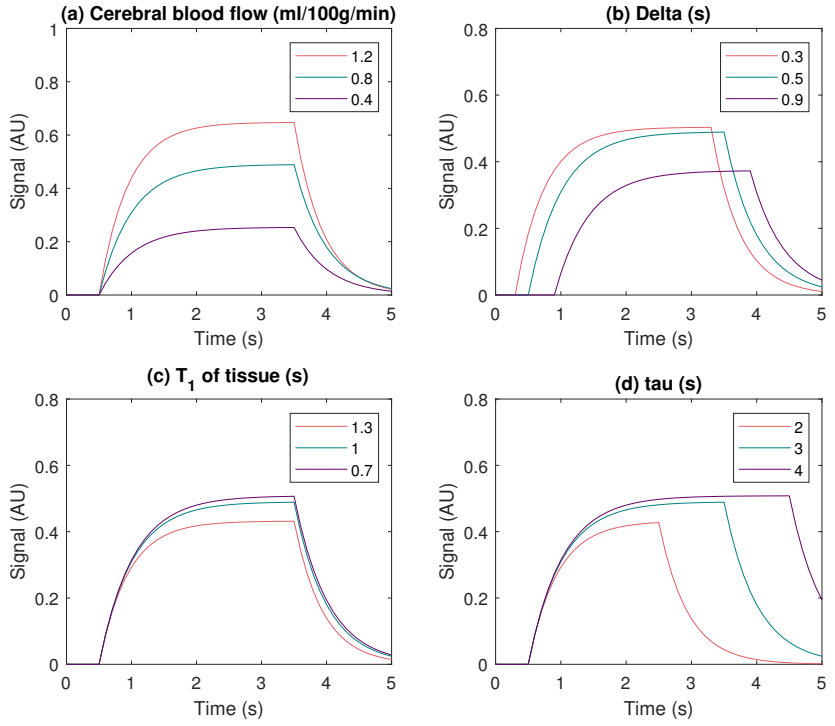

Figure 4.2: Theoretical Buxton signal graphs for CASL

Theoretical graphs produced using the Buxton standard kinetic model for CASL. Graphs show the signal against time (s). The (green) line parameters are: f = 0.8, δ = 0.5s, T_1 tissue = 1s and τ = 3s. The top left graphs demonstrates the increase in overall signal as CBF increases, with the shape of the curve staying the same. The top right shows that by increasing delta, the signal arrives later and the overall signal is lower than when a shorter value of delta is used. The bottom left shows the effect of changing the T_1 of tissue and the bottom right shows as τ increases, the start of the decay of signal shifts.

4.3.3 A mbASL Kinetic Model

The mbASL sequence has similarities to both pCASL and PASL, but cannot be fully described by either model. mbASL is different to pCASL as it uses a large inversion slab for labelling compared to the thin labelling slice used in pCASL. The mbASL sequence is different to PASL as it uses multiple inversion pulses (instead of a single inversion pulse) which are applied in the neck region, similar to pCASL. Overall, the mbASL sequence is most similar to PASL because of the thick labelling slab and therefore mbASL can be described as a multiple PASL. The value of L_i, the distance from the edge of the labelling plane to the edge of the imaging plane, and the thickness of the labelling slab L_{inv} can be varied dependent on the species of animal being imaged (Figure 4.3). For the following study, the value of L_i was kept constant and L_{inv} varied for experimental comparison.

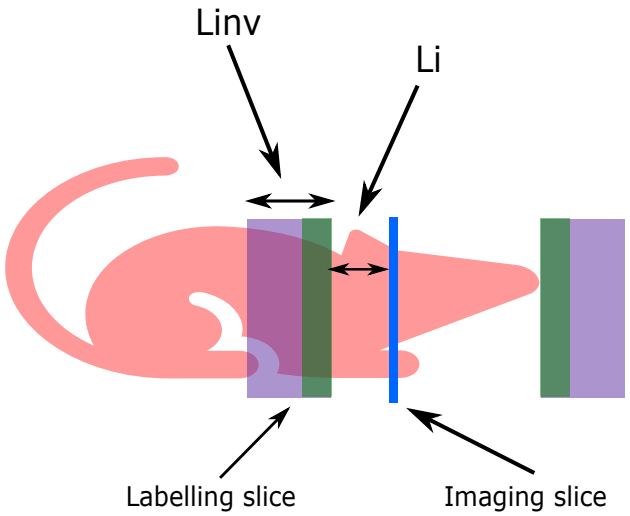

Figure 4.3: mbASL slice setup

The labelling slab is placed in the neck region for mbASL. The distance between the labelling and imaging plane (L_i) is kept constant. The labelling slab thickness (L_{inv}) can varied with the slab being extended backwards.

Similar to Buxton's standard kinetic model, multiple assumptions have been made in our model of mbASL. A uniform plug flow was assumed, where the mean velocity of labelled blood was calculated as:

$$V_{blood} = \frac{L_{inv} \times np}{CI} \tag{4.5}$$

where CI is the labelling time. The assumption was made that if enough labelling pulses are used a continuous style arrival of labelled blood into the imaging plane will occur, as seen in CASL or pCASL. Hence, V_{blood} is calculated as the mean velocity of blood crossing the total labelling slab distance during the labelling time. A value for the T_1 relaxation of arterial blood was assumed using the literature. For the value of tissue T_1, this was measured using a T_1 mapping sequence for in-vivo experiments and assumed for theoretical predictions. By using a RARE sequence

with a varying TR, the signal from each image voxel is fitted to Equation 2.24 and gives a value of T_1 for each brain voxel. For τ, Buxton defined this as the duration of arrival of labelled blood. For mbASL, the optimal number of pulses for imaging will give a pseudo-continuous labelling and is a condition that is assumed. However, due to the fragmented description of mbASL, *tau* is defined as the time taken for the labelled blood of one pulse to cross both L_{inv} and L_i:

$$\tau = \frac{L_{inv} + L_i}{V_{blood}} \tag{4.6}$$

The ATT is defined as the time it takes for labelled blood to cross the distance between the labelling slab and imaging slice, L_i, and is calculated as:

$$ATT = \frac{L_i}{V_{blood}} \tag{4.7}$$

To describe the overall ΔM signal produced by mbASL, a fragmented description was used, hence the mbASL model can be described by:

$$\Delta M_{mbASL}(t) = f \sum_{i=1}^{np} \Delta M_{i,PASL}(t) \tag{4.8}$$

With $\Delta M_i(t)$ being the magnetisation from pulse i, and ΔM being described by the standard kinetic model for PASL (Equation 4.3).

4.3.4 Producing Theoretical Graphs Using the mbASL Model

Using the mbASL kinetic model described in Section 4.3.3, theoretical predictions were made of the signal curves (Figure 4.4). The similarity of the shape of the signal curve in mbASL to CASL when using a long labelling duration and a sufficient number of labelling pulses is clearly demonstrated. At a low number of pulses, the peak of the signal from each pulse can be seen, showing that an optimal value of pulses has not been reached. As the number of pulses increases, the overall signal curve will smooth and becomes similar to CASL. Experimentally, the signal would not continue to increase with the number of pulses, due to multiple inversion. By increasing the labelling thickness, the number of pulses needed to achieve continuous labelling decreases. This can clearly be seen with the comparison of of np = 16 between Figure 4.4 (a) and (b).

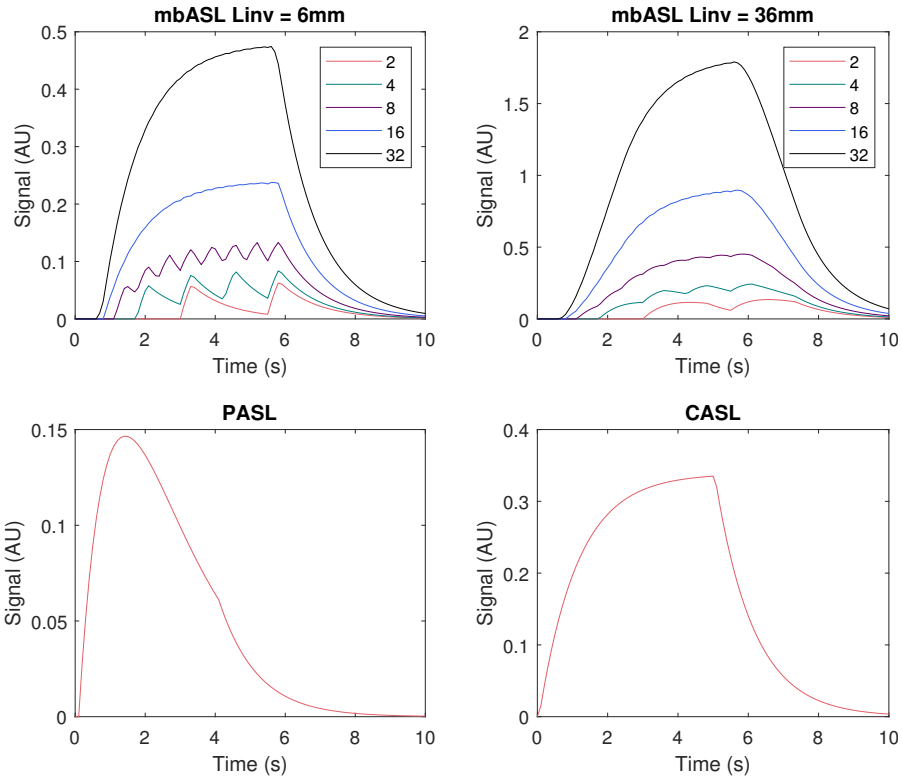

Figure 4.4: Theoretical mbASL signal graphs

Theoretical signal predictions from the mbASL kinetic model, with comparison to PASL and CASL. For all graphs f = 1, λ = 0.8, ATT = 50ms, T_1 tissue = 1.76s and T_1 blood = 2.1s. For the top left and right graphs CI = 5s and the number of pulses were varied for two different labelling slab thicknesses. The top left graph shows that at a short labelling thickness, more pulses are needing to obtain continuous labelling when compared to the top right graph. The bottom left graph shows a PASL signal curve and the bottom right a CASL signal curve. As the number of pulses increase in the top graphs the signal curve represents the CASL signal.

By changing the value of CI, the signal distribution from mbASL can be made to reflect a CASL or PASL distribution. Using a short CI of 500ms (Figure 4.5a) shows the signal as a PASL distribution with the peak of the signal shifting as the labelling thickness increases. The number of pulses needed for continuous labelling also decreases as the labelling thickness increases. When using a labelling duration of 5s (Figure 4.5b), the signal resembles a CASL distribution and shows a plateau of signal before the signal decays after labelling stops. This demonstrates the hybrid nature of the mbASL sequence with the signal replicating both PASL and CASL, whilst using a range of labelling slab thicknesses and number of pulses.

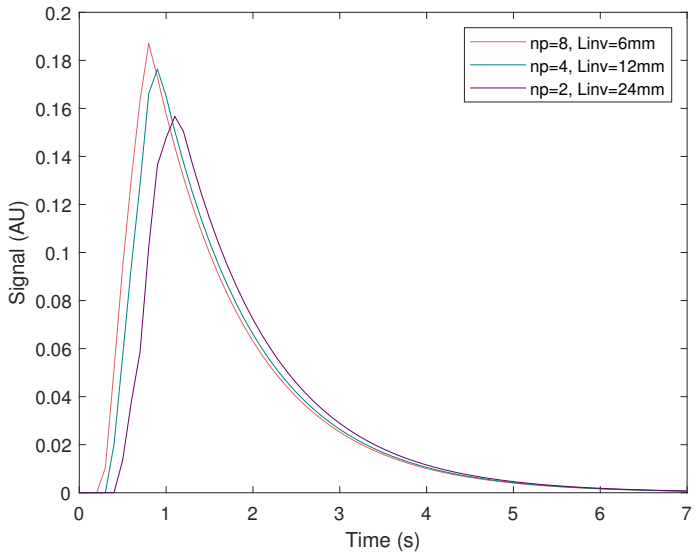

(a) Signal from mbASL at CI = 0.5s

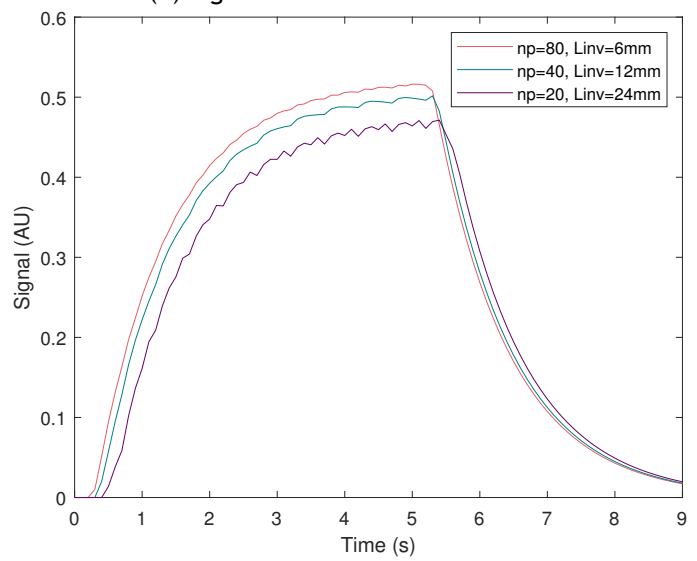

(b) Signal from mbASL at CI = 5s

Figure 4.5: Comparison of mbASL signal at different CI values

Comparison of the mbASL signal at two different labelling durations. Both graphs use the same number of pulses (80, 40 and 20) and labelling thicknesses (L_{inv} = 6mm, 12mm and 24mm). Figure a) shows the signal at CI = 0.5s with a higher signal seen the at the short labelling thickness of 6mm and the peak of the signal shifting towards the right for the larger labelling thicknesses. Figure b) shows the same parameters but using CI = 5s. The signal curve resembles a more CASL distribution with a higher signal seen for the short labelling thickness. The graph demonstrates that more pulses are needed for the 24mm labelling thickness to produce continuous labelling.

4.4 Experimental Validation

To validate the mbASL quantification, multiple experiments were performed using three rodent strains: CD-1 mice, C57 mice and SD rats. The experiment was conducted in two parts: the first part consisted of all experiments being performed on SD rats and CD-1 mice. Following analysis of the initial results, a second part of the experiment involved performing the experiments using C57 mice to examine if changes between mouse strains could be detected. Experimental parameters were altered accordingly. Each strain underwent the following experiments:

1. Varying the number of pulses and thickness of the labelling slab to find the optimal number for each rodent strain
2. Examination of the distribution of signal for each labelling slab thickness at multiple inversion delays to confirm theoretical predictions
3. Using optimal parameters from the experiments described above, CBF is measured by fitting of data to the mbASL kinetic model
4. Comparison of the signal from mbASL against the standard FAIR sequence, demonstrating the high SNR of the sequence

4.5 Methods

4.5.1 Animal Set Up

All experiments were carried out in accordance to the local ethics review panel and the UK Home Office Animals (Scientific Procedures) Act 1986. Experiments were performed on C57 black mice (n = 5, weight = 20 $\pm$ 1g), CD-1 white mice (n = 6, weight = 35 $\pm$ 3g) and SD rats (n = 6, weight = 465 $\pm$ 8g). All animals originated from Charles River Laboratories, Glasgow, UK. The animals were anaesthetised in a chamber using 5% isoflurane and a 30:70 O_2/NO_2 ratio before being transferred to the MRI scanner. The animals were positioned in an adapted cradle for rodents with a hot-water jacket used to regulate physiological temperature ($36.5°C - 37.5°C$). The head of the animal was kept central with ear bars placed in the ears and a nose cone used to deliver anaesthetic gas. The animals were spontaneously breathing using isoflurane levels of 1% - 3% and 30:70 O_2/NO_2 ratio at a constant flow of 1Lmin^{-1}. The isoflurane concentration was varied for each animal to keep a stable respiration rate of 40 - 70 breaths per minute for mice and 60 - 90 breaths per minute for rats. To measure the respiration, a pressure sensor connected to

an air-filled balloon was placed under the animal's abdomen (Biotrig 1.03, Bruker Biospin, Ettlingen, Germany).

4.5.2 Scanner Set Up

Experiments were performed on a horizontal 7 T Bruker PharmaScan Avance III system (300 MHz). A Bruker BGA9 imaging gradient insert (300 mT/m) was used to provide linear magnetic field gradient pulses. A 72mm diameter, 110mm length birdcage Radio-Frequency (RF) volume resonator was used to transmit, with a four-channel phased array receive only head coil used to detect the signal (22mm length for mice and 35mm for rats (Rapid Biomedical GmbH, Rimpar, Germany)). Experiments were performed using either the mbASL sequence or the manufacturer's standard FAIR pulse sequence (Bruker Paravision 5.0). The imaging acquisition module was echo planar imaging (EPI). For direct comparison of methods, identical imaging parameters were used. All scans used a matrix of 96×96, with mice having an imaging slab thickness of 1mm, positioned 4mm posterior from the rhinal fissure and for rats a thickness of 1.5mm, positioned 7mm posterior. Labelling slab and imaging slice positions are shown in Figure 4.3. For mice the field-of-view (FOV) = 2.5×2.5cm and for rats the FOV = 1.76×1.76cm. The mbASL-EPI method was implemented by pre-weighting an EPI sequence with a train of slice-selective hyperbolic secant (HS) inversion pulses. For each rodent, the distance between the edge of the labelling slab and imaging slice (L_i) was varied. Multiple labelling slab widths (L_{inv}) were used in the experiment (Table 4.1).

4.5.2.1 Number of Pulses

To achieve optimal pseudo continuous labelling, the number of pulses needed will vary for each labelling thickness. To optimise the number of inversion pulses needed, scans were performed using a single shot mbASL-EPI sequence with the following parameters: continuous inversion time (CI) = 5000ms, inversion delay (TI) = 50ms, TR = 7000ms, NA = 8. The experimental parameters are given in Table 4.1. The inversion pulses were spread evenly over the inversion time.

4.5.2.2 Varying the Inversion Time

A short labelling duration and various inversion delays were used to examine the distribution of signal for each labelling slab thickness. Single shot mbASL was used with CI = 500ms and a variable TI with overall TR kept at 7000ms (TI+TR) (Figure

Strain	Inversion length (mm)	L_i (mm)	Number of Pulses (np)
CD-1	3	5.5	2, 4, 8, 16, 32, 34, 36, 38, 40, 42, 44
CD-1	6	5.5	2, 4, 8, 16, 24, 32, 34, 36, 38
CD-1	12	5.5	2, 4, 8, 16, 20, 24, 32, 34
C57	4	11	2, 3, 4, 5, 6, 7, 8, 9
			10, 11, 12, 13, 14, 15, 16, 17
C57	8	11	2, 3, 4, 5, 6, 7, 8, 9, 10
C57	16	11	2, 3, 4, 5, 6, 7, 8
SD Rat	6, 12, 36	24.25	10, 15, 20, 30, 40, 50, 60

Table 4.1: Number of pulses used for the optimisation of pulses experiment for mice and rats.

4.6). The number of pulses used for each thickness was chosen based on the previous optimisation of pulses 4.5.2.1. For mice this was np = 8, 4 and 2 for L_{inv} = 4, 8 and 16 mm for C57 mice and np = 12, 6, 3 for L_{inv} = 3, 6, 12 mm for CD-1 mice. For rats, np = 5, 3, 2, 2 for L_{inv} = 6, 12, 24 and 36 mm respectively. To calculate values of ATT for each labelling slab thickness, the signal curve for each thickness was averaged and fitted to the mbASL kinetic model using in-house MATLAB code.

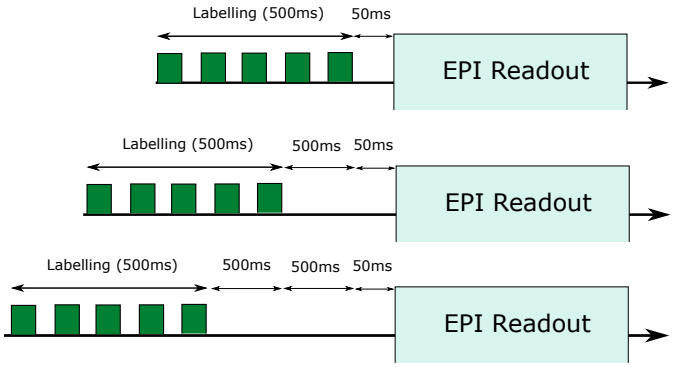

Figure 4.6: Simplified diagram of the inversion time experiment for mbASL

For each scan, the labelling time was kept constant at 500ms. The inversion delay to allow labelled blood to travel to the imaging plane was increased by 500ms for each scan. The delay increased from 50ms to 4050ms, with the overall TR value decreased each time to keep a constant TI + TR = 7s.

4.5.2.3 CBF Maps

For full quantification of mbASL, high SNR 4-shot mbASL images were obtained using TI = 50ms, CI = 5000ms, TR = 2000ms, NA = 10. For C57 mice np = 20, 10, 5 for L_{inv}= 4, 8, 16mm and for CD-1 mice np = 45, 30, 15 for L_{inv} = 3, 6, 12mm. For the rats, np = 50, 30, 20 for L_{inv} = 6, 12, 24, 36mm. A T_1 map was obtained for each animal using NA = 8, TE = 12.29ms, TR = 916ms. Seven slices were used with a RARE factor of 4. For comparison of mbASL with FAIR, the Bruker instruments (Paravision 5.0) standard FAIR EPI method was used, with the same TR, imaging parameters and scan time as mbASL. A 12mm slice thickness was used for both mice and rats, with an inversion pulse of 5ms and delay between inversion and imaging of 1750ms.

To calculate quantitative cerebral blood flow maps, a quantitative model of CBF was used:

$$CBF = 6000 \frac{\Delta M_{mbASL}}{\sum_{i=1}^{np} M_i(t)} \tag{4.9}$$

where $M_i(t)$ is:

$$M_i(t) = 2M_{b0}\tau\alpha \frac{e^{\frac{-t}{T_{1b}}} e^{kt} e^{-k\delta} - e^{-k(\tau+\delta)}}{k\tau} \tag{4.10}$$

with T_{1b} = 1.65s for 7T, α = 0.96, λ = 0.9. The modification of M_{b0} was used due to using a TR of less than 5s (Alsop, Detre, et al. 2015). τ, δ and k were calculated for each species as per the definitions above. ΔM_{mbASL} is the signal obtained from subtracting the control and label images and a factor of 6000 is used to convert the CBF values into units of mL/100g/min. CBF values were calculated per voxel with a map produced for each animal. ROIs were taken for the full brain and cortex region for quantitative comparison between ASL methods and labelling thickness. For qualitative comparison of signal between the mbASL and FAIR images, the same scale is used.

4.6 Results

Two species of rodents were used to experimentally validate mbASL: mice and rats. Furthermore, two strains of mice were used: C57 mice and CD-1 mice. Parameters were optimised for each rodent/strain with mbASL images and CBF maps produced.

4.6.1 Optimal Number of Pulses to Maximise Signal

The optimal number of pulses varied with the thickness of the labelling slab (Figure 4.7). Three animals were used for each species with all scans taking place in the same scanning session. For the SD rats, a plateau of signal was seen for L_{inv} = 12mm starting at 30 pulses, with a decrease in signal observed when more pulses were used. For L_{inv} = 36mm, although a peak was seen at 50 pulses, the data suggests that after 20 pulses, the plateau of signal has began. For L_{inv} = 6mm, a maximum of 60 pulses was used, but a plateau was not seen. Experiments using L_{inv} = 24mm in SD rats were performed in a different session with no number of pulses optimisation performed.

In the C57 mice, the optimal labelling thickness fell between the L_{inv} = 8mm and

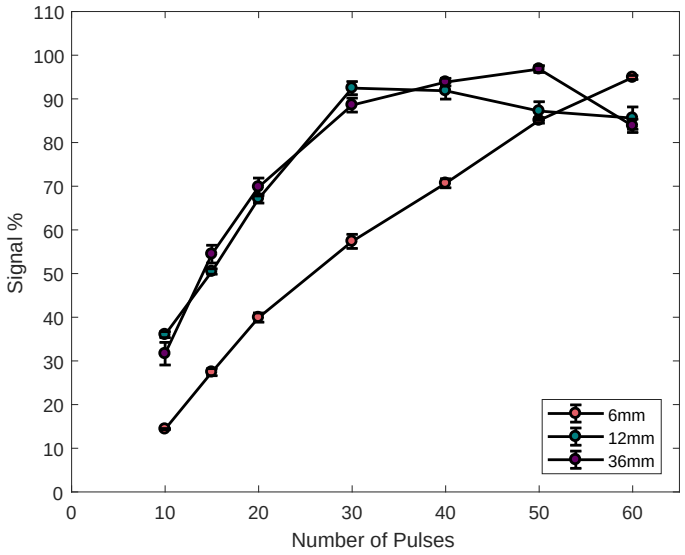

Figure 4.7: Number of pulses optimisation for SD rats

A range of labelling pulses between 10 and 60 were used to optimise the signal seen for SD rats for different inversion slab thicknesses. The data were plotted as a percentage of the maximum signal at each value of pulses. N = 3 animals were used and error bars were calculated as the standard deviation.

16mm thicknesses (Figure 4.8a). The peak number of pulses was five pulses for the 8mm thickness and four pulses for the 16mm thickness. The optimal number of pulses was not reached for L_{inv} = 4mm, but the curve suggests that the plateau was nearly reached at seventeen pulses, with a suggested optimal of around twenty pulses. In the CD-1 mice, the optimal number of pulses needed was higher than the number of pulses used in the C57 mice (Figure 4.8b). The peak number of pulses was 20 for L_{inv} = 12mm with a plateau of signal seen for L_{inv} 6mm from 32 - 38 pulses. For L_{inv} = 3mm, a maximum of 44 pulses were used, with a plateau not reached.

The number of inversion pulses used was limited due to the RF duty cycle ($\sim$ 2.5mW) of the surface coil and SAR restraints. The full range of pulses used are presented in Table 4.1.

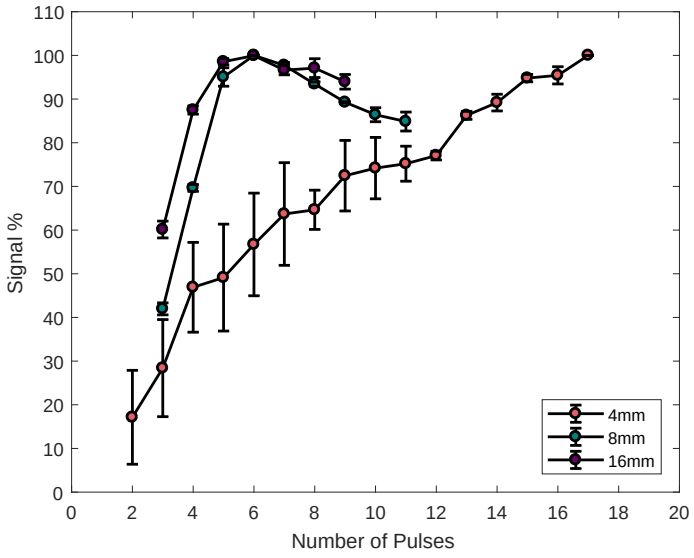

(a) Number of pulses optimisation for C57 mice

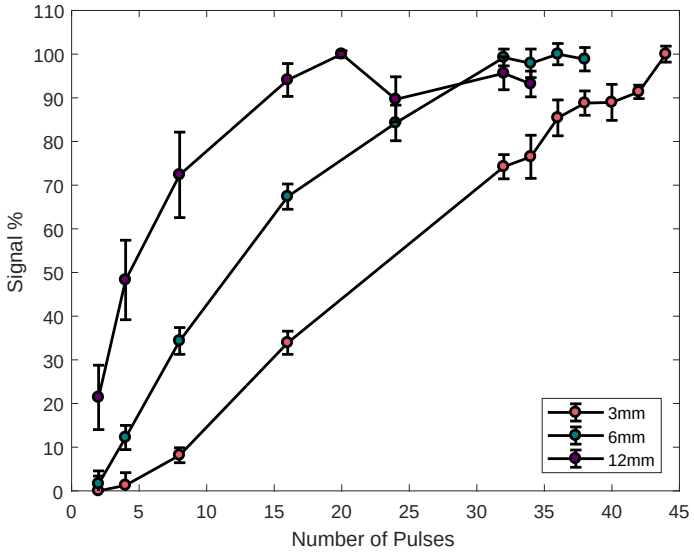

(b) Number of pulses optimisation for CD-1 mice

Figure 4.8: Number of pulses optimisation for mice

a) For 4mm, the plateau in signal was not reached but the trend suggests this would happen at approximately 20 pulses. The optimal signal was seen at five pulses for L_{inv} = 8mm and four pulses for 16mm with a drop in signal seen after this. The data are presented as a percentage of the maximum signal reached. b) The optimal signal was not reached for the smallest labelling slab (L_{inv} = 3mm) with the signal still increasing at 44 pulses. For L_{inv} = 6mm, a plateau was reached after 30 pulses. The signal peak was seen at 20 pulses for L_{inv} = 12mm with the signal dropping after this. N = 3 mice were used in each experiment and error bars were calculated as the standard deviation.

4.6.2 ATT Measurement

The mean velocity of blood crossing the labelling slab and hence mean ATT was calculated using Equation 4.7 for each value of L_{inv}. The distance L_i was 24.25mm for rats, 11mm for C57 mice and 5.5mm for CD-1 mice. Values of np were chosen based on when continuous labelling was reached in the data produced from Section 4.6.1. As the optimal number of pulses was not reached for the smallest labelling thickness in all species, these ATT values were not considered to be accurate (Table 4.2).

	SD Rats			C57 Mice			CD-1 Mice		
	6mm	12mm	36mm	4mm	8mm	16mm	3mm	6mm	12mm
V_{blood} (mm/s)	60	72	144	11.2	9.6	12.8	24	36	48
ATT (s)	0.40	0.34	0.21	0.98	1.1	0.859	0.23	0.152	0.114
np	50	30	20	14	6	6	40	30	15

Table 4.2: ATT values from the mbASL study

4.6.3 Fitting mbASL Data to the Kinetic Model

4.6.3.1 Graphs

The signal obtained at the varying inversion times (TI) was fitted to the mbASL kinetic model and plotted for each value of L_{inv}, for all species. Figure 4.9 demonstrates the fit for the SD rats. The peak of the signal is at 50ms for L_{inv} = 6mm and shifts to 1000ms for L_{inv} = 12mm. For the larger slabs, L_{inv} = 24mm and 36mm, multiple peaks appear across the four second inversion time, with more variance in the data. The quality of the fit of data to the model was high for the smaller values of L_{inv} = 6mm and 12mm (R^2 = 0.92 and 0.82), but was poor for the larger L_{inv} values of 24mm and 36mm (R^2 = 0.46 and 0.011).

For the CD-1 mice, although the labelling thickness was varied between 3mm and 12mm, no change in peak signal was seen between the curves. This is assumed to be from using a smaller value of L_i, compared to the C57 mice (L_i = 5.5mm for CD-1 in comparison to L_i = 11mm for C57 mice). The peak signal was at 50ms for each curve. The fitting of data to the mbASL model for 3mm, 6mm and 12mm resulted in R^2 values 0.98, 0.98 and 0.62. For the C57 mice, a shift in the peak of the signal at each labelling thickness was seen after a 50ms delay for L_{inv} = 4mm, but shifted to one second for L_{inv} = 8mm and 1.5 seconds for L_{inv} = 16mm (Figure 4.10a). The fitting of data to the mbASL model for 4mm, 8mm and 16mm resulted in an R^2 value of 0.96, 0.96 and 0.96.

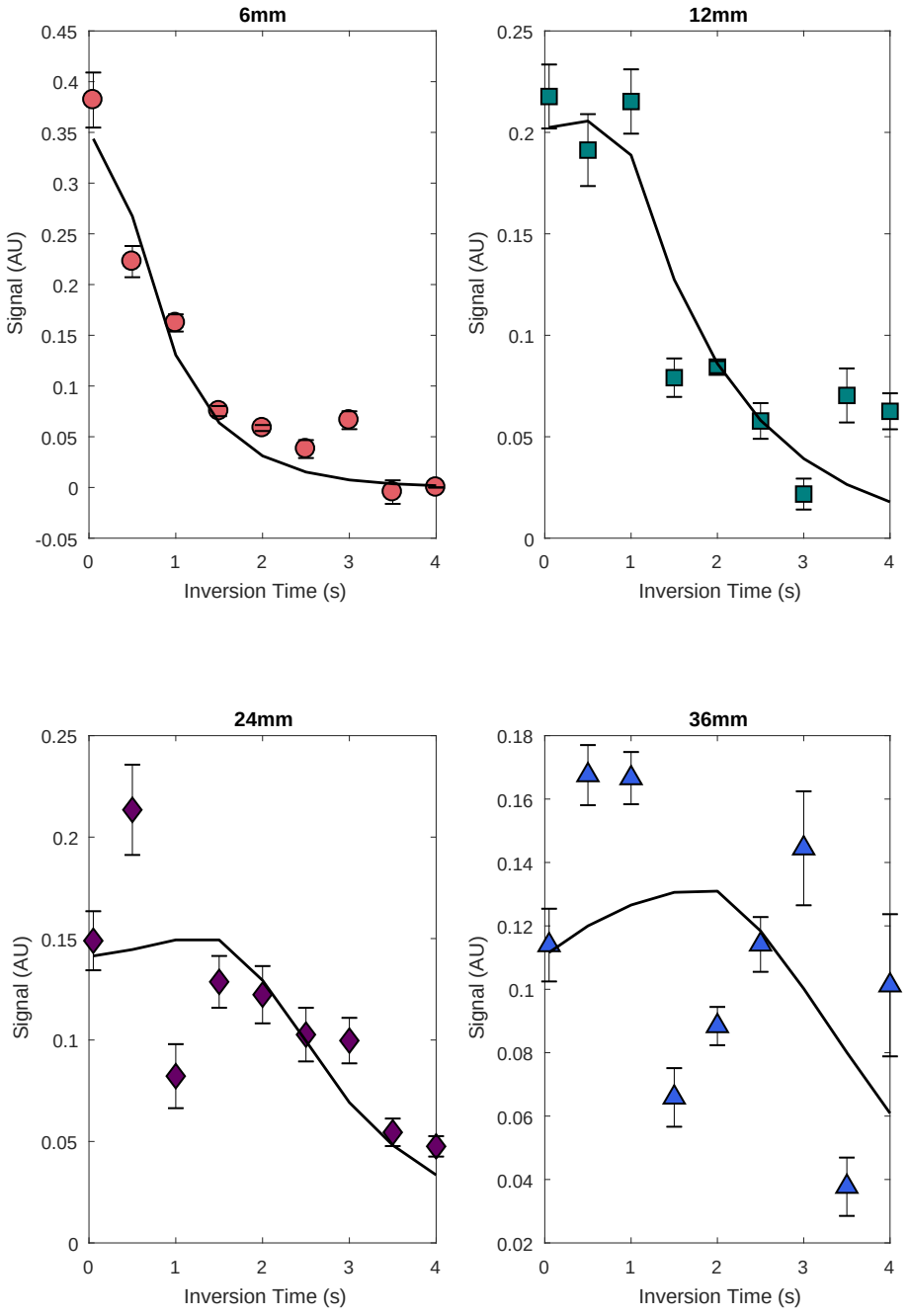

Figure 4.9: Variable TI data for SD rats fitted to the mbASL kinetic model

The thinner slabs had a high R^2 fitting value for the mbASL model (R^2 = 0.92 for L_{inv} = 6mm and 0.82 for L_{inv} = 12mm). For the larger 24mm and 36mm labelling slabs the signal is lower from being outside of the homogeneous region of the magnet. This results in a poorer fit to the model (R^2 = 0.46 for L_{inv} = 24mm and 0.01 for L_{inv} = 36mm). N = 6 rats were used and error bars were calculated as the standard deviation.

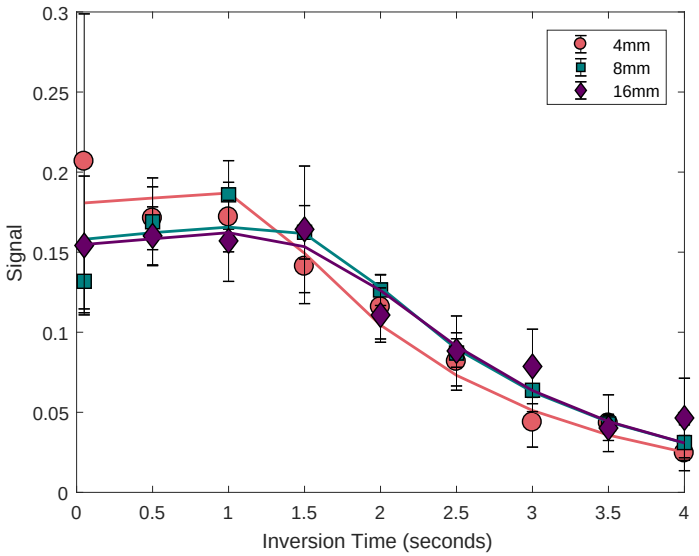

(a) Variable TI data fitted to the mbASL kinetic model for C57 mice

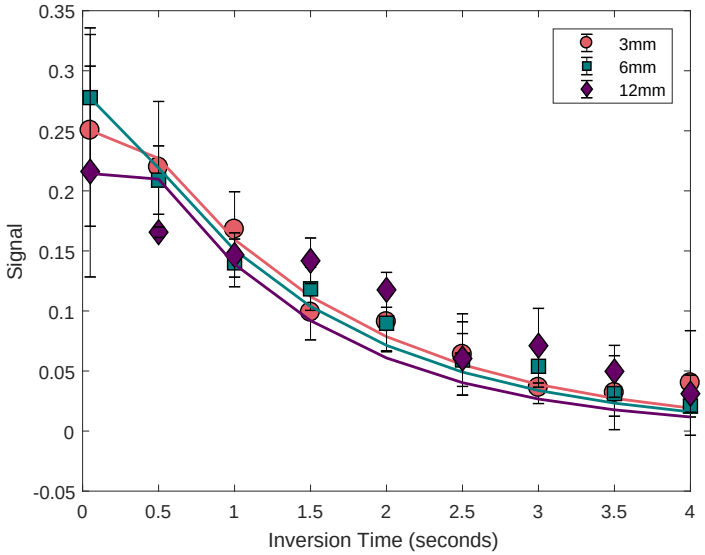

(b) Mean signal for variable TI data from CD-1 mice fitted to the mbASL kinetic model.

Figure 4.10: mbASL data fitted to the kinetic model for mice

a) Each labelling thickness displayed a different distribution of signal, with the peak of the signal shifting to a higher TI value as the labelling thickness increased. b) The signal curve seen at all three labelling thicknesses showed the same distribution of signal, with the peak signal seen at 50ms. N = 6 C57 or CD-1 mice were used and error bars were calculated as the standard deviation.

4.6.3.2 Obtaining ATT Values from the Fitted Data

Values of ATT found from fitting the variable TI data to the mbASL, PASL and CASL kinetic models (Table 4.3) were compared with values found in Section 4.6.2. Values of ATT were only considered comparable if a sufficient R^2 fitting values was found ($R^2 > 0.75$).

	SD Rats		C57 Mice			CD-1 Mice		
	6mm	12mm	4mm	8mm	16mm	3mm	6mm	12mm
ATT (s)	0.4	0.34	0.98	1.1	0.86	0.23	0.15	0.11
ATT (s) mbASL	0.24	0.6	0.96	1.13	0.9	0.036	0.073	-
ATT (s) PASL	0.24	0.08	0.09	0.11	0.1	0.08	0.08	0.08
ATT (s) CASL	0.84	-	-	-	-	-	-	-

Table 4.3: ATT values from fitting to the mbASL, PASL and CASL kinetic models.

Only values were the R^2 value is $>$0.75 are displayed, with values $<$0.75 considered not accurate. The top line represents the ATT values that were previously calculated in Section 4.6.2

4.6.4 Comparison of ΔM mbASL to ΔM FAIR

The mean ΔM signal from different brain regions was compared between images produced using the mbASL sequence and the Bruker FAIR sequence. For the SD rats, the mbASL images had a much higher ΔM signal compared to FAIR for all labelling slab thicknesses (Figure 4.11). For a full brain ROI, the ΔM signal was 375% of the ΔM FAIR signal for L_{inv} = 12mm. A similar increase was seen for the cortex with a value of 365% of the FAIR signal.

A large ΔM signal increase was seen in the brain for C57 mice compared to FAIR. The comparison of ΔM mbASL to FAIR was 467% and 546% in the full brain for L_{inv} 8mm and 16mm respectively. In the cortex, the comparison was 428% and 510%. The large increase in ΔM signal can be attributed to a low overall signal from the FAIR images. The ΔM mbASL signal for CD-1 mice showed higher signal than FAIR at all labelling slab values. The highest ΔM signal increase was seen for L_{inv} = 16mm at 162 %. For the 12mm slab thickness, the mean signal was 128 % of FAIR. An increase in ΔM signal was seen for each labelling thickness for CD-1 mice. For L_{inv} = 6mm and 12mm, the ratio of mbASL ΔM signal to FAIR in the whole brain was 128% and 162%. In the cortex ROI, the ΔM signal was 133% and 165%.

4.6.5 Calculation of CBF Maps using the mbASL Kinetic Model

An optimal labelling slab thickness was chosen for each strain. This was based on the fitting of the signal to the mbASL kinetic model and if a plateau of signal had

been reached when optimising the number of labelling pulses. For SD rats, this was L_{inv} = 12mm, L_{inv} = 8mm for C57 mice and L_{inv} = 6mm for CD-1 mice.

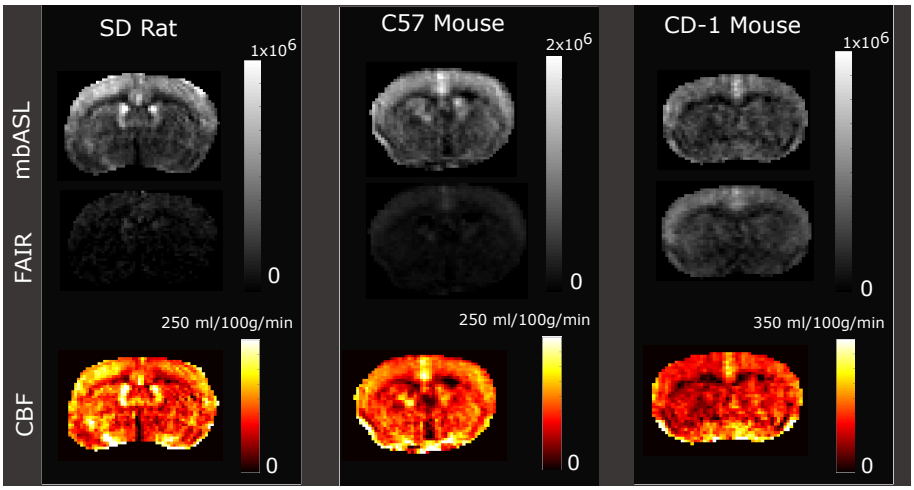

Figure 4.11: mbASL images and CBF maps for all strains

An mbASL image and corresponding CBF map (presented in units ml/100g/min ± standard deviation) at the optimal labelling slab thickness are shown for each rodent strain. A FAIR image is shown as a comparison for mbASL. mbASL and FAIR images are shown with arbitrary units. For SD rats at L_{inv} = 12mm, the mean CBF value was calculated to be 120 ± 14 ml/100g/min using a whole brain ROI and 138 ± 28 ml/100g/min in the cortex. A value of L_{inv} = 8mm for C57 mice gave a mean value of CBF as 110 ± 9 ml/100g/min for the full brain and 128 ± 8 ml/100g/min in the cortex. For CD-1 mice, the optimal labelling thickness was L_{inv} = 6mm, with a CBF value of 172 ml/100g/min ± 31 in the full brain and 195 ± 44 ml/100g/min in the cortex.

CBF maps were calculated for each strain using the mbASL kinetic model, mbASL images and T_1 maps. In the SD rats, a mean CBF value of 120 ± 14 ml/100g/min was calculated for the full brain ROI and for the cortex as 138 ± 28 ml/100g/min. For the C57 mice, the mean value of CBF produced was 110 ± 9 ml/100g/min for the full brain. Using an ROI in the cortex, the mean CBF value was 128 ± 8 ml/100g/min. The CD-1 mice had a higher mean CBF value with 172 ml/100g/min ± 31 in the full brain and 195 ± 44 ml/100g/min in the cortex.

4.7 Discussion

The aim of this work was to produce a kinetic model for the mbASL sequence, which was used to generate CBF maps. A modification to Buxton's kinetic model showed the mbASL signal could be accurately described mathematically. Using this model, the effects of np and L_{inv} on the mbASL signal were theoretically assessed and in-vivo experimental validation of the sequence undertaken.

4.7.1 Quantification

As mbASL uses a train of adiabatic pulses paired with a thick labelling slab, it is better described as a multiple PASL, rather than a pCASL sequence, which uses a thin slice for labelling. Our mbASL kinetic model therefore made the same assumptions and had the same limitations of the original Buxton model. The mbASL model assumed that all the blood in the labelling slab is inverted during the inversion time. The assumption that the labelled blood has travelled to the imaging slice when imaging takes place was also used. For the larger slabs this may not be true, as seen when increasing the labelling slab thickness the peak of the signal shifts. Another assumption was made that if a sufficient number of pulses are used, then continuous labelling will be reached, and the signal would compare to CASL. The model was examined theoretically, by changing the number of inversion pulses and the size of the labelling slab (Figure 4.4). If a small number of pulses are used, the peak of each signal can be seen and continuous labelling is not reached. Furthermore, the importance of the size of the labelling slab is shown, with the model demonstrating that less pulses are needed to reach continuous labelling for the larger slab (L_{inv} = 36mm) compared to the thinner slab (L_{inv} = 6mm). The hybrid nature of the sequence was shown in two ways. First between Figure 4.4 where a long CI value was used and Figure 4.5 where a short value was used. By using a long CI the demonstration of the CASL curve is seen and a plateau of signal reached with enough inversion pulses. Using a short CI demonstrates the typical mbASL signal curve which is similar to PASL. Figure 4.5 also demonstrates that by changing the size of the labelling slab, the peak of the signal will shift.

4.7.2 Experimental Validation

To experimentally validate the mbASL sequence and explore the theoretical predictions, multiple in-vivo experiments were performed on SD rats and two strains of mice. This was for two reasons: to explore if any major differences were seen

between the mouse strains and to further validate the quantification of mbASL by showing its ability to produce CBF values for multiple strains.

4.7.2.1 Number of Pulses

The number of pulses needed for each labelling thickness was optimised to produce a continuous labelling. This optimisation was able to show that using a larger labelling slab generally needed a lower number of pulses to label the arterial blood. The number of pulses used were limited for the thinnest slabs for each species due to the duty cycle of the coil and SAR levels. The number of pulses needed for rats was higher than in mice. This confirms what was previously described by Vallatos et al. (Vallatos et al. 2018), where similar results were produced with rats needing more pulses overall to label the blood compared to mice.

The mbASL model assumed that a sufficient number of pulses are used to create continuous labelling. If the number of pulses chosen is not from the plateau region, this may violate this assumption, resulting in a non-continuous labelling and overall lower SNR. The curves produced for the larger labelling thickness in both rodents showed that using too many pulses would also produce a detrimental effect and the overall ΔM signal, which will decrease due to over-labelling of the arterial blood. Furthermore, optimisation of the number of pulses avoided unnecessary pulses being used, especially in the smaller labelling thicknesses. The difference in optimal pulses between the CD-1 and C57 mouse (Figure 4.8a and Figure 4.8b) demonstrates the importance of not only optimising for each rodent but also for different strains. Furthermore, it demonstrates there is a minimum labelling thickness that can be practically used for mbASL.

4.7.2.2 Obtaining ATT values

As the mbASL protocol is novel to other ASL sequences (Figure 4.3), it was considered that literature values of ATT would be inappropriate. Hence, ATT was calculated from the number of pulses optimisation (Section 4.6.1. A simplified approach was used, with the optimal number of pulses found from the pulse optimisation graphs and Equation 4.7. This gave sensible results compared to the literature. Hirschler et al. reported a range of measured ATT values across the brain in mice from 169ms in the hippocampus to 284ms in the cortex (Hirschler et al. 2018). Thomas et al. measured the ATT in rats used CASL with a range of 177ms for the caudate putamen to 339ms in the visual/auditory cortex (Thomas et al. 2006). Similar values were also reported by Wells et al. with a transit time of 240ms (Wells, Siow, et al. 2013). The ATT for rats in this experiment generally

matches well with our value in rats being 340ms (Section 4.6.2). In CD-1 mice a range of ATT values between 110ms and 230ms were calculated. These again agree with what has been seen in the literature. For the C57 mice, much longer ATT times were found, with over one second for L_{inv} = 8mm. This has been attributed to the long distance between the labelling and imaging slice planes, relative to the size of the animal being imaged. The velocity in these mice was lower than the CD-1, which was perhaps to be expected as the mice were smaller. Furthermore, a lower number of pulses was needed to label the blood. Further studies of the C57 mice using a large group of animals would be useful to explore the accuracy of these results, as from Figure 4.10, labelled blood has arrived after a CI of 500ms labelling.

4.7.2.3 Fitting to the Kinetic Model

To examine the hybrid nature of the mbASL sequence, data were acquired at multiple TI values using a short labelling duration of 500ms. For small values of L_{inv}, the peak of the signal was seen after a delay of 50ms, with the signal curve mimicking the decay of signal seen in a pCASL experiment (C57 mice (Figure 4.10a) and rats (Figure 4.9)). The lack of a peak shift for the CD-1 mice was believed to be due to the small distance chosen between the labelling and imaging slice and, hence, the peak signal was seen at 50ms for all L_{inv}. This was one of the reasons a second strain of mouse was included in the experiments as previous research (Vallatos et al. 2018) had shown for C57 mice the peak occurred at a time point larger than 50ms with similar experimental parameters. Double peaks seen in the 24mm and 36mm data produced from the rats. This could result for two potential reasons. Either the recirculation of the heart causes the labelled blood to take longer to reach the imaging slice or the number of inversion pulses were too low. A similar effect was seen from the theoretical predictions when using similar values (Figure 4.4). The overall ΔM signal for these thicker slabs were lower than for the smaller slab thicknesses. This may be due to part of the inversion slab being outside of the homogeneous region of the RF coil, stressing there is a limit beyond which mbASL will not produce optimal results. In addition, a lower ΔM signal will be produced when using a large labelling slab due to T_1 relaxation effects.

The variable TI data were fitted to the mbASL model to see if an accurate value of ATT could be produced. In addition, the data were also fitted to the PASL and CASL models, to examine if ATT values would change between the three models depending on the labelling slab thickness. In rats, the PASL models produced values that resembled the literature, but differed from the values calculated in Section 4.6.2. For mbASL, a longer value was found from fitting with the 12mm thickness than from the calculated value. In the C57 mice, the CASL fitting value was low for

all labelling thicknesses. This is most likely due to the longer distance of L_i used compared to a standard CASL or pCASL sequence. Only one value was obtained with a high fitting R^2 value for mbASL. This did not agree with either the calculated ATT or PASL. Overall this suggests that when too large an L_i or L_{inv} is used, the ATT values are not accurate. PASL fitting values were similar to literature but were vastly different from the calculated ATT. In CD-1 mice, the fitted mbASL values were higher than the calculated values, but were still within literature range. Overall this research has shown that accurate values of ATT cannot be obtained by fitting to the mbASL kinetic model. This will be due to the model not taking a number of factors into consideration, including the heart circulatory system and considering the labelled blood to travel with a constant velocity, with further work on the model needed to be able to obtain similar ATT values from both a calculation (Section 4.6.2) or fitting to the model.

4.7.2.4 CBF maps

Cerebral blood flow maps were produced for each animal, using the ATT values found using Equation 4.7 (Section 4.6.2). The mean CBF seen across all the subject groups were within the literature range (Duhamel et al. 2012; Baskerville et al. 2012; Larkin et al. 2019; Buck et al. 2018). For SD rats, the mean CBF value was 120 ml/100g/min. Larkin et al. reported values of 111 ml/100g/min using a pCASL sequence. Wells et al. also reported similar results with a value of CBF as 123 ml/100g/min using a FAIR sequence (Wells, Siow, et al. 2013). For mice, the mean CBF was higher for the CD-1 mice compared to the C57 mice (172 ml/100g/min compared to 110 ml/100g/min). This was expected as the CD-1 mice were larger in size and weight and hence needed a larger number of labelling pulses to reach a plateau of signal. This suggests these mice had a faster blood velocity than the C57 mice and hence a higher CBF. Both values compared to what is reported in the literature. Buck et al. reported CBF values of 96 ml/100g/min using BALB/c mice (Buck et al. 2018). Duhamel measured values of CBF of 116 ml/100g/min on C57 male mice, comparing well to the values found for C57 mice. Although in rats, Baskerville et al. reported values of 157 - 177 ml/100g/min using a pCASL sequence, showing our results fall within a range seen in the literature using both pCASL and FAIR. Most models of CBF (Larkin et al. 2019; Alsop, Detre, et al. 2015) use a simplified model to calculate the maps. This work has shown that the mbASL kinetic model can be used to produce accurate CBF values that agree with values in the literature and can account for differences between strains.

4.7.2.5 Comparison of mbASL and FAIR ΔM Signal

The mean signal from the ΔM mbASL images was compared to the values in the FAIR images under the same conditions. It should be stressed that it was attempted to keep as many parameters the same for both sequences; overall scan time, FOV, matrix size, labelling duration and receiver gain. Both scans were also performed in the same imaging session. An increase in ΔM signal was seen in multiple brain ROIs, for all animals over FAIR, and confirms what was presented previously for mbASL (Vallatos et al. 2018). In both mouse species, the largest increase in ΔM signal was seen in the thicker slabs (L_{inv} = 12mm CD-1 and L_{inv} = 16mm C57), with an increase between 300 % and 500 % in the C57 mice. This is much higher than a mean increase of 130 % over FAIR for the CD-1 mice. This large difference is mainly due to the poorer quality FAIR images in the C57 mice. For the rats, an increase of 200 % - 300 % of the FAIR signal is seen. The highest increase in ΔM signal is seen for L_{inv} = 12mm, with the lowest signal seen at L_{inv} = 36mm. This data shows overall that mbASL can consistency produce higher ΔM signal than FAIR for both mice and rats.

4.7.2.6 Comparison to other ASL sequences

The mbASL sequence has been qualitatively compared to FAIR, showing a much higher signal for all values of L_{inv}. A quantitative comparison was not suitable for this study due to the scan parameters chosen for the FAIR used. Furthermore, the discrepancies shown between FAIR and pCASL by Duhamel (Duhamel et al. 2012), demonstrates a straight comparison of values may not be suitable. A better comparison for mbASL would be to compare the signal, SNR and CBF between mbASL And pCASL on the same animals. The pCASL sequence has a higher SNR that PASL and could be a fairer comparison in overall signal and SNR of ASL sequences. However, as shown previously (Alsop, Detre, et al. 2015) there are many variations of pCASL, making comparison more difficult.

4.7.2.7 Limitations

The mbASL kinetic model makes multiple assumptions in the fitting of the TI data. It is assumed that a constant blood velocity takes place for the labelled spins travelling from the labelling slab to the imaging slice. The original Buxton model assumes a constant velocity with a plug flow. A further variation of the mbASL model would be to include a varying velocity when obtaining a value of ATT. The mbASL sequence has a limited thickness range which varies not only between animals, but

between species. Paired with the drastically different amount of labelling pulses needed, this means optimisation of the sequence is needed before it can be used. This study used only a small number of animals, in keeping with the 3Rs guidelines. A larger experimental group however would provide much needed data for better fitting to the mbASL kinetic model.

4.8 Conclusions

A quantitative model for mbASL has been developed and validated successfully, allowing high quality CBF maps to be produced. By optimising the number of pulses and showing how crucial the labelling thickness is in calculating ATT values, the hybrid nature of mbASL has been shown. The kinetic model is able to describe the signal seen from mbASL in different rodents using a varying labelling thickness, which has not been seen in the literature previously.

Chapter 5

Development of Diffusion Weighted Multiple Boli Arterial Spin Labelling

5.1 Abstract

The mbASL sequence, described in Chapter 4, was combined with a pair of gradient pulses to develop a diffusion weighted mbASL sequence (DWASL). The aim of this chapter was to develop the DWASL sequence to be sensitive to changes in water exchange in the brain. Furthermore, the sequence was altered to examine the effect of the observation time between the gradient pulses, Δ, on the signal when the same b-values were used. Multiple experiments were designed to test and validate the diffusion weighted mbASL sequence.

5.2 Experimental Setup

Animal ethics, scanner set up and protocols have been previously described in Chapter 4. Animals used in the development of DWASL were female CD-1 mice, weight = 30 - 40g. Specific sequence parameters are defined in each section. All data were analysed using in-house MATLAB code written by myself (Mathsworks, Inc).

The equation for bi-exponential fitting is shown below, where A_1 and A_2 represent weightings and D_{cap} and D_{tis} (mm^2/s) are the apparent diffusion coefficient of the capillary and tissue water respectively. S represents the signal and b is the b-value, measured in s/mm^2.

$$\frac{S(b)}{S_0} = A_1 e^{D_{cap} \cdot b} + A_2 e^{D_{tis} \cdot b} \tag{5.1}$$

5.3 Initial Development of DWASL

To develop the mbASL sequence into a DWASL sequence, initial studies used a phantom of $CuSO_4$ solution. Further studies were applied in-vivo, with CD-1 mice.

5.3.1 Qualitative Development of Readout Module

A comparison of readout methods was undertaken as the first part of the project, before the research in Chapter 4 and prior to the addition of diffusion gradients. A RARE readout after ASL labelling was qualitatively compared to an EPI readout. Parameters for the RARE readout were: NA = 24, slice thickness = 1.5mm, np = 25, matrix size = 64×64. Parameters for the EPI readout were: NA = 10, np = 35, matrix size = 96×96. To determine the overall signal and SNR of the images, pair-wise subtraction of the label and control images was undertaken. A full brain ROI was used and the signal averaged. Figure 5.1 shows the images obtained from both sequences. The matrix size was increased from 64×64 in the RARE images to 96×96 in the EPI images for qualitative comparison, with a decrease in the number of averages used for EPI lowering the overall scan time.

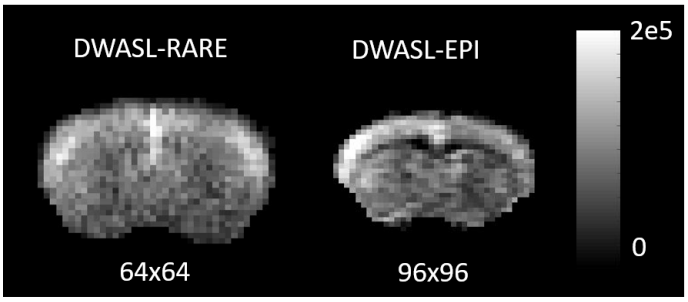

Figure 5.1: Comparison of ASL images acquired using a mbASL-RARE and mbASL-EPI sequence

A DWASL-RARE and DWASL-EPI image with b = 0 s/mm^2 shown with arbitrary units. A higher signal and SNR were seen when using DWASL-EPI compared with DWASL-RARE. This higher SNR meant a larger matrix of 96×96 was able to be used for the DWASL-EPI, with more detail able to be seen when using DWASL-EPI.

Following the results of this study, it was decided to use EPI for the remainder of the experiments in this thesis. The RARE readout showed an overall low SNR and signal, with a lack of structural detail in the images.

5.3.2 Interleaved Readout Module

In anticipation of adding diffusion gradients to the mbASL sequence, multiple changes were made to the acquisition module. This involved modifying the looping structure and changing the user interface and pulse programme.

5.3.2.1 Looping Structure

In a conventional Bruker EPI sequence, the order of looping is: number of slices, number of averages, number of shots and number of repetitions. As the mbASL was a modification of the Bruker FAIR EPI sequence, the mbASL looping order was: pulse train, number of slices, number of averages, number of EPI shots and number of repetitions (Figure 5.2). As the number of averages and number of EPI shots comes before the number of repetitions, all the label ASL averages are acquired before all the control ASL averages. This was acceptable for short acquisitions, but for the DWASL sequence with multiple b-values, the images could be affected by physiological parameters from longer scan times. A single shot EPI readout module was used to shorten the scan time, however, multiple physiological parameters could change throughout the scan, for example the heart rate, breathing and anaesthetic levels for the animal, in addition to changes in CBF. To try to minimise the effects of these physiological parameters, the looping structure was changed (Figure 5.3), by rewriting the source code. The definition of the number of repetitions (NR) was changed so that:

$$Number\ of\ repetitions = 2 * Number\ of\ Averages \tag{5.2}$$

The looping was changed to: pulse train, number of slices, number of EPI shots, number of repetitions.

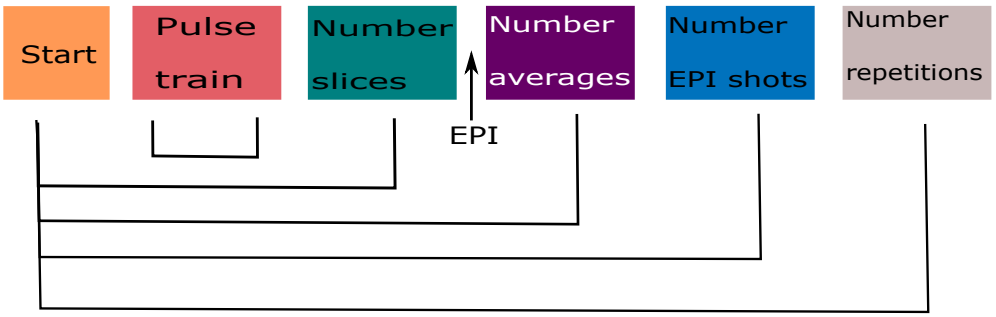

Figure 5.2: Looping structure of conventional DWASL

The looping structure originates from Bruker's EPI sequence. Following the addition of a pulse train and diffusion gradients, the structure of the sequence, where the number of averages of each EPI shot for the label image are acquired before the control image, can lead to physiological effects in the images.

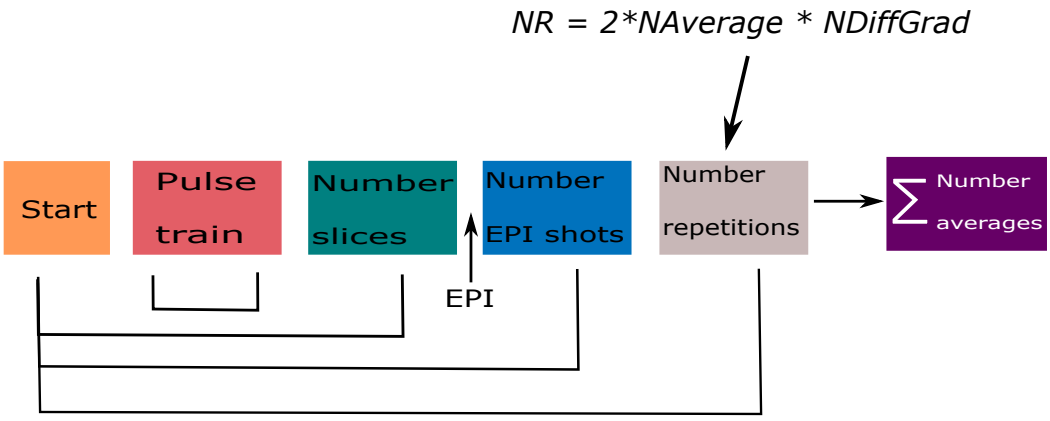

Figure 5.3: Looping structure of modified DWASL

Modifying the looping structure so that the number of EPI shots for a label and a control image are acquired before the next average allowed the physiological effects on the images to be minimised.

5.3.2.2 Modification of the Paravision User Interface

For the initial development of DWASL, the addition of diffusion gradients meant only a single diffusion value could be used in each scan. For user convenience, the pulse programme was altered so the user interface included the option to acquire multiple b-values during the same scan (Figure 5.4). The b-value of the sequence was controlled by changing the strength of the gradient. For this DWASL sequence, this involved calculating a percentage ($G\%$) of the maximum gradient G_{max}:

$$G = \sqrt{\frac{b}{\gamma^2\delta^2(\Delta - \frac{\delta}{3})}}$$
$$G\% = \frac{G}{G_{max}} \tag{5.3}$$

Where γ = 42.6 MHz/T and G_{max} = 2.94×10^{-4} mT/m.

Additional parameters include the number of inversion pulses used for the mbASL labelling (Npul), the length of labelling (InvTime) and the delay between the labelling and imaging (TrainDelay). The time between the inversion pulses (SepTime) was calculated by the pulse programme dependent on the value of Npul and InvTime.

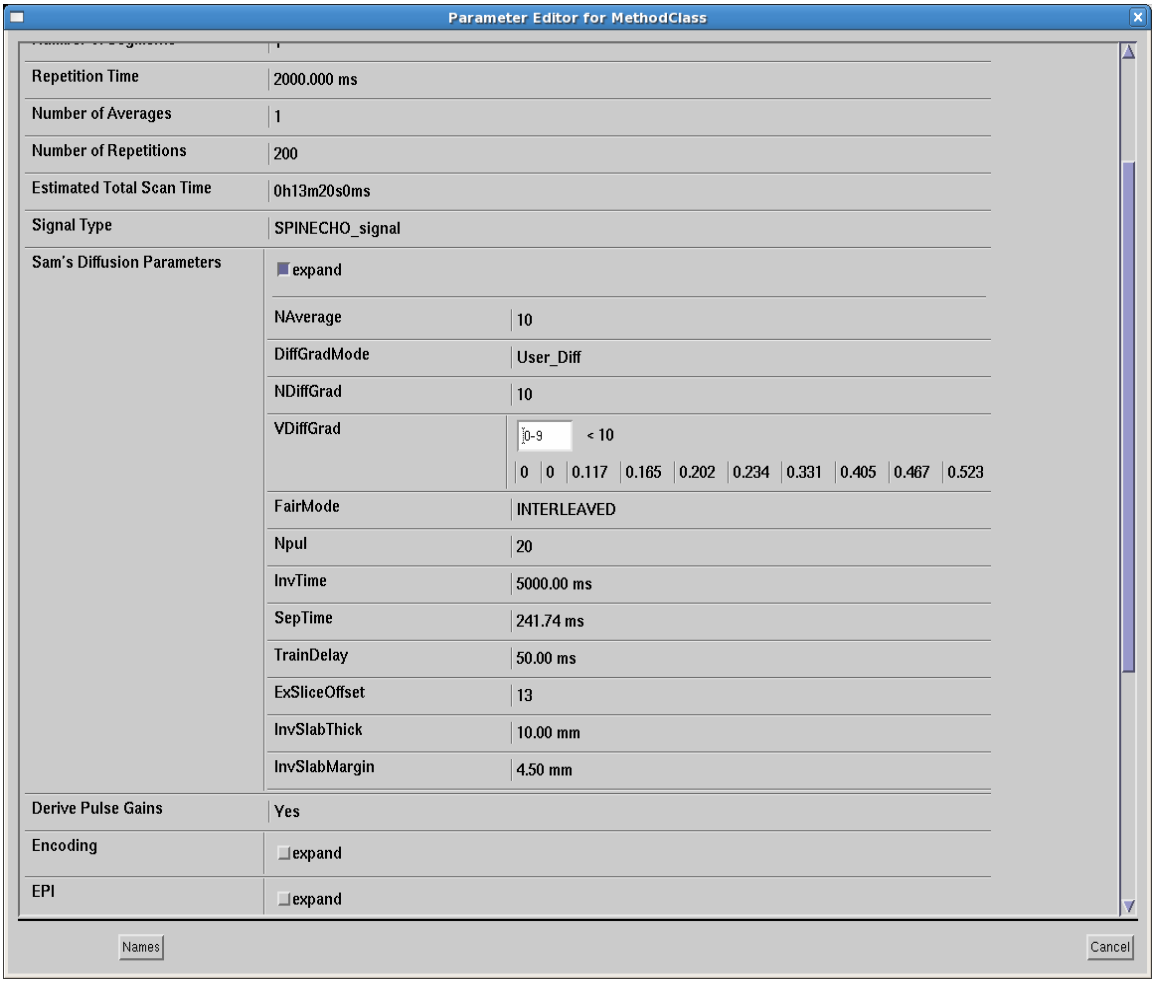

Figure 5.4: DWASL user interface

The menu for the mbASL labelling pulses was modified to include diffusion values for the diffusion weighting and the option for the number of averages and diffusion values used for interleaving the sequence. By setting NAverage and NDiffGrad, the subsequent images produced by the DWASL sequence can be combined in MATLAB. The value of b for diffusion weighting is entered as a percentage of the maximum gradient.

5.3.2.3 Combining Multiple b-values and Interleaved Readout Module

The original mbASL looping structure acquired all averages of the label image before acquiring all the averages of the control image. The modifications made to the looping structure meant one average of a label and control image were acquired in an interleaved fashion before moving to the next average. The number of images acquired for DWASL was:

$$Images = 2 * NAverage * NDiffGrad \tag{5.4}$$

This resulted in a one average pair of DWASL images for every b-value. These images were then exported in a DICOM format to MATLAB where in-house MATLAB code was used to combine the images into the conventional one label and one control ASL image set. Figure 5.5 shows the original looping structure. For the interleaved modification, the label and control k-spaces were collected in a different order

from the original method (Figure 5.6). Each k-space was Fourier transformed into a one average image. These one average images were combined using MATLAB code post-imaging.

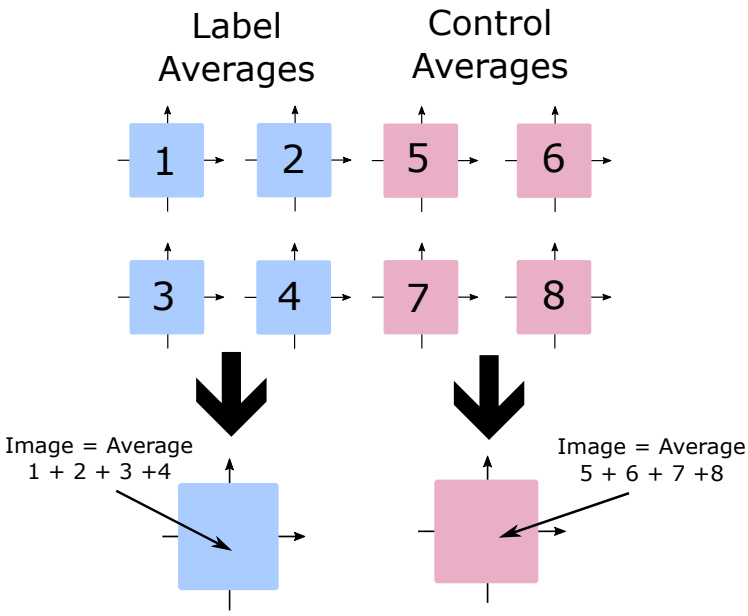

Figure 5.5: Schematic of original acquisition of DWASL data

The method of collecting the images from the original Bruker looping structure is to collect all the averages of the label image before collecting all the averages of the control images. This is shown in the above figure with the numbered k-spaces, where 1, 2, 3 and 4 are collected first before 5, 6, 7 and 8. These k-spaces are acquired and combined to provide two images for the user.

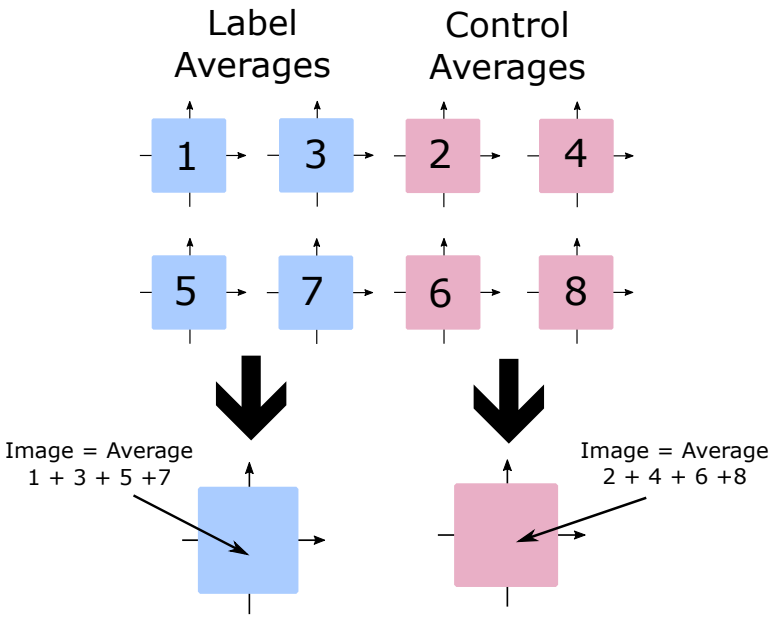

Figure 5.6: Schematic of modified acquisition of DWASL data

The modified image acquisition sees the label and control images acquired in an interleaved fashion. These are produced as one average images. As in the figure above, the user will acquire eight of these images and will then combine them using MATLAB software. The label image is combined from images 1, 3, 5 and 7. The control image is combined from images 2, 4, 6 and 8.

5.3.3 Adding Gradients to the mbASL Sequence

After altering the pulse programme and adding the interleaving option, the interleaved mbASL sequence was made diffusion weighted by adding a pair of gradient pulses (Figure 5.7). Multiple development tests were performed to ensure the sequence was producing labelling of spins and measuring accurate diffusion coefficients.

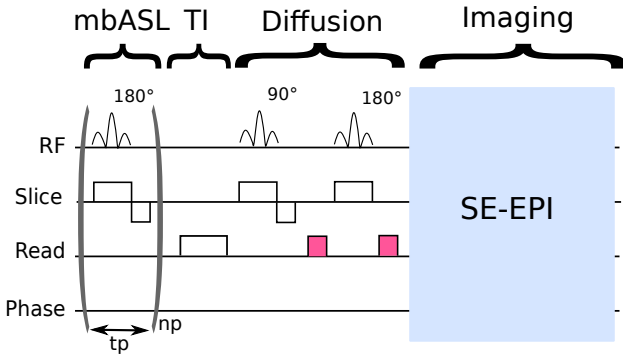

Figure 5.7: A schematic of the DWASL sequence

The DWASL sequence used in this thesis is based on a spin-echo EPI sequence pre-weighted with a train of adiabatic pulses (mbASL). Between the labelling train and the imaging module, a gradient pair was used to attenuate the signal. The first gradient dephases the signal with the second gradient pulse after the 180° pulse used to rephase the signal from the labelled spins. A single-shot spin-echo EPI readout module was used to acquire the imaging data.

5.4 Testing and Validation of DWASL

To confirm the DWASL sequence produced the expected signal attenuation, experiments were performed using phantoms and in-vivo using mice.

5.4.1 Validating Diffusion Gradients with a Phantom

Images of the $CuSO_4$ phantom were acquired using a diffusion gradient strength of zero to test the stability of DWASL against the previous mbASL sequence. Twenty image pairs were acquired with NA = 2 and G = 0. The matrix size was 96×96 with np = 20 and CI = 5s. The control image for each pair was used for analysis, with a ROI taken near the top of the phantom where the highest signal was seen. Analysis of the signal for each ROI gave a coefficient of variation of 0.37%, indicating that any changes in signal were not due to the DWASL sequence (Figure 5.8).

To test that the DWASL sequence produces diffusion values that correspond to the literature, varying b-values were acquired on a phantom, n = 1. Figure 5.9 shows the corresponding data plotted on a log scale. The average diffusion value was

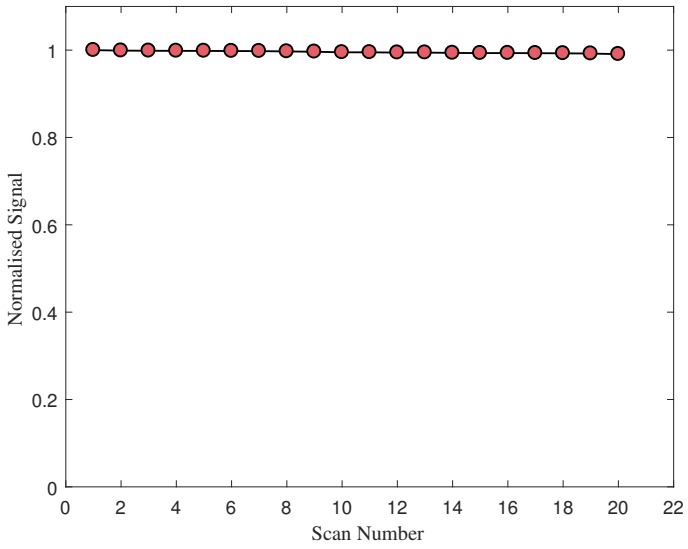

Figure 5.8: Multiple scans using G = 0 on a phantom model

The stability of the DWASL sequence using no gradient was tested using multiple value of b = 0 s/mm^2 on a phantom. The coefficient of variation was 0.37 %. The data were normalised to the first signal value before being plotted.

$D = 2.26 \times 10^{-3}\ mm^2/s$ which matches with literature values for water diffusion ($2.2 \times 10^{-3}\ mm^2/s$ (Tanaka 1978)). Further tests (not shown) used gradients in different orders, rapid switching between high and low b-values and multiple repetitions of the same b-value. These tests were designed to check that the MRI system could cope with high gradient strength, the rapid switching between high and low gradient strengths and produce results consistent with the zero gradient measurement.

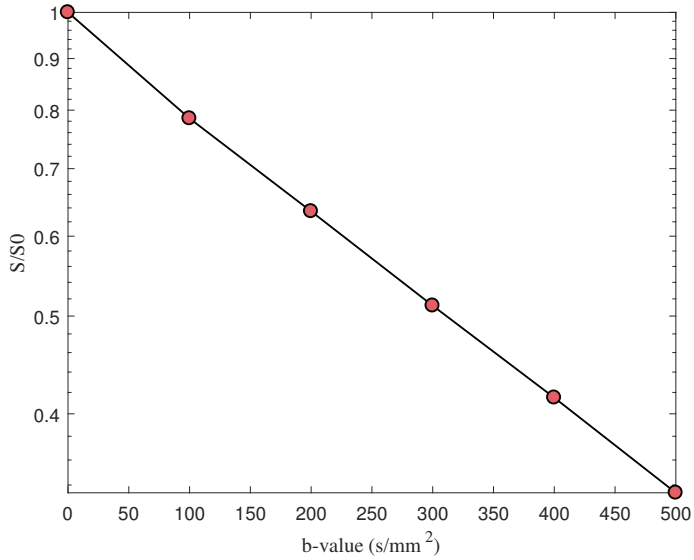

Figure 5.9: Diffusion of a water phantom using the control image of a DWASL sequence

The diffusion of water was tested using varying b-values between b = 0 and b = 500 s/mm^2 and plotted using a log-linear scale. The signal from the control image acquired at each b-value was plotted and the value of ADC found by fitting to a mono-exponential. The value of diffusion found was $D = 2.26 \times 10^{-3} mm^2/s$.

5.4.2 Validating Diffusion Gradients In-Vivo

After successfully obtaining an accurate value of the diffusion of water using a phantom, the sequence was applied in-vivo. Only limited information could be obtained from a phantom, with an in-vivo model making development more realistic.

To examine any changes in the image signal in-vivo, both the control image and the subtracted DWASL images were examined using one mouse with a full brain ROI. Six averages were used, with the same parameters as previously. Five image pairs were taken for the experiment. A variation of 0.10% was seen between the signal from the control image ROIs and 3.97% between the subtracted DWASL image ROIs. A higher variation coefficient was seen in the DWASL images due to lower SNR. Figure 5.10 shows the normalised signal from the subtracted image ROI. Similar gradient tests to the phantom experiments were performed as described above in Section 5.4.1.

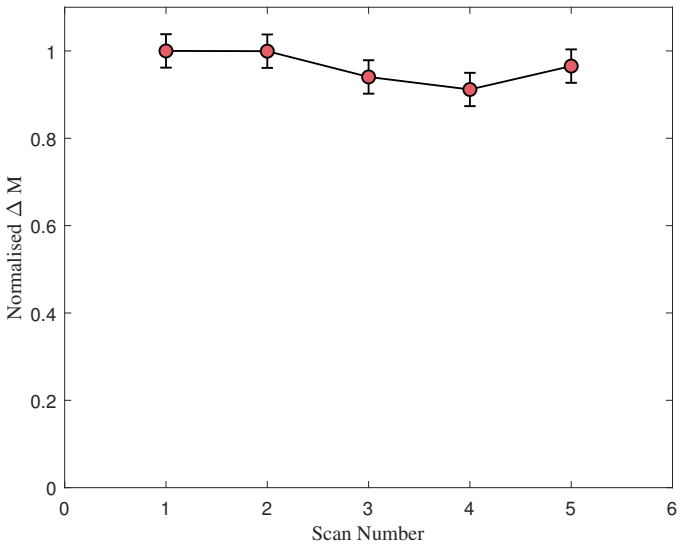

Figure 5.10: Variation of the DWASL sequence in-vivo

The variation of the DWASL was tested in-vivo using a single mouse. The normalised data shows a change of $\sim$ 4% over the first value of ΔM. A larger variation is expected from the subtraction of in-vivo images. Error bars depict the SD from the signal from all scans.

5.4.3 Proof of Concept Study

Two different experiments were performed as a proof of concept for DWASL. Thie first experiment used n = 6 mice, with varying b-values from b = 0 to 500 s/mm^2 used with the same parameters as above with NA = 10. A full brain ROI was used and the signal from each image plotted. Figure 5.11 shows the DWASL signal from the obtained data fitted to a bi-exponential model with the signal from the corresponding control image plotted as a reference. The control image has no labelling and thus provides a diffusion weighted image. The drop in the signal is from the attenuation of the labelled blood in the capillaries. This attenuation happens because of flow dispersion and the diffusion gradients. As the b-value increases, a slower decay of the signal is observed. The signal from images with higher b-values comes from the labelled water in the tissue. The labelled water in the tissue travels at a slower rate due to the restricted diffusion of the tissue (in comparison to the unrestricted capillaries). The signal from labelled tissue water matches the same signal attenuation seen for a DWI image, represented on the graph by the control signal, showing the change between labelled water in the IV or EV compartments. The results from fitting the signal from the control signal and the DWASL signal to a bi-exponential model are seen in Table 5.1.

Image type	A_1	$ADC_{capillary}$ (mm^2/s)	A_2	ADC_{tissue} (mm^2/s)
Control	0.05	1.7×10^{-2}	0.95	7.4×10^{-4}
DWASL	0.13	1.1	0.87	9.3×10^{-4}

Table 5.1: Fitting values for the DWASL proof of concept study.

Fitting results from the DWASL images and control images for the proof of concept DWASL study. The control image from the label-control pair provides a DWI image, for comparison to the DWASL signal. R^2 = 0.99 for the control signal and R^2 = 0.99 for the DWASL signal to the mono-exponential and bi-exponential models respectively.

For the second experiment, the signal at three different b-values were compared at varying inversion times. The inversion time controls the fraction of labelled arterial spins that exchange from the capillaries into the tissue (Figure 5.12). By increasing the inversion time, it was expected that the ratio of the labelled spins in the intravascular (IV) and extravascular (EV) compartments would change when compared at each b-value. Three mice were used with multiple TI values. As the TI value increased, the ratio of the signal from the tissue component increased, with the signal from the DWASL control image used for comparison. At b = 50 s/mm^2, there was a significant difference ($p<0.05$) between TI = 10ms and 300ms (p = 0.045), TI = 10ms and 600ms (p = 0.015) and TI = 10ms and the control signal (p = 0.0033). For b = 75 s/mm^2, a significant difference was seen between TI = 10ms and the control signal (p = 0.028) but not between TI = 10ms and 300ms (p = 0.079) or TI = 10ms and 600ms (p = 0.056). At b = 100ms, there was a significant difference between TI = 10ms and 600ms (p = 0.046) Overall, this confirms that by increasing the exchange time, TI, this will result in a significant increase in

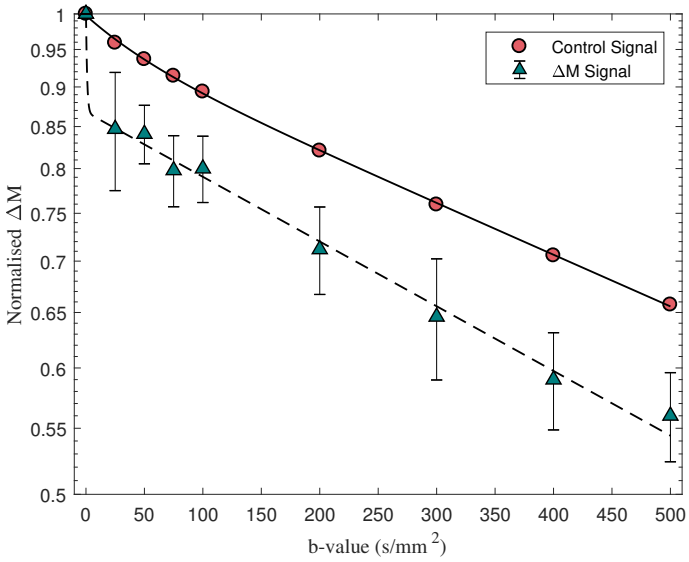

Figure 5.11: In-vivo DWASL data fitted to a bi-exponential model

The ΔM signal and control signal from DWASL was fitted to the bi-exponential model and plotted using a log-linear scale for n = 6 mice. The difference between the signal for the IV and EV spins can be seen in the DWASL graph with a sharp drop before the signal decays at the same rate as the signal from the control image.

exchange of arterial blood water with tissue water.

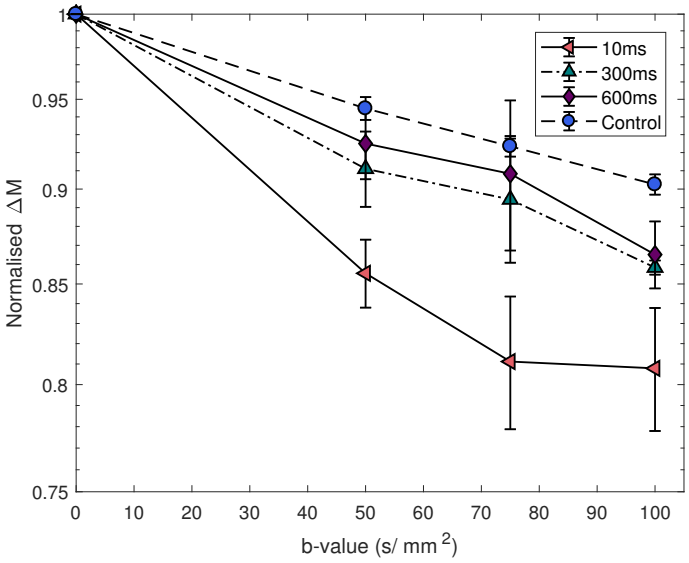

Figure 5.12: Comparison of the ΔM signal using different TI values

The signals for n = 3 mice at different TI values were compared on a log-linear scale. Error bars are the standard deviation. As the TI increased from 10ms to 600ms, the ratio of IV to EV signal changed, with a larger number of labelled spins diffusing into the tissue when using a longer TI value. The control image signal was plotted for comparison. There was a significant difference ($p<0.05$) between the signal for TI = 10ms and the longer TI values and control signal.

5.5 Modifying DWASL to Incorporate a Bi-Polar Diffusion Gradient Pair

It was shown in Section 5.4.3 that from $b = 25\ s/mm^2$ the signal seen was from labelled spins in the tissue (EV compartment) rather than the capillaries (IV compartment). At low b-values we speculated there was instability in the signal due to the low diffusion gradients needed. This was important as the signal is normalised to b = 0 s/mm^2. To address this instability and to allow for more low b-values, a suggestion was to decrease the value of Δ which, in turn, increased the value of gradient needed to give the same b-value. To do this, we moved the second diffusion gradient to before the spin echo pulse, in a bi-polar configuration (Figure 5.13). This modification of DWASL was termed single sided diffusion weighted arterial spin labelling (SS-DWASL). To test this new sequence and develop the optimal value of Δ, multiple phantom and in-vivo experiments were performed.

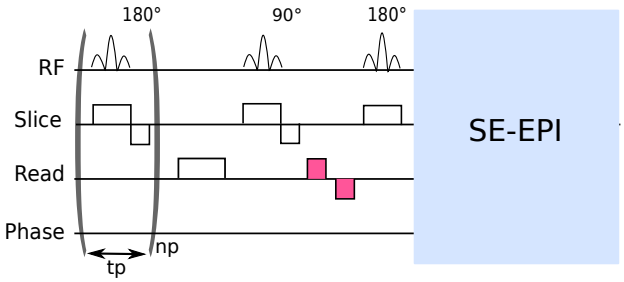

Figure 5.13: A schematic of single sided DWASL

The main difference between DWASL and single sided DWASL is the moving of the gradient pair. By moving the gradients to create a bipolar pair before the 180 ° pulse, this shortens Δ and increases the strength of gradient needed.

5.5.1 Testing SS-DWASL Using a Phantom

To test what effect moving the diffusion gradients would have on the signal, three different phantoms were used: $CuSO_4$, ethanol and 2-butanone. One signal average was acquired with varying b-values. Figure 5.14 shows the plotted data set. Both DWASL and SS-DWASL signal attenuation were used to evaluate the diffusion value of water. Table 5.2 shows the average diffusion value calculated for each phantom using a single exponential fit. All phantoms had an R^2 value of 0.99. A literature value for each liquid is shown for comparison (Tanaka 1978; Hurle et al. 1985; Zhu et al. 1992).

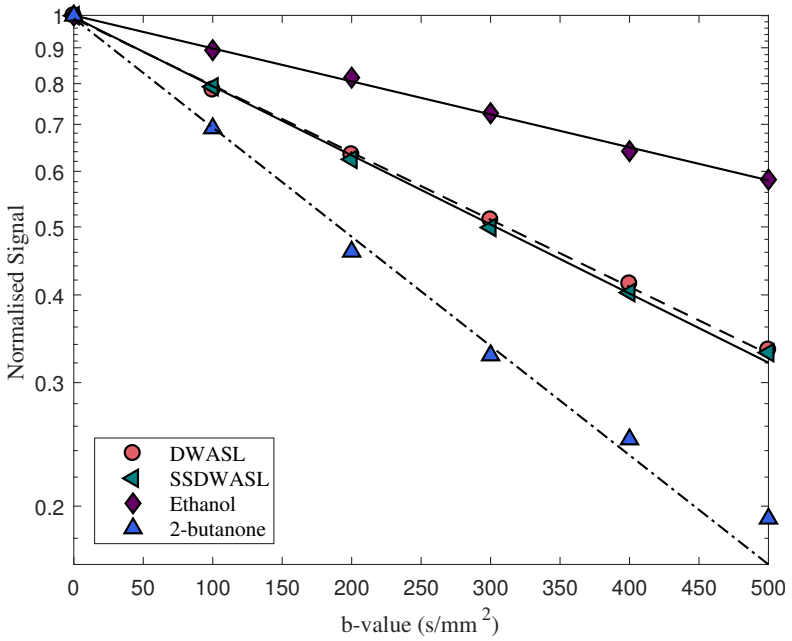

Figure 5.14: Diffusion plot using DWASL and multiple phantoms

The SS-DWASL sequence was compared against the DWASL sequence using a water phantom. The data were plotted using a log-linear scale. Both sequences produced the same diffusion values (2.20×10^{-3} mm^2/s and 2.23×10^{-3} mm^2/s). SS-DWASL was also used to measure the diffusion of Ethanol an 2-butanone with the diffusion values matching the literature (1.08×10^{-3} mm^2/s and 3.58×10^{-3} mm^2/s respectively).

Phantom	Average Diffusion ($\times 10^{-3} mm^2/s$)	Literature ($\times 10^{-3} mm^2/s$)
H_2O (DWASL)	2.2	2.3
H_2O (SS-DWASL)	2.2	2.3
Ethanol	1.1	1.1
2-butanone	3.6	3.6

Table 5.2: Diffusion values for multiple phantoms determined using DWASL and SS-DWASL, acquired at room temperature (22 °C)

5.5.2 Varying the Value of δ and Δ

The variation of δ and Δ on the signal attenuation was tested on a phantom. It was expected that the same attenuation would be produced. Figure 5.15 shows the signal produced for Δ = 11.2, 13.2 ms and δ = 3.2, 5.2, 7.2 ms. The sequence showed signs of variance when using a large gradient. Overall, at b-values less than b = 300 s/mm^2, all values of Δ and δ produced nearly identical signal attenuation. For further studies, it was decided a value of δ = 3.2 ms was kept the same as the original DWASL sequence and a value of Δ = 9.2 ms was chosen.

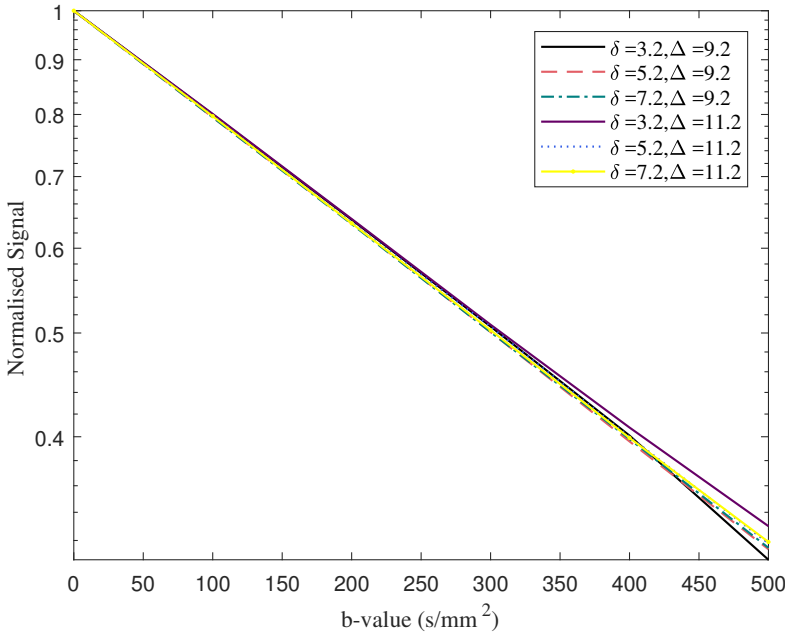

Figure 5.15: Comparison of varying Δ and δ in SS-DWASL

Values of Δ and δ were varied whilst maintaining the range of b-values between 0 and 500 s/mm^2. Slight deviation was seen at high b-values when a large gradient was needed. The graph is plotted using a log-linear scale.

To check the stability of the sequence, the sequence was run with b = 0 s/mm^2 for 10 repetitions and NA = 1. The same gradient tests in Section 5.4.1 were performed to test the reliability of SS-DWASL. All tests produced the expected results that were seen in DWASL.

5.5.3 Optimising Diffusion Gradients In-Vivo

To examine the effect of bipolar gradients in-vivo, six mice were used. b-values and parameters were the same as in Section 5.4.3. Diffusion gradient strengths were set to values that corresponded to b-values between 0 and 500 s/mm^2. The signal attenuation from the control and SS-DWASL images are shown in Figure 5.16. The fitted curve shows a smoother line for the SS-DWASL signal, with the same decay of signal seen as the control signal from b = 200 s/mm^2. Coefficients from the fitting are displayed in Table 5.3.

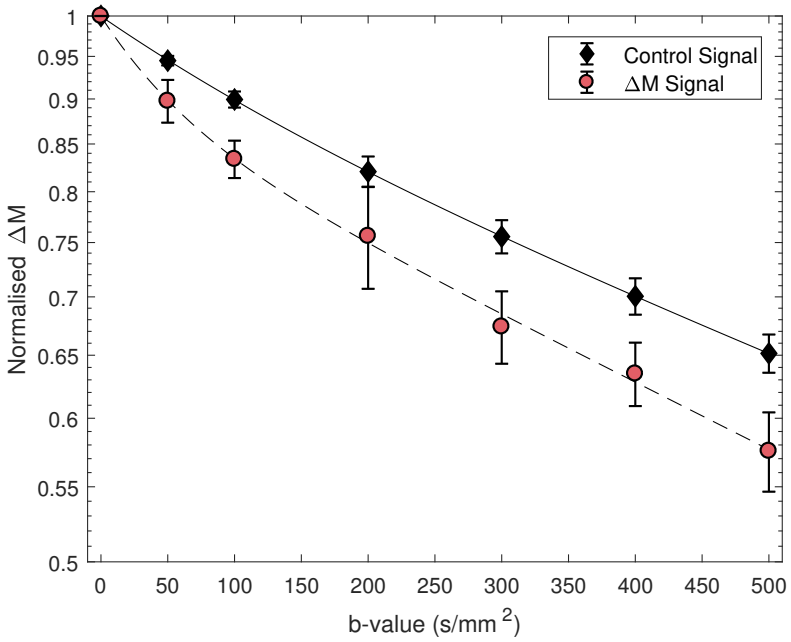

Figure 5.16: Signal at various b-values using SS-DWASL in-vivo

The fitting of the SS-DWASL signal to the bi-exponential model shows a smooth curve than the fitting curve seen in DWASL. The graph is plotted using a log-linear scale, error bars are the standard deviation and n = 6 mice were used. From b = 200 s/mm^2, the curve follows the same decay as the control signal fit.

Image type	A_1	$ADC_{capillary}$ (mm^2/s)	A_2	ADC_{tissue} (mm^2/s)
Control	0.093	5.9×10^{-3}	0.99	8.7×10^{-4}
SS-DWASL	0.12	1.6×10^{-2}	0.88	8.6×10^{-4}

Table 5.3: Fitting values for SS-DWASL from Figure 5.16

5.6 Comparing DWASL and SS-DWASL In-Vivo

The data collected in Sections 5.4.3 and 5.5.3 for DWASL and SS-DWASL are compared below in Figure 5.17. A difference between the two sequences was seen, with the sharper drop in signal for DWASL and a more subtle drop for SS-DWASL. Both sequences showed a similar value for ADC_{tissue} compared to each other and both control image values ($8.29 \times 10^{-4}\ mm^2/s$ for DWASL and $8.64 \times 10^{-4}\ mm^2/s$ for SS-DWASL). A large difference was seen in the $ADC_{capillary}$ values.

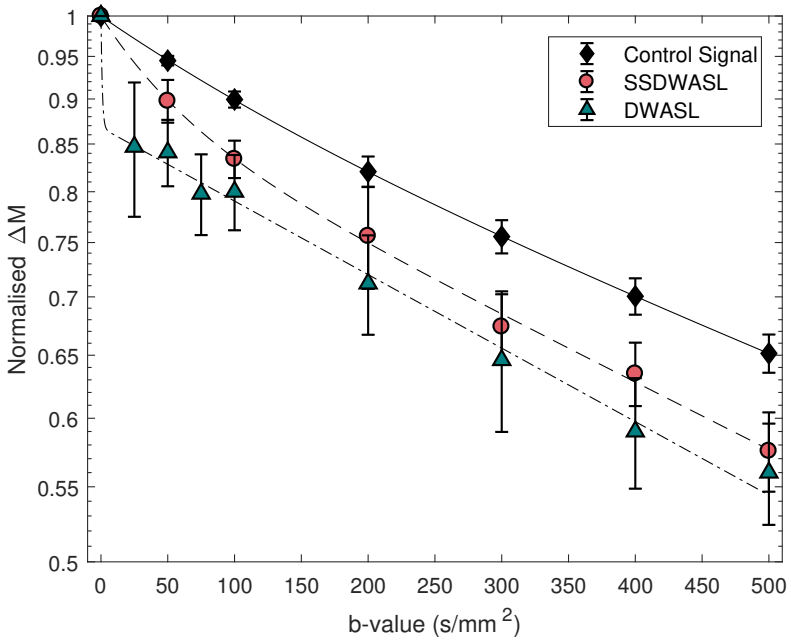

Figure 5.17: Comparison of DWASL and SS-DWASL pilot data

Comparison of the two fitting curves for DWASL and SS-DWASL shows a qualitative difference in shape in addition to different ADC values for the capillaries (1.052 for DWASL and 1.62×10^{-2} for SS-DWASL). The ADC values for tissue were similar between DWASL, SS-DWASL and the control ADC value. The graph is plotted using a log-linear scale, error bars are the standard deviation and n = 6 mice used for both signals.

A study group of n = 6 mice was used to further compare DWASL and SS-DWASL by examining if SS-DWASL was a viable alternative to DWASL. Both DWASL and SS-DWASL were used in the same scanning session. The same parameters and b-values, as described above, were used. The results of this study showed no clear difference between the two sequences (Figure 5.18). Fitting data to the bi-exponential model (Equation 5.1) produced very similar values for ADC_{tissue} with 7.9×10^{-4} for DWASL and 7.1×10^{-4} for SS-DWASL (Table 5.4). Above b = 200 s/mm^2 the two curves followed the same signal attenuation. The values for $ADC_{capillary}$ are closer than the values produced in the pilot study, with 3.5×10^{-2} for DWASL and 1.4×10^{-2} for SS-DWASL.

Image type	A_1	$ADC_{capillary}$ (s/mm^2)	A_2	ADC_{tissue} (s/mm^2)
Control	0.027	4.3×10^{-2}	0.97	6.4×10^{-4}
DWASL	0.10	3.5×10^{-2}	0.90	7.9×10^{-4}
SS-DWASL	0.13	1.41×10^{-2}	0.87	7.1×10^{-4}

Table 5.4: Fitting values from DWASL and SS-DWASL from the comparison study of both sequences

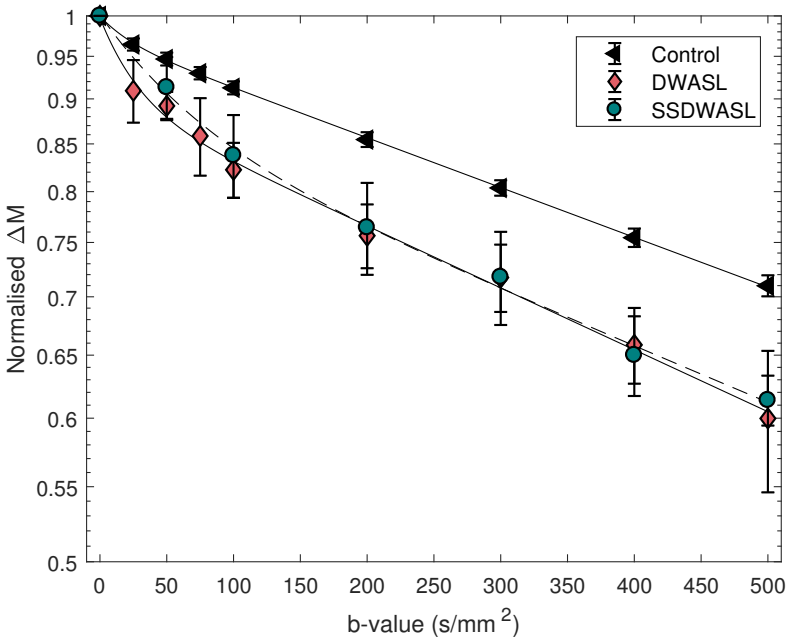

Figure 5.18: Comparison of SS-DWASL and DWASL in a group of mice

A group of n = 6 mice were used to compare the two sequences. Both DWASL and SS-DWASL produced similar fitting curves, with the same signal attenuation seen from b = 200 s/mm^2. The graph is plotted using a log-linear scale and error bars are the standard deviation.

5.7 Discussion

5.7.1 DWASL

The purpose of this chapter was to convert the mbASL sequence into a diffusion weighted mbASL sequence that could probe capillary water exchange in the brain. As over 95% of the signal in an ASL sequence is lost due to subtraction, it is important to have a high SNR sequence that is sensitive to changes in the brain. After preliminary experiments, a single shot EPI readout was chosen for all DWASL scanning.

The modification of the looping structure of DWASL was designed to minimise the physiological effects the longer DWASL scans. A one shot one average EPI scan takes only a few seconds to acquire meaning any physiological parameter changes will make minimal difference to the acquired data. The DWASL sequence with the addition of the pulse train and multiple b-values increased the overall scan time significantly. A ten average DWASL sequence with ten b-values takes $\sim$ 20 minutes, where multiple changes including scanner drift, anaesthetic changes, CBF changes and animal movement can occur during this time. We proposed changing the structure of the sequence, where the acquisition of a label and control image was interleaved before the next average, in contrast to collecting all averages of the label image before the control image.

In addition we added the option of acquiring multiple b-values in the same scan. This involved multiple changes to the Bruker source code to define new parameters and modifying the looping of the scan repetitions. The resulting sequence produced separate one average images which were combined in MATLAB to create a label and control image. A limitation of this method of collecting images and manually combining them them could lead to increased noise in the final image. A further improvement to this method would be to combine the k-space of each image rather than the magnitude image. This was too complex to complete in the time-frame available but would be a future progression of this new interleaved method of acquisition. This modified looping structure is more suitable for preclinical imaging where scan times are typically longer for developmental studies.

A number of steps were taken to develop mbASL into a diffusion weighted sequence that could detect changes in the IV and EV compartments. By first performing experiments with no diffusion gradient, this tested the variability of the sequence which was shown to be very low, at a 0.37% change in signal demonstrating the stability of the sequence. The sequence was examined in-vivo by using a range of b-values to examine the signal attenuation. A sharp drop in signal was seen for low

b-values before the drop in signal became smoother at high b-values, similar to the signal seen from the tissue. This effect (Figure 5.11) has been seen in the literature previously, where Wang (Wang, Fernandez-Seara, et al. 2007) demonstrated the separation of the signal from the IV and EV departments in humans at different labelling delays.

The proof of concept study of the DWASL sequence was important to show that our DWASL sequence would be able to detect changes in the ratio of IV to EV signal in the brain. Comparison was made at three different b-values using three different inversion times. By using different TI values, this allowed less or more time for the labelled arterial water spins to exchange into the brain tissue. This would change the ratio of IV to EV spins in the imaging plane. It was hypothesis that the ratio of IV to EV signal would change as the TI was increased. At the lower value of b = 50 s/mm^2 it was expected there would be a larger difference between the data points compared to the higher values of b = 75 and 100 s/mm^2. This is because the increased attenuation of the signal would mean the majority of the signal would come from the EV compartment. It was shown (with $p < 0.05$) that at b = 50 s/mm^2 there was a significant difference between the signal value at each inversion time. This is similar to the experiment reported in Wang's article on DWASL (Wang, Fernandez-Seara, et al. 2007), where the signal at three different inversion times in clinical patients showed a significant difference between the signals. This has not been shown in the mouse brain until now. Limited data exists for demonstrating the effect of the post label delay in rats with Kim et. al showing the contribution of arterial blood to the image signal decreases as the post label delay increases (Kim and Kim 2006). This study uses the concept of IVIM but demonstrates that a significant difference can be detected in the IV and EV compartments by changing the post label delay.

Other methods have been used to non-invasively image changes in the water exchange in the brain. A multiple echo time ASL has been developed at UCL (Wells, Thomas, et al. 2017; Ohene et al. 2019). By varying the echo times, the permeability of the blood-brain interface can be examined. Ohene's study focused on examining the water transport due to using AQP4 deficient mice, with a change in exchange time seen between the deficient mice and a wild type group. This signifies the importance of having non-invasive methods of imaging BBB permeability and water exchange.

One of the main limitations at this stage is the need for a quantitative model of the DW mbASL sequence. Although Chapter 4 has shown we have quantified the mbASL sequence, the use of diffusion gradients to suppress the signal means that the model would not be able to reflect the signal that we receive from DWASL images. The overall low levels of signal and SNR in any pre-clinical ASL MRI are always

a limitation. By using a high SNR ASL sequence such as mbASL, we have managed to increase the resolution and produced a high quality pre-clinical DWASL sequence. Although DWASL has been applied in rats previously (Wells, Thomas, et al. 2017; Tiwari et al. 2017), there have been no reports in the literature on its application on mice. It has been shown previously that there is a dependence on the direction of the DWASL gradients (Wells, Thomas, et al. 2017). This thesis used a single direction for all DWASL scanning. Developmental work (not presented) was undertaken to examine the difference in signal using different directional gradients, with the highest overall signal direction chosen. Further work would be to implement a multi-directional DWASL, in addition to an option for multi-slice imaging. This chapter has focused on the separation of the signal from the IV and EV compartments. The sequence can, however, be used to examine the permeability of the brain by the use of a ratio of the signal from a diffusion weighted and non diffusion weighted ASL image.

5.7.2 SS-DWASL

Current DWASL literature uses the traditional method of a small gradient to suppress the intravascular signal. A novel change has been made to DWASL by changing the timing of the gradients in the DWASL sequence. This increased the gradient strength that was used in the conventional DWASL sequence and was achieved by moving the gradients together rather than either side of the 180° spin echo pulse. This was primarily to increase the stability of the sequence. A larger number of points at low b-values would be useful to further explore the IV signal (as seen in (Silva et al. 1997)), but the sequence needed to be altered to have b-values lower than 25 s/mm^2, as the value of G needed to be larger for this to happen. Multiple experiments were performed both in-vivo and on a phantom to test the diffusion values produced. SS-DWASL was able to produce accurate diffusion values for multiple substances that corresponded to literature values. The same H_2O diffusion values were obtained using both DWASL sequences. Further tests proved that by varying the values of Δ & δ, the same diffusion values were produced for the same b-value.

Using SS-DWASL in a pilot in-vivo study, the data collected showed a difference in the bi-exponential fit compared to conventional DWASL. When a further study was performed that compared both sequences, very similar results were produced, with the results achieved in the pilot study not being replicated. A comparison was made between both sequences, to examine whether a difference in the A_1 fitting value would be seen. The value for A_1 was very similar between both sequences ($p > 0.05$), suggesting that changing the gradients made no difference to the over-

all output of the SS-DWASL sequence. There could be multiple reasons why this occurred, including poor labelling and artefacts in the images, or physiological changes in the mouse. Further research is needed into SS-DWASL to examine if it is a viable alternative to DWASL for imaging water content in the brain.

5.8 Conclusion

To summarise, a diffusion weighted mbASL sequence was successfully developed to probe water changes in the brain. By using a pair of diffusion gradients, the signal from labelled spins was suppressed and a ratio between the spins in the intravascular and extravascular compartments was shown. Using a high SNR ASL sequence as the base, high resolution pre-clinical images, which are able to challenge DWASL data that are currently in the literature, were produced. The DWASL sequence was able to significantly image changes in the ratio of labelled spins by changing the inversion time of the sequence. Further implementation of this sequence could lead to applications in animal models of disease, specifically where there is damage and permeability changes to the blood brain barrier.

The effect of moving the gradient pair to change the Δ time was explored. Although promising phantom data were found from pilot studies, in-vivo experiments failed to deliver the changes in intravascular and extravascular signal that were expected. Further research is needed to optimise the sequence so it is viable for further research.

Chapter 6

Applying DWASL to a Trypanosome Mouse Model

6.1 Introduction

This chapter demonstrates the use of diffusion weighted arterial spin labelling to image changes in the permeability of the BBB for mice infected with human African trypanosomiasis.

Study 1: Diffusion weighted ASL was used to probe BBB permeability in early stage HAT in mice. Multiple time points and separate groups of mice were imaged, with the end point set as day fourteen post-infection, based on previous time points in the literature.

Study 2: A serial study was designed to examine changes in BBB permeability in one group of mice over the course of infection, with time points in the early and late stage of the disease.

Study 3: To investigate whether water permeability changes occur at the later stage of the disease, the experimental dates were extended forward to include multiple later stage data points.

Study 4: The wet-dry method was used to compare the water content in the mouse brain for healthy and infected mice.

6.2 Methods

6.2.1 Stabilate GVR 35

The *T. b. brucei* trypanosomes were originally isolated from an infected wildebeest from the Serengeti National Park in 1966. This stabilate was sent to the London School of Hygiene and Tropical Medicine where the stabilate LUMP 22 was produced by passaging the parasite in rats. Another passage using parasites from LUMP 22 produced LUMP 1001. Dr Frank Jennings at the University of Glasgow obtained a clone of LUMP 1001. This clone was passaged through sub-lethally irradiated mice and named GVR35/C1. The stabilate is stored in liquid nitrogen. Working stabilates are produced from the reserve stabilate GVR35/C1.1 using passage mice. Throughout this project, the working stabilate GVR35/1.9 was used to establish infections in mice.

6.2.2 Animals

For all studies, female CD-1 mice were purchased from Charles River Ltd, Margate, England. Animals were between 30 - 40g in weight and 6 - 8 weeks in age. All mice were allowed to acclimatise to the animal unit in the University of Glasgow for at least one week before any procedures were carried out. Mice were stored in a mix of standard caging and individually ventilated cages with free access to water and food. Group sizes in cages varied between two and four dependent on experimental numbers. The mice were maintained with a temperature range between 19-23 °C, a humidity of 45 $\pm$ 10 % and a light/dark cycle of 12 hours light and 12 hours dark.

6.2.2.1 Animal Infections

For each experiment, two passage mice were infected with *T. b. brucei* GVR35/C1.9 described above. These mice were used to generate trypanosomes for infection of the larger groups of experimental animals. To initiate the infection, a small section of the frozen stabilate was mixed with phosphate buffered saline plus glucose (PBGS), pH 8 (recipe in Appendix A). A dilution containing 2-trypanosomes per field was used for infection of the passage mice. A volume of 0.1-0.3ml of the diluted stabilate was injected intraperitoneally (IP) into the mice. The development of the trypanosome infection was monitored by wet blood films under the light microscope using a x400 magnification. This was achieved by removing $<$0.5mm from the end of the mouse tail using sharp scissors. A drop of blood was then placed

onto a glass microscope slide and covered with a 6mm circular slip. The level of the parasitemia was estimated using a modified Herbert scale and Lumsden scale (Herbert et al. 1976). The number of trypanosomes per field were scored using the scale seen in Figure 6.1. This method was employed to monitor parasitemia in both passage and experimental animals.

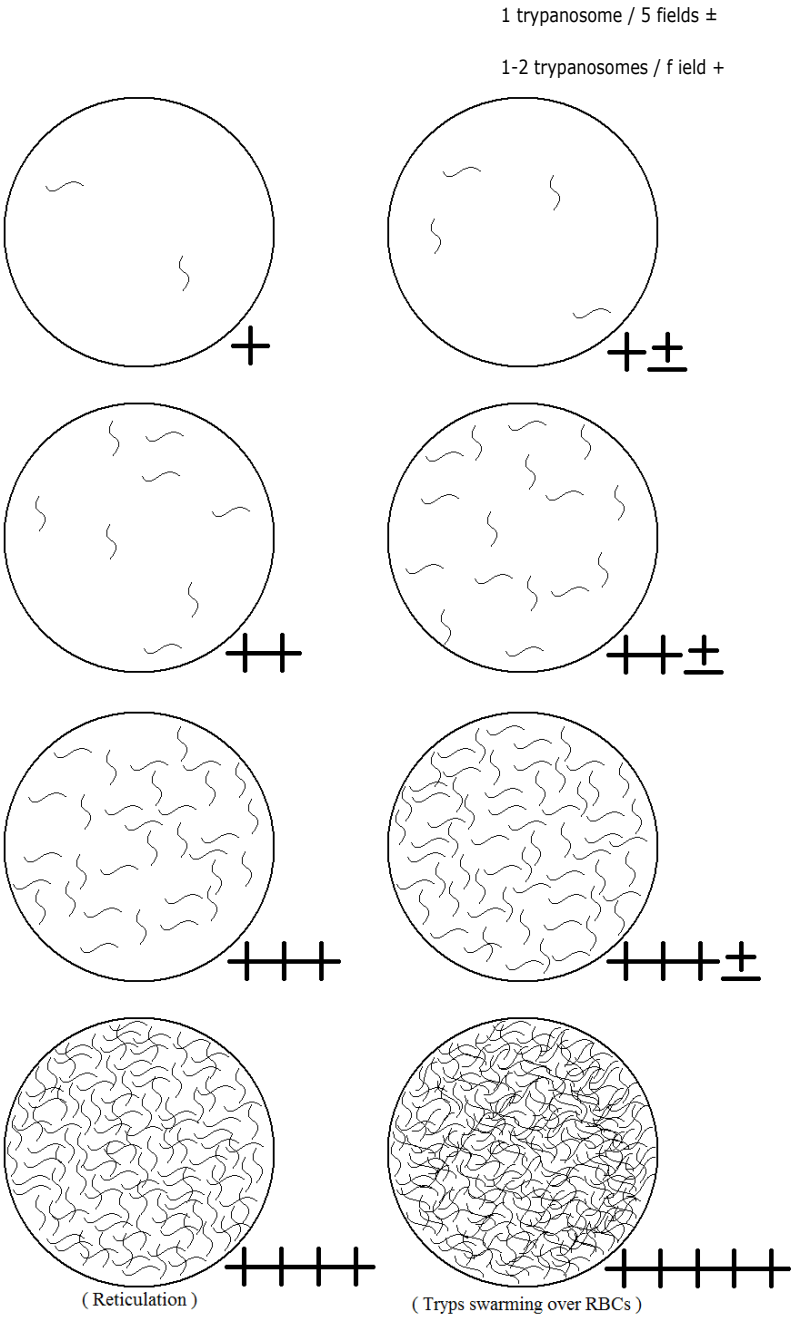

Figure 6.1: Modified Herbert and Lumsden scale

The number of trypanosomes present in a wet blood film under a light microscope was examined. By using a modified Herbert and Lumsden scale, the number of trypanosomes were estimated in each visual field and graded.

6.2.2.2 Infection of Mice

When the first peak of parasitemia was seen in the passage mice, the mouse was culled by overdose of anaesthetic with a neck dislocation to confirm death and blood taken by cardiac puncture. The blood was diluted to 1 - 2 trypanosomes per field with the PBGS solution described above and used to infect the experimental mice. To establish infection 0.1ml of the diluted blood was injected intraperitoneally and the developing parasitemia monitored as described above.

6.2.3 Scanning

6.2.3.1 Animal Preparation for MRI

Animals were anaesthetised using 5% isoflurane in a mixture of 70:30 NO_2:O_2, and then reduced to 1 - 2% isoflurane for maintenance. For injection of the contrast agent, cannulation of the tail vein was performed using a 26 gauge $\times$ 19mm cannula. The animal was placed in a mouse cradle designed for pre-clinical imaging. The animal was restrained using tooth and ear bars with the animal's head placed in the same position for each scan. The respiration rate was measured throughout the experiment, along with the body temperature via a rectal probe. The body temperature was maintained by using a water jacket and the anaesthetic adjusted according to temperature and respiration rate.

6.2.3.2 Scanner and Sequence Setup

Experiments were performed on a horizontal 7T Bruker PharmaScan Avance III system (300 MHz). A Bruker BGA9 imaging gradient insert (300 mT/m) was used to provide linear magnetic field gradient pulses, a 72mm birdcage Radio-Frequency (RF) volume resonator was used to transmit and a 4-channel phase array coil to receive.

A DWASL sequence (developed in Chapter 5) was used throughout the first three studies. The parameters associated with each study are shown in Tables 6.1 and 6.2. Further parameters unique to each study are described in the appropriate section.

For contrast enhanced MRI, a T1-MSME sequence was used with the following parameters: FOV = 25$\times$25mm, TE = 12.28ms, TR = 800ms, slice thickness = 1.5mm, matrix size = 176$\times$176, NA = 16. A single imaging slice in the centre of the brain

was taken. The T1-MSME sequence was performed before the injection of the contrast agent, diethylenetriaminepentaacetic acid (Gd-DPTA Magnevist). A volume of 0.1ml containing 50μL Gd-DPTA Magnevist and 50μL of sterile water via the cannulated tail vein was used. Following a five minute delay, to allow the contrast agent to travel to the brain, the T1-MSME was repeated.

Study	CI (ms)	TI(ms)	TR(ms)	TE(ms)	np	NA	Label slice (mm)
1 (RARE)	5000	50	3000	7.26	20	16	8.5
1 (EPI)	5000	200	7000	18.4	35	10	9
2	5000	500	7000	15.1	20	10	1
3	5000	50	7000	27.33	20	10	10

Table 6.1: Table of parameters for DWASL

The major parameters used in each DWASL study. These are labelling time (CI), delay time (TI), repetition time (TR), echo time (TE), number of pulses (np), number of scan averages (NA), labelling slice thickness (mm).

Study	b-value (s/mm^2)
1 (RARE)	0, 448
1 (EPI)	0, 448
2	0, 12, 18, 41, 73, 165, 292, 458, 659
3	0, 25, 50, 75, 100, 200, 300, 400, 500

Table 6.2: b-values used in each DWASL study

6.2.4 Data Processing of MRI Images

All processing of images was completed using in-house MATLAB (Mathworks, Inc) code. Data were transferred from Paravision to MATLAB via DICOM format. All images were normalised by dividing each image by its respective reco_map_slope value. DWASL images were processed as described previously (Section 5.4.3) and pseudo-permeability maps calculated. No image manipulation was performed.

6.2.4.1 Processing of CE-MRI Images

The percentage signal change seen by the subtraction of the post-contrast and pre-contrast images was calculated using the following equation:

$$\%\ \textit{Signal change} = \frac{\textit{post contrast image} - \textit{pre contrast image}}{\textit{pre contrast image}} \times 100 \qquad (6.1)$$

The mean signal for each brain slice was calculated by selecting the full brain area as the ROI and averaging the signal. Using this information, signal change maps were produced.

6.2.4.2 Statistics

Data were processed using MATLAB (described above) and statistical analysis performed using Minitab 17 (Minitab Inc). Differences between the means of groups of mice were investigated across experiments using the general linear model procedures and the randomised block analysis of variance (ANOVA) and groups compared using Tukey's comparison test. Statistical significance was considered for p-values < 0.05. Log transformations of data were performed where appropriate. Means, standard errors (SE) and 95% confidence intervals (CI) are provided as summary statistics.

Where appropriate, DWASL data were fitted to a bi-exponential model:

$$S = A_1 \, e^{b \cdot D_{cap}} + A_2 \, e^{b \cdot D_{tis}} \tag{6.2}$$

where S represents the signal and b is the b-value. A_1 and A_2 represent weightings. D_{cap} and D_{tis} are the apparent diffusion coefficient of the capillaries and tissue respectively, measured in mm^2/s.

For estimation of pseudo-permeability, two DWASL scans were used, with and without diffusion gradients. For studies two and three, a b-value of b = 74 and 75 s/mm^2 respectively were chosen. This method is based on (St Lawrence, Owen, et al. 2012) where a b-value was chosen that would have minimal effect on the tissue component but suppress the intravascular signal.

6.2.5 Preparation of Brains for Histology

All mice were euthanised using an overdose of anaesthetic at the end of scanning. Brains were removed for histological examination and placed in 4% neutral buffered formalin (NBF). Brains were removed from the NBF and processed to paraffin. Sections (3μm) were cut from the paraffin blocks and mounted on glass microscope slides. The sections were stained using haematoxylin and eosin (H & E) so that the severity of the inflammatory response of the brain could be assessed. All histopathological processes were performed in the University of Glasgow Veterinary Diagnostic Service Histopathology Laboratory. The brain sections stained with H & E were examined using light microscopy at a magnification of 200 fold. To measure the inflammatory response, a neuropathological grading scale was used (Kennedy, Rodgers, et al. 1997). Each brain section was graded by assessing the severity of the meningitis, the occurrence of perivascular cuffing and the degree of inflammatory cell infiltration of the brain parenchyma (Table 6.3).

	0	1	2	3	4
Meningitis	None	Mild	Moderate	Severe	Severe
Perivascular Cuffing	None	None	Mild cuffing of some vessels	Prominent cuffing of some vessels	Prominent cuffing of most vessels
Encephalitis	None	None	None	Moderate	Severe

Table 6.3: Neuropathological grading scale

This table outlines the criteria used to assess the inflammatory response seen in the brain tissue taken from mice used in Section 6.5. A score of 0 showed normal histopathology, with no infiltration of inflammatory cells. Grade 1 represents animals which showed mild meningitis and no perivascular cuffing. Mice with a moderate meningitis and some perivascular cuffing were graded as a 2.

6.3 Study 1: Examining BBB Permeability Changes at the Early Stage of HAT Infection

6.3.1 Methods

Twenty-four female CD-1 mice were randomly assigned to eight separate groups of n = 3 for scanning. Six groups were infected as previously described (Section 6.2.2.2). Two different sequences were used for the DWASL imaging, DWASL-RARE and DWASL-EPI. Scanning parameters are shown (Table 6.1). Additional DWASL-RARE parameters are: effective TE = 36.3ms, RARE factor = 32. Scanning took place on days 8, 10 and 14 post-infection with the two uninfected groups scanned as controls. Two DWASL scans were performed for each mouse, using b = 0 and 448 s/mm^2 plus CE-MRI where possible. CE-MRI parameters are described above (Section 6.2.3.2).

6.3.2 Results

6.3.2.1 DWASL-RARE

Fourteen DWASL data sets were obtained overall from the potential 24 scans in the experiment. It was not always possible to collect CE-MRI data and DWASL data from the same animal.

For the DWASL-RARE sequence, six DWASL scans were obtained and eight CE-MRI scans (Table 6.4).

Day of Infection	DWASL	CE-MRI
Uninfected	× ✓ ×	✓ ✓ ×
8	×× ✓	✓ × ✓
10	✓ ✓ ✓	✓ ✓ ✓
14	✓ ××	✓ ××

Table 6.4: Scans performed in Study 1 using DWASL-RARE

The number of scans performed using DWASL-RARE and CE-MRI in the first study. Successful scans are denoted ✓. In some instances scans could not be completed or the data were unsuitable for analysis (×).

Two scans were performed for each mouse, with b = 0 and 448 s/mm^2. The mean drop in the ΔM signal, calculated using a full brain ROI for all DWASL-RARE data sets, was 36 $\pm$ 11 % (Figure 6.2). Comparison of the mean signal change at each point of infection showed no significant change ($p > 0.05$). A full brain ROI was used for comparison due to the low mean signal seen in all images. Unfortunately no further comparison could be made due to the low number of data sets acquired.

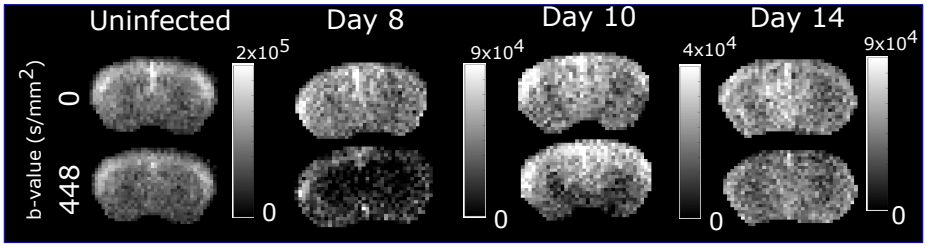

Figure 6.2: DWASL images for n=2 mice

Two images are shown for each mouse, with b = 0 and 448 s/mm^2 to suppress signal. A 12% and a 20% reduction in signal was measured between the two b-values at the uninfected time point and day 14 respectively.

To assess BBB function, the ratio between the images produced using b = 0 and 448 s/mm^2 was calculated and used to produce pseudo-permeability maps (Figure 6.3). The maps show no changes in pseudo-permeability between the time points of infection. The values of permeability found at each time point are detailed in Table 6.5. Only one data set was able to be obtained for the uninfected, day 8 and day 14 post-infection groups. There was a large variance in the data with pseudo-permeability values ranging from 0.31 to 0.91. No conclusions on permeability could be drawn from this experiment due to the small sample size of data and the large variation seen between pseudo-permeability values.

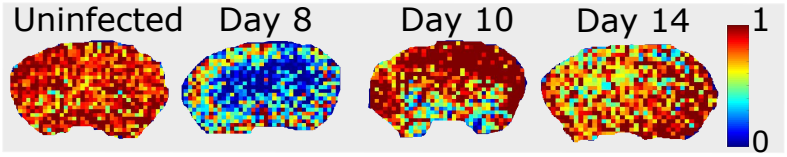

Figure 6.3: Pseudo-permeability maps for Study 1 using DWASL-RARE

Pseudo-permeability maps were produced and averaged over the whole brain with values of permeability as 0.91 and 0.86 respectively for day zero and day fourteen post-infection.

Day of Infection	Pseudo-permeability		
Uninfected	×	0.91	×
8	×	×	0.34
10	0.69	0.89	0.31
14	0.86	×	×

Table 6.5: Pseudo-permeability values using DWASL-RARE

To confirm if changes in the BBB function could be seen with a contrast agent, CE-MRI was performed at each time point and a signal change map produced for each CE-MRI data set (Figure 6.4). The sequence used a single slice for imaging.

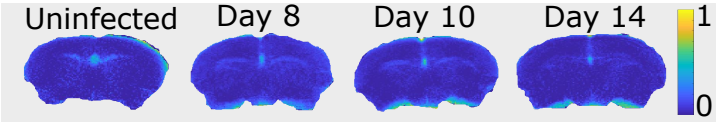

Figure 6.4: Signal enhancement maps produced for Study 1

CE-MRI data showed a signal change of 5.9 %, 6.6 %, 11.6 % and 5.2 % for the uninfected time point, day 8, 10 and 14 respectively. No significant changes were seen between the mean signal measure at each infection time point ($p > 0.05$).

CE-MRI data were collected at all time points (Table 6.6). A single data set was able to be collected at day fourteen but the low signal change (5.2 %), suggests a failure of the contrast agent to enter the blood stream. Although an increase in mean signal enhancement over the whole brain was seen from the different time points, no significant difference ($p > 0.05$) was found. The mean percentage change seen at these time points reflects values seen in previous literature.

Day of Infection	% Change of signal			Mean % change
Uninfected	6.7	5.2	×	5.9
8	7.8	×	5.4	6.6
10	15.7	7.4	12.6	11.9
14	5.2	×	×	5.2*

Table 6.6: CE-MRI data for Study 1 examining DWASL-RARE

Table of % signal change values for the CE-MRI data. No changes were seen between the mean value at each infection time point ($p > 0.05$). A * indicates that the contrast agent may not have fully entered the brain.

6.3.2.2 DWASL-EPI

The second experiment in this study was to repeat the first experiment using a DWASL-EPI sequence. The DWASL-EPI scans obtained in the first study were seven out of a potential twelve scans. The number of CE-MRI scans that were successful were five (Table 6.7).

Day of Infection	DWASL	CE-MRI
Uninfected	✓ ✓ ✓	✓ × ×
8	× ✓ ✓	× × ✓
10	✓ × ✓	× × ✓
15	× × ×	✓ ✓ ×

Table 6.7: Scans performed in Study 1 using DWASL-EPI

The number of scans obtained using DWASL-EPI and CE-MRI in the first study. Three data sets were unusable for analysis (one at day 10 and two at day 15 post-infection).

Images obtained using DWASL-EPI had a substantially higher overall SNR compared to DWASL-RARE, for approximately the same scan duration. For b = 0 s/mm^2, the SNR for DWASL-EPI was 9 ± 0.8. Regions including the cerebral cortex, hippocampus and external capsule are distinguishable in the images that previously were not for DWASL-RARE (Figure 6.5). The mean drop in signal using the whole data set at b = 0 and 448 s/mm^2 was 34 ± 7 %.

To examine any qualitative changes in BBB function, the two DWASL-EPI images for each mouse were used to create pseudo-permeability maps (Figure 6.6). The mean pseudo-permeability values for the whole brain at each infection point are shown in Table 6.8. The variability of the permeability values was less for DWASL-EPI than

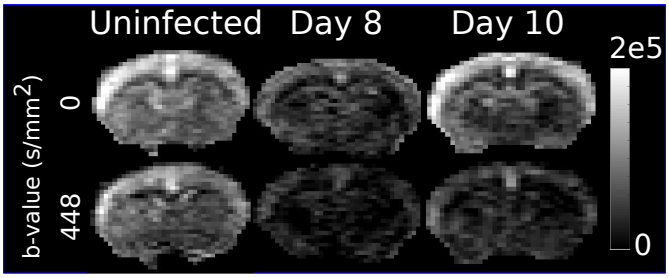

Figure 6.5: DWASL-EPI images from Study 1

b-values of 0 and 448 s/mm^2 were used to suppress signal from the capillaries. DWASL-EPI scans from an uninfected, day 8 and 10 post-infection mouse are shown. A drop in signal of 34 $\pm$ 7 % over the whole brain was seen for the scans using b = 448 s/mm^2.

for DWASL-RARE. Comparison of the groups found no significance between any of the study time points ($p > 0.05$).

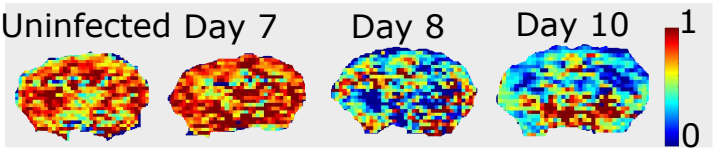

Figure 6.6: Pseudo-permeability maps for Study 1 using DWASL-EPI

Pseudo-permeability maps were produced using DWASL-EPI data with b = 0 and 448 s/mm^2. The mean permeability values over the full brain were 0.68 $\pm$ 0.09, 0.75 $\pm$ 0.09 and 0.69 $\pm$ 0.2 for uninfected, day 8 and 10 post-infection respectively.

Day of Infection	Pseudo-permeability			Mean
Uninfected	0.75	0.78	0.51	0.68 $\pm$ 0.09
8	-	0.83	0.66	0.75 $\pm$ 0.09
10	0.46	-	0.91	0.69 $\pm$ 0.2

Table 6.8: Pseudo-permeability values found for DWASL-EPI scans performed in Study One

No significant difference was seen between the pseudo-permeability values measured in this study. The range of values seen compared to the values obtained from DWASL-RARE was smaller.

The contrast maps produced using the CE-MRI data sets showed no significant changes between any of the groups ($p > 0.05$). Only one usable data set was able to be obtained for the control group, day 8 and day 10 post-infection. Two data sets were obtained for day 15 post-infection (Table 6.9). The signal change values were similar to the values for the first part of the study. No real comparison could be made between the time points from the limited data, with no significant difference seen between them (Figure 6.7).

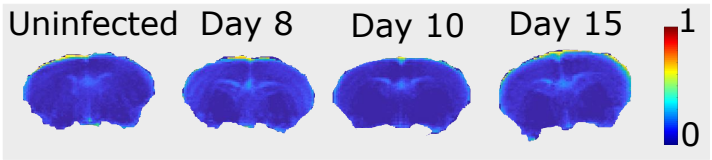

Figure 6.7: CE-MRI images produced for comparison with DWASL-EPI

Signal enhancement maps produced from CE-MRI data taken during the DWASL-EPI study. There is no significant change in overall signal between the days of infection.

Day of Infection	% Change of signal			Mean % change
Uninfected	8.8	-	-	8.8
8	-	-	9.6	9.6
10	-	-	6	6
15	10.2	11.7	-	11 ± 0.8

Table 6.9: Values of percentage signal change in the brain using CE-MRI

6.3.3 Discussion

This was the first study to attempt to measure changes in water permeability in trypanosome infected mice using DWASL. Multiple time points were chosen in the early stage of the infection, to try and detect changes in the brain that could not be detected using the standard CE-MRI. These earlier time points were chosen due to the mice becoming sicker in the later stages of the disease. The study was also used to compare the DWASL-RARE and DWASL-EPI sequences and was conducted at the beginning of the research project before the experiments in Chapters 4 and 5.

By using a DWASL-RARE sequence, it was possible to avoid the typical ghosting artefacts associated with an EPI sequence. This study therefore examined whether a DWASL-RARE sequence was suitable for imaging. The DWASL-RARE images had a poor SNR and low signal. Low resolution images with no anatomical detail was seen in both DWASL-RARE images, suggesting the data were of overall poor quality. A low b-value was required to suppress the signal from the arterial blood water in the capillaries. For this pilot study, a gradient value of 20 % was chosen as it suppressed all the intravascular signal and only gave signal from the tissue. Post-experimental analysis gave b = 448 s/mm^2 but previous studies have shown a reduction in arterial component using b-values of less than 50 s/mm^2, suggesting that using such a large b-value is not recommended.

The mean signal and pseudo-permeability values were calculated for a full brain ROI, with no smaller ROIs able to be examined. This was due to the lack of detail in the images and the low SNR. The data demonstrated that high quality DWASL images could not be achieved and suggested that a RARE readout module was not suitable for DWASL imaging.

A second experiment was performed using an EPI readout instead of a RARE readout. Although the use of EPI typically introduces artefacts into the images the SNR from the subtracted DWASL images was higher for both sets of images acquired. The DWASL images were of a higher quality than those obtained with DWASL-RARE with regions such as the cortex identifiable. Overall, there was no significant issue with ghosting in the DWASL images.

Pseudo-permeability values from DWASL-RARE had a large range, suggesting the

sequence was not functioning correctly. The standard deviation in the permeability values for DWASL-EPI was reduced compared to the RARE sequence, although there was no statistical changes seen overall between the different points of infection. These findings suggest that BBB permeability to water may not be altered at this stage in the infection, or that any changes present are below the detection level of the DWASL sequence.

Contrast enhanced data for both studies at each time point showed no BBB leakage, and no significant enhancement of signal was seen at any stage of the disease. Rodgers et al. reported a significant change at day 14 post-infection (Rodgers, Bradley, et al. 2017), but not at day 7 post-infection. The limited number of successful scans at day 14 and 15 post-infection meant no comparison could take place, but the data obtained at earlier time points further confirmed that no BBB breakdown could be seen at a time point previous to day 14 post-infection.

This study was designed as a qualitative pilot study to examine whether DWASL would be able to pick up changes in BBB permeability. The study focused on the early stage of the trypanosome infection in mice. No image detail could be seen using DWASL-RARE with the DWASL sequence being of higher quality. The combination of no significant changes seen in either the pseudo-permeability maps and CE-MRI contrast maps, meant a further study was conducted to examine the permeability of the barrier in the later stages of the disease. The permeability of the BBB has not been previously explored in HAT, so this was a novel use of DWASL with no previous comparison. The large variation of pseudo-permeability values and limited data sets suggested a further developed DWASL sequence was needed to be more sensitive to any changes that may occur in the permeability of the BBB in HAT at early stages. It was decided to continue using the EPI readout as it produced better DWASL images than the RARE readout for the rest of the research throughout this thesis.

6.4 Study 2: Examining Permeability Changes in the HAT Brain using a Serial Study

6.4.1 Methods

Eight female CD-1 mice were randomly assigned to two cages and infected as outlined above (Section 6.2.2.2). Each mouse was scanned before infection and then on days 7, 9, 11 and 14 post-infection. A final scan point was scheduled at day 18 post-infection, however, this was prevented by an unexpected closure of the MRI centre. A DWASL single shot EPI sequence was used. Scanning parameters are shown (Table 6.1). Additional parameters are matrix = 64×64, FOV = 25×25mm. Contrast enhanced MRI was performed as above (Section 6.2.3.2).

6.4.2 Results

For scanning, the DWASL sequence incorporated the interleaving modification introduced in Section 5.3.2.3, with a range of b-values from b = 0 to 500 s/mm^2. These values were chosen based on the strength of the diffusion gradients, rather than the b-value. DWASL data sets were obtained at all time points for five mice, and partial data sets were acquired for the remaining three mice (Table 6.10). A progressive drop in the signal over the whole brain was seen qualitatively as the b-value increased by raising the gradient strength (Figure 6.8).

Day of Infection	DWASL
Uninfected	✓ ✓ ✓ ✓ ✓ ✓ ✓ ✓
7	✓ ✓ ✓ ✓ ✓ ✓ ✓ ✓
9	× ✓ × ✓ ✓ ✓ ✓ ✓
11	× ✓ ✓ ✓ ✓ ✓ ✓ ✓
14	× ✓ ✓ ✓ ✓ ✓ ✓ ×

Table 6.10: Scans performed in Study 2

The number of data sets obtained in Study 2 using a single group of mice n = 8. Successful scans are denoted ✓ and unsuccessful scans (×). No usable CE-MRI data were obtained.

Due to the higher quality of the images obtained, smaller ROIs were able to be used for analysis. ROIs were selected to include the full brain region as before and the cerebral cortex (Figure 6.9).

For each data set, the mean signal was calculated for both ROIs and the data plotted on a log-linear scale to examine the signal change for multiple b-values. The data were fitted to the bi-exponential model (Equation 6.2). The coefficients A_1

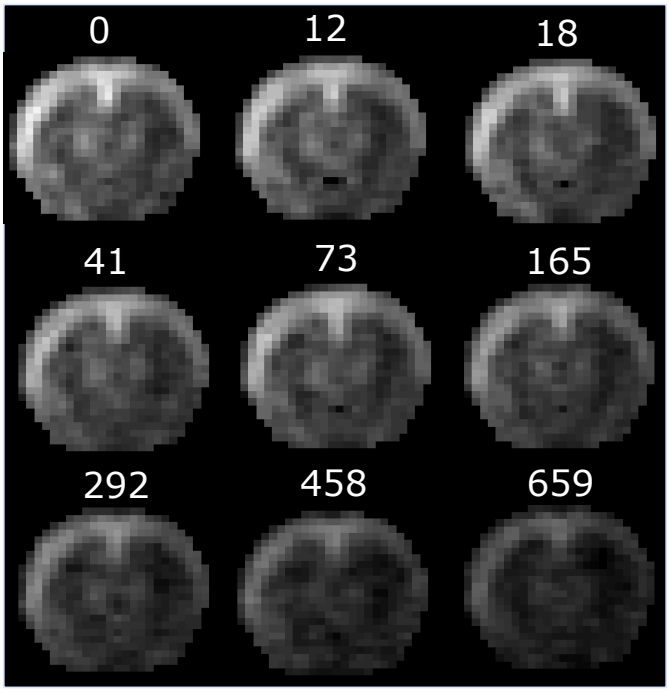

Figure 6.8: DWASL images for one mouse in Study 2

For one mouse, all ΔM images are shown. The image colour scale is set from $0 - 2x10^5$ for all images. The b-values in units s/mm^2 are shown above each image. As the b-value increases, the signal intensity decreases.

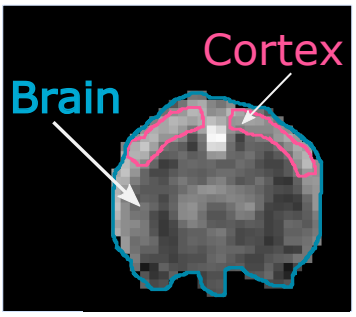

Figure 6.9: Regions of interest used for DWASL images

The regions of interest used for the study are shown in this image. The full brain region is shown in blue while the cortex is outlined in pink.

and A_2 represent the proportion of signal in the intravascular (IV) and extravascular (EV) compartments respectively. The mean ADC was calculated for the arterial blood water (IV) and tissue water (EV) compartments. The DWASL signal plot for one mouse, at the five MRI time points, is shown in Figure 6.10. Data were plotted from b = 0 - 200 s/mm^2 to examine any changes observed at low b-values. The signal attenuation matched what had been seen previously in the development of the DWASL sequence (Section 5.4.3). Similar results were seen across all mice and all infection time points. To examine if there were significant differences between the groups, the A_1 coefficient was compared as an estimation of how much labelled water has exchanged.

No changes were seen between the DWASL signal for an individual mouse. The individual data also appeared noisy. To examine if any changes could be seen

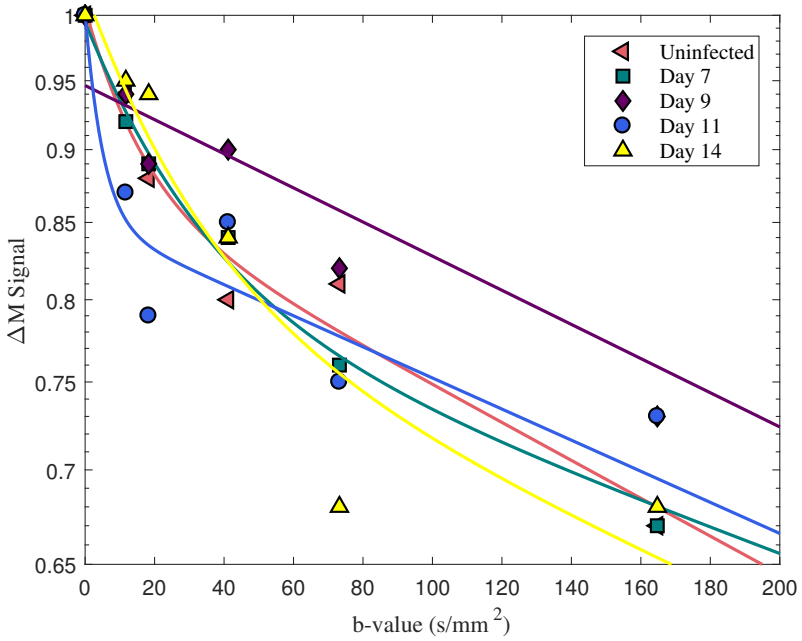

Figure 6.10: DWASL signal decay for Study 2 for a single mouse

DWASL data sets obtained at multiple time points from one mouse, were fitted to a bi-exponential model and plotted using a log-linear scale. At each stage in the infection, the data shows a fast drop in signal at low b-values before a slow decay at high b-values. This figure demonstrates the signal obtained from the IV compartment followed by the EV compartment.

in the group, the signal was averaged over each time point and the mean signal examined. There were no statistical changes seen between the mean data at each infection time point.

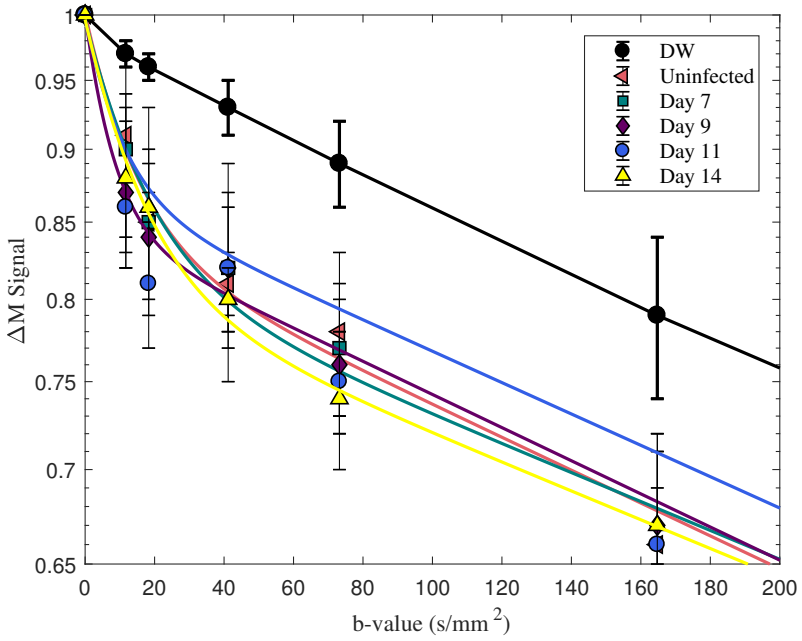

Figure 6.11: Overall signal from Study 2 using DWASL

The mean signal over all mice at each time point was normalised and fitted to the bi-exponential model. The signals are plotted on a log-linear scale. Error bars are the standard error. The mean signal from the control images of the non-infected mice is plotted as a comparison. n = 6-8 dependent on the infection time point.

For the mean signal at each time point, the data were fitted to the bi-exponential model and the values for the IV coefficient at each time point compared. The value ADC_{tis} value corresponds to values available in the literature (Ohene et al.

2019). All values obtained from the bi-exponential fitting for each infection point are displayed in Table 6.11. Between the groups, no significance was seen for the IV compartment coefficient (A_1) or the EV coefficient (A_2) ($p > 0.05$). However, comparison of ADC_{cap} and ADC_{tis} shows that the ADC_{tis} is significant lower ($p < 0.05$) than the value for ADC_{cap}. A comparison of the signal at each time point can be seen in Figure 6.11, along with the mean signal from the brain tissue for the uninfected group.

Day of Infection	A_1	ADC_{cap} $\times 10^{-2}$ (mm^2/s)	A_2	ADC_{tis} $\times 10^{-4}$ (mm^2/s)	n
Uninfected	0.163	6.82	0.84	12.9	8
7	0.18	5.57	0.82	11.3	8
9	0.15	12.1	0.85	13	6
11	0.12	9.3	0.87	12.3	7
14	0.19	5.78	0.806	11.27	6

Table 6.11: Fitting coefficients for DWASL in Study 2

Coefficients from fitting the mean normalised signal at each time point of infection to a bi-exponential model. No significant differences ($p>0.05$) were seen between the values at the multiple time points. The number of scans used for each fitting is represented by 'n'. ADC values are measured in mm^2/s.

To measure the value of pseudo-permeability for each mouse, a b-value of 0 and 74 s/mm^2 was used. Pseudo-permeability maps (Figure 6.12) showed no changes in permeability of the BBB as the infection progressed to day 14 post-infection. When the data from each group were compared (using the GLM), no significant differences were found between any of the groups ($p> 0.05$).

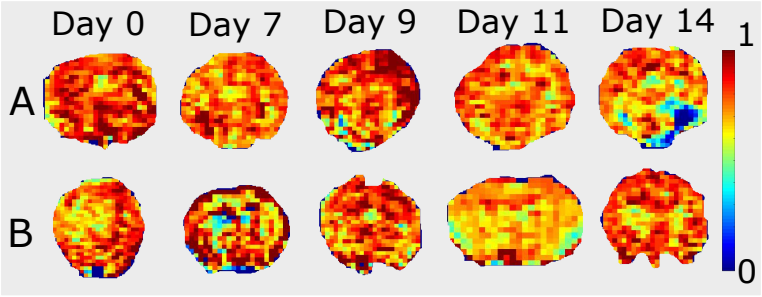

Figure 6.12: Permeability maps for Study 2

Pseudo-permeability maps constructed following DWASL scans, produced using the ratio of signal b = 0 & 75s/mm^2 at each infection time point (uninfected, day 7, 9, 11, 14 post-infection). Two sets of maps are shown for the full experiment (mouse A and mouse B). No overt changes in permeability were seen between the infection points.

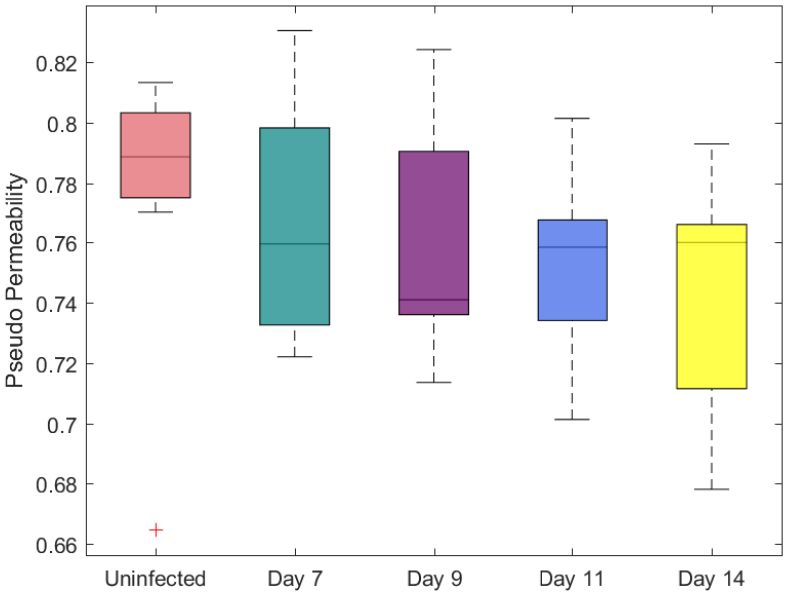

Figure 6.13: Comparison of DWASL permeability values for Study 2

The comparison of mean pseudo-permeability value for each infection time point showed no significant difference between any of the values ($p > 0.05$). Comparison is made using a box plot with the mean, 25% and 75% quartiles, and maximum and minimum values shown.

6.4.3 Discussion

To determine whether changes in water permeability in the brain could be detected using the DWASL sequence at later stages in the trypanosome infection, a second study was designed to include a time point of day 18 post-infection along with multiple earlier stage time points. Based on the literature, the breakdown of the BBB occurs around day 14 post-infection and beyond. By including a time point of day 18 post-infection, this would give DWASL data from the later stages of infection when a change in BBB permeability could be detected with CE-MRI. Rodgers et al. reported a significant change of 15.2% for day 14 post-infection signal enhancement maps, compared to 7.1% for the uninfected mice. A significant rise to 24% at day 21 post-infection further suggested that DWASL data should show changes in the permeability of the BBB at day 18 post-infection. Enhancement was seen in multiple brain regions, indicating that the use of a more specific ROI may be appropriate. The cortex was therefore examined individually as well as looking at overall brain changes. Unfortunately, data from the later time point could not be collected due to not being able to access the scanner. This meant only data up to day 14 post-infection was available for analysis.

Improvements to the DWASL sequence resulted in higher quality DWASL images with the study designed to include images at multiple b-values. The study was designed to look at how the signal changes with an increasing b-value, and values were chosen based on an increasing gradient strength. This method has been shown by Wang previously (Wang, Fernandez-Seara, et al. 2007), with changes in the plotted data observed by changing the inversion time. The data obtained in Study 2 demonstrated a fast drop in the signal from the low b-values. This indicated the signal from the fast flowing labelled arterial blood in the intravascular compartment had been attenuated. The signal decay then followed that of tissue, which was comparable to the signal of the control image. DWASL has been applied by Tiwari et al. (Tiwari et al. 2017) in rats, however only one b-value was used along with different parameters make comparing coefficients unsuitable. Silva et al. has shown this curve pre-clinically in rats (Silva et al. 1997) demonstrating a difference in fitting coefficients for rats under normocapneic and hypercapneic conditions. Our results compared favourable to the A_1 fitting coefficient found by Silva. Furthermore, the shape of decay in this research is the same as Silva and other clinical DWASL papers (Wang, Fernandez-Seara, et al. 2007; Shao et al. 2019).

The trypanosome infection produces different levels of disease severity in mice. This was observed in the varying parasitemia levels when animals were monitored for infection. To further explore changes in barrier impairment, the mice in this study were serially scanned to follow any changes. Looking at each individual animal, results did not show any significant changes as hoped, in either the per-

meability maps or the plot of different b-values. More variation was seen in the individual results, showing DWASL was not sensitive enough to examine data from a single animal.

No changes were seen in the plots between the infection time points compared to the uninfected time point. This suggests that either there was no detectable change in the BBB permeability or the sequence was not sensitive enough to identify changes. As the water content of the brain in HAT infected mice had not been examined previously, it is difficult to compare the results to literature. It was clear that a later stage time point was needed where significant barrier impairment had previously been identified using CE-MRI to further explore the application of DWASL to detect BBB impairment.

6.5 Study 3: Examining BBB Changes Throughout the Infection

6.5.1 Methods

Thirty-eight female CD-1 mice were used for the study. Experimental days were set at days 7, 14, 21 and 28 post-infection plus an uninfected control group. Mice were split into groups of n = 6 for the uninfected, day 7 and day 14 post-infection groups and n = 8 for day 21 and day 28 post-infection. A DWASL sequence was used to image mice at each time point with matrix = 96×96, FOV = 2.5×2.5cm. Additional parameters are outline in Table 6.1. The b-values chosen were based on values used in the literature (Wang, Fernandez-Seara, et al. 2007). Ten sets of DWASL images were collected for each mouse. CE-MRI was performed as previously described (Section 6.2.3.2) with n = 3 mice at each time point.

6.5.2 Results

The DWASL and CE-MRI data sets acquired at each time point are detailed in Table 6.12. A set of CE-MRI scans (n = 3 at each time point) was collected. One DWASL data set was not acquired at day 21 post-infection due to time constraints associated with use of the MRI system.

Day of Infection	DWASL	CE-MRI
Uninfected	✓ ✓ ✓ ✓ ✓ ✓	✓ ✓ × × ✓ ×
7	✓ ✓ ✓ ✓ ✓ ✓	✓ ✓ ✓ × × ×
14	✓ ✓ ✓ ✓ ✓ ✓	× ✓ ✓ × ✓ ×
21	✓ ✓ ✓ ✓ ✓ -	✓ ✓ ✓ × × -
28	✓ ✓ ✓ ✓ ✓ ✓	✓ ✓ ✓ × × ×

Table 6.12: Data sets from Study 3 collected using DWASL and CE-MRI

Only three CE-MRI scans were performed at each time point with ✓ indicating which animals were employed for CE-MRI

For each data set, ROIs were selected in the cerebral cortex and full brain regions as used in the previous study (Figure 6.9). The mean signal from the cortex region was plotted for all b-values (Figure 6.14a). Each data set was fitted to a bi-exponential model and coefficients obtained (Table 6.13). The proportion of signal in the intravascular (IV) and extravascular (EV) compartments were assessed together with the diffusion values for both compartments. Although the fitted data displayed changes in the signal decay for the signal from the days 21 and 28 post-infection compared to to the earlier time points, no significance was seen between the groups for coefficients A_1 and A_2 ($p > 0.05$). For data at the uninfected time

point and day 28 post-infection, p = 0.27 for A_1 and p = 0.3 for A_2 respectively. Significance was seen for comparison of the mean values of ADC_{cap} and ADC_{tis} found from fitting ($p < 0.0001$).

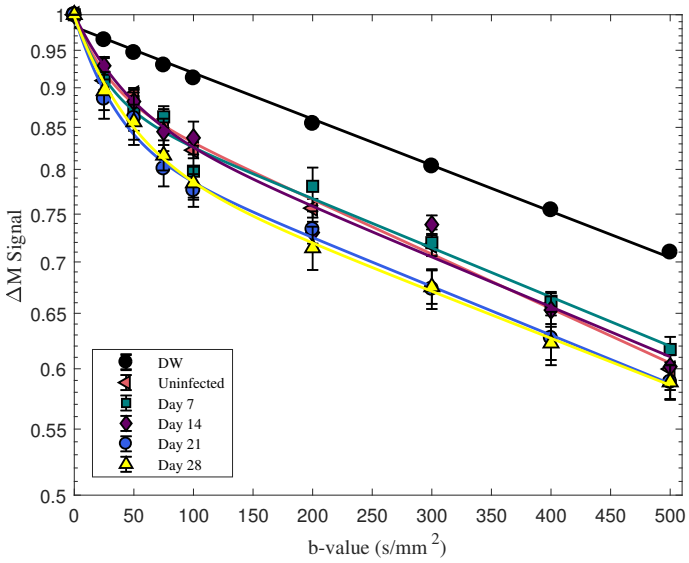

(a) Signal ranging from b = 0 - 500 s/mm^2

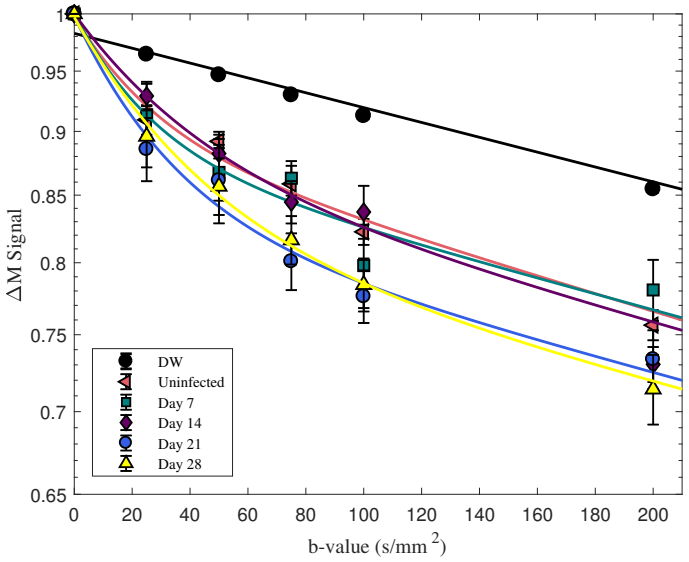

(b) Signal ranging from b = 0 - 200 s/mm^2

Figure 6.14: Full comparison of the DWASL signal for all points of infection at multiple b-values

A comparison of DWASL signal at all dates of infection, with the signal from the control image (diffusion weighted image, DW) plotted for further comparison. The ROI was taken from the cortex region and the signal from the control image of an uninfected scan is shown as a comparison. The fast and slow separation of signal can be seen at all time points but no significant difference ($p > 0.05$) was seen between the infection points. Figure a) shows all b-values where the comparison of signal from the tissue can be easily seen. Figure b) shows the b-values from b = 0 - 200 s/mm^2. There is overlap between all the plots. A log-linear scale is used in both graphs with error bars representing the standard error.

The two b-values used for producing pseudo-permeability maps were b = 0 and 75 s/mm^2. The permeability maps are shown along with the corresponding DWASL image in Figure 6.15. The mean signal magnitude for the DWASL images has increased for these images compared to the previous studies. The pseudo-permeability maps do not show any qualitative changes between the different stages of infection. Permeability values are shown for the cortex region. A mean permeability of 0.73 was observed for the uninfected group with a value of 0.71 for day 28 post-infection.

Day of Infection	A_1	ADC_{cap} $\times 10^{-2}$ (mm^2/s)	A_2	ADC_{tis} $\times 10^{-4}$ (mm^2/s)
Uninfected	0.101	3.5	0.9	7.9
7	0.12	3.8	0.88	7.1
14	0.13	2.4	0.88	7.2
21	0.16	3.0	0.83	7.0
28	0.18	2.3	0.82	6.8

Table 6.13: Fitting coefficients from Study 3

Coefficients from fitting the mean normalised signal at each time point of infection to a bi-exponential model. An change in the ratio of IV to EV signal is seen as the disease progresses.

All values are in Table 6.14. No statistical difference ($p > 0.05$) were detected between the values from each infection time point.

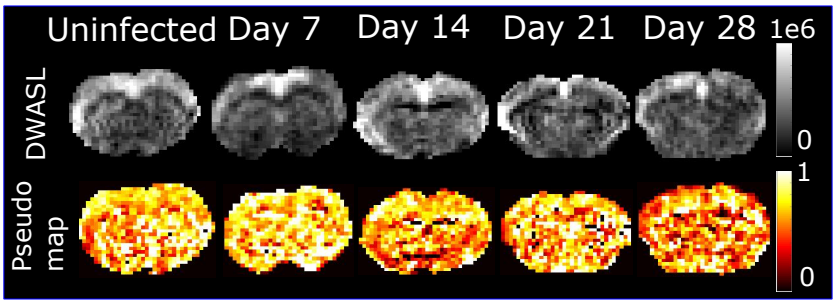

Figure 6.15: DWASL images and pseduo-permeability maps from Study 3

DWASL images and pseudo-permeability maps produced using b = 0 and 75 s/mm^2 for each infection time point. High quality DWASL images are observed at each time point, but qualitatively no changes are detected between either the DWASL images or the pseudo-permeability maps.

Day of Infection	Pseudo-permeability
Uninfected	0.73 ± 0.03
7	0.72 ± 0.04
14	0.70 ± 0.05
21	0.69 ± 0.06
28	0.71 ± 0.08

Table 6.14: Pseudo-permeability values from Study 3

Values for mean pseudo-permeability at each infection time point for the full brain. No statistical difference ($p>0.05$) were observed between values.

6.5.2.1 CBF Results

Values for CBF were calculated using the method outlined in Chapter 4. The average CBF value for the full brain and cortex are displayed below (Table 6.15). The mean CBF values at each infection point were within the values previously stated in the literature (Baskerville et al. 2012; Duhamel et al. 2012). A significant difference ($p < 0.05$) was seen between Day 28 and Days 7, 14 and 21 ($p = 0.008$, $p = 0.002$ and $p = 0.032$ respectively) in the full brain ROI. The same significant difference was seen in the cortex region ($p = 0.01$, $p = 0.002$ and $p = 0.019$ respectively). The average CBF value for the uninfected group was 144 ± 11 ml/100g/min. This value was not significantly different to any other time point. The range of CBF values was 75 to 328 ml/100g/min.

Day of Infection	CBF (Full Brain)	CBF (Cortex)
Uninfected	144 ± 11	160 ± 13
7	125 ± 2	143 ± 3
14	112 ± 12	126 ± 11
21	134 ± 18	145 ± 21
28	204 ± 24	227 ± 27

Table 6.15: CBF values for mice in Study 3

The CBF values found using the mbASL sequence. Significant ($p < 0.05$) differences were found between the values at day 28 and day 7, 14 and 21. There was no significant difference between the uninfected and day 28 values of CBF. CBF values are displayed in the units ml/100g/min. The standard error is shown with the mean value.

6.5.2.2 CE-MRI Results

CE-MRI scans were collected at each time point (n = 3) to give n = 15 for the full study. Percentage signal change (% SC) maps were produced for each image set with the signal averaged over a full brain ROI. Figure 6.16 demonstrates maps for each stage of infection. Signal enhancement can be seen for the later stage of HAT, where higher levels of contrast agent were present. Day 21 (% SC = 25 ± 9 %) and 28 (% SC = 19 ± 7 %) post-infection show a significant ($p < 0.05$) change in signal compared to the earlier time points. No significant change was seen in the % SC for the uninfected group (% SC = 7 ± 3 %), day 7 (% SC = 7 ± 3 %) and day 14 (% SC = 12 ± 8 %) post-infection as shown in previous studies.

Figure 6.17 demonstrates the mean % SC seen at each time point with significance ($p<0.05$), denoted by $*$. The highest percentage change was detected at day 21 post-infection.

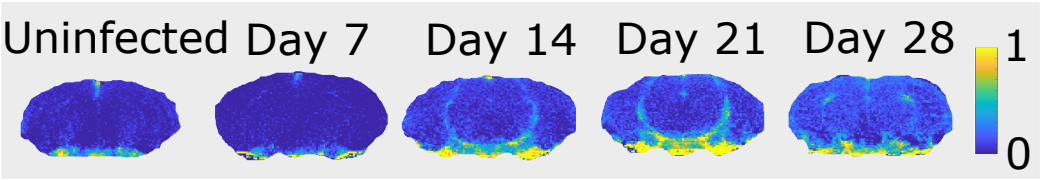

Figure 6.16: Contrast enhanced MRI images for Study 3

CE-MRI images for each infection time point. Evidence of the contrast agent crossing the BBB is seen from day 14 on wards, shown by an increase in signal enhancement. Images are scaled between 1 and 0 which represents the signal enhancement.

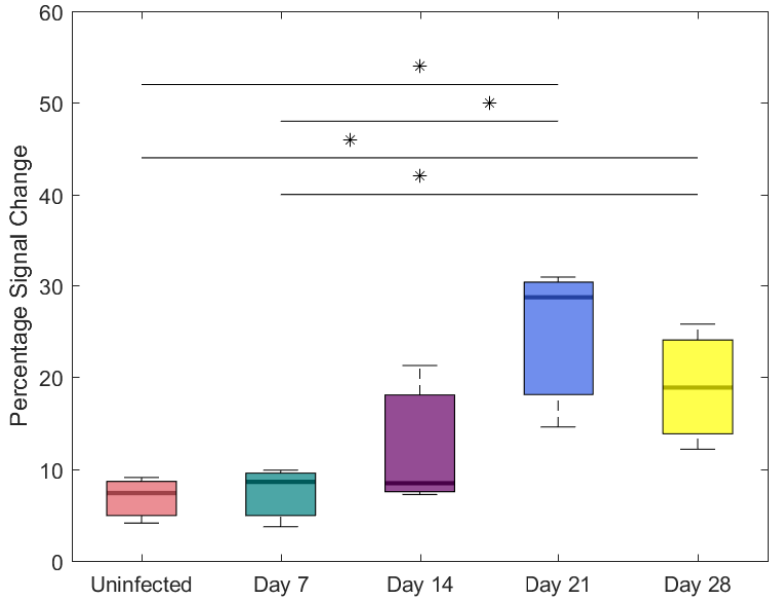

Figure 6.17: Box plot of contrast enhanced MRI

Using CE-MRI and a full brain ROI, the mean signal for n = 3 mice demonstrates a significant difference in % signal enhancement for late stage HAT compared to early stage HAT and uninfected mice, with significant differences ($p < 0.05$) between the groups denoted by $*$. The mean, 25% and 75% quartiles, and maximum and minimum values are shown.

6.5.2.3 Neuropathological Reaction

The inflammatory reaction of the infected brains at each time point was scored using the neuropathological grading score (Table 6.3). The mean reaction score for each time point is outlined in Table 6.16. Every group of infected animals had a score significantly different to the uninfected group ($p<0.05$). Figure 6.18 displays H & E stains for a non-infected mouse (A and B), a mouse at day 14 post-infection (C and D) and at day 28 post-infection (E and F). At day 14 post-infection, the disease was progressing with a mild meningitis seen. A further significant ($p<0.001$) increase in the severity of the neuroinflammatory reaction was seen between day 14 and day 28 post-infection. At this late stage of the disease, there was moderate inflammatory cell infiltration in the meninges with an increase in the number of cells around the vessels (Figure 6.18F). Perivascular cuffing was seen around the vessels in the hippocampus (Figure 6.18E).

	Uninfected	Day 7	Day 14	Day 21	Day 28
Day 7	p = 0.002 (0.155, 0.845)				
Day 14	$p < 0.001$ (0.238, 0.928)	p = 0.953 (-0.262, 0.428)			
Day 21	$p < 0.001$ (1.668, 2.332)	$p < 0.001$ (1.168, 1.832)	$p < 0.001$ (1.084, 1.749)		
Day 28	$p < 0.001$ (1.405, 2.095)	$p < 0.001$ (0.905, 1.595)	$p < 0.001$ (0.822, 1.512)	p = 0.211 (-0.582, 0.082)	
Mean $\pm$ SE	0 ± 0	0.5 ± 0	0.58 ± 0.08	2 ± 0	1.75 ± 0.171

Table 6.16: Neuropathology score of the brain for Study 3

Comparison of the neuropathology reaction from each time point of infection. No significant difference was seen between day 7 and 14 post-infection, or day 21 and 28 post-infection. The mean score at each time point is shown and the standard error. 95 % confidence intervals are noted under each p-value. For uninfected, day 7, 14 and 28 n = 6 animals were used. For day 21 post-infection, n = 7.

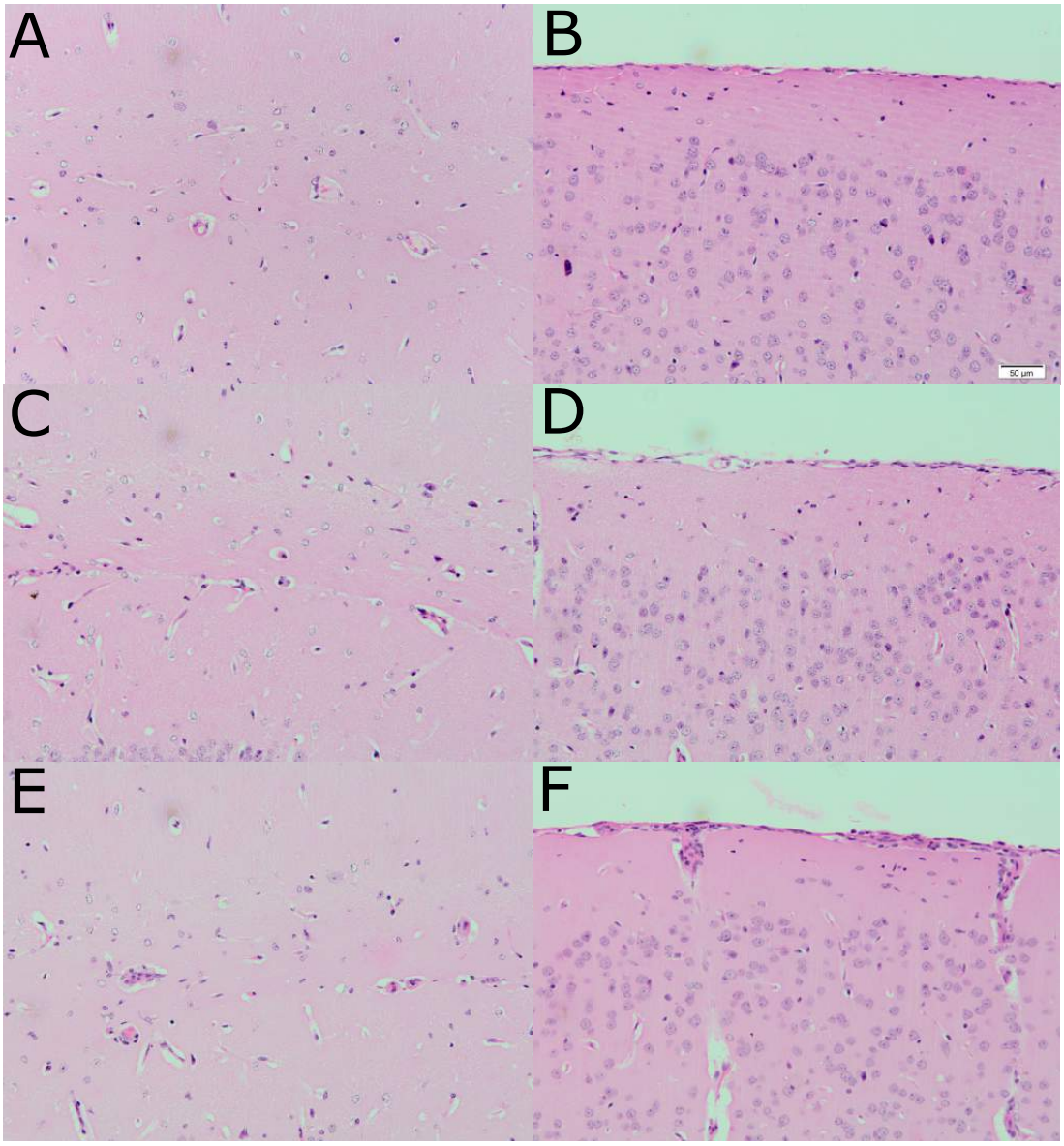

Figure 6.18: H & E staining of brain slices for Study 3

Histology slices of the hippocampus and cerebral cortex are shown for an uninfected mouse (A and B), a day 14 post-infection mouse (C and D) and a day 28 post-infection (E and F). At day 14 post-infection a slight meningitis is seen with cell infiltration in the cerebral cortex. At day 28 post-infection, a high cell infiltration is seen with perivascular cuffing around the vessels.

6.5.3 Discussion

This study was used to examine changes in permeability of the BBB during the early and late stages of the HAT infection. MRI scans were performed before infection, early stage and late stage points of the infection. Significant changes in the signal intensity of the contrast enhanced images were seen at days 21 and 28 post-infection, which was in the late stage classification of the disease. Changes were observed in the coefficients from the bi-exponential model fitting at days 21 and 28 post-infection. Although no statistical significance was seen between the groups at each stage, an increase in the value of the IV fitting coefficient suggested a drop in the exchange of water across the BBB. This does not fit with the expected hypothesis that the exchange rate of water across the BBB would increase with BBB impairment. A suggestion as to why this was seen could be due to the Aquaporin-4 (AQP4) channels not functioning correctly as the disease progresses, resulting in a change of water crossing the BBB.

Changes in AQP4 have been detailed in a recent study by Ohene (Ohene et al. 2019) where AQP4 knockout mice displayed a significant difference in the exchange time of water compared to normal animals. A study using DWASL to image AQP4 knockout mice would be welcomed but time constraints restricted this study being attempted in the limited research period of this thesis. There has been no research into the AQP4 channels or in water exchange in HAT infected mice. With only minor changes in the neuropathology of the infected brains, further investigation into any changes in the AQP4 channels could give more information about how the brain has been affected by the disease.

Pseudo-permeability maps were produced for all mice. No changes were seen between the mean permeability of the brain using b = 0 and 75 s/mm^2 for all time points. These results indicate that any changes in water exchange across the BBB are either too subtle to be detected by DWASL or there is no change in water exchange even when the BBB is impaired in HAT.

Investigation of inflammation in the brain was undertaken for all mice using histology. H & E staining showed that mild neuroinflammation was present for all infected time points. The inflammation increased from the early stage of the infected to the late stage, with a higher density of inflammatory cells in the meninges and perivascular cuffing of the vessels. The highest score was at day 21 post-infection with a grade of two. At this stage there is only a mild-moderate level of meningitis and no encephalitis seen. Imaging of a different strain of the infection producing a higher neuroinflammatory score could potentially see a difference in the water exchange.

Values for cerebral blood flow were calculated using the recently quantified mbASL sequence (Chapter 4 and (Vallatos et al. 2018)). There is no previous literature on CBF values in HAT, with no expectation on whether changes would be seen. There was a significant increase in CBF at the end point of infection (day 28) compared with day 7, 14 and 21 post-infection. There was no significant difference between day 0 and day 28 post-infection, demonstrating a drop in mean CBF in the brain during the early stage of the disease. However, this drop did not reach a significant level. By the end point of the experiment, the CBF increased again and was significant higher than the earlier infection time points. The mechanism behind this is not currently known and further research into these changes are needed. Large variation is seen in the values across all time points, but values agree with both the literature and values found for CD-1 mice in Chapter 4. The relationship between CBF and the IV fraction of signal needs to be further explored. A lower value of CBF could result in a lower value of IV due to the labelled blood not reaching the imaging plane during the inversion time. This could result in misleading changes in BBB permeability. To explore this, an experiment could be designed to examine the effect of CBF changes on the IV and EV fractions.

6.6 Study 4: Measuring Changes in Water Content using the Wet-Dry Method

6.6.1 Methods

As a quantitative measure of the water content in the brain, a pilot study was designed to compare uninfected and infected mice. A group of n = 8 mice were separated into two groups of n = 3 control mice (uninfected) and n = 5 trypanosome infected mice (as in Section 6.2.2.2). The infection progressed naturally until day 21 post-infection when the mice were treated with 40mg/kg diminazene aceturate. Mice were culled 7 days following treatment using an overdose of anaesthetic. The brains were excised, weighed, and then placed in an oven at 100°C to dehydrate. Weights were taken at multiple time points until no further decrease in the weight of the brain was detected. This final weight was considered as the dry weight. The percentage water content was calculated using the following equation:

$$\% \textit{ water content} = \frac{\textit{wet weight} - \textit{dry weight}}{\textit{wet weight}} \times 100 \tag{6.3}$$

6.6.2 Results

The mean wet weight, mean dry weight and percentage water content from the infected and control groups taken at the beginning and end of the experiment are shown in Table 6.17, with the standard error given. Five animals were used for the infected group and three for the control group.

Day of Infection	Wet brain (g)	Dry brain (g)	Water Content (%)	n
Uninfected	0.46 ± 0.008	0.099 ± 0.0009	78.4 ± 0.3	3
28	0.5 ± 0.009	0.11 ± 0.002	77.3 ± 0.3	5

Table 6.17: Brain weights for the water content study

The mean values of wet weight, dry weight and water content for an uninfected and infected group of mice. The brains were taken after scanning and weighed before being dried to obtain a dry weight.

A significant difference in wet weight between the control and infected brains (p = 0.045) was found, with the mean infected wet weight higher than the mean control wet weight (Figure 6.19). Furthermore, the weight of the brains once dehydrated was significantly different (p = 0.003), with the uninfected group mean weight lower than the infected group mean weight. In contrast, the % water content was found to be significantly lower (p = 0.044) between the infected group and the control group, indicating an overall decrease in water content in the infected

brains.

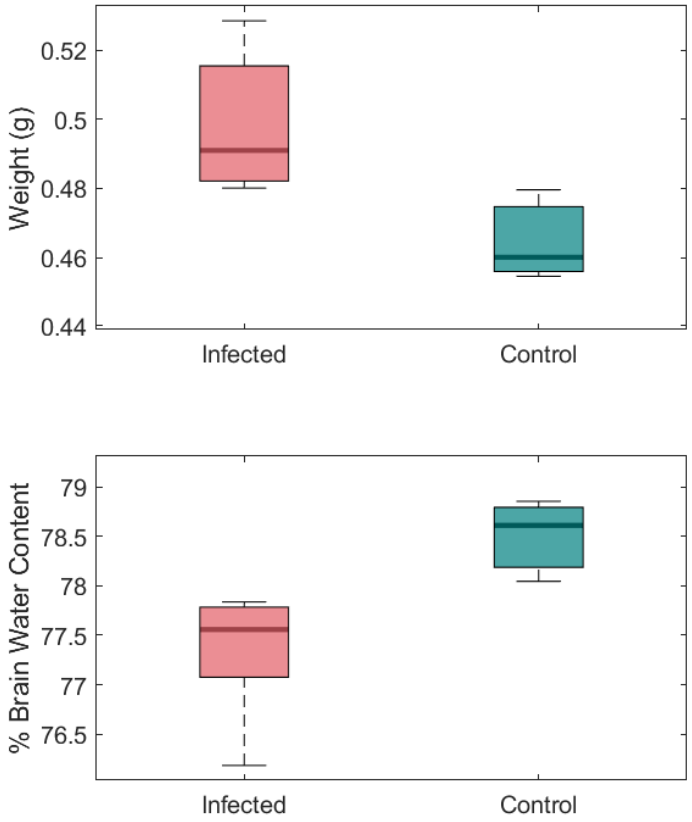

Figure 6.19: Comparison of wet weights for the water content study

The top plot is a comparison of the wet brain weight between the infected and uninfected group. The brain weight of the infected group was significantly higher ($p < 0.05$) than the control group. The bottom plot depicts the water content of the brain as a % between the wet and dry weight for the infected and control groups. The infected brains weighed significantly lower than the control group brains ($p < 0.05$). The median, 25 % and 75 % quartile ranges and maximum and minimum values are shown.

6.6.3 Discussion

This study was designed to quantitatively examine the water content of the mouse brain in non-infected and HAT infected mice. It was expected that the water content in the HAT infected brains would be higher due to inflammation in the brain and the impairment of the BBB, which has been shown in late stage HAT. By using the wet-dry method to measure the percentage of water in the brain, the late stage HAT group showed a significantly lower water content compared to the control group. This was opposite to the expected increase in water content. This compares positively with the DWASL data, which suggested a lower exchange rate of water across the BBB. The drop in water in the brain could explain why there was not an increase exchange as expected in the DWASL data. The decrease in the percentage of water in the brain was only 1 % and this slight variation could explain why changes in water content could not be measured using DWASL. The DWASL sequence appears to be not sensitive enough to pick up changes of 1 % in water exchange in the brain.

The water content in HAT infected mouse brain has not been explored previously. Astrocyte activation in the CNS is a common feature during the late stage of HAT (Rodgers, Bradley, et al. 2017; Kennedy and Rodgers 2019). AQP4 water channels are present on astrocytes therefore an increase in water content of the brain could be expected in conditions where astrocyte proliferation is present. However, the opposite was seen in this study, with the water content decreasing. This stresses the need for further investigation into the expression of AQP4 in the HAT infected mouse brain. Although BBB impairment is present in this infection, and astrocytes play a key role in the neuroinflammatory reaction (Section 6.5.2.2, (Rodgers, McCabe, et al. 2011; Rodgers, Bradley, et al. 2017)) this is not accompanied by an increase in water content in the brain. The results of this study indicate that the BBB impairment may be more complex than initially expected and highlight the need for further study in this area.

Hong et al. reported that AQP4 measure can be used as a measure of the integrity of the endothelial cell-astrocyte relationship (Hong et al. 2016). Furthermore, they showed that in a study on paediatric tumours, there was a disruption in this relationship along with reduced and disorganised staining of AQP4. In another study on astrocytes in brain tumours, Nduom et al. demonstrated there was a breakdown in the astrocyte-endothelial cell interaction where there was BBB disruption, which was demonstrated by MRI. There was also a diffuse staining of APQ4 but there was a lack of the normal pattern associated with a healthy and intact BBB (Nduom et al. 2013). Kaur et al. demonstrated an increase in AQP4 on astrocytes in rats after being exposed to hypoxia (Kaur et al. 2006). An increase in vascular permeability was shown with this study further confirming a link between AQP4 and BBB impair-

ment. Overall, this research further suggests that exploration of AQP4 in HAT may be beneficial to understanding the nature of the BBB impairment.

6.7 Conclusion

This chapter outlined the use of diffusion-weighted arterial spin labelling to measure the permeability of the blood brain barrier in the HAT infected mouse. Although the pseudo-permeability of the brain had been examined at both early and late stage of the trypanosome infection, no significant changes were seen between the infection time-points. This work presents evidence that although a contrast agent can cross the barrier demonstrating there is barrier impairment, the permeability of the barrier to water may not have changed as was originally expected. It also shows that the complexity of the trypanosome infection, with the impairment of the barrier may not be as simple as was initially expected. More work is needed to explain the lack of changes seen from the data in this chapter. Changes in the AQP4 channels may explain the significant change in water content in the infected brains and this merits further exploration.

Chapter 7

Measuring Serial Changes in Splenomegaly in the Trypanosome Infected Mouse

7.1 Introduction

Splenomegaly is a common clinical sign associated with trypanosome infection in both man and animals. This study is the first to image splenomegaly serially in a mouse model of trypanosome infection. Two hypothesis were made:

- MRI can be used to follow the development of splenomegaly as the trypanosome infection progresses.
- Haematological changes will develop alongside the splenomegaly.

Studies were performed to examine both hypothesis. For the first hypothesis, groups of infected and uninfected mice were serially scanned to assess the spleen volume at five MR scan points. For the second hypothesis, blood samples were taken after each scanning session for both groups, along with histology at the end point of both studies.

7.2 Methodology

7.2.1 Animals, Infection and Sampling

A group of n = 6 female CD-1 mice, weight = 35 $\pm$ 3g were infected as outline in Section 6.2.3.2. Each mouse was scanned pre-infection and at day 7, 14, 21 and 28 post-infection. A second group of n = 5 CD-1 mice with weight = 34 $\pm$ 4g were used as a control. These mice were not infected but were scanned at the same time points as the infected mice.

A 100μL blood sample was taken from each mouse at each scan day to assess haematological parameters. The blood was obtained by puncturing the tail vein and the sample collected in a hepranised microvette collection vial and immediately taken to the University of Glasgow Veterinary Diagnostic Service Histopathology Laboratory for haematological analysis detailed below. Due to clotting some samples were unsuitable for analysis (Table 7.1).

Following the final scan the mice were sacrificed, exsanguinated by cardiac puncture and the spleens removed. The spleens were weighed and fixed in neutral buffered formalin to allow histopathological assessment (previously described in Section 6.2.5). H & E stains were prepared to assess the histopathology, in addition to special stains.

Day of Infection	Infected	Uninfected
Uninfected	✓✓✓✓✓✓	✓✓✓✓✓
7	××××××	✓✓✓✓✓
14	××××××	×××××
21	××××××	✓✓✓✓✓
28	✓✓✓✓✓✓	✓✓✓✓✓

Table 7.1: Blood samples obtained from mice in the study

Although blood was successfully obtained from all animals, some samples clotted which resulted in those samples not being suitable for processing. Successful blood counts are indicated by ✓, whilst clotted samples are indicated as ×.

Following haematological analysis, one mouse from the infected group was removed from the study results due to the presence of anaemia before infection had taken place.

7.2.2 MRI and Animal Setup

A custom built cradle was designed for full body imaging of the mouse using a 4-channel Bruker rat head coil (Figure 7.1). The coil was placed upside down and secured in the cradle with a movable section above to lay the mouse in. The mouse

was positioned so that the spleen would be above one of the four receiver coils for maximum signal. The cradle was designed so that anaesthetic and a water jacket could be used as described previously (Section 4.5.1).

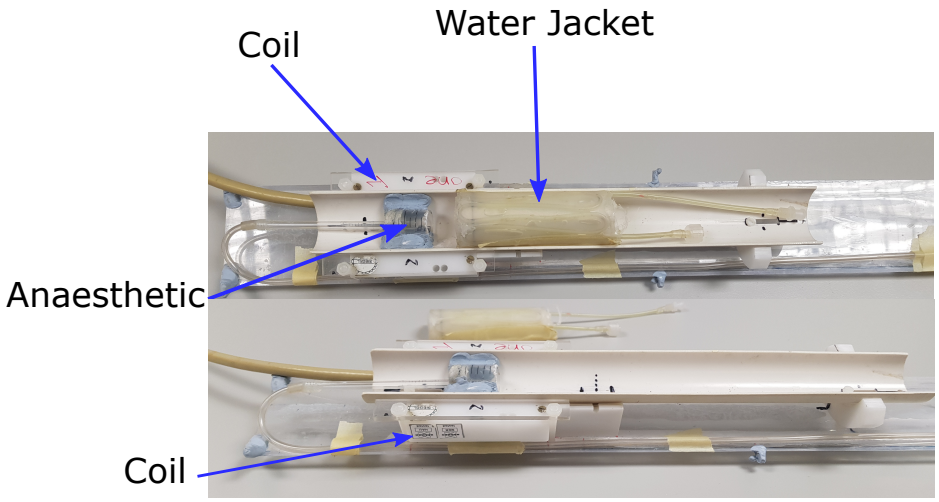

Figure 7.1: Cradle used in splenomegaly study

A custom made cradle was designed for full body mouse imaging. The cradle housed a 4-channel Bruker rat head coil in which the mouse could be positioned above the desired coil. The cradle was designed so that the animal could be moved for adjustment of positioning to allow optimal scanning.

For each animal, a T_1 and T_2 weighted whole body scan was performed, with the use of respiratory gating. T_1 FLASH parameters were as follows: TE = 2.534ms, TR = 600ms, NA = 4, flip angle = 30°, hermite pulse length 0.9ms. T_2 RARE parameters were as follows: TE = 13.75ms, effective TE = 55ms, RARE Factor = 8, TR = 8000ms, NA = 1. For both T_1 and T_2: FOV = 5×5cm. Matrix size = 200×200 with a resolution of 250 μm/pixel. Slice thickness = 1mm with 30 slices taken covering the whole abdomen. Scan time was approximately 8 minutes for the T_1 scan and approximately 4 minutes for the T_2 scan. Total scan time was less than 20 minutes including a preliminary scan to ensure optimal positioning of the mouse.

7.2.3 Image Analysis

In-house MATLAB (Mathworks, Inc.) code was written to analyse the MR images. Scans were imported into MATLAB in a DICOM format. For each T_1 and T_2 image set, all images were examined and if determined to include the spleen, an ROI was hand drawn and saved. The number of voxels in each spleen ROI were summed together giving a total number of voxels for the full spleen. The total voxel number was multiplied by the volume of one slice (0.25×0.25×1mm) to give the total volume of the spleen from MRI in mm^3.

7.2.3.1 Statistics

MRI data and haematology results were statistically analysed using Minitab 17 (Minitab Inc.). The general linear model and ANOVA were used to compare the groups while Tukey's multiple range comparison test was employed to identify differences between the groups. P-values of $<5\%$ were considered as statistically significant. Means, standard errors (SE) and 95% confidence intervals (CI) are provided as summary statistics.

7.3 Results

7.3.1 MRI

7.3.1.1 Serial MRI of Splenomegaly

The set of images produced for each mouse showed the spleen in its entirety, along with the kidneys, stomach, bladder and other organs, depending on the position of the mouse in the cradle. The spleen cross-section in each 1mm slice appeared triangular in shape in the scans taken before infection. Once the animals were infected, the increase in the size of the spleen was clearly visible in the MR images from day 7 post-infection onward. The spleen size, shape and position appeared different for each mouse. Figure 7.2 demonstrates one slice of the body from each T_1 data set for a single mouse. As the spleen increased in size, it changed shape and displacement of other organs was seen. On clinical examination, the enlarged spleen could be observed from day 14 post-infection around the abdomen area of the mouse. In Appendix C, a full set of images from a mouse at day 21 post-infection is shown.

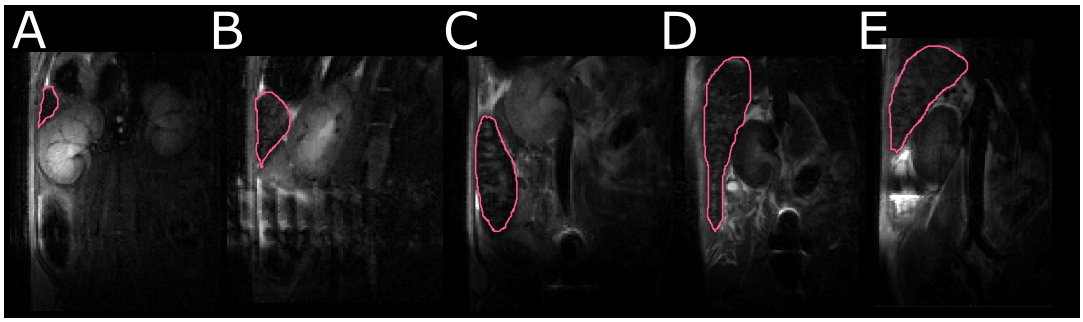

Figure 7.2: Spleen in one infected animal

One 1mm slice from each MR data set is shown for an infected mouse which had been serially scanned at uninfected (A), day 7 (B), day 14 (C), day 21 (D) and day 28 (E) post-infection. The spleen enlarged from as early as day 7 post-infection, increasing in size throughout the infection. The spleen is highlighted in pink. The kidney was used to estimate the same spatial position in the body for each image used for this demonstration.

For each mouse, the spleen volume from the MR scans from each session was calculated from the T_1 and T_2 scans. The total volume from each scan type was compared, with no statistical significance seen between the data sets ($p > 0.05$) of the infected animals. Following this, the T_1 scan data sets were used for statistical analysis.

The mean volume of the spleen from the T_1 image set was compared between each scan point (Table 7.2). There was a significant difference in the mean spleen volume between the first scan point (uninfected) and all infected scan points ($p < 0.005$). The mean volume was plotted to compare the difference at each scan point (Figure 7.3). A sharp increase in spleen volume was seen between the uninfected (82 ± 12 mm^3) and day 7 post-infection (627 ± 14 mm^3 p = 0.005 CI = [144, 946]) time point. This increase continued until day 21 post-infection (1783 ± 108 mm^3), when the disease had entered the late stage. There was no significant difference between the mean volume at day 28 post-infection (1483 ± 121 mm^3) compared to day 14 (1339 ± 135 mm^3) and day 21 post-infection ($p > 0.05$).

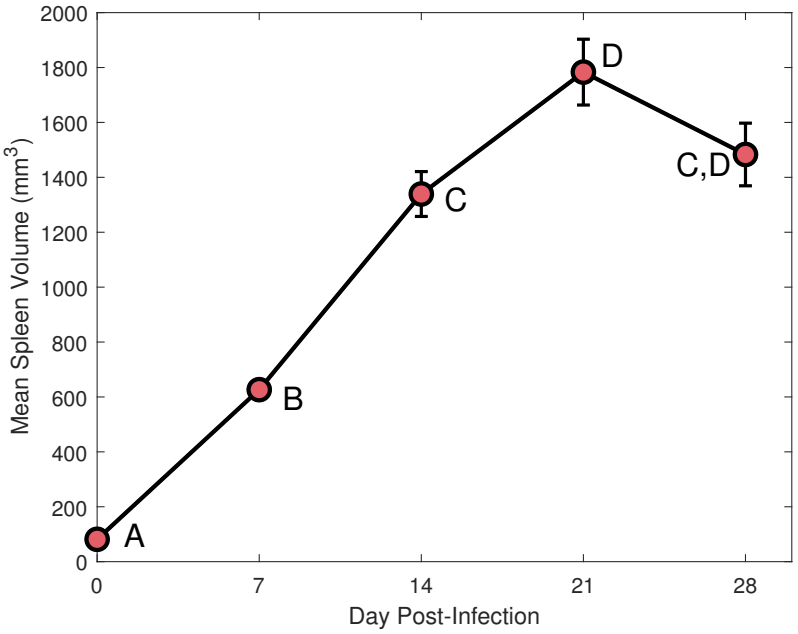

Figure 7.3: Volume of spleen at each infection point

The mean volume of the spleen from each scanning session is plotted in mm^3. Significance is denoted by groups not sharing a letter. There was a large increase in the mean spleen volume from the first scan point. There was no significant difference between day 21 and 28 post-infection or day 14 and 28 post-infection. Error bars are denoted as the standard error and n = 5 mice were used.

	Uninfected	Day 7	Day 14	Day 21	Day 28
Day 7	p = 0.005 (144, 946)				
Day 14	$p < 0.001$ (857, 1659	$p < 0.001$ (312, 1113)			
Day 21	$p < 0.001$ (1301, 2103)	$p < 0.001$ (756, 1557)	p = 0.026 (43, 845)		
Day 28	$p < 0.001$ (1001, 1803)	$p < 0.001$ (756, 1557)	p = 0.817 (43, 845)	p = 0.206 (-701, 101)	
Mean volume $\pm$ SE mm^3	82 ± 12	627 ± 14	1339 ± 135	1783 ± 108	1483 ± 121

Table 7.2: Comparison of mean spleen volume in the infected group

In the infected group, the mean spleen volume was compared between each scan point. There is a significant difference between the uninfected scan point and the other scan points. No significant difference was seen between day 21 and 28 post-infection or day 14 and 28 post-infection. The mean spleen volume and standard error at each scan point is shown. 95 % confidence intervals are noted under each p-value.

7.3.1.2 Serial MRI Imaging of Uninfected Mice

Examination of the MR images at all scan points for the uninfected mice showed the expected triangular cross-section spleen shape. No qualitative changes were seen in the MR images throughout the repeated scanning sessions. For a single mouse, one image is shown from the T_2 data set (Figure 7.4). The shape and size of the spleen was maintained across the five scan points. In Appendix C, a full set of images of the spleen for an uninfected mouse are shown.

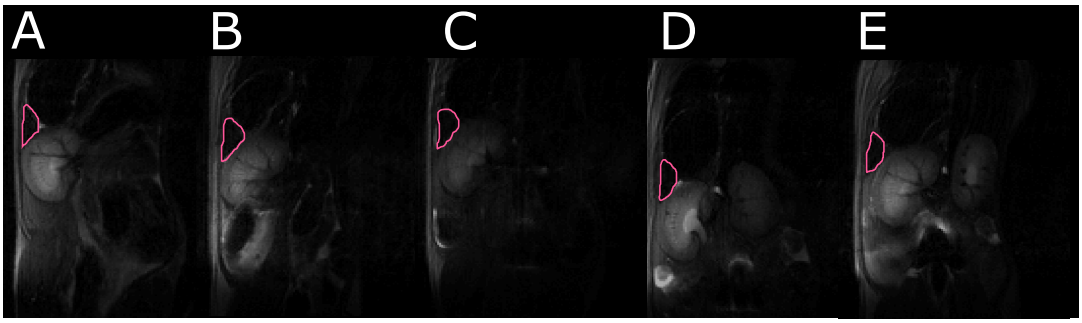

Figure 7.4: Spleen images for one mouse in the uninfected group

The spleen in the uninfected group was examined by MR scanning at five scan points corresponding to those in the infected group; uninfected (A), day 7 (B), day 14 (C), day 21 (D) and day 28 (E). The spleen size and shape was maintained throughout the study. One mouse is shown from the T_2 data set with the spleen highlighted in pink.

The mean volume of the spleen calculated from the T_1 and T_2 images showed no significant difference from each other ($p>0.05$). Comparison of the mean volume of the spleen, calculated from the T_1 images, for the uninfected mice showed no significant difference ($p>0.05$) between any of the scan points (Table 7.3). The range of mean spleen volumes from the uninfected mice was $133 \pm 6\ mm^3$ at day 0 to $137 \pm 6\ mm^3$ at day 28. The mean volume was plotted (Figure 7.5) with only a small variation in the mean spleen volume seen across all scan points.

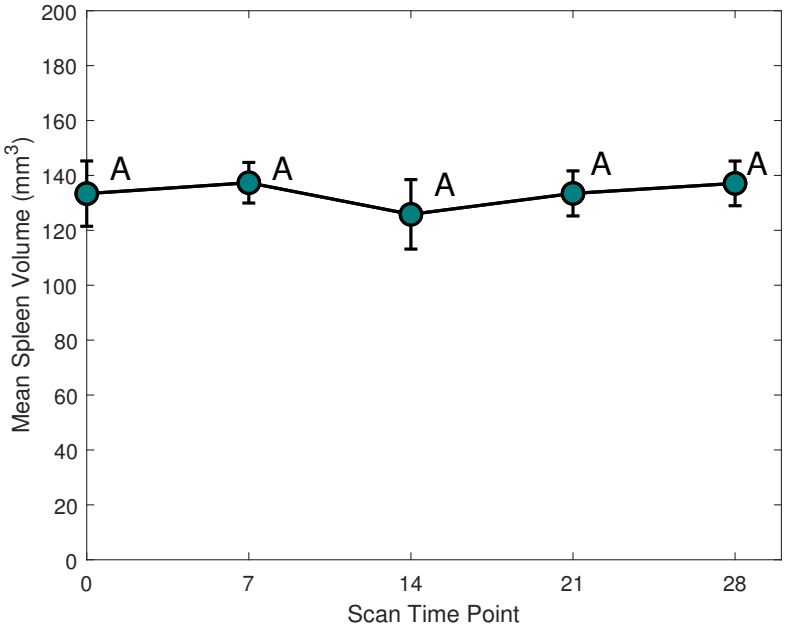

Figure 7.5: The volume of the spleen for the uninfected mice at each scan point

Only a small variation in the mean volume of the spleen calculated from each scanning session. The average volume in mm^3 was 133 $\pm$ 6, 137 $\pm$ 7, 126 $\pm$ 8, 133 $\pm$ 12 and 137 $\pm$ 6 for the scan points 0, 7, 14, 21 and 28. There was no significant difference between any of the groups. This is denoted by each group sharing the same letter. n = 5 mice are used and error bars denote the standard error.

	Uninfected	Day 7	Day 14	Day 21	Day 28
Day 7	p = 0.996 (-29.8, 37.7)				
Day 14	p = 0.961 (-41.3, 26.2)	p =0.843 (-45.3, 22.3)			
Day 21	p = 1 (-33.7, 33.9)	p = 0.997 (-37.7, 29.9)	p = 0.96 (-26.2, 41.4)		
Day 28	p =0.997 (-30.1, 37.5)	p =1 (-34.0, 33.5)	p = 0.853 (-22.5, 45.1)	p = 0.997 (-30.1, 37.4)	
Mean volume $\pm$ SE mm^3	133 $\pm$ 6	137 $\pm$ 7	126 $\pm$ 8	133 $\pm$ 12	137 $\pm$ 6

Table 7.3: Comparison of mean spleen volume for the uninfected group

Comparison between mean spleen volume at all scan points showed no statistical difference ($p > 0.05$) between any of the values. The mean spleen volume at each scan point is shown with the standard error. 95 % confidence intervals are noted under each p-value.

7.3.2 Haematology

For haematology analysis, the following parameters were examined: red blood cell (RBC) count, haemoglobin (Hb), haematocrit (HCT %), white blood cells (WBC), neutrophils, lymphocytes and monocytes. Table 7.4 displays the mean cell counts for each scan point in infected or uninfected mice, where blood analysis was possible. The normal range of values seen in the literature is also displayed (O'Connell et al. 2015; Weiss et al. 2010).

7.3.2.1 Infected mice

A comparison was made between the haematological parameters measured at the first scan point (before infection) and day 28 post-infection. There was a significant difference ($p<0.05$) for the following counts: RBC, Hb and HCT % with reduced levels seen at the later time point. In contrast, there was a significant increase in the number of neutrophils ($1.65 \pm 0.04 \times 10^3/\mu$L) and monocytes ($0.61 \pm 0.2 \times 10^3/\mu$L) compared to the cell count at day 0 ($p = 0.024$ [2.1×10^3, 2.2×10^4]; $p = 0.049$ [1.2, 1.1×10^3]). There was no change in the white blood cell count between the two points, with values of ($5.4 \pm 1 \times 10^3/\mu$L) and ($5.6 \pm 1 \times 10^3/\mu$L) at day 0 and day 28 respectively. In comparison to the normal ranges shown in the literature, the red blood cell count, haemaglobin and haematocrit at day 28 post-infection were lower than the expected values.

7.3.2.2 Uninfected Mice

For the uninfected mice, the only blood samples that clotted were for the day 14 scan point. For the RBC count, there was a significant difference ($p < 0.05$) between the day 0 ($8.2 \pm 0.7 \times 10^6/\mu$L) and day 7 ($10.5 \pm 0.4 \times 10^6/\mu$L) scan point, and the day 0 and day 21 ($10.1 \pm 0.2 \times 10^6/\mu$L) scan point. All the values were, however, within the normal ranges. A similar pattern was seen for the value of haemoglobin, with a significant increase between the day 0 (13.4 ± 1.1 g/dl) and day 7 (16 ± 0.2 g/dl) scan point, but all values were within the normal range. For HCT, a significant increase ($p < 0.05$) was found at day 7 (38.8 ± 3 %) and day 21 (48.5 ± 2 %) compared to the first scan point. At day 28 the value of HCT (38 ± 1 %) had decreased back to a similar value at day 0.

At the day 28 scan point, the WBC count ($2.0 \pm 0.4 \times 10^3/\mu$L) had significantly decreased ($p < 0.05$) compared to all the other scan points. There was no change in the number of neutrophils, although the lymphocyte count did show a significant

	Infected		Uninfected				Normal
	Day 0	Day 28	Day 0	Day 7	Day 21	Day 28	Range
RBC ($\times 10^6/\mu$L)	10.3 ± 0.8	5.8 ± 0.4	8.2 ± 0.7	10.5 ± 0.4	10.1 ± 0.2	9.1 ± 0.3	7 - 11
Hb (g/dl)	15.0 ± 1.5	7.8 ± 0.5	13.4 ± 1.1	16.0 ± 0.2	15.7 ± 0.5	13.9 ± 0.2	13.2 - 16.4
HCT (%)	42.4 ± 3	29.3 ± 2	38.8 ± 3	48.5 ± 2	48.5 ± 2	38.0 ± 1	35 - 52
WBC ($\times 10^3$ / μL)	5.4 ± 1	5.6 ± 1	7.8 ± 2	9.7 ± 2	10.2 ± 2	2.0 ± 0.4	2 - 10
Neutrophils ($\times 10^3/\mu$L)	0.421 ± 0.09	1.65 ± 0.04	0.36 ± 0.01	0.45 ± 0.01	0.57 ± 0.01	0.14 ± 0.005	0.04 - 2
Lymphocytes ($\times 10^3/\mu$L)	5 ± 1	3.2 ± 1	7.4 ± 1	9.1 ± 2	9.1 ± 2	1.7 ± 0.4	1.4 - 7
Monocytes ($\times 10^3/\mu$L)	0.05 ± 0.02	0.61 ± 0.2	0.0082 ± 0.0007	0.081 ± 0.05	0.24 ± 0.04	0.049 ± 0.01	0 - 0.02

Table 7.4: Blood cell counts for the spleen study

Haematological parameters for infected and uninfected mice that were analysed successfully. These are: red blood cell count (RBC), haemaglobin (Hb), haematocrit (HCT), white blood cell count (WBC), neutrophils, lymphocytes and monocytes. Values are shown with the mean $\pm$ standard error. Values obtained from literature are shown in the end column (O'Connell et al. 2015; Weiss et al. 2010), with the infected group and uninfected group separated by a line. Values shown in colour are significantly different from the value at day zero for the infected or uninfected group. Values shown in pink are outwith the normal range and values in green are significantly different but not outwith the normal range displayed.

difference between day 7 (9.1 $\pm$ 2 $\times 10^3/\mu$L) and day 28 (1.7 $\pm$ 0.4 $\times 10^3/\mu$L), and also between day 21 (9.1 $\pm$ 2 $\times 10^3/\mu$L) and day 28.

7.3.2.3 Comparison Between Infected and Uninfected Cohorts

The cell counts for the day 0 pre-infection group were similar to those seen in the uninfected cohort ($p > 0.05$). For the last scan point (day 28 post-infection), there was a significant difference between all the cell counts ($p < 0.05$) apart from lymphocytes. For the infected mice, a significant decrease in the RBC, Hb and HCT levels were seen, whereas there was a significant increase in the WBC count and neutrophils. There was no change in lymphocytes. The WBC count was still within the normal range for a mouse, with the RBC, Hb and HCT values below the normal range observed in the literature.

7.3.3 Spleen: Gross Anatomy and Histology

7.3.3.1 Gross Findings

The spleens were removed at the end of the study for the infected group (Figure 7.6). The average spleen weight was 1.51 $\pm$ 0.04g making the spleen 4.1% of the mean body weight (37 $\pm$ 5g). The mean spleen volume calculated from the MR images was 1.48 $\pm$ 0.3 mm^3. This was very close to the actual weight and no significant difference was found between the volume from the MR images or the weight of the spleens ($p > 0.05$). The average spleen weight of the uninfected mice was 0.094 $\pm$ 0.007g and constituted 0.27% of the body weight (35 $\pm$ 2g) at the end of the experiment (Figure 7.6). The mean volume from the MR images was 0.13 $\pm$ 0.01 mm^3 and this was significantly higher than the actual weight ($p = 0.002$). This may be a factor of the much smaller range of spleen size found in this group in both actual weight and extrapolated volume.

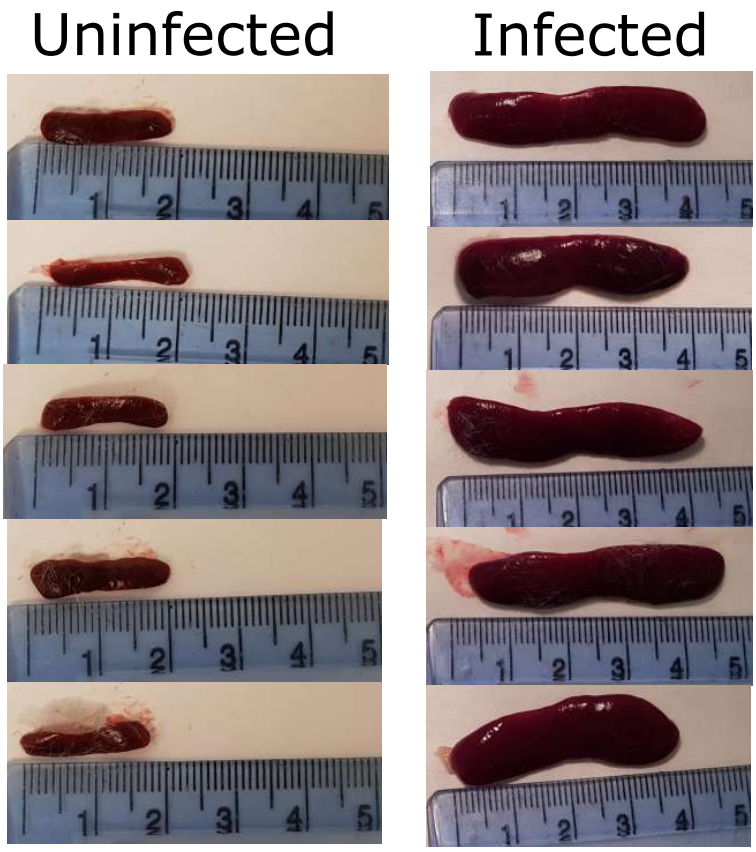

Figure 7.6: Excised spleens for the infected and uninfected mice

Spleens taken from mice in both the infected and uninfected group were photographed using the same parameters to examine changes between the two groups. The infected spleens are clearly larger than the uninfected spleens, being on average double the length.

7.3.3.2 Histopathology

Histopathological analysis was carried out on the spleens excised after the last scan point (day 28), for both infected and uninfected groups of mice.

In the uninfected animals, the H & E staining (Figure 7.7A) demonstrated the normal architecture of the spleen, with a clear distinction seen between the white pulp and the red pulp. Numerous T cells were found within the PALS surrounding the central arteries with smaller numbers extending into the marginal zone and the red pulp. Large numbers of B cells were present in the follicles, the marginal zone and spreading into the surrounding red pulp.

In the infected mice, H & E staining showed many pathological changes in the spleen (Figure 7.7D) with an obvious breakdown in the distinction between the red pulp and the white pulp. The central arteries were still visible, but the follicles had become indistinct with more diffuse margins. Although numerous T cells could still be found surrounding the central arteries, they also appeared to be more diffusely spread throughout the tissue (Figure 7.7E) compared to the pattern seen in the uninfected mice. The effect of trypanosome infection on the presence of B cells in the spleen was much more overt (Figure 7.7F) with only small numbers of B cells detected in the follicle and the marginal zone and an almost complete absence of any B cells in the red pulp.

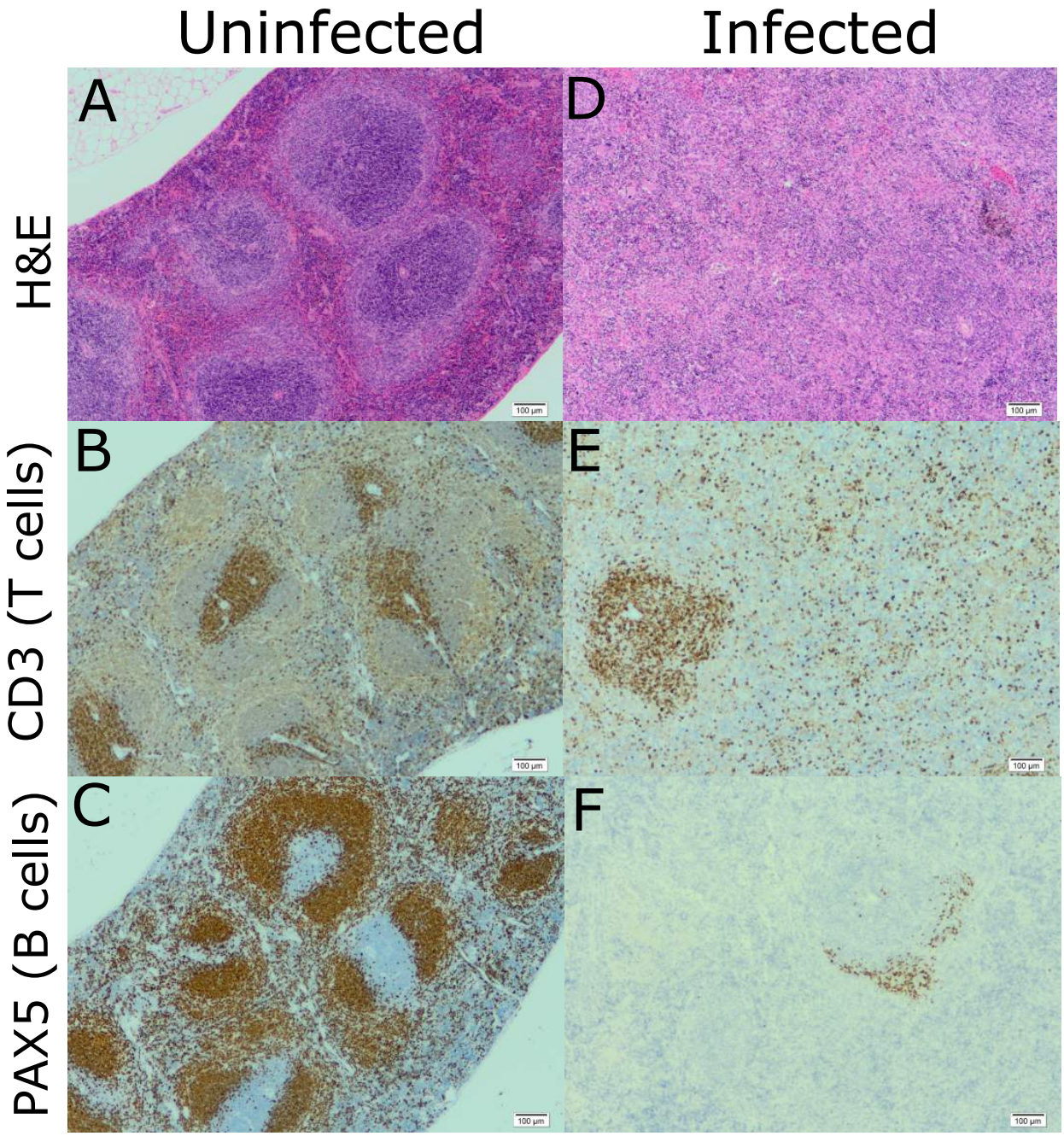

Figure 7.7: Histology of the spleen

Three stains; H & E, CD3 (T cell marker) and Pax5 (B cell marker) are shown for an uninfected mouse (left) and an infected mouse (right). There was a clear breakdown in the architecture of the spleen in the infected animal, with the T cells becoming more diffuse and a distinct lack of B cells. Images are shown at a $\times$40 magnification.

7.4 Discussion

Splenomegaly is a known symptom of trypanosome infection in humans and animals, therefore the aim of this study was to explore the development of the splenomegaly in a murine model of HAT over the course of infection. Splenomegaly has been explored in rodents previously, but this has been achieved by examining the spleen invasively through histology. This study for the first time, uses a non-invasive imaging approach to explore splenomegaly development through the early and late stages of HAT in the same group of mice.

7.4.1 Infected mice

7.4.1.1 MRI

The infected mice were scanned at weekly intervals from day 0, before infection, until day 28 post-infection. The splenomegaly was obvious in both the T_1 and T_2 images from the MRI beginning at day 7 post-infection. At this early stage of infection the splenomegaly could not be detected on clinical examination of the mouse but the MRI indicated that spleen enlargement was already present. Two different measurements were made of the spleen using a T_1 and T_2 weighted sequence with the spleen volume calculated from both image sets. As expected, comparison of the average spleen volume was very similar from both sequences, therefore further analysis was performed using only the T_1 data set. All infected animals showed splenomegaly in the MR images. Although the rate at which the spleen size increased varied, the same trend was seen for all mice.

The spleen volume was significantly lower when comparing the first scan point day 0 (before infection), with day 7, 14, 21 and 28 post-infection in the infected animals. Compared to the volume at day 0, an average increase of $\sim$ 2200% was observed by day 21 post-infection, when the infection had entered the late stage. There was no significant difference between day 14 and day 28 post-infection and day 21 and day 28 post-infection, however the spleen continued to enlarge between day 14 and day 21 post-infection. This provides new insights into the changing of the spleen throughout the whole infection, which has not been measured serially before and shows that spleen enlargement occurs quickly after infection. This however is not apparent on clinical examination. Amole et al. reported that splenomegaly occurred 8 days after infection with *T. brucei*, with a splenic weight of 0.8g, and a weight of 0.85g after 30 days of infection. This increase is smaller than seen in this study, which may be due to a difference in infections. Overall, this reflects the change in spleen volume that was seen in this study, with a large

increase in weight at an early infection point.

At the end of the study, the volume of the spleen from the MR images (1.48 ± 0.3 mm^3) was not significantly different to the actual weight of the spleens ($1.51 \pm$ 0.04g). Overall, this demonstrates that repeated MR scanning is a viable technique for accurately measuring changes in the volume of the spleen.

7.4.1.2 Haematology and Histology

A small volume of blood was taken after each scanning session. For serial bleeding only 10% of the total blood volume of the mouse could be taken at each scan point, with 100 μL being taken for each mouse. Unfortunately some blood samples clotting prior to analysis. Although haematological analysis was successful at the first and last scan point of the study (before infection and day 28 post-infection), all results between these scan points clotted. This prevented any correlation between changes in spleen size and haematological parameters from being compared further. In the infected group there was a significant reduction in the red blood cell count, haemoglobin and haematocrit counts for day 28 post-infection, compared to the uninfected point. This drop indicated that the mice were suffering from anaemia, which has been noted in other studies in trypanosome infection (Anosa et al. 1984). Amole et al. also noted anaemia in both the acute and chronic stages of their mice infected with *T. brucei* (Amole et al. 1982). In the present study, all values of RBC count, Hb and HCT were considered outside of the normal range of cell counts seen in mice. There was a significant increase in the number of neutrophils and monocytes, however, the total white blood cell count was not significantly different at the end scan point. Although no changes were detected in the total number of lymphocytes, further analysis, where the number of T cells and B cells are examined would potentially show a difference between the uninfected and infected data, since an almost complete lack of B-cells and a change in the distribution of T cells was detected in the spleen on histological examination.

The spleens were removed at the end of the study to compare to the MR images (Figure 7.6). The infected spleens appeared grossly enlarged confirming the splenomegaly seen in the MRI. Histology showed that the distinction between the red pulp and white had pulp had become indistinct in the infected mice. A decreased level of T cells was apparent with the cells more diffusely spread throughout the tissue and fewer were located around the central arteries. However, the most overt change was seen in the pattern of B cell staining, with an almost complete loss of this cell type in the spleen. When B cells come into contact with an antigen they transform into plasma cells and this may explain the reduced B cell staining in the infected group. Although plasma cells were apparent in the H

& E stained spleen, special stains to enhance their detection were unsuccessful. Other trypanosome studies have found similar results. Morrison et al. reported a drop in lymphocytes in the spleen, along with cells mixing between the red and white pulp following the infection of mice with *Trypanosoma congolense* (Morrison et al. 1981). Murray et al. (Murray et al. 1974b) reported similar findings in mice infected with *T. brucei* an increase in mature plasma cells in the white pulp of infected spleens with the white pulp extending into the red pulp.

7.4.2 Uninfected Mice

7.4.2.1 MRI

The average volume at all the scan points for the uninfected mice remained similar throughout the study. There was a minimal change of approximately one percent between the volumes, in contrast to the 2200% increase seen in the infected animals. There was no obvious change in the visual size or shape of the spleen on the images. These findings confirm that the procedures associated with serial MRI and blood sampling do not precipitate changes in the volume of the spleen and indicate that the splenomegaly noted in the infected group is attributable to the trypanosome infection.

7.4.2.2 Haematology and Histology

All cell counts for the uninfected mice at the first scan point were within the normal range. Blood samples were successfully analysed for four of the five scan points in the uninfected mice. Only the blood collected at day 14 could not be analysed due to clotting. Changes in cell counts can be expected between the scan points from natural fluctuations. In the RBC count, Hb concentration and HCT, changes were detected between the various time points, but all values fell within the normal ranges, again confirming serial blood sampling had a minimal impact on the health of the mice.

The histology images compared favourably with the literature for non-infected mice. A clear distinction was seen between the red pulp and white pulp, with T cells and B cells seen in the relevant staining. Estimation of the volume of the spleen was over-estimated using MR for the uninfected mice. This is believed to be due to the small size of the uninfected spleens on the MR images with the edges of the spleen over estimated when the ROI was selected.

7.4.3 Comparison of Infected and Uninfected Mice

The two studies can not be compared directly as the two groups of mice had a significantly different spleen volume at the beginning of each study. However, as there was no significant difference between any of the volumes measured at the various time points in the uninfected group, any changes in the volume of the spleen seen in the infected animals are attributed to the trypanosome infection, and not from the MR scanning or sampling.

Comparison of the haematology results between the infected and uninfected groups at day 28 post-infection saw the same changes as seen between the first (uninfected) and last scan points in the infected mice, with a significant reduction in the RBC count, Hb and HCT% and a significant increase in neutrophils and monocytes in the day 28 post-infection mice. This demonstrated that changes that occurred in the infected mice at the end point of the study, were not a result of serial bleeding or repeated anaesthetics.

Comparison between the weight of the spleen showed the infected spleens to be an average of 16 times bigger compared to the spleens from the uninfected animals. Similar results have been reported in the literature, where Anosa et al. measured a 25 fold increase in spleen weight, with a rise from 0.026g to 0.673g, in deer mice (Anosa et al. 1984). An increase in spleen size of up to 30 times was noted by Murray et al. who attributed the change to a marked rise in plasma cell hyperplasia (Murray et al. 1974a). Furthermore, an increase of greater than 20 times in spleen weight was measured by Morrison et al. who measured the weight between 4 and 24 days post-infection (Morrison et al. 1981). They also found that the spleen weight remained constant after this point. This suggests that if the infected group had continued, there may not have been any further significant changes in the weight of the spleen since no significant changes in volume were detected between day 21 and day 28 post-infection. An increase from 0.23g to 0.85g in mean spleen weight was reported by Amole et al. in mice infected with *T. brucei*, where the percentage size of the spleen compared to the body weight had changed from 0.8% to 2.4% (Amole et al. 1982). This was smaller than the change seen in this study, which saw an increase from 0.27 % to 4.1 %.

7.5 Conclusion

This study has been able to show successfully for the first time, the progression of splenomegaly in trypanosome infected mice by using a combination of MRI, haematology and histology. A significant increase in the spleen size was shown from MR

images until day 21 post-infection. The spleen did not continue to increase in size past day 21 post-infection, demonstrating new information about splenomegaly in trypanosome infections. This suggests that expansion of the spleen tissue is finite in this infection model. Analysis of haematology results revealed the infected animals developed anaemia at the end point of the study with a marked increase in neutrophils and monocytes. Histology sections of the spleen from infected and uninfected mice showed a clear loss of architecture of the white and red pulp in the infected mice and with a marked reduction in T cells and B cells. The MR findings were confirmed by the weight of the infected spleen comparing favourably with the MR images. This study provides new insights into the development of splenomegaly in HAT and indicates that further research is required to understand why the enlargement of the spleen appears to plateau at day 21 post-infection. Possible further studies would include an in depth haematological analysis and more infection points for comparison. Following this, serial MRI could be used to image the effects of trypanosomal drug treatment in the spleen, and monitor changes in the spleen. This technique could also potentially be used to image microhaemorrhages or congestion in the spleen using serial MRI.

Chapter 8

Conclusion

This thesis was focused on the development of a non-invasive MR sequence, diffusion weighted ASL, that would be sensitive to changes in water permeability in the rodent brain. By the quantification of a new high SNR ASL sequence, multiple boli ASL, and multiple developmental experiments, DWASL was shown to be sensitive to changes in water exchange in the mouse brain. The DWASL sequence was applied to a biological model where blood brain barrier impairment had been identified previously. This approach investigated whether changes in water exchange could be detected prior to the onset of the BBB damage that was known to occur in the infection timeline. When DWASL was applied, no changes in water exchange were seen during the late stage of the infection, while impairment can be seen using a contemporary contrast agent approach. Although these findings were in contrast with the expected outcome, the research provided a new insight into BBB impairment in HAT.

The development of a quantitative model for mbASL means the sequence can be used to quantify cerebral blood flow. As ASL sequences are inherently low in SNR, the increase in SNR compared to FAIR makes the sequence a viable alternative in pre-clinical imaging. This research highlights the importance of using an appropriate value for the number of pulses and labelling slab thickness, not just for different rodent species, but for different strains. This was clearly seen in C57 and CD-1 mice for example, where the CD-1 mice needed more labelling pulses to reach a signal plateau compared to the C57 mice, as they were larger. The comparison of various labelling thicknesses demonstrates that there is a limited range that can be used for optimal scanning, but also shows the versatility of sequence to adapt, for example, to the size of the animal being scanned.

The modification of the Buxton kinetic model for ASL to incorporate the multiple pulses, labelling slab thickness and varying distance between the imaging and labelling slab means the model does not need to make large assumptions or simpli-

fications, which have been seen in the literature previously when calculating CBF. Although some assumptions still remain, for example a constant blood velocity and an infinitely long tube for a capillary, the model predicts value of CBF which agree with the current literature. A quantitative comparison of mbASL to PASL and pCASL sequences on the same group of rodents, along with implementation at other pre-clinical MR sites would be a logical extension to the investigations completed in the current study. The mbASL sequence was shown in Chapter 6, to be sensitive to changes in CBF during the HAT infection. This suggests that the application of mbASL to other neurological diseases such as cancer or stroke, where changes in CBF are known to be important in the disease pathology, may be favourable.

At the present moment, the mbASL sequence is designed primarily for pre-clinical imaging, and has currently only been developed using rodents. The adaption of mbASL to be used in a clinical setting is desirable for a number of reasons. mbASL is non-invasive, as with other ASL sequences, making ASL safer for the patient than other invasive techniques, such as DCE-MRI. Although comparison with pCASL is still needed for mbASL, it has a higher SNR and signal than FAIR, which is important in both clinical and pre-clinical imaging, due the inherently low SNR associated with ASL. Furthermore, by altering the thickness of the labelling slab and the number of pulses used, it may be possible to adapt the sequence to suit the needs of each patient, due to the SAR levels associated with multiple adiabatic inversion pulses. More research is needed into the feasibility of transferring this sequence to the clinical setting. However, this may not be an issue with the large labelling slabs in humans, hence mbASL could be a a robust sequence in the future in both pre-clinical and clinical perfusion imaging.

The combination of mbASL and diffusion weighted ASL has resulted in the first successful research to demonstrate changes in water exchange in the mouse brain using DWASL. Previous work in this area has only been performed in humans and rats. Although the DWASL sequence has been applied in models of sleep apnea and ischaemic stroke, the sequence is inherently low in signal. The current project used mbASL to provide a higher SNR than would be seen using FAIR. Multiple development experiments were performed to make the sequence user friendly and facilitate longer scanning sessions, where physiological effects would previously lead to anomalies.

The DWASL sequence was shown to be sensitive to changes in water exchange in the mouse brain, providing a proof of concept of the sequence, comparable to results seen previously in human and rat studies. To try and improve the signal seen at low b-values, the DWASL sequence was altered to incorporate a bipolar gradient pair. Although this research did not show any improvement of the DWASL signal using this new sequence, it does warrant further research using a larger study of

smaller b-values.

This validation of DWASL in mice is extremely important for pre-clinical imaging, as having such a MR sequence available opens research opportunities into disease models that are used primarily in mice but not rats. It also provides a non-invasive method to examine changes in BBB permeability, where using the current invasive gold-standard contrast agent may not be suitable. Furthermore, the sequence is more sensitive than a contrast agent, providing opportunities to examine diseases such as cancer and stroke in earlier stages.

The application of DWASL to human African trypanosomiasis is the first research to examine the permeability of the BBB throughout this infection without using a contrast agent. With BBB impairment already shown in both clinical and pre-clinical cases using CE-MRI, this research has demonstrated that the impairment of the BBB is more complex than first expected. Multiple experiments were undertaken to examine the permeability of the BBB during the early and late stage of the HAT infection. These experiments confirmed that BBB impairment can be seen in the late stage of infection, but demonstrated there were no significant changes in water exchange at any point in the infection timeline. This result highlights the complexity of the mechanisms behind BBB impairment in infectious diseases and warrants further research in this area.

Astrocyte activation has been demonstrated in trypanosome infections. Hence, increased water exchange was expected due to the assumed increase in expression of AQP4 proteins on the astrocyte end-feet, which is known to facilitate water exchange into the tissue. However, this research found no significant difference in the pseudo-permeability of the BBB throughout the early and late stage of infection and provides an opportunity for further research into AQP4 during the HAT infection. As the method of transport across the BBB for trypanosomes is currently unclear, this research demonstrates that more exploration of the role of astrocytes and the mechanisms resulting in impairment of the BBB would be useful in this model. A final study on the BBB in HAT using the wet-dry method saw a significant decrease in the water content in the infected mouse brains compared to non-infection mice. This further provides evidence that BBB impairment can not be easily understood in HAT. Overall this research has opened up more questions about the process of BBB impairment in HAT and warrants further research, using both MRI and histological approaches.

The limited research and application of MR imaging in HAT was a motivating factor in the exploration of the spleen in HAT infected mice in Chapter 7. This study is the first to apply MR techniques to examine the spleen over the course of infection in individual animals using a serial study. Although splenomegaly was a recognised

symptom of HAT, there was no research looking at how the enlargement develops over the course of infection individually, or any research into splenomegaly in the GVR35 strain. Overall, it was shown that there is a significant increase in the spleen size during the early stage of infection before external signs of splenomegaly occur. The spleen continued to increase in size up to day 21 post-infection, but then decreased, with no significant difference in size between day 14 and 28 post-infection. Hence, this provides new insights into how the spleen responds to the HAT infection. Most studies into splenomegaly in HAT compare limited time points, making this study extremely useful in tracking the changes occurring in the spleen. This study is also the first to look at splenomegaly in the GVR35 strain, providing more information about this strain of trypanosome which may provide researchers with further insight into the pathology of this infection in the future.

Furthermore, this research provides HAT researchers with a non-invasive serial method to explore not just splenomegaly but other organs such as the kidneys, liver and heart. Further research into this area would be beneficial, especially when looking at drug treatments. It also provides evidence of early splenomegaly before other symptoms, which could help in a clinical setting, where symptoms for HAT are non-specific.

Overall, this project has developed and adapted novel methodologies that provide valuable new tools to facilitate further research in the investigation of the pathogenesis of trypanosomiasis. In addition, many of the sequences developed could be applied to investigate other conditions of novel therapeutic approaches in a pre-clinical setting. Furthermore, it is possible that the approaches could be translated to a clinical setting allowing improved, safer and non-invasive disease investigation.

References

Abbott, N. J. (2004). “Evidence for bulk flow of brain interstitial fluid: significance for physiology and pathology”. In: *Neurochem Int* 45.4, pp. 545–52.

Abbott, N. J., A. A. Patabendige, D. E. Dolman, S. R. Yusof, and D. J. Begley (2010). “Structure and function of the blood-brain barrier”. In: *Neurobiol Dis* 37.1, pp. 13–25.

Abbott, N. J., L. Ronnback, and E. Hansson (2006). “Astrocyte-endothelial interactions at the blood-brain barrier”. In: *Nat Rev Neurosci* 7.1, pp. 41–53.

Almutairi, M. M., C. Gong, Y. G. Xu, Y. Chang, and H. Shi (2016). “Factors controlling permeability of the blood-brain barrier”. In: *Cell Mol Life Sci* 73.1, pp. 57–77.

Alsop, D. C. and J. A. Detre (1996). “Reduced transit-time sensitivity in noninvasive magnetic resonance imaging of human cerebral blood flow”. In: *J Cereb Blood Flow Metab* 16.6, pp. 1236–49.

Alsop, D. C., J. A. Detre, X. Golay, M. Gunther, J. Hendrikse, L. Hernandez-Garcia, H. Lu, B. J. MacIntosh, L. M. Parkes, M. Smits, M. J. van Osch, D. J. Wang, E. C. Wong, and G. Zaharchuk (2015). “Recommended implementation of arterial spin-labeled perfusion MRI for clinical applications: A consensus of the ISMRM perfusion study group and the European consortium for ASL in dementia”. In: *Magn Reson Med* 73.1, pp. 102–16.

Amole, B. O., A. B. Clarkson, and H. L. Shear (1982). “Pathogenesis of anemia in Trypanosoma brucei-infected mice”. In: *Infect Immun* 36.3, pp. 1060–8.

Anosa, V. O. and J. J. Kaneko (1984). “Pathogenesis of Trypanosoma brucei infection in deer mice (Peromyscus maniculatus). Ultrastructural pathology of the spleen, liver, heart, and kidney”. In: *Vet Pathol* 21.2, pp. 229–37.

Armitage, P. A., A. J. Farrall, T. K. Carpenter, F. N. Doubal, and J. M. Wardlaw (2011). “Use of dynamic contrast-enhanced MRI to measure subtle blood-brain barrier abnormalities”. In: *Magn Reson Imaging* 29.3, pp. 305–14.

Ballabh, P., A. Braun, and M. Nedergaard (2004). “The blood-brain barrier: an overview: structure, regulation, and clinical implications”. In: *Neurobiol Dis* 16.1, pp. 1–13.

Barnes, S. R., T. S. Ng, A. Montagne, M. Law, B. V. Zlokovic, and R. E. Jacobs (2016). “Optimal acquisition and modeling parameters for accurate assessment of low

Ktrans blood-brain barrier permeability using dynamic contrast-enhanced MRI". In: *Magn Reson Med* 75.5, pp. 1967–77.

Baskerville, T. A., C. McCabe, C. J. Weir, I. M. Macrae, and W. M. Holmes (2012). "Noninvasive MRI measurement of CBF: evaluating an arterial spin labelling sequence with 99mTc-HMPAO CBF autoradiography in a rat stroke model". In: *J Cereb Blood Flow Metab* 32.6, pp. 973–7.

Bisoffi, Z., A. Beltrame, G. Monteiro, A. Arzese, S. Marocco, G. Rorato, M. Anselmi, and P. Viale (2005). "African trypanosomiasis gambiense, Italy". In: *Emerg Infect Dis* 11.11, pp. 1745–7.

Brix, G., W. Semmler, R. Port, L. R. Schad, G. Layer, and W. J. Lorenz (1991). "Pharmacokinetic parameters in CNS Gd-DTPA enhanced MR imaging". In: *J Comput Assist Tomogr* 15.4, pp. 621–8.

Brodal, P. (2010). *The Central Nervous System*. Oxford University Press.

Bronte, V. and M. J. Pittet (2013). "The spleen in local and systemic regulation of immunity". In: *Immunity* 39.5, pp. 806–18.

Bruce, David (1895). *Preliminary report on the tsetse fly disease or nagana, in Zululand*. Durban: Bennett & Davis.

Buck, J., J. R. Larkin, M. A. Simard, A. A. Khrapitchev, M. A. Chappell, and N. R. Sibson (2018). "Sensitivity of Multiphase Pseudocontinuous Arterial Spin Labelling (MP pCASL) Magnetic Resonance Imaging for Measuring Brain and Tumour Blood Flow in Mice". In: *Contrast Media Mol Imaging* 2018, p. 4580919.

Bushong, Stewart C. (1996). *Magnetic resonance imaging : physical and biological principles*. 2nd ed. St. Louis, Mo. ; London: Mosby.

Buxton, R. B., L. R. Frank, E. C. Wong, B. Siewert, S. Warach, and R. R. Edelman (1998). "A general kinetic model for quantitative perfusion imaging with arterial spin labeling". In: *Magn Reson Med* 40.3, pp. 383–96.

Callaghan, Paul T. (1991). *Principles of nuclear magnetic resonance microscopy*. Clarendon.

Cano RLE, Lopera HDE. (2013). "Introduction to T and B lymphocytes." In: *Autoimmunity: From Bench to Bedside*. Bogota (Colombia): El Rosario University Press.

Cardoso, F. L., D. Brites, and M. A. Brito (2010). "Looking at the blood-brain barrier: molecular anatomy and possible investigation approaches". In: *Brain Res Rev* 64.2, pp. 328–63.

Carr, D. H., J. Brown, G. M. Bydder, R. E. Steiner, H. J. Weinmann, U. Speck, A. S. Hall, and I. R. Young (1984). "Gadolinium-DTPA as a contrast agent in MRI: initial clinical experience in 20 patients". In: *AJR Am J Roentgenol* 143.2, pp. 215–24.

Castellani, Aldo (1903). "ON THE DISCOVERY OF A SPECIES OF TRYPANOSOMA IN THE CEREBROSPINAL FLUID OF CASES OF SLEEPING SICKNESS". In: *The Lancet* 161.4164, pp. 1735–1736.

Cesta, M. F. (2006). "Normal structure, function, and histology of the spleen". In: *Toxicol Pathol* 34.5, pp. 455–65.

Dai, W., D. Garcia, C. de Bazelaire, and D. C. Alsop (2008). “Continuous flow-driven inversion for arterial spin labeling using pulsed radio frequency and gradient fields”. In: *Magn Reson Med* 60.6, pp. 1488–97.

Deeken, J. F. and W. Loscher (2007). “The blood-brain barrier and cancer: transporters, treatment, and Trojan horses”. In: *Clin Cancer Res* 13.6, pp. 1663–74.

Detre, J. A., J. S. Leigh, D. S. Williams, and A. P. Koretsky (1992). “Perfusion imaging”. In: *Magn Reson Med* 23.1, pp. 37–45.

Dickie, B. R., M. Vandesquille, J. Ulloa, H. Boutin, L. M. Parkes, and G. J. M. Parker (2019). “Water-exchange MRI detects subtle blood-brain barrier breakdown in Alzheimer’s disease rats”. In: *Neuroimage* 184, pp. 349–358.

Duhamel, G., V. Callot, M. Tachrount, D. C. Alsop, and P. J. Cozzone (2012). “Pseudo-continuous arterial spin labeling at very high magnetic field (11.75 T) for high-resolution mouse brain perfusion imaging”. In: *Magn Reson Med* 67.5, pp. 1225–36.

Dutton, Joseph Everett and England Royal College of Surgeons of (1902). “Preliminary note upon a trypanosome occurring in the blood of man”. In:

Edelman, R. R., B. Siewert, D. G. Darby, V. Thangaraj, A. C. Nobre, M. M. Mesulam, and S. Warach (1994). “Qualitative mapping of cerebral blood flow and functional localization with echo-planar MR imaging and signal targeting with alternating radio frequency”. In: *Radiology* 192.2, pp. 513–20.

Ehrlich, P. (1900). “Das Sauerstoff-Bed urfnis des Organismus Eine Farbenanalytische Studie”. In: *Z Klin Med*.

Elmore, S. A. (2006). “Enhanced histopathology of the spleen”. In: *Toxicol Pathol* 34.5, pp. 648–55.

Elster, A. D. (1993). “Gradient-echo MR imaging: techniques and acronyms”. In: *Radiology* 186.1, pp. 1–8.

Engelhardt, B., P. Vajkoczy, and R. O. Weller (2017). “The movers and shapers in immune privilege of the CNS”. In: *Nat Immunol* 18.2, pp. 123–131.

Fan, A. P., H. Jahanian, S. J. Holdsworth, and G. Zaharchuk (2016). “Comparison of cerebral blood flow measurement with [15O]-water positron emission tomography and arterial spin labeling magnetic resonance imaging: A systematic review”. In: *J Cereb Blood Flow Metab* 36.5, pp. 842–61.

Feynman, Richard P., Robert B. Leighton, and Matthew L. Sands (2006). *The Feynman lectures on physics*. Definitive ed. San Francisco, [Calif.] ; London: Pearson / Addison-Wesley.

Franco, J. R., G. Cecchi, G. Priotto, M. Paone, A. Diarra, L. Grout, P. P. Simarro, W. Zhao, and D. Argaw (2018). “Monitoring the elimination of human African trypanosomiasis: Update to 2016”. In: *PLoS Negl Trop Dis* 12.12, e0006890.

Giraudeau, C., B. Djemai, M. A. Ghaly, F. Boumezbeur, S. Meriaux, P. Robert, M. Port, C. Robic, D. Le Bihan, F. Lethimonnier, and J. Valette (2012). “High sensitivity 19F MRI of a perfluorooctyl bromide emulsion: application to a dynamic

biodistribution study and oxygen tension mapping in the mouse liver and spleen". In: *NMR Biomed* 25.4, pp. 654–60.

Goldmann, E. E. (1909). "Dieaussere und innere Sekretion des gesunden und kranken Organismus im Lichte der vitalen Farbung". In:

Goldmann, E. E. (1913). "Vitalfarbung am Zentralnervensystem: beitrag zur Physiopathologie des plexus chorioideus der Hirnhaute". In: *Abh Preuss Akad Wiss Physik-Math 1*.

Grobner, T. (2006). "Gadolinium–a specific trigger for the development of nephrogenic fibrosing dermopathy and nephrogenic systemic fibrosis?" In: *Nephrol Dial Transplant* 21.4, pp. 1104–8.

Gursoy-Ozdemir, Yasemin and Yagmur Cetin Tas (2017). "Chapter 1 - Anatomy and Physiology of the Blood-Brain Barrier". In: *Nanotechnology Methods for Neurological Diseases and Brain Tumors*. Ed. by Yasemin Gursoy-Ozdemir, Sibel Bozdag-Pehlivan, and Emine Sekerdag. Academic Press, pp. 3–13.

Haines, D.E. (2018). "Chapter 7 - The Meninges". In: *Fundamental Neuroscience for Basic and Clinical Applications (Fifth Edition)*. Ed. by Duane E. Haines and Gregory A. Mihailoff. Fifth Edition. Elsevier, 107–121.e1.

Henkelman, R. M., J. J. Neil, and Q. S. Xiang (1994). "A quantitative interpretation of IVIM measurements of vascular perfusion in the rat brain". In: *Magn Reson Med* 32.4, pp. 464–9.

Hennig, J., A. Nauerth, and H. Friedburg (1986). "RARE imaging: a fast imaging method for clinical MR". In: *Magn Reson Med* 3.6, pp. 823–33.

Herbert, W. J. and W. H. Lumsden (1976). "Trypanosoma brucei: a rapid "matching" method for estimating the host's parasitemia". In: *Exp Parasitol* 40.3, pp. 427–31.

Hirschler, L., L. P. Munting, A. Khmelinskii, W. M. Teeuwisse, E. Suidgeest, J. M. Warnking, L. van der Weerd, E. L. Barbier, and M. J. P. van Osch (2018). "Transit time mapping in the mouse brain using time-encoded pCASL". In: *NMR Biomed* 31.2.

Hong, C. S., W. Ho, M. G. Piazza, A. Ray-Chaudhury, Z. Zhuang, and J. D. Heiss (2016). "Characterization of the blood brain barrier in pediatric central nervous system neoplasms". In: *J Interdiscip Histopathol* 4.2, pp. 29–33.

Hurle, Robert L., Allan J. Easteal, and Lawrence A. Woolf (1985). "Self-diffusion in monohydric alcohols under pressure. Methanol, methan(2H)ol and ethanol". In: *Journal of the Chemical Society, Faraday Transactions 1: Physical Chemistry in Condensed Phases* 81.3, pp. 769–779.

Ichikawa, Y. and A.P.S. Selvadurai (2012). *Transport Phenomena in Porous Media: Aspects of Micro/Macro Behaviour*. Springer Berlin Heidelberg.

Kager, P. A., H. G. Schipper, J. Stam, and C. B. Majoie (2009). "Magnetic resonance imaging findings in human African trypanosomiasis: a four-year follow-up study

in a patient and review of the literature". In: *Am J Trop Med Hyg* 80.6, pp. 947–52.

Kanda, T., K. Ishii, H. Kawaguchi, K. Kitajima, and D. Takenaka (2014). "High signal intensity in the dentate nucleus and globus pallidus on unenhanced T1-weighted MR images: relationship with increasing cumulative dose of a gadolinium-based contrast material". In: *Radiology* 270.3, pp. 834–41.

Kaur, C., V. Sivakumar, Y. Zhang, and E. A. Ling (2006). "Hypoxia-induced astrocytic reaction and increased vascular permeability in the rat cerebellum". In: *Glia* 54.8, pp. 826–39.

Kennedy, P. G., J. Rodgers, F. W. Jennings, M. Murray, S. E. Leeman, and J. M. Burke (1997). "A substance P antagonist, RP-67,580, ameliorates a mouse meningoencephalitic response to Trypanosoma brucei brucei". In: *Proc Natl Acad Sci U S A* 94.8, pp. 4167–70.

Kennedy, Peter. (2008). "The continuing problem of human African trypanosomiasis (sleeping sickness)". In: *Ann Neurol* 64.2, pp. 116–26.

Kennedy, Peter. (2013). "Clinical features, diagnosis, and treatment of human African trypanosomiasis (sleeping sickness)". In: *The Lancet Neurology* 12.2, pp. 186–194.

Kennedy, Peter. and J. Rodgers (2019). "Clinical and Neuropathogenetic Aspects of Human African Trypanosomiasis". In: *Front Immunol* 10, p. 39.

Kety, S. S. (1951). "The theory and applications of the exchange of inert gas at the lungs and tissues". In: *Pharmacol Rev* 3.1, pp. 1–41.

Kim, S. G. (1995). "Quantification of relative cerebral blood flow change by flow-sensitive alternating inversion recovery (FAIR) technique: application to functional mapping". In: *Magn Reson Med* 34.3, pp. 293–301.

Kim, T. and S. G. Kim (2006). "Quantification of cerebral arterial blood volume using arterial spin labeling with intravoxel incoherent motion-sensitive gradients". In: *Magn Reson Med* 55.5, pp. 1047–57.

Kindt, Thomas J., Richard A. Goldsby, Barbara Anne Osborne, and Janis Kuby (2007). *Kuby immunology*. New York: W.H. Freeman.

Kristensson, K., M. Nygard, G. Bertini, and M. Bentivoglio (2010). "African trypanosome infections of the nervous system: parasite entry and effects on sleep and synaptic functions". In: *Prog Neurobiol* 91.2, pp. 152–71.

Kwong, K. K., D. A. Chesler, R. M. Weisskoff, K. M. Donahue, T. L. Davis, L. Ostergaard, T. A. Campbell, and B. R. Rosen (1995). "MR perfusion studies with T1-weighted echo planar imaging". In: *Magn Reson Med* 34.6, pp. 878–87.

Lalatsa, A. and A. M. Butt (2018). "Chapter 3 - Physiology of the Blood- Barrier and Mechanisms of Transport Across the BBB". In: *Nanotechnology - Targeted Drug Delivery Systems for Brain Tumors*. Ed. by Prashant Kesharwani and Umesh Gupta. Academic Press, pp. 49–74.

Larkin, J. R., M. A. Simard, A. A. Khrapitchev, J. A. Meakin, T. W. Okell, M. Craig, K. J. Ray, P. Jezzard, M. A. Chappell, and N. R. Sibson (2019). “Quantitative blood flow measurement in rat brain with multiphase arterial spin labelling magnetic resonance imaging”. In: *J Cereb Blood Flow Metab* 39.8, pp. 1557–1569.

Le Bihan, D., E. Breton, D. Lallemand, P. Grenier, E. Cabanis, and M. Laval-Jeantet (1986). “MR imaging of intravoxel incoherent motions: application to diffusion and perfusion in neurologic disorders”. In: *Radiology* 161.2, pp. 401–7.

Lejon, V. and P. Buscher (2005). “Review Article: cerebrospinal fluid in human African trypanosomiasis: a key to diagnosis, therapeutic decision and post-treatment follow-up”. In: *Trop Med Int Health* 10.5, pp. 395–403.

Levitt, Malcolm H. (2008). *Spin dynamics : basics of nuclear magnetic resonance*. 2nd ed. Hoboken, N.J.: Wiley ; Chichester : John Wiley [distributor].

Lewandowsky, M. (1900). “Zur Lehre der Zerebrospinalflussigkeit”. In: *Z Klin Med*.

Lohrke, J., T. Frenzel, J. Endrikat, F. C. Alves, T. M. Grist, M. Law, J. M. Lee, T. Leiner, K. C. Li, K. Nikolaou, M. R. Prince, H. H. Schild, J. C. Weinreb, K. Yoshikawa, and H. Pietsch (2016). “25 Years of Contrast-Enhanced MRI: Developments, Current Challenges and Future Perspectives”. In: *Adv Ther* 33.1, pp. 1–28.

MacLean, L. M., M. Odiit, J. E. Chisi, P. G. Kennedy, and J. M. Sternberg (2010). “Focus-specific clinical profiles in human African Trypanosomiasis caused by Trypanosoma brucei rhodesiense”. In: *PLoS Negl Trop Dis* 4.12, e906.

Matthews, Keith R. (2005). “The developmental cell biology of Trypanosoma brucei”. In: *Journal of Cell Science* 118.2, pp. 283–290. eprint: `https://jcs.biologists.org/content/118/2/283.full.pdf`.

McDonald, R. J., J. S. McDonald, D. F. Kallmes, M. E. Jentoft, M. A. Paolini, D. L. Murray, E. E. Williamson, and L. J. Eckel (2017). “Gadolinium Deposition in Human Brain Tissues after Contrast-enhanced MR Imaging in Adult Patients without Intracranial Abnormalities”. In: *Radiology* 285.2, pp. 546–554.

McKenzie, C. V., C. K. Colonne, J. H. Yeo, and S. T. Fraser (2018). “Splenomegaly: Pathophysiological bases and therapeutic options”. In: *Int J Biochem Cell Biol* 94, pp. 40–43.

Mebius, R. E. and G. Kraal (2005). “Structure and function of the spleen”. In: *Nat Rev Immunol* 5.8, pp. 606–16.

Moffat, B. A., T. L. Chenevert, D. E. Hall, A. Rehemtulla, and B. D. Ross (2005). “Continuous arterial spin labeling using a train of adiabatic inversion pulses”. In: *J Magn Reson Imaging* 21.3, pp. 290–6.

Morrison, W. I., M. Murray, and D. L. Bovell (1981). “Response of the murine lymphoid system to a chronic infection with Trypanosoma congolense. I. The spleen”. In: *Lab Invest* 45.6, pp. 547–57.

Muir, E. R., Q. Shen, and T. Q. Duong (2008). “Cerebral blood flow MRI in mice using the cardiac-spin-labeling technique”. In: *Magn Reson Med* 60.3, pp. 744–8.

Mulenga, C., J. D. Mhlanga, K. Kristensson, and B. Robertson (2001). “Trypanosoma brucei brucei crosses the blood-brain barrier while tight junction proteins are preserved in a rat chronic disease model”. In: *Neuropathol Appl Neurobiol* 27.1, pp. 77–85.

Murray, P. K., F. W. Jennings, M. Murray, and G. M. Urquhart (1974a). “The nature of immunosuppression in Trypanosoma brucei infections in mice. I. The role of the macrophage”. In: *Immunology* 27.5, pp. 815–24.

Murray, P. K., F. W. Jennings, M. Murray, and G. M. Urquhart (1974b). “The nature of immunosuppression in Trypanosoma brucei infections in mice. II. The role of the T and B lymphocytes”. In: *Immunology* 27.5, pp. 825–40.

Nduom, E. K., C. Yang, M. J. Merrill, Z. Zhuang, and R. R. Lonser (2013). “Characterization of the blood-brain barrier of metastatic and primary malignant neoplasms”. In: *J Neurosurg* 119.2, pp. 427–33.

O’Connell, K. E., A. M. Mikkola, A. M. Stepanek, A. Vernet, C. D. Hall, C. C. Sun, E. Yildirim, J. F. Staropoli, J. T. Lee, and D. E. Brown (2015). “Practical murine hematopathology: a comparative review and implications for research”. In: *Comp Med* 65.2, pp. 96–113.

Ohene, Y., I. F. Harrison, P. Nahavandi, O. Ismail, E. V. Bird, O. P. Ottersen, E. A. Nagelhus, D. L. Thomas, M. F. Lythgoe, and J. A. Wells (2019). “Non-invasive MRI of brain clearance pathways using multiple echo time arterial spin labelling: an aquaporin-4 study”. In: *Neuroimage* 188, pp. 515–523.

Ouyang, C. and B. P. Sutton (2011). “Pseudo-continuous transfer insensitive labeling technique”. In: *Magn Reson Med* 66.3, pp. 768–76.

Palas, J., A. P. Matos, and M. Ramalho (2013). “The spleen revisited: an overview on magnetic resonance imaging”. In: *Radiol Res Pract* 2013, p. 219297.

Palomares, J. A., S. Tummala, D. J. J. Wang, B. Park, M. A. Woo, D. W. Kang, K. S. St Lawrence, R. M. Harper, and R. Kumar (2015). “Water Exchange across the Blood-Brain Barrier in Obstructive Sleep Apnea: An MRI Diffusion-Weighted Pseudo-Continuous Arterial Spin Labeling Study”. In: *Journal of Neuroimaging* 25.6, pp. 900–905.

Papadopoulos, M. C. and A. S. Verkman (2013). “Aquaporin water channels in the nervous system”. In: *Nat Rev Neurosci* 14.4, pp. 265–77.

Parkes, L. M., W. Rashid, D. T. Chard, and P. S. Tofts (2004). “Normal cerebral perfusion measurements using arterial spin labeling: reproducibility, stability, and age and gender effects”. In: *Magn Reson Med* 51.4, pp. 736–43.

Patel, N. K., A. Clegg, M. Brown, and H. Hyare (2018). “MRI findings of the brain in human African trypanosomiasis: a case series and review of the literature”. In: *BJR Case Rep* 4.4, p. 20180039.

Persidsky, Y., S. H. Ramirez, J. Haorah, and G. D. Kanmogne (2006). “Blood-brain barrier: structural components and function under physiologic and pathologic conditions”. In: *J Neuroimmune Pharmacol* 1.3, pp. 223–36.

Philip, K. A., M. J. Dascombe, P. A. Fraser, and V. W. Pentreath (1994). “Blood-brain barrier damage in experimental African trypanosomiasis”. In: *Ann Trop Med Parasitol* 88.6, pp. 607–16.

Raja, R., G. A. Rosenberg, and A. Caprihan (2018). “MRI measurements of Blood-Brain Barrier function in dementia: A review of recent studies”. In: *Neuropharmacology* 134.Pt B, pp. 259–271.

Reese, T. S. and M. J. Karnovsky (1967). “Fine structural localization of a blood-brain barrier to exogenous peroxidase”. In: *J Cell Biol* 34.1, pp. 207–17.

Rodgers, J., B. Bradley, and P. Kennedy (2017). “Delineating neuroinflammation, parasite CNS invasion, and blood-brain barrier dysfunction in an experimental murine model of human African trypanosomiasis”. In: *Methods* 127, pp. 79–87.

Rodgers, J., A. Jones, S. Gibaud, B. Bradley, C. McCabe, M. P. Barrett, G. Gettinby, and P. G. Kennedy (2011). “Melarsoprol cyclodextrin inclusion complexes as promising oral candidates for the treatment of human African trypanosomiasis”. In: *PLoS Negl Trop Dis* 5.9, e1308.

Rodgers, J., C. McCabe, G. Gettinby, B. Bradley, B. Condon, and P. Kennedy (2011). “Magnetic Resonance Imaging to Assess Blood-Brain Barrier Damage in Murine Trypanosomiasis”. In: *American Journal of Tropical Medicine and Hygiene* 84.2, pp. 344–350.

Sandoval, K. E. and K. A. Witt (2008). “Blood-brain barrier tight junction permeability and ischemic stroke”. In: *Neurobiol Dis* 32.2, pp. 200–19.

Schmidt, H. (1983). “The pathogenesis of trypanosomiasis of the CNS. Studies on parasitological and neurohistological findings in trypanosoma rhodesiense infected vervet monkeys”. In: *Virchows Arch A Pathol Anat Histopathol* 399.3, pp. 333–43.

Segal, M. B. (2000). “The choroid plexuses and the barriers between the blood and the cerebrospinal fluid”. In: *Cell Mol Neurobiol* 20.2, pp. 183–96.

Shao, X., S. J. Ma, M. Casey, L. D’Orazio, J. M. Ringman, and D. J. J. Wang (2019). “Mapping water exchange across the blood-brain barrier using 3D diffusion-prepared arterial spin labeled perfusion MRI”. In: *Magn Reson Med* 81.5, pp. 3065–3079.

Silva, A. C., D. S. Williams, and A. P. Koretsky (1997). “Evidence for the exchange of arterial spin-labeled water with tissue water in rat brain from diffusion-sensitized measurements of perfusion”. In: *Magn Reson Med* 38.2, pp. 232–7.

Smirnov, P., F. Gazeau, M. Lewin, J. C. Bacri, N. Siauve, C. Vayssettes, C. A. Cuenod, and O. Clement (2004). “In vivo cellular imaging of magnetically labeled hybridomas in the spleen with a 1.5-T clinical MRI system”. In: *Magn Reson Med* 52.1, pp. 73–9.

Sourbron, S. P. and D. L. Buckley (2013). “Classic models for dynamic contrast-enhanced MRI”. In: *NMR Biomed* 26.8, pp. 1004–27.

St Lawrence, K. S., J. A. Frank, and A. C. McLaughlin (2000). “Effect of restricted water exchange on cerebral blood flow values calculated with arterial spin tagging: a theoretical investigation”. In: *Magn Reson Med* 44.3, pp. 440–9.

St Lawrence, K. S., D. Owen, and D. J. Wang (2012). “A two-stage approach for measuring vascular water exchange and arterial transit time by diffusion-weighted perfusion MRI”. In: *Magn Reson Med* 67.5, pp. 1275–84.

Stehling, M. K., R. Turner, and P. Mansfield (1991). “Echo-planar imaging: magnetic resonance imaging in a fraction of a second”. In: *Science* 254.5028, pp. 43–50.

Stejskal, E. O. and J. E. Tanner (1965). “Spin Diffusion Measurements: Spin Echoes in the Presence of a Time-Dependent Field Gradient”. In: *The Journal of Chemical Physics* 42.1, pp. 288–292.

Stephens, J. and H. Fantham (1910). “On the Peculiar Morphology of a Trypanosome from a Case of Sleeping Sickness and the Possibility of Its Being a New Species (T. rhodesiense)”. In: *Proceedings of the Royal Society of London. Series B, Containing Papers of a Biological Character* 83.561, pp. 28–33.

Stern, L. (1921). “II. Les Rapports Entre Le Liquide Cephalo-Rachidien Et Les elements Nerveux De L’axe Cerebrospinal”. In: *Archives Internationales de Physiologie* 4, p. 391.

Stern, L. (1922). “Recherches Sur Le Liquide Cephalo-Rachidien: I. Les Rapports Entre Le Liquide Cephalo-Rachidien et la Circulation Sanguine”. In: *Archives Internationales de Physiologie* 2, p. 138.

Tanaka, Kazuko (1978). “Self-diffusion coefficients of water in pure water and in aqueous solutions of several electrolytes with 18O and 2H as tracers”. In: *Journal of the Chemical Society, Faraday Transactions 1: Physical Chemistry in Condensed Phases* 74, pp. 1879–1881.

Thomas, D. L., M. F. Lythgoe, L. van der Weerd, R. J. Ordidge, and D. G. Gadian (2006). “Regional variation of cerebral blood flow and arterial transit time in the normal and hypoperfused rat brain measured using continuous arterial spin labeling MRI”. In: *J Cereb Blood Flow Metab* 26.2, pp. 274–82.

Tilanus, Hugo W. (2005). “The Spleen”. In: *Upper Gastrointestinal Surgery*. London: Springer London, pp. 59–67.

Tiwari, Y. V., J. Lu, Q. Shen, B. Cerqueira, and T. Q. Duong (2017). “Magnetic resonance imaging of blood-brain barrier permeability in ischemic stroke using diffusion-weighted arterial spin labeling in rats”. In: *J Cereb Blood Flow Metab* 37.8, pp. 2706–2715.

Tofts, P. S. (1997). “Modeling tracer kinetics in dynamic Gd-DTPA MR imaging”. In: *J Magn Reson Imaging* 7.1, pp. 91–101.

Tofts, Paul (2003). *Quantitative MRI of the brain : measuring changes caused by disease*. Chichester: Wiley.

Vallatos, A., L. Gilmour, A. J. Chalmers, and W. M. Holmes (2018). “Multiple boli arterial spin labeling for high signal-to-noise rodent brain perfusion imaging”. In: *Magn Reson Med* 79.2, pp. 1020–1030.

Varatharaj, A. and I. Galea (2017). “The blood-brain barrier in systemic inflammation”. In: *Brain Behav Immun* 60, pp. 1–12.

Vein, A. A. (2008). “Science and fate: Lina Stern (1878-1968), a neurophysiologist and biochemist”. In: *J Hist Neurosci* 17.2, pp. 195–206.

Vickerman, K. (1985). “Developmental cycles and biology of pathogenic trypanosomes”. In: *Br Med Bull* 41.2, pp. 105–14.

Vickerman, K., L. Tetley, K. A. Hendry, and C. M. Turner (1988). “Biology of African trypanosomes in the tsetse fly”. In: *Biol Cell* 64.2, pp. 109–19.

Wang, J., D. C. Alsop, H. K. Song, J. A. Maldjian, K. Tang, A. E. Salvucci, and J. A. Detre (2003). “Arterial transit time imaging with flow encoding arterial spin tagging (FEAST)”. In: *Magn Reson Med* 50.3, pp. 599–607.

Wang, J., M. A. Fernandez-Seara, S. Wang, and K. S. St Lawrence (2007). “When perfusion meets diffusion: in vivo measurement of water permeability in human brain”. In: *J Cereb Blood Flow Metab* 27.4, pp. 839–49.

Wegener, S., W. C. Wu, J. E. Perthen, and E. C. Wong (2007). “Quantification of rodent cerebral blood flow (CBF) in normal and high flow states using pulsed arterial spin labeling magnetic resonance imaging”. In: *J Magn Reson Imaging* 26.4, pp. 855–62.

Weiss, Douglas J., K. Jane Wardrop, and O. W. Schalm (2010). *Schalm’s veterinary hematology*. Ames, Iowa: Wiley-Blackwell.

Wells, J. A., B. Siow, M. F. Lythgoe, and D. L. Thomas (2013). “Measuring biexponential transverse relaxation of the ASL signal at 9.4 T to estimate arterial oxygen saturation and the time of exchange of labeled blood water into cortical brain tissue”. In: *J Cereb Blood Flow Metab* 33.2, pp. 215–24.

Wells, J. A., D. L. Thomas, T. Saga, J. Kershaw, and I. Aoki (2017). “MRI of cerebral micro-vascular flow patterns: A multi-direction diffusion-weighted ASL approach”. In: *J Cereb Blood Flow Metab* 37.6, pp. 2076–2083.

Wengert, O., M. Kopp, E. Siebert, W. Stenzel, G. Hegasy, N. Suttorp, A. Stich, and T. Zoller (2014). “Human African trypanosomiasis with 7-year incubation period: clinical, laboratory and neuroimaging findings”. In: *Parasitol Int* 63.3, pp. 557–60.

Werner, E. J., A. Datta, C. J. Jocher, and K. N. Raymond (2008). “High-relaxivity MRI contrast agents: where coordination chemistry meets medical imaging”. In: *Angew Chem Int Ed Engl* 47.45, pp. 8568–80.

WHO (2013). *WHO, Control and surveillance of human African trypanosomiasis: report of a WHO expert committee., WHO technical report series, Geneva 984*.

Williams, D. S., J. A. Detre, J. S. Leigh, and A. P. Koretsky (1992). “Magnetic-Resonance-Imaging of Perfusion Using Spin Inversion of Arterial Water”. In: *Pro-*

ceedings of the National Academy of Sciences of the United States of America 89.1, pp. 212–216.

Wu, W. C., M. Fernandez-Seara, J. A. Detre, F. W. Wehrli, and J. Wang (2007). "A theoretical and experimental investigation of the tagging efficiency of pseudo-continuous arterial spin labeling". In: *Magn Reson Med* 58.5, pp. 1020–7.

Young, Hugh D. and Roger A. Freedman (2011). *Sears and Zemansky's University Physics with Modern Physics*. Thirteenth Edition, Pearson New International Edition.

Zenaro, E., G. Piacentino, and G. Constantin (2017). "The blood-brain barrier in Alzheimer's disease". In: *Neurobiol Dis* 107, pp. 41–56.

Zhang, X., C. Ingo, W. M. Teeuwisse, Z. Chen, and M. J. P. van Osch (2018). "Comparison of perfusion signal acquired by arterial spin labeling-prepared intravoxel incoherent motion (IVIM) MRI and conventional IVIM MRI to unravel the origin of the IVIM signal". In: *Magn Reson Med* 79.2, pp. 723–729.

Zhu, X. X. and P. M. Macdonald (1992). "Pulsed-gradient spin-echo NMR measurements of the diffusion coefficients of ketones in poly(methyl methacrylate)". In: *Macromolecules* 25.17, pp. 4345–4351.

Appendix A

Classical Derivation of the Larmor Equation

If a magnetic moment μ is placed in a magnetic field, it will experience a torque τ equal to:

$$\tau = \mu \times B \tag{A.1}$$

And will precess around the axis of the magnetic field, where the change in angular momentum is equal to:

$$\Delta \mathbf{L} = \mathbf{L} sin(\theta)\omega\Delta t \tag{A.2}$$

for a small time Δt with ω the angular velocity, and $\mathbf{L} sin\theta$ the radius from the magnetic field axis. The rate of change of angular momentum (which is equivalent to torque) can be written as:

$$\frac{d\mathbf{L}}{dt} = \mathbf{L} sin(\theta)\omega \tag{A.3}$$

By combining A.2 and A.3, the following relationship occurs
(where $\mu = \mu sin\theta$):

$$\mu \mathbf{B}\ sin(\theta) = \omega \mathbf{L} sin(\theta) \tag{A.4}$$

Where the Larmor equation is:

$$\omega_0 = \frac{\mu}{\mathbf{L}}\mathbf{B} = \gamma \mathbf{B}_0 \tag{A.5}$$

Appendix B

Recipe for solutions in HAT Infection

Phosphate buffered saline (PBS)

Di-sodium hydrogen phosphate (anhydrous) 1.48g
Potassium di-hydrogen pohsphate (anhydrous) 0.43g
Sodium chloride 7.2g

Add the above to 800ml of distilled water with the solution stirred constantly. Adjust to pH to a value of 7.4 and then add distilled water untill the volume is one litre.

Phosphate glucose buffer saline (PGBS)

Stock buffer (containing no glucose

Di-sodium hydrogen phosphate (anhydrous) 13.48g
Potassium di-hydrogen pohsphate (anhydrous) 0.622g
Sodium chloride 4.25g

Dissolve the above in one litre of distilled water and adjust the pH to 8.0.

Working solution (containing glucose)

Dilute the stock buffer in a ratio of 6:4 distilled water and add 15g/l of glucose

Appendix C

MR Images of the Spleen

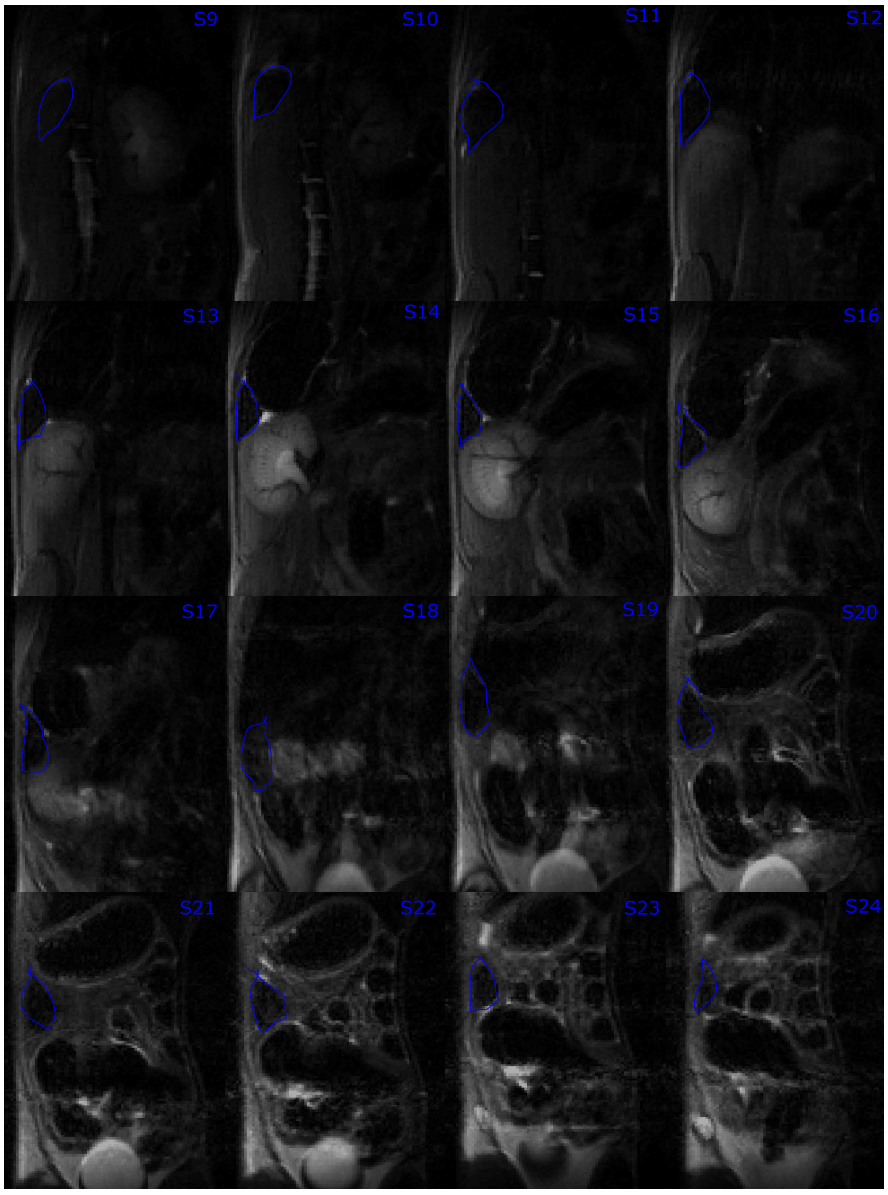

Figure C.1: T_2 images of the spleen for one healthy animal

For one healthy mouse, all slices containing the spleen are shown from a T_2 weighted scan. The typical triangular cross section is seen.

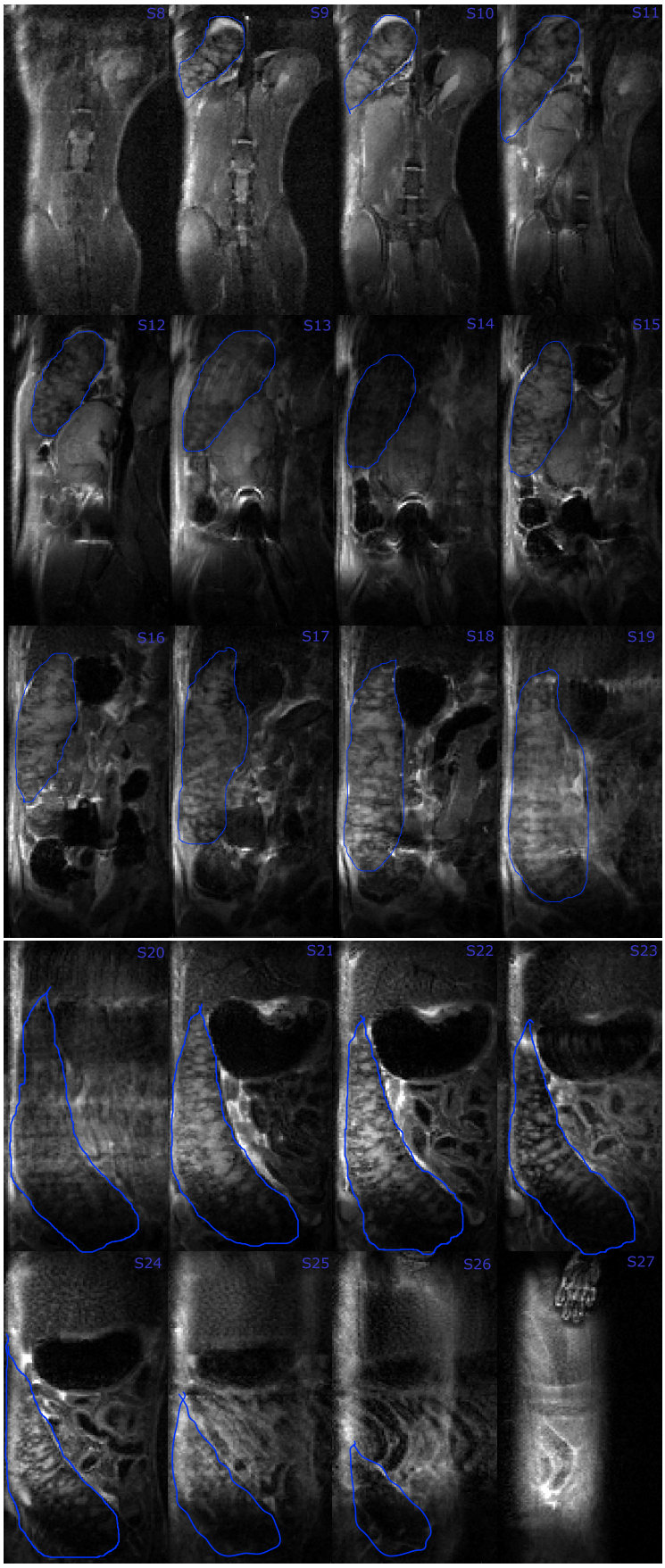

Figure C.2: T_1 images of the spleen for one infected animal

For one infected mouse, all slices containing the spleen are shown from a T_1 weighted scan. The splenomegaly is clear throughout all the images, with an elongated shape and displacement of other organs seen throughout.